

UNDERSTANDING VEHICLE-BRIDGE INTERACTION
THROUGH FIELD MEASUREMENTS AND MODEL-BASED SIMULATIONS

By

JOHN BURTON BRALEY

A dissertation submitted to the

School of Graduate Studies

Rutgers, The State University of New Jersey

In partial fulfillment of the requirements

For the degree of

Doctor of Philosophy

Graduate Program in Civil & Environmental Engineering

Written under the direction of

Franklin L Moon

And approved by

New Brunswick, New Jersey

October 2019

ABSTRACT OF THE DISSERTATION

Understanding Vehicle-Bridge Interaction through Field Measurements and Model-Based Simulations

By JOHN BRALEY

**Dissertation Director:
Franklin L Moon**

Driven by a desire for simplicity, bridge design and assessment approaches have historically employed a static model to estimate the forces and displacements resulting from trucks (the largest live loads that bridges experience). While these methods apply a constant factor in an attempt to account for the amplification that occurs due to the dynamic nature of truck loads, this approach fails to properly account for the dynamic interaction between trucks and bridges. As bridge designs continue to trade-off conservatism for cost savings, and loadings continue to increase (both in terms of magnitude, frequency, and nature (e.g. truck platooning)), historically-adequate simplifying assumptions (such as those associated with modeling truck loads in a static manner) must be critically examined to ensure their continued applicability.

Towards that end, the overarching aim of this research is to critically examine vehicle-bridge interaction (VBI) and develop a series of recommendations for how it should be addressed within the context of bridge design and assessment. More specifically, the following three objectives were identified to guide this research:

- (1) Establish the mechanisms that result in levels of VBI that render the common static live load model unconservative,
- (2) For the cases identified in (1) develop and validate a practical approach to estimating the effects of truck loads inclusive of VBI, and
- (3) Identify bridge vulnerabilities associated with truck platooning and make recommendations related to how VBI should be estimated and mitigated.

These objectives were realized by taking an inductive approach whereby a structure exhibiting large vibration levels was investigated to identify and characterize the underlying mechanisms through the Structural Identification (StId) framework. A series of field tests of this structure were performed to obtain operational responses that were subsequently used to calibrate and validate an FE model that was subsequently employed to simulate VBI using modal superposition methods. The parameters examined in this study include roadway profile, vehicle suspension parameters, and bridge dynamic characteristics. The results from this study were employed to develop and validate a practical, simplified model for estimating dynamic load levels. This model was employed through a series of parametric studies to generate recommendations related to a wide range of issues including bridge assessment, construction, and policies related to truck platooning. Key findings include:

- A simple model that reduces both the bridge and vehicle to single degree-of-freedom systems was shown to reliably predict dynamic amplification and is recommended when FE simulation is impractical.
- Bridge responses are greatest when the profile induces oscillation in the vehicle close to the bridge's natural frequency and when the vehicle's natural frequency is 10-20% greater than that of the bridge.
- Rolling-straightedge length should be no less than 16 feet for a specified deviation of $1/8^{\text{th}}$ inch, and no less than 30 feet for a specified deviation of $\frac{1}{4}$ inch.
- Traffic and truck platoons can result in increased dynamic amplification because even a single previous truck can induce the bridge conditions (motion) that result in increased dynamic response.
- As spacing between vehicles decreases and more vehicles are present on the bridge, the static load effect increases, but the dynamic amplification will likely be less than what would occur for a single vehicle.

Acknowledgements

This research was funded in part by contributions from the Federal Highway Administration.

I would like to thank my dissertation committee: H Wang, H. Najm, and N. Dubbs for their comments, criticisms, and advice. My advisor, Frank Moon, has been a great mentor throughout my graduate studies and a constant source of inspiration. I would like to extend my sincere gratitude to him for providing me this opportunity.

I'd like to thank my family and friends for their good humor and support during this endeavor. I am especially grateful to my friends and colleagues, John DeVitis, David Masceri, Nick Romano and Dom Wirkijowski for their extensive help over these several years.

Table of Contents

ABSTRACT OF THE DISSERTATION	ii
Acknowledgements.....	iv
Table of Contents.....	v
List of Tables	viii
List of Figures	xi
Chapter 1: Introduction	1
Societal Context	1
Current State of Transportation Infrastructure	1
Key Knowledge Gap: Influence of Trucks on Bridge Performances.....	2
Overview of Vehicle-Bridge Interaction.....	3
Research Objectives and Scope	5
Summary of Thesis Chapters	6
Chapter 2: Literature Review.....	12
Dynamic Amplification in Bridge Codes.....	12
Experimental Evaluation of Amplification Factors.....	13
Modeling Vehicle-Bridge Interaction	15
Influential Parameters for Dynamic Amplification	18
Effects of Platooned Vehicles	21
Bridge Vibration Limits.....	22

Knowledge Gaps	23
 Part 1: Understanding Vehicle-Bridge Interaction and Dynamic Amplification.....	25
Chapter 3: Description of Case Structure	29
Chapter 4: Preliminary Modeling of Test Structure.....	33
Chapter 5: Phase 1 Testing	39
Chapter 6: Phase 2 Testing	46
Chapter 7: Phase 3 Testing	81
Chapter 8: VBI Model Validation	101
Chapter 9: Part 1 Summary and Conclusions	126
 Part 2: Estimating Dynamic Amplification.....	127
Chapter 10: Components of Vehicle Bridge Interaction.....	129
Chapter 11: In-Situ Measurement	131
Chapter 12: Model-Based Simulation	140
Chapter 13: Simplified Model Formulation	145
Chapter 14: IRI & Other Vehicle-Only Models.....	173
Chapter 15: VBI Mechanisms and Parameters	176
Chapter 16: Part 2 Summary and Conclusions	194
 Part 3: Applications in Vehicle-Bridge Interaction	196
Chapter 17: Remediation and Smoothness Criteria	197
Chapter 18: Multiple Vehicles.....	202

Chapter 19: Conclusions and Future Work.....	217
Appendix	221
Testing Equipment	221
Phase 1 Testing	221
Phase 2 Testing	223
Phase 2 FE Model Validation	226
Methods of Performing Load Rating through Refined Analysis	227
Comparison of Experimental and FEM Mode Shapes	229
VBI Modeling Validation	231
State-Space Model Validation.....	241
Simulation of VBI with Traffic	244
List of References.....	248

List of Tables

Table 1.3.1: NBI Details of Case Structure	32
Table 1.4.1: Cross-Girder Boundary Conditions (Nodal Restraints).....	35
Table 1.5.1: Testing Equipment Model Info.....	41
Table 1.6.1: Phase 2 Testing Equipment Details.....	49
Table 1.6.2: Phase 2 Testing Weather Conditions	52
Table 1.6.3: Model Parameter Values	74
Table 1.6.4: Frequency of Mode Shapes from Experimental Data and FEA.....	74
Table 1.6.5: LRFD flexural ratings using refined analysis for 0.4 of span length	77
Table 1.6.6: Operational vs Rating Bridge Responses (Midspan, Bottom-Flange)	77
Table 1.6.7: Live Load and Impact Factors.....	79
Table 1.7.1: Phase 3 Test Equipment Model Specifications	84
Table 1.7.2: Test Vehicle Wheel Weights	86
Table 1.7.3: Meta Data for Test Runs	87
Table 1.7.4: Ames Model 8300 Profiler Specifications	87
Table 1.7.5: RMS Values for (Run 6) Truck Acceleration Before and On Bridge.....	91
Table 1.7.6: Girders Reported Corresponding to Lane of Travel	100
Table 1.8.1: Displacement Comparison for Different Representations of Diaphragms	104
Table 1.8.2: Diaphragm Equivalent Beam Element Section Properties.....	104
Table 1.8.3: Pedestal Beam Element Attributes	105

Table 1.8.4: Pedestal Element End Releases (Translational)	105
Table 1.8.5: Cross-Girder Boundary Node Restraints	106
Table 1.8.6: Influence of Mesh Size on Model Responses.....	106
Table 1.8.7: Comparison of Experimental and FE (LUSAS) Mode Shape Frequencies.....	109
Table 1.8.8: Parameter Values for Initial Vehicle Model	111
Table 1.8.9: SDOF Vehicle Model Final Parameter Values	114
Table 1.8.10: Mean Absolute Errors for Experiment vs Simulation.....	119
Table 1.8.11: Error of Maximum Responses for Experiment vs Simulation	119
Table 2.11.1: Displacement and Stress Equations for Point Load and Sinusoidal Distributed Load	132
Table 2.13.1: Beam and Sprung Mass Parameter Values for Validation Simulations	157
Table 2.13.2: Difference between FEM Predicted Midspan Displacement with Varied Time-Step Size	158
Table 2.13.3: Differences between FEM and State-Space Displacement Predictions	159
Table 2.13.4: Differences between FEM Displacement Predictions with 1 Mode and 5 Modes	161
Table 2.13.5: Midspan Stiffness Values for 140 ft. Bridge Models	164
Table 2.13.6: Midspan Stiffness Values for 100 ft. Bridge Models	164
Table 2.13.7: Midspan Stiffness Values for 40 ft. Bridge Models	165
Table 2.13.8: State-Space Beam Parameters.....	166
Table 2.13.9: SDOF Vehicle Model Parameters	167

Table 2.13.10: 2.8 Hz SDOF Vehicle Model Parameters	167
Table 2.13.11: Profile Parameters for Performance Assessment Study.....	167
Table 2.13.12: Moving Mass Simulation Decisions.....	168
Table 2.15.1: Coupled and Decoupled Model Parameters.....	179
Table 2.15.2: Difference between Predicted Midspan Displacement for Coupled and Decoupled Models	181
Table 2.15.3: Bridge Attributes for Parametric Study.....	184
Table 2.15.4: Vehicle Attributes for Parametric Study	185
Table 2.15.5: Frequency Factor for Maximum Amplification	189
Table 3.17.1: Simulation Parameters for Smoothing Studies	199
Table 3.18.1: Vehicle Parameters for Traffic Simulations.....	203
Table 3.18.2: Traffic Pattern Parameters.....	204
Table 3.18.3: Maximum Responses from Traffic Simulations	204
Table 3.18.4: Single Vehicle Responses for Vehicles 3 and 5	206
Table 3.18.5: Maximum Responses for Final Vehicle Loading Event.....	208

List of Figures

Figure 1.0.1: Diagram of StID Framework.....	26
Figure 1.3.1: Elevation View of Case Structure.....	29
Figure 1.3.2: Schematic of Case Structure Elevation	29
Figure 1.3.3: Cross-Section Diagram of Case-Structure from Construction Documents	30
Figure 1.3.4: View of Case Structure from Underside Featuring Deck Separation.....	30
Figure 1.3.5: Schematic of Case Structure Typical Girder Layout with Numbered Girders.....	31
Figure 1.3.6: View of Case Structure Bearings.....	32
Figure 1.4.1: Schematic of Generic Element-level FEM Model	33
Figure 1.4.2: Illustration of Element-Level Representation of 3D Geometry	34
Figure 1.4.3: Illustration of FE Representation of Connectivity between Girders and Cross-Girders	36
Figure 1.4.4: Apriori FEM Mode 1 – 2.37 Hz.....	37
Figure 1.4.5: Apriori FEM Mode 2 – 2.73 Hz.....	37
Figure 1.4.6: Apriori FEM Mode 3 – 3.22 Hz.....	37
Figure 1.4.7: Apriori FEM Mode 4 – 3.71 Hz.....	37
Figure 1.4.8: Apriori FEM Mode 5 – 3.77 Hz.....	37
Figure 1.4.9: Apriori FEM Mode 6 – 4.22 Hz.....	37
Figure 1.4.10: Apriori FEM Mode 7 – 4.25 Hz.....	38
Figure 1.4.11: Apriori FEM Mode 8 – 4.58 Hz.....	38

Figure 1.5.1: Schematic of Sensor Locations at a Given Pier Location	40
Figure 1.5.2: Schematic Showing Piers Chosen for Instrumentation	40
Figure 1.5.3: Accelerometer (PCB 393A03) with Magnetic Base (PCB 080A54).....	40
Figure 1.5.4: Top View of Mode 4 (3.71 Hz)	41
Figure 1.5.5: Underside View of Mode 4 (3.71Hz).....	41
Figure 1.5.6: Transverse Acceleration Time Histories	42
Figure 1.5.7: Comparison of Vertical Acceleration RMS for Different Piers	43
Figure 1.5.8: Comparison of Transverse Acceleration RMS for Different Piers.....	43
Figure 1.5.9: Comparison of Longitudinal Acceleration RMS for Different Piers	44
Figure 1.6.1: Accelerometer Installation Locations for Phase 2 Testing.....	47
Figure 1.6.2: Strain Gauge Installation Locations for Phase 2 Testing.....	48
Figure 1.6.3: Photo Featuring Sensor Installation with Boom Lift	49
Figure 1.6.4: Typical Accelerometer Installation on Steel Girder with Magnetic Base	50
Figure 1.6.5: Typical Strain Gauge Installation on Steel Girder with Epoxied Mounting Blocks ...	51
Figure 1.6.6: Event Acceleration Time History for Girder 5 at Middle of Span 7	52
Figure 1.6.7: Frequency response of 6 th order Elliptic filter	54
Figure 1.6.8: Filtered Event Acceleration Time History for Girder 5 at Middle of Span 7	54
Figure 1.6.9: Filtered Acceleration Time History for Girder 5 at the Middle of Span 7	55
Figure 1.6.10: Count of Acceleration Exceedance Events over 4.5 Hours	55
Figure 1.6.11: PSD Estimate of Girder Accelerations	56

Figure 1.6.12: Performance of "Omega" Method for Data Without Low-Frequency Content	57
Figure 1.6.13: Performance of "Modified Omega" Method.....	58
Figure 1.6.14: Displacement for Event as Estimated by "Omega Arithmetic" for Girder 5 at Middle of Span 7	59
Figure 1.6.15: Parent FFT of Displacement Estimate by "Omega" Methods for Girder 5, Middle of Span 7.....	59
Figure 1.6.16: Strain Time History for Girders 4 and 5 at the Middle of Span 7.....	60
Figure 1.6.17: High-strain event occurrence count over 24 hours	61
Figure 1.6.18: Frequency Response for Elliptic Filter (1.5 Hz Cutoff)	62
Figure 1.6.19: Comparison of Simulated Static Midspan Moment and Low-Pass Filtered Moment	62
Figure 1.6.20: Filtered and Raw Strain for Girder 5 Bottom Flange at Middle of Span 7	63
Figure 1.6.21: Live-Load Deflection Components for 2-Span Continuous Bridge	64
Figure 1.6.22: Extrapolated Strain in Top of Deck at Midspan over Girder 4	64
Figure 1.6.23: Strain Time History for Girder 4 Bottom Flange at 2' West of Cross-Girder 7 (Neg. Mom. Region)	65
Figure 6.24: CMIF Singular Values with Peaks Identified.....	69
Figure 1.6.25: Experimental Mode 1 – 2.00 Hz.....	69
Figure 1.6.26: Experimental Mode 4 – 2.44 Hz.....	69
Figure 1.6.27: Experimental Mode 7 – 2.83 Hz.....	70

Figure 1.6.28: Experimental Mode 12 – 3.56 Hz.....	70
Figure 1.6.29: Comparison of Experimental and A-priori FEM Mode 1 Shape.....	71
Figure 1.6.30: Experimental Mode 1 – 2.00 Hz.....	72
Figure 1.6.31: Experimental Mode 4 – 2.44 Hz.....	72
Figure 1.6.32: Experimental Mode 7 – 2.83 Hz.....	72
Figure 1.6.33: Experimental Mode 9 – 3.20 Hz.....	72
Figure 1.6.34: Experimental Mode 12 – 3.56 Hz.....	73
Figure 1.6.35: Experimental Mode 13 – 3.56 Hz.....	73
Figure 1.6.36: Experimental Mode 1 – 2.00 Hz.....	75
Figure 1.6.37: Updated FEM Mode 1 – 2.00 Hz	75
Figure 1.6.38: Experimental Mode 4 – 2.44 Hz.....	75
Figure 1.6.39: Updated FEM Mode 3 – 2.28 Hz	75
Figure 1.6.40: Experimental Mode 7 – 2.83 Hz.....	75
Figure 1.6.41: Updated FEM Mode 5 – 3.06 Hz	75
Figure 1.6.42: Experimental Mode 9 – 3.20 Hz.....	76
Figure 1.6.43: Updated FEM Mode 6 – 3.17 Hz	76
Figure 1.6.44: Experimental Mode 12 – 3.56 Hz.....	76
Figure 1.6.45: Updated FEM Mode 7 – 3.68 Hz	76
Figure 1.6.46: Experimental Mode 13 – 3.56 Hz.....	76
Figure 1.6.47: Update FEM Mode 8 – 3.68 Hz	76

Figure 1.6.48: Human Perception to Vibrations (Reiher and Meister, 1931)	79
Figure 1.7.1: Test Truck Instrumentation Layout.....	83
Figure 1.7.2: Span 2 Instrumentation Layout	83
Figure 1.7.3: Spans 3 & 4 Instrumentation Layout	84
Figure 1.7.4: Spans 7 & 8 Instrumentation Layout	84
Figure 1.7.5: Photo of Test Truck.....	86
Figure 1.7.6: Truck Raw Acceleration Time History for Run 6	88
Figure 1.7.7: PSD Estimate of Test Truck Acceleration (Full Bandwidth)	88
Figure 1.7.8: PSD Estimate of Test Truck Acceleration (<10 Hz).....	89
Figure 1.7.9: Frequency response of 6 th order Elliptic filter	90
Figure 1.7.10: Filtered Truck Acceleration Time History (Before and On Bridge)	90
Figure 1.7.11: Filtered Truck Acceleration Time History for Period before Bridge (A)	91
Figure 1.7.12: Filtered Truck Acceleration Time History for Period on Bridge (B).....	91
Figure 1.7.13: PSD Estimate for Acceleration from Front Sensors, On and Off Bridge	92
Figure 1.7.14: PSD Estimate for Acceleration from Rear Sensors, On and Off Bridge.....	93
Figure 1.7.15: PSD Estimate from Truck Acceleration	94
Figure 1.7.16: RMS of Filtered Truck Acceleration while on Bridge versus Truck Speed	95
Figure 1.7.17: Acceleration Time History (Filtered) for Girder 5 at the Middle of Spans 2	96
Figure 1.7.18: Acceleration Time History (Filtered) for Girder 5 at the Middle of Spans 3 & 4	96
Figure 1.7.19: Acceleration Time History (Filtered) for Girder 5 at the Middle of Spans 7 & 8	97

Figure 1.7.20: PSD Estimate for Acceleration of Girder 5 at the Middle of Span 2 over Period That Truck is on the Span.....	97
Figure 1.7.21: PSD Estimate for Acceleration of Girder 5 at the Middle of Spans 3 & 4 over Period the Truck is on the Spans	98
Figure 1.7.22: PSD Estimate for Acceleration of Girder 5 at the Middle of Spans 7 & 8 over Period the Truck is on the Spans	98
Figure 1.7.23: RMS of Filtered Midspan Acceleration of Span 2	99
Figure 1.7.24: Average RMS Value for Filtered Midspan Acceleration of Spans 3 & 4.....	99
Figure 1.8.1: Schematic of Plate Eccentric-Beam FEM Model.....	102
Figure 1.8.2: Plate Eccentric-Beam Representation and 3D Rendering with Assigned Eccentricities	102
Figure 1.8.3: Diagram of FE Representation of Diaphragms	103
Figure 1.8.4: LUSAS FEM Mode 1 – 1.98 Hz.....	107
Figure 1.8.5: Experimental Mode 1 – 2.00 Hz.....	107
Figure 1.8.6: LUSAS FEM Mode 3 – 2.45 Hz.....	108
Figure 1.8.7: Experimental Mode 7 – 2.83 Hz.....	108
Figure 1.8.8: Connectivity at discontinuous joints.....	109
Figure 1.8.9: Measured Profile	111
Figure 1.8.10: Comparison of span 3 midspan acceleration for simulations with and without a profile included	113

Figure 1.8.11: Comparison of truck vertical acceleration for simulations with and without a profile included	113
Figure 1.8.12: Experiment vs Simulation for Vehicle Acceleration for Run 14 over Bridge (Raw Data).....	115
Figure 1.8.13: Filtered Experimental Vehicle Acceleration for Run 14 over Bridge	116
Figure 1.8.14: Experiment vs Simulation for Vehicle Acceleration for Run 14 over Bridge (Filtered and Decimated).....	117
Figure 1.8.15: “Warped” Experimental and Simulated Truck Acceleration from DTW	118
Figure 1.8.16: Experiment vs Simulation for Span 2 Midspan Acceleration of Girder 8 for Run 14 (Filtered and Decimated)	120
Figure 1.8.17: Experiment vs Simulation for Span 3 Midspan Acceleration of Girder 8 for Run 14 (Filtered and Decimated)	120
Figure 1.8.18: Experiment vs Simulation for Span 7 Midspan Acceleration of Girder 8 for Run 14 (Filtered and Decimated)	121
Figure 1.8.19: Experiment vs Simulation for Vehicle Acceleration for Run 3 over Bridge (Filtered and Decimated).....	121
Figure 1.8.20: Experiment vs Simulation for Span 2 Midspan Acceleration of Girder 8 for Run 3 (Filtered and Decimated)	122
Figure 1.8.21: Experiment vs Simulation for Span 3 Midspan Acceleration of Girder 8 for Run 3 (Filtered and Decimated)	122

Figure 1.8.22: Experiment vs Simulation for Span 4 Midspan Acceleration of Girder 8 for Run 3 (Filtered and Decimated)	123
Figure 1.8.23: Experiment vs Simulation for Span 7 Midspan Acceleration of Girder 8 for Run 3 (Filtered and Decimated)	123
Figure 1.8.24: Simulated Bridge Midspan Displacement Amplification Time History	124
Figure 1.8.25: Simulated Bridge Midspan Moment Amplification Time History	124
Figure 1.8.26: Maximum Displacement Amplification for Varying Speeds	125
Figure 2.10.1: Schematic of Combined Vehicle and Bridge Systems	129
Figure 2.11.1: Additional Amplification as a Function of Bridge Inertial Force	133
Figure 2.13.1: Diagram of Simplified 2-DOF Model	145
Figure 2.13.2: Diagram of Single-Span 2-DOF Model	147
Figure 2.13.3: Diagram of 2-Span 2-DOF Model	151
Figure 2.13.4: Difference between FEM Predicted Midspan Displacement with Varied Time-Step Size	158
Figure 2.13.5: Comparison of Single-Span Beam Model Displacement Simulations.....	159
Figure 2.13.6: Comparison of 2-Span Beam Model Displacement Simulations	159
Figure 2.13.7: First Two Mode Shapes for 2-Span Continuous Beam	160
Figure 2.13.8: FEM Displacement Predictions with 1 Mode and 5 Modes for 2-span Continuous Beam	161
Figure 2.13.9: Performance of 2DOF State-Space Models for Predicting Dynamic Amplification	170

Figure 2.13.10: Performance of 2DOF State-Space Model Grouped by Vehicle	172
Figure 2.14.1: Performance on ISO 8608 Parameters for Predicting Dynamic Amplification	173
Figure 2.14.2: Performance of IRI for Predicting Dynamic Amplification	174
Figure 2.14.3: Performance of Quarter-Car Vehicle Model for Predicting Dynamic Amplification	175
Figure 2.15.1: Diagram of Decoupled Model.....	176
Figure 2.15.2: Diagram of Coupled 2-DOF Model.....	177
Figure 2.15.3: Displacement Predicted by Coupled Model and Decoupled Model.....	179
Figure 2.15.4: Difference between Displacement from Coupled Model and Uncoupled Model as a Percent of Maximum.....	180
Figure 2.15.5: Difference between Contact Force from Coupled Model and Uncoupled Model as a Percent of Vehicle Weight	180
Figure 2.15.6: Free Decay of Vehicle Contact Force	182
Figure 2.15.7: Effect of Vehicle Forcing Frequency on Bridge Displacement and Vehicle Contact Force	184
Figure 2.15.8: Effect of Bridge and Vehicle Frequency on Bridge Displacement and Vehicle Contact Force (1/4)	185
Figure 2.15.9: Effect of Bridge and Vehicle Frequency on Bridge Displacement and Vehicle Contact Force (2/4)	186
Figure 2.15.10: Effect of Bridge and Vehicle Frequency on Bridge Displacement and Vehicle Contact Force (3/4)	186

Figure 2.15.11: Effect of Bridge and Vehicle Frequency on Bridge Displacement and Vehicle Contact Force (4/4)	187
Figure 2.15.12: Effect of Bridge and Vehicle Frequency on Bridge Displacement and Vehicle Contact Force (Total)	187
Figure 2.15.13: Effect of Vehicle Frequency as a Fraction of Bridge Natural Frequency on Bridge Displacement Amplification.....	189
Figure 2.15.14: Profiles with Matching Frequency Content but Different Phase Angle Distribution	190
Figure 2.15.15: Bridge Displacement for Profiles with Different Phase Distribution	191
Figure 2.15.16: Effect of Profile Position on Bridge Displacement Amplification	191
Figure 3.17.1: Effect of Smoothing (1/8" over 10ft.) on Real Profile.....	198
Figure 3.17.2: Effect of Smoothing (1/4" over 30ft.) on Real Profile.....	198
Figure 3.17.3: Comparison of Bridge Dynamic Amplification with Rough Profile and with Smoothed Profile	199
Figure 3.17.4: Effect of Smoothing Parameters on Dynamic Amplification	200
Figure 3.18.1: Span-1 response to traffic pattern no. 1.....	205
Figure 3.18.2: Span-2 response to traffic pattern no. 2	205
Figure 3.18.3: Time History of Bridge Displacement for Last Vehicle in Traffic Patterns	206
Figure 3.18.4: Span-1 Response to final vehicle (#5) in traffic pattern 1	207
Figure 3.18.5: Span-2 Response to final vehicle (#5) in traffic pattern 2	207
Figure 3.18.6: Effect of Number of Sequential Vehicles on Bridge Response	210

Figure 3.18.7: Response summary for 140ft single-span model	211
Figure 3.18.8: Response summary for 100ft single-span model.	211
Figure 3.18.9: Response Summary for 140ft 2-Span Model (Span 1).....	213
Figure 3.18.10: Response Summary for 140ft 2-Span Model (Span 2).....	213
Figure 3.18.11: Span 2 Displacement Time History for Varied Platoon Headway Spacing	214

Chapter 1: Introduction

Societal Context

In 1908, Henry Ford's first Model T rolled off the assembly line. Less than 20 years later an estimated 15 million Model T cars had been sold. By 1956 there were more than 65 million registered vehicles on America's roads (FHWA, 2012). That same year Congress enacted the Federal-Aid Highway Act, creating what is now known as the interstate highway system. Over the next half-century, the number of vehicles swelled to 240 million as a generation of Americans returned from World War II to a relatively unscathed nation, rich with natural resources, and an industrial complex created in a large part by the war effort that would fuel economic development for the next several decades.

Just as America experienced a cultural and transportation transformation in the 1950's, so too is our current transportation system on the verge of major transformation. New technologies (automated vehicles, electric cars) promise to dramatically alter the way Americans and American goods travel.

Furthermore, the demand on our transportation systems will continue to increase. America's population will grow by 70 million and freight volume will increase by more than 40 percent by 2045 (*Beyond Traffic 2045*, 2017). This will require an increase in infrastructure capacity by building new roads, bridges, and other facilities; as well as maintaining existing infrastructure to ensure continued use and extend service life.

Current State of Transportation Infrastructure

However, providing funding for these projects presents a continuing challenge. Federal fuel taxes per gallon has not increased since 1993. Improved vehicle fuel economy reduces fuel consumption on a per vehicle basis, further reducing the revenue from gas taxes. Inflation

continues to degrade the purchasing power of transportation funds and states are increasingly using debt to fund transportation projects.

At the same time, it is becoming more costly to maintain transportation systems as many of America's roadways and bridges, many of which were constructed in the 1950s and 1960s, are nearing or have exceeded their design lifespan. Of the 611,845 public road bridges, 58,791 were classified as structurally deficient in the 2015 National Bridge Inventory (NBI), and another 84,124 were classified as functionally obsolete. In recent years more than 15 percent of state capital spending on highways has gone to bridge rehabilitation and replacement.

The changing societal expectations related to infrastructure stewardship and the new demands emerging from connected vehicles cannot be met by the current practice of bridge engineering. Cost-effectively addressing the challenges associated with the aging U.S. bridge stock necessitates a more accurate, quantitative and objective understanding of bridge performance and deterioration. Without the ability to forecast performance and distinguish between over- and under-performing bridges, the paradigms of life-cycle analysis and asset management will remain on the sidelines. Although the qualitative and empirical approaches that define today's bridge engineering practice have served the profession well over the past five decades, they are wholly incapable of operating under the current fiscal pressures or answering the calls for more efficient and transparent resource allocation.

Key Knowledge Gap: Influence of Trucks on Bridge Performances

Principal among the shortcomings of current design and assessment approaches is their inability to accurately address the effects of trucks, which provide the primary means of freight transportation for distances under 750 miles and may present the largest demands a bridge will experience, on bridge performance. While the trucking industry continues to push for heavier

vehicle limits, the latest design codes (LRFD) are producing more flexible bridges with reduced reserve capacity. The reduction in conservatism can only be justified if the assumptions inherent to our design and evaluation methodologies are made more certain. However, the simple live-load models and analysis methods currently used in design are unable to accurately predict live-load responses, address limit states related to reliability and resilience, or assess the performance of in-service bridges.

Our lack of understanding of how trucks influence bridge performance also represents a key barrier to meeting the needs of emerging connected vehicle technology, specifically truck platooning (which will likely be one of the first applications of connected vehicles). Truck platooning is driven by safety and energy efficiency concerns and involves virtually connecting trucks into a train with extremely small headway in between vehicles. This not only drastically changes the level of live load on bridges (and violates many of the underlying assumptions associated with design and assessment live load models), it creates a more steady-state dynamic loading, which cannot simply be accounted for with an amplification factor. To inform platooning policies and avoid potentially costly unintended consequences, better understanding of how trucks influence bridge performance is needed.

Overview of Vehicle-Bridge Interaction

Of particular interest in both of these regards is dynamic vehicle-bridge interaction (VBI). VBI refers to a complex dynamic loading condition in which one dynamic system (vehicle) traverses a second dynamic system (bridge), thereby exciting the response of the second system which, in turn, influences the response of the former system. To date, most of the work in this area has focused on railway bridges where such dynamic interactions have resulted in significant consequences. The 1847 collapse of the Dee Bridge in England prompted some of the earliest

work examining the dynamic effects of moving loads (Willis, 1849). In the case of highway bridges, the lack of repetitive, steady-state-type loading, together with the large safety factors historically employed, have prevented the issues of dynamic interaction from being considered of great consequence. However, changing societal expectations and emerging technologies may provide scenarios in which the dynamic interaction produces amplified bridge responses and demand better understanding of VBI.

The amplification of bridge responses due to dynamic response is termed “dynamic amplification” and quantifies the inability of static analyses to predict the maximum response of a dynamic system. It is expressed as a ratio of maximum dynamic response to static response. For a bridge, moving vehicles excite the coupled system resulting in bridge motion which in turn causes member level responses unequal to those that would result from the force of the vehicles’ weight alone (static).

For many civil applications, static analyses have proven adequate for determining the demands of structures. Structures often remain near enough to a motionless state that the structure can be described as a static system, and the resulting error from employing this assumption can be accounted for with a small increase in the factor of safety. However, in some cases, the excitation of the bridge mass results in appreciable bridge motion.

Live load demands have historically been estimated using static analysis. The dynamic amplification factor that should be used depends on the design specification with jurisdiction. According to AASHTO, a maximum factor of 1.33 is to be used (1.75 for joints). However, there have been numerous reports of bridges experiencing dynamic amplification well in excess of this number, thereby suggesting that the old assumptions are no longer conservative for every

bridge. We are therefore compelled as designers, builders and operators to identify the shortcomings of old assumptions and develop more accurate methods as required.

Research Objectives and Scope

Given the above discussion, this research has adopted the following three primary objectives:

1. Establish the mechanisms that result in levels of VBI that render the common static live load model unconservative,
2. For the cases identified in (1) develop and validate a practical approach to estimating the effects of truck loads inclusive of VBI, and
3. Identify bridge vulnerabilities associated with truck platooning and make recommendations related to how VBI should be estimated and mitigated.

These objectives were realized by taking an inductive approach whereby a structure exhibiting large dynamic responses was investigated to identify and characterize the mechanisms and parameters influential to VBI using the Structural Identification (StId) framework (Çatbaş et al., 2013). Field testing of this structure was performed to obtain measurement of operational responses. These responses would provide quantification of the bridge's dynamic behavior and provide data to inform and "calibrate" FE models, thus ensuring that the models could accurately simulate VBI.

The validated models were subsequently leveraged to investigate the effect of various mechanisms and parameters on VBI and dynamic amplification. These parameters included roadway profile, vehicle suspension parameters, and bridge dynamic characteristics. Armed with this knowledge, methods for predicting dynamic amplification were assessed and a new simplified model was developed that can be easily implemented by practicing engineers.

Summary of Thesis Chapters

Chapter 2: Literature Review

Presented in this chapter is an overview of current engineering practice as it relates to dynamic amplification and vehicle-bridge interaction. Dynamic amplification factors as specified by different design codes are presented as well as a brief summary of dynamic amplification factors determined through field testing. Methods for modeling vehicle-bridge interaction are also presented, including profile generation with the ISO 8608 standard. The effect of vehicle, bridge and road surface parameters have been the subject of many previous studies. Their conclusions are summarized. The effect of repeated vehicles (platoons) on bridge responses has not been extensively researched, however, similar loading is experienced by railway bridges. The work in this area is summarized. Finally, human perception of bridge vibrations is reviewed, as well as the attempts of design codes to limit vibrations that cause user discomfort.

Part 1: Understanding Vehicle Bridge Interaction and Dynamic Amplification

This first part details the experimental testing and investigation of a real bridge and documents the knowledge gained from such efforts. A total of three field tests were carried out. These tests provided quantitative measure of the bridge dynamic behavior and indicated that this bridge was experiencing dynamic amplification as high as 2.0. The recorded responses were also utilized for the validation of FE models and VBI simulation methods.

Chapter 3: Description of Case Structure

This chapter provides a detailed description of the 11-span viaduct that was subjected to multiple field tests. The structure was selected for investigation due to the large vibrations reported by motorists and was therefore suspected of exhibiting high dynamic amplification.

Chapter 4: Preliminary Modeling of Test Structure

As a first step in investigating the behavior of the test structure, an element-level 3D FE model was constructed. The details of this model and the process of its construction are documented.

Chapter 5: Phase 1 Testing

The purpose of the first phase of testing was to identify which portions of the structure were experiencing the greatest vibration and should receive further testing. Design of the instrumentation plan and test activities are documented. The results of the testing are presented which indicated that all instrumented locations are experiencing similar levels of vibration. Spans 7 and 8 were subsequently chosen for further testing.

Chapter 6: Phase 2 Testing

The purpose of this phase of testing was to characterize the superstructure using operational dynamic data and to quantify the dynamic amplification experienced by the bridge during typical traffic conditions. Design of the instrumentation plan and test activities are documented. The resulting data is processed and interpreted to estimate the in-situ dynamic amplification and identify the structure's operational mode shapes and corresponding frequencies. The extracted modal parameters were used to update and validate the 3D FE model.

Chapter 7: Phase 3 Testing

This phase of testing was designed to provide a more thorough understanding of the coupled behavior of bridge and vehicle by capturing the motion of the bridge and a vehicle synchronously. Design of the instrumentation plan and test activities are documented. The resulting data demonstrated that a single truck is capable of inducing vibrations in the bridge that lead to dynamic amplification of bridge responses. Understanding of the mechanisms and

influential parameters associated with dynamic amplification could not be directly interpreted from the test data.

Chapter 8: VBI Model Validation

It was the goal of the simulation efforts presented in this section to identify the bridge and vehicle attributes that were responsible for the observed bridge vibrations and dynamic amplification. The process of constructing and validating a model that was capable of reproducing the responses observed in the field is documented. The model was found to adequately predict the responses measured in the field when the bridge roadway profile was included in simulations.

Part 2: Estimating Dynamic Amplification

This part summarizes the various methods of predicting dynamic amplification using both experimental and analytical methods. These methods are time-consuming to perform and require considerable expertise. Therefore, a simplified model is proposed that reduces the bridge and vehicle to two degrees of freedom. The ability of this model to predict dynamic amplification is assessed by comparing its predictions to those obtained from 3D FE models. The simplified model as well as the 3D FE models are further used to investigate the parameters that are influential to dynamic amplification.

Chapter 10: Components of Vehicle Bridge Interaction

This chapter provides a brief summary of vehicle-bridge interaction distilled into its most basic components. Therefore, the bridge and vehicle are visualized as two dynamic systems coupled at the point of contact between wheel and bridge roadway. This representation is used to identify those components which must be considered when investigating VBI and must be included in any analytical representation of VBI.

Chapter 11: In-Situ Measurement

This chapter provides methods of estimating dynamic amplification of existing structures with field testing, including load testing and operational monitoring. It is shown that amplification factors determined from displacement measurements will be greater than those determined from strain measurements. Brief guidance is also provided for the measurement of the bridge roadway profile for use in VBI simulations.

Chapter 12: Model-Based Simulation

This chapter provides an analytical approach to estimating dynamic amplification using finite element analysis. Common structural model types are presented, and guidance is provided for modeling the vehicle. Brief guidance is also provided for the validation and implementation of analytical models for simulating VBI.

Chapter 13: Simplified Model Formulation

This chapter details the development of a simplified model for estimating dynamic amplification. This model reduces the bridge to a single beam and a single degree of freedom through generalized coordinates. The vehicle is also modeled as a single degree of freedom. The equations of motion for the coupled system are provided as well as a state-space representation of the system. Validation of the model is presented. Performance of the model is assessed by comparing dynamic amplification predictions to those obtained from 3D FE models.

Chapter 14: IRI & Other Vehicle-Only Models

This chapter demonstrates the shortcomings of common profile roughness metrics in predicting dynamic amplification by examining the correlation between FE predicted dynamic amplification and IRI values, ISO 8608 parameters, and responses from quarter-car simulations. All of these models fail to consider the bridge and ultimately fail at reliably indicating dynamic amplification.

Chapter 15: VBI Mechanisms and Parameters

This chapter examines the parameters influential to dynamic amplification through simulation studies. The effect of coupling the vehicle and bridge systems in analysis is first investigated. These studies suggest that coupling of the systems serves to reduce the contact force and bridge response. Multiple parametric studies are performed to investigate the interdependency of parameters influential to dynamic amplification. These studies confirm that maximum bridge response occurs when the vehicle and bridge natural frequencies are close to matching. The importance of profile location in simulations is also demonstrated.

Part 3: Applications in Vehicle-Bridge Interaction

The simulation tools demonstrated in Part 1 and developed in Part 2 are leveraged in this part to address some of the challenges facing bridges associated with VBI.

Chapter 17: Remediation and Smoothness Criteria

This chapter addresses profile roughness by examining rolling straightedge criteria. Various straightedge limits are used to modify a real (measured) profile and the effect of these modifications on dynamic amplification is quantified. It is shown that rolling straightedge criteria with common limits (i.e. 1/8 to ¼ inch deviation over 10 to 16 feet) are not effective at reducing dynamic amplification. It is further shown that the straightedge length should be at least 16 feet (4.88 m) for a deviation limit of 1/8th inch (0.318 cm), and at least 30 feet (9.14 m) for a deviation limit of ¼ inch (0.635 cm).

Chapter 18: Multiple Vehicles

This chapter seeks to identify the effect of multiple vehicles on dynamic amplification and provide guidance on how the effect of multiple vehicles should be considered when it is impractical to perform VBI simulation (i.e. static analysis). This is accomplished by first

examining the effects of a few traffic patterns and then extended to truck platoons. The simulation studies show that traffic and truck platoons can result in increased dynamic amplification because even a single previous truck can induce the bridge conditions (motion) that result in increased dynamic response. Furthermore, as spacing between vehicles decreases and more vehicles are present on the bridge, the static load effect increases, but the dynamic amplification will likely be less than what would occur for a single vehicle.

Chapter 2: Literature Review

Structural analysis of traffic loading on bridges is performed primarily for the purposes of design or evaluation. The methods of analysis and technological tools historically available have limited the analyses to evaluate the traffic as static loads (i.e. location and magnitude of load remain constant with time), rather than as moving masses where the true response of the structure is actually due to the interaction of the two dynamic systems. The industry accounts for this disparity by applying a “dynamic amplification” factor to the static load or response, thereby attempting to increase the calculated response to match that which the bridge may actually experience under moving vehicles.

The magnitude of this factor (IM or DAF) differs depending on the reference code being used, but in many cases, has been developed from extensive surveying of existing structures and the amplifications they experience.

Dynamic Amplification in Bridge Codes

The various design and evaluation codes handle dynamic amplification in slightly different ways, but they all specify a factor that is to be applied to the loading model. In the current AASHTO (2014) *LRFD Bridge Design Specification* the impact factor is dependent on road surface roughness, ranging from 0.1 to 0.3. The AASHTO (2018) *Manual for Bridge Evaluation* specifies an impact factor of 0.33 (0.15 for fatigue limit states, 0.75 for joints). The British code includes an IM of 0.25 in its two design load models.

The factors specified by the Ontario and Canadian Highway design codes are dependent on the number of vehicle axles, with lower factors for more axles. A factor of 0.25 is specified for vehicles with 3 or more axles. Similarly, the Australian code specifies factors based on load type.

An impact factor of 0.4 is specified for wheel and axle loads, and 0.35 for triaxle truck and lane load. (Canadian Standards Association, 2006)

The Chinese code's factors are a function of bridge's first natural frequency, with a lower bound of 0.05 and an upper bound of 0.45. A bridge with a first natural frequency below 5 Hz would have a specified impact factor less than 0.25. (Ministry of Transport of the People's Republic of China (MTPRC), 2004)

The New Zealand, European, and Japanese codes all specify factors as a function of bridge span length with the factors decreasing with increased span length. The New Zealand code has a maximum IM of 0.30 for span lengths less than 12 meters (New Zealand Transport Agency (NZTA), 2013). The equation for IM specified by the Japanese code is different for different bridge types (Japan Road Association (JRA), 1996). A steel or RC bridge with a span length of 40 feet for instance would be assigned an IM equal to 0.32.

The equation specified by the European code differs dependent on the number of lanes. For a single-lane bridge, the impact factor may range from 0.4 to 0.7, while that for a two-lane bridge ranges from 0.1 to 0.3. (European Committee for Standardization (CEN), 2003)

Experimental Evaluation of Amplification Factors

A large number of field tests were carried out in various countries over the years, in-part, for the development of bridge design codes. In the 1950's, AASHTO sponsored a major investigation, for which 18 newly constructed bridges were selected for the purpose of testing and determining the dynamic effects of moving vehicles on the bridges. This study concluded that the dynamic amplification generally increases with increased vehicle speed, is sensitive to vehicle suspension performance, and that the initial oscillations of the vehicle are responsible for a large amount of uncertainty in the dynamic response of the bridge. The maximum dynamic amplification factor

recorded from these tests was 1.63 for displacements and 1.41 for strains, however, 95% of the measured amplification factors fell below the value specified by the current code at the time. (Paultre et al., 1992)

In 1956 and 1957, field tests were completed on 52 bridges in Canada, with specific attention paid to dynamic amplification. Amplification factors were observed as high as 1.75, while values near 1.30 were more typical. These tests concluded that the amplification factors were higher for flexible bridges and were greatly affected by the road surface roughness and irregularities on the bridge as well as approach (Wright and Green, 1964). In fact, Write and Green recommended that irregularities in the road profile should be eliminated, as this was more influential on dynamic amplification than the many other structural parameters considered (Paultre et al., 1992). Additional tests were carried out in Canada in the 1970s and 1980s. Amplifications factors were obtained as high as 1.85 with higher factors obtained from bridges with first fundamental frequencies of 2 to 5 Hz (Billing, 1984). Similar results were obtained from field tests of more than 200 bridges in Switzerland, with amplification factors as high as 1.7 for bridges with a first fundamental frequency between 2 and 4 Hz (Cantieni, 1983). (Deng et al., 2015)

A more recent field test was completed in Florida of a 3-span prestressed multi-girder bridge. Amplification factors were determined experimentally by measuring the bridge response from loaded five-axle trucks. The amplification factors for one truck was found to be 1.82 while that for two trucks was found to be 1.50 and were observed at higher speeds (80 km/h). The authors were able to reasonably reproduce the bridge response recorded in the field by using FE simulation and incorporating the measured road profile of the approach. By comparing

responses with and without road profile, the authors were able to show that road surface irregularities have a significant impact on dynamic amplification. (Kwasniewski et al., 2006b)

Modeling Vehicle-Bridge Interaction

While much can be gleaned from experimental investigations, they are often expensive, and require a large amount of resources and time. For this reason, analytical methods are often employed, especially where a large number of situations need to be investigated (i.e. parametric studies).

Model Forms

In early studies, vehicle-bridge interaction was analyzed by representing the bridge as a beam, and the vehicles as point forces or point masses moving across the beam (Willis, 1849). As computational tools advanced, bridge models gained complexity and are now commonly modeled as grillage models (Ashebo et al., 2007) or full 3D FE models (Kwasniewski et al., 2006a). Similarly, the vehicle models have advanced to multiple degrees of freedom (DOF). The minimum vehicle model is composed of a single sprung-mass system (Yang et al., 2004). It often consists of a single DOF but may have two if the wheel weight and tire stiffness is to be modeled separately from the suspension system. Two dimensional models can also be used, whereby each axle is represented by a sprung-mass system that may optionally be connected (Chatterjee et al., 1994). Finally, a full 3D model of the vehicle may be constructed, for which the vehicle body is modeled as a rigid mass (or multiple connected masses) with multiple DOF, and the suspension system will be modeled as lumped masses connected to the vehicle body and bridge surface via spring-dashpots elements (OBrien et al., 2010).

Traffic Models

In some cases, the effect of traffic is considered, and multiple vehicle models are employed in the analysis. The traffic parameters (e.g. weights, spacing, speed, etc.) can be obtained directly from weigh-in-motion (WIM) data but are often generated using statistical methods, whereby the distributions of traffic parameters are derived from WIM data or from traffic flow simulations. The traffic model is then formed using Monte Carlo methods. (Caprani, 2012; Zhang et al., 2001)

Profile Generation

The interface between the traffic/vehicles and structure is the road surface. The motion of the vehicle tires over the bridge is dictated by the geometry of that surface (i.e. road profile). Therefore, it is important that it be included in any modeling effort. The profile can be specified in 1D (i.e. an elevation dimension specified for every unit length of the bridge) or 2D, whereby the profile is provided for multiple wheel lines (Liu et al., 2002). The road profile can be generated from field measurements of an actual roadway, or computer generated. For the latter case, the profile is often generated with the Power Spectral Density (PSD) function (Honda et al., n.d.). Standards have been developed for the function parameters based on road roughness categories, and while the profiles generated using these standards are useful, Loprencipe and Zoccali argue that they are no substitute for in-situ measurements when the behavior of a specific vehicle and structure is being investigated (2017).

The most common standard for describing and generating artificial profiles is the ISO 8608 standard. This standard describes the (spatial) frequency content of the profile with two terms that described a PSD function. The artificial profile is subsequently generated by summing a series of sine functions with amplitudes set according to PSD parameters (Tyan et al., 2009). These parameters include a waviness value (w) and the amplitude of the PSD function at a

spatial wavelength equal to 10 meters (C_{10}). The PSD amplitude of each spatial frequency band (n) is therefore assigned according to the following equation.

$$G_d = C_{10} * (10n)^{-w} \quad (1)$$

The amplitude of each frequency band in dimensional units is given by the following equation.

$$A_i = \sqrt{\frac{G_d(\Omega_i)}{\pi} * \frac{\Omega_N - \Omega_i}{N - 1}} \quad (2)$$

Where Ω is the angular spatial frequency in rad/meter, and N is the number of included frequency bins. The profile may then be generated with the following equation, where ϕ_i are the phase angles in radians.

$$z(x) = \sum_{i=1}^N A_i \sin(\Omega_i(x) - \phi_i) \quad (3)$$

Profiles should include approach roadway to allow for simulation and consideration of vehicle motion induced by the approach roadway profile. An approach length of 100 meters is common (González et al., 2011; McGetrick et al., 2013; O'Brien et al., 2014; O'Brien and Keenahan, 2015).

Solution Methods

There are different methods of solving the vehicle-bridge system, depending partially on the modeling methods employed. For simpler models, the equations of motion of both the vehicle and bridge can be explicitly derived. Their interaction can then be solved by coupling the equations or by using an iterative approach. For the coupled method, the equations of motion of the two systems are assembled into single mass, damping, and stiffness matrices for each time step (Kim et al., 2005, p.). Alternatively, for the iterative approach, the bridge and vehicle equations of motion are solved separately, and the force and displacement results of each used in the solution of the other (Wang and Huang, 1992, p.). The process is therefore repeated until convergence is achieved. Modal superposition can be used in the iterative approach and is also used in many commercially available FE software packages to drastically reduce the

computational burden of solving the bridge response compared to time-step solutions (Au et al., 2001a; Yang and Lin, 2005).

Influential Parameters for Dynamic Amplification

Many analytical and experimental studies throughout the past several decades have investigated which parameters are influential to dynamic amplification. These parameters have included: road surface condition, bridge span length and natural frequency, bridge type, vehicle speed, and vehicle weight and suspension characteristics. Of these, research has shown that road surface condition, vehicle speed, and vehicle weight and suspension type have the most effect on dynamic amplification.

Bridge Parameters

Although some codes include span length or first natural frequency in their calculations of IM, studies have shown poor correlation between either of these parameters and dynamic amplification (Cantieni, 1983; Chang and Lee, 1994; Huang et al., 1993; Schwarz and Laman, 2001). Furthermore, although bridge type may have a significant impact on the dynamic behavior of a bridge, there are a wide variety of bridge types and even more varied structural characteristics within each type preventing any consistent relationship from being established (Deng et al., 2015).

Vehicle Parameters

Vehicle speed has been shown to have a significant effect on dynamic amplification. Generally higher amplification factors result from higher speeds. In some studies, it has been shown that there is a critical speed for which the amplification factor is a maximum (González et al., 2010). However, although the various studies generally agree that vehicle speed is an important factor, the proposed relationships between vehicle speed and amplification factors is inconsistent,

suggesting that this relationship is complicated and dependent on other factors (Deng et al., 2015). Similarly, vehicle mass and suspension characteristics have been shown to effect dynamic amplification, but again, no definitive relationship has been established. However, studies generally agree that the amplification factors decrease with increased vehicle weight and damping and with decreased suspension stiffness (Green et al., 1995a; Nassif and Nowak, 1995).

Road Surface Roughness

Previous studies have examined the impact that the road surface has on impact factors. Many analytical studies have shown that a rough road surface may result in higher dynamic amplification (Deng and Cai, 2010; Huang et al., 1995; Kim et al., 2007; Wang and Huang, 1992). However, the studies do not agree on the significance of the effect road surface has on dynamic amplification, which is likely due to variety of bridge types and geometry, road profiles, and model types employed.

Most analytical studies have used a single-line beam model in which the width of the bridge is reduced to a single beam with appropriate mass and stiffness. Some of the earliest simulation work was done by Aramraks at Purdue University. In his research, single span, 2-span and 3-span bridges were represented as single-line beam models. Surface roughness was idealized as a number of half sine waves, resulting in beam accelerations as much as 10 times those obtained with a smooth road surface (Aramraks, 1975).

As computing technology has progressed, more complex simulations have been carried out. A simply supported box girder was modeled with a moving mass over a rough road surface that was simulated by using PSD functions to produce a more realistic road profile, and obtained dynamic amplification factors (DAF) as high as 3.0 (Inbanathan and Wieland, 1987). Simulations of a 3-span continuous box-girder bridge (modeled as a beam) for a rough road surface

generated a maximum DAF of 2.3 (Law and Zhu, 2005). Chatterjee et al. used a single line girder model of a continuous bridge, and showed that for certain combinations of speed and frequency ratios between the vehicle and structure, the DAF could exceed 4.0 (Chatterjee et al., 1994).

The effect of long term deflections in addition to road surface roughness was investigated for a simple span and a 3-span prestressed concrete bridge and it was concluded that the long-term deflections had negligible effect on amplification factors, but the road surface roughness could cause amplification factors in excess of 2.0 (Au et al., 2001b).

The effect of road surface on bridge responses was further investigated with 3-dimensional FE models. Kou and DeWolf modeled a 4-span continuous plate-girder bridge, and examined the effect of smooth road surface versus 0.5 inch and 1 inch amplitude roughness and concluded that the road roughness had negligible effect on bridge deflections (Kou and DeWolf, 1997). In contrast, 3-D FE simulations of a 3-span non-continuous bridge by Li et al. showed that the surface roughness had a large effect on dynamic amplification, especially with increased speed. Based on simulation efforts, a maximum dynamic amplification of nearly 3.0 was reported for poor road condition and at 70 mph, while a DAF of only 1.2 was recorded from field measurements of the bridge (Li et al., 2008).

Indeed, the dynamic amplification factors obtained from field measurements are consistently lower than the factors suggested by analytical research and have similarly wide variation from bridge to bridge. Cooper instrumented two bridges in England and recorded a maximum DAF of 1.42. Cooper also created a probabilistic model of DAF based on field measured road roughness and span length that suggests a maximum mean DAF of 1.27 (Cooper, 1997). Park et al. examined the effect of road roughness on dynamic amplification by testing 25 highway bridges in South Korea. None of the bridges exhibited amplification factors greater than 1.25, but their

results clearly showed that the amplification factors increased with the International Roughness Index (IRI) (Park et al., 2005). However, further research suggests that no single measure of road roughness can accurately predict DAF because of the many other influential parameters that contribute to DAF (i.e. bridge geometry, mass and stiffness; vehicle dynamic properties; vehicle speed; etc.). (Li et al., 2006; OBrien et al., 2006).

Effects of Platooned Vehicles

Much research has focused on the load effect of congested traffic on bridges, whereby larger loads are applied to the structure due to the increased number of vehicles present. The increased load is exacerbated by the tendency of long lines of trucks to form (Han et al., 2015). While any traffic pattern of repeated trucks is often referred to as truck platoons, in this research platoons will refer to trucks that are virtually coupled by wireless communication and sensing that allows on-board computers to control headway and speed. Some research has looked into how this headway should be controlled to reduce congestion (Lipari et al., 2017), but little work has been done to understand the dynamic effect of platooned trucks on highway bridges.

In contrast, the problem has been extensively studied for railway bridges, where train cars present regular wheel spacing, vehicle spacing, and weight (Bolotin and Armstrong, 1965; Kurihara and Shimogo, 1978; Li and Su, 1999; Yang et al., 1997). Research has shown that railway bridges are susceptible to large dynamic amplifications (Wu et al., 2001), and that the amplification is dependent on such parameters as wheel spacing, train speed, bridge span length, and bridge first fundamental frequency (Kwark et al., 2004; Majka and Hartnett, 2008).

However, while the loading conditions of railway bridges are similar to that induced by platooned trucks, the structural system is markedly different. The tracks of railway bridges are

often isolated from the structure by ballast, providing different load distribution and significantly higher damping than is accomplished by the deck of a highway bridge. Furthermore, the track of a railway bridge is typically smoother and with fewer irregularities than a highway bridge roadway.

Bridge Vibration Limits

The dynamic effect of traffic on bridges is not just of concern for amplification factors or strength limit states (i.e. rating factor). Excessive vibrations may result in reduced fatigue life, as the vibrations can result in more stress cycles per loading event. Furthermore, structural vibrations should be limited so as not to upset the bridge users.

Past studies have looked at what constitutes objectionable vibrations and the characteristics that influence a human's perception of those vibrations. In general, these studies concluded that as the displacement and frequency increase, the vibration is considered more intolerable to users. However, there is no single parameter that can predict a human's perception of a given vibration (Gaunt and Sutton, 1981). Some of the earliest work on this topic was carried out by Reiher and Meister. They developed sensitivity curves by subjecting people to vertical harmonic vibration (Reiher and Meister, 1931). These sensitivity curves still provide an acceptable characterization of human perception to vibrations.

AASHTO bridge specifications state that bridges should be designed to avoid psychological effects and that acceleration is the primary factor for human sensitivity to bridge deformations, but fails to provide any specific limits for vibrations (AASHTO, 1998). Instead they placed limits on span-to-depth ratios and live load deflections in hopes that this would prevent unsatisfactory dynamic behavior. The Ontario Highway Bridge Design Code of 1983 introduced a new serviceability limit state that was meant to control vibrations that would be objectionable to

pedestrians by restricting deflections based on the first frequency of the structure (Csagoly and Dorton, 1978). The Eurocode also advises bridge designers to limit vibrations to avoid the discomfort to users, but again, fails to provide guidance as to how that may be accomplished (BS, 2006).

Knowledge Gaps

Much study has been devoted to understanding the factors that affect dynamic amplification and to the development of methods for calculating it. However, numerous bridges have been identified as having amplifications far outside those predicted by established methods, thus suggesting there are mechanisms whose effect on dynamic behavior is still poorly understood. Even though past studies have identified influential parameters that may contribute to the apparent outliers, there has been no consensus on how to incorporate those parameters into dynamic response predictions. This is due, in part, to the failure of studies to consider all influential parameters simultaneously and thus their interdependency. Furthermore, much of the previous research considered only simple loading models (i.e. design trucks) that cannot possibly account for the variety of vehicles that any given bridge experiences every day. With the advancement of computational tools and processing power, a comprehensive parametric study is only recently feasible.

Dynamic amplification factors, due to the nature of their formulation, are incapable of applying to all structures. They were developed by applying statistical methods to a population of bridges that were selected for investigation (Fenves et al., 1962), and therefore, while applicable to a majority of that population, cannot be expected to remain accurate for every single bridge in the population. Furthermore, there is no assurance that the chosen sample sets are

representative of the entire bridge stock, nor can it be assumed that the characteristics of the entire bridge stock are time invariant.

There is therefore a need, in the interest of developing methods whose range of applicability includes a larger portion of the bridge stock, to investigate the effect and interdependency of a more comprehensive set of parameters and to identify and characterize those bridges that are “outliers” and non-conservative. Furthermore, changes in bridge design, loading, maintenance practices, etc. and their influence on population characteristics should be considered in an effort to ensure resulting conclusions will continue to be applicable.

As truck platoons are introduced to America’s highways, the lack of understanding of vehicle-bridge interaction could further threaten the bridge stock. To date, research on the impact of repeated vehicles has been limited to railway bridges, for which the loading and structural characteristics are significantly different. Before this novel mode of transportation is implemented, investigation of its impact on bridge response should be conducted for which the bridge and load patterning are represented in a manner that is realistic of actual structures and truck platoon scenarios.

Part 1: Understanding Vehicle-Bridge Interaction and Dynamic Amplification

This first part details the experimental testing and investigation of a real bridge and documents the knowledge gained from such efforts. The bridge was selected for investigation due to the high vibrations reported by motorists and was therefore suspected to be experiencing significant dynamic amplification. The objectives for the first part of this paper are as follows.

1. Determine the effect of vehicle-bridge dynamics on bridge live load responses.
2. Identify the mechanisms and conditions that are influential to dynamic amplification.
3. Develop suitable methods for simulating vehicle-bridge dynamics for the purpose of estimating dynamic amplification.

To achieve these objectives, a series of field tests were carried out. Each phase of testing sought to progressively answer the following questions.

1. What region of the structure should receive instrumentation (is experiencing the greatest vibration).
2. What is the operational response of the structure (and characterize structure mass and stiffness).
3. What is the cause of dynamic amplification (and how can it be modeled).

A total of three field tests were carried out. The first test monitored acceleration of several cross-girders and piers under operational conditions. The second test monitored the acceleration and strain of two spans under operational conditions. The third test recorded the acceleration of a loaded dump truck and multiple spans. These tests provided quantitative measure of the bridge dynamic behavior and indicated that this bridge was experiencing

dynamic amplification as high as 2.0. The recorded responses were also utilized for the validation of FE models and VBI simulation methods.

The framework of structural identification (St-ID) was employed to guide the field-testing efforts. St-Id is a 6-step iterative process formulated by an ASCE committee which leverages experimental data to influence analytical models in an effort to reduce epistemic uncertainty. A summary of the process is provided in the following pages.

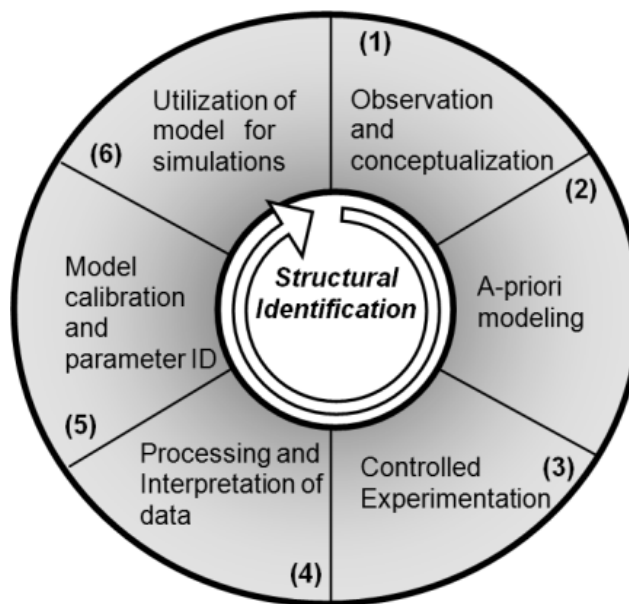


Figure 1.0.1: Diagram of StID Framework

St-Id Step 1: Establish clear objectives for the St-Id effort and identify critical constraints and any missing information by meeting with the owner and visiting the bridge. Collect and evaluate the reliability of all available legacy data and information.

St-Id Step 2: Observe the bridge system and even measure selected responses under different operational and environmental conditions to conceptualize the system for a-priori modelling. This may include checking the dimensions, sampling and coring to verify material properties, scanning for rebar details, and boring to evaluate the soil conditions. The data and insight from

these studies will help construct a 3D FE model that will simulate the important structural mechanisms.

It is important to note that an infinite number of FE models can be constructed that are geometrically consistent with the structure but may still fall short of accurately capturing the behavior of the structure. Given that the model should simulate all movements, restraints, joint and member deformations and mechanisms, it is important to utilize appropriate element types and sufficient mesh resolution. Furthermore, boundary conditions and connectivity between elements must be considered and modelled effectively.

St-Id Step 3: Instrument the bridge structure according to the established objectives and based upon results from the *a-priori* model to perform operational monitoring of critical structural responses (e.g. temperature, strain, rotation, displacement, acceleration).

St-Id Step 4: The metadata and test data are evaluated, synchronized and data quality is verified before archival. Data is visualized and interpreted for patterns and response quantities. This will start while performing the experiment to identify and rectify issues and mistakes.

St-Id Step 5: Modify, validate and finalize the a-priori FE model before calibrating it with selected data sets from the field testing, which may include bridge dynamic characteristics (i.e. mode shapes and frequencies). A critical issue is making sure that the model is complete (i.e. the model can explicitly simulate all of the critical loading and response mechanisms). There will always be a larger number of parameters to calibrate (material properties and dimensions of all elements as well as all joint, bearing, connection and boundary properties, including those at foundations) than the number of measurements, therefore one cannot expect a unique calibrated model. However, if a model is calibrated to mimic all of the measured input-output or

load-response relations of the bridge with acceptable level of discrepancy, it may be considered suitable to serve the objectives of St-Id.

St-Id Step 6: Leveraging the calibrated model for the objectives of St-Id. The calibrated model is especially powerful when used to identify mechanisms contributing to the bridge's actions and the corresponding capacity. Although the FE model is often used to compute a load rating, it can be further leveraged to simulate other loading scenarios and to gain a better understanding of the structural characteristics of the bridge. A more detailed description of the structural identification process can be found elsewhere, but the above discussion sufficiently summarizes the process.

The St-ID process may be performed several times during the exercise of investigating a structure. The case study presented in the following pages employed the process three times, each time marrying experimental data and FE simulation to answer specific questions about the structure and its performance.

Chapter 3: Description of Case Structure



Figure 1.3.1: Elevation View of Case Structure

The structure is an 11-span viaduct that carries 4 lanes of a major interstate highway. The viaduct was first constructed in 1952 but the superstructure was replaced in 1986 while retaining the concrete piers. East-bound and west-bound lanes are carried by adjacent steel multi-girder spans, which are supported by steel box-girders spanning between two piers. The structure was overall in good condition with no significant cracking or corrosion visible.

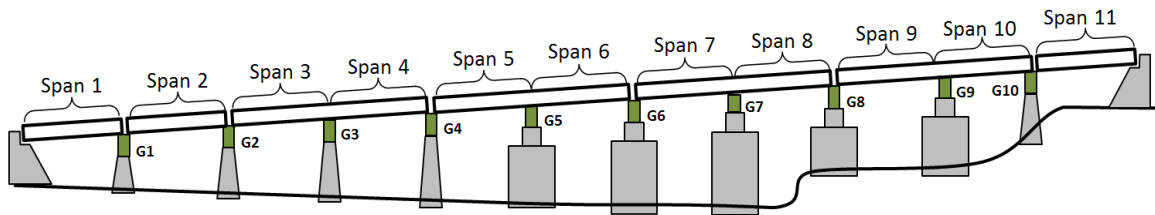


Figure 1.3.2: Schematic of Case Structure Elevation

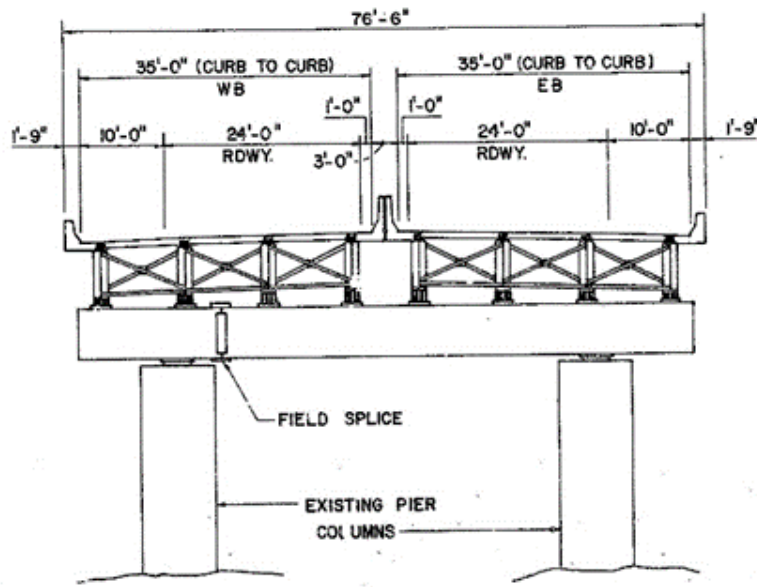


Figure 1.3.3: Cross-Section Diagram of Case-Structure from Construction Documents

Superstructure

The structural type is steel multi-girder. Eight girders run longitudinally, resting on steel box girders that span transversely and are supported by the concrete piers. A reinforced concrete composite deck was cast in place, with a “raked” finish and no overlay. The deck is discontinuous between girders 4 and 5, thereby creating two adjacent structures.



Figure 1.3.4: View of Case Structure from Underside Featuring Deck Separation

There is no skew. The bridge has eleven spans. The maximum span length is 140' (42.7 m). The out-to-out width is 76'6" (23.2 m). Three spans are simply supported (spans 1, 2 & 11), while the remaining eight are two-span continuous. Each span has five interior rows of X-framed diaphragms and chevron diaphragms over the piers. The following figure enumerates the girder layout which will be referenced in the following sections.

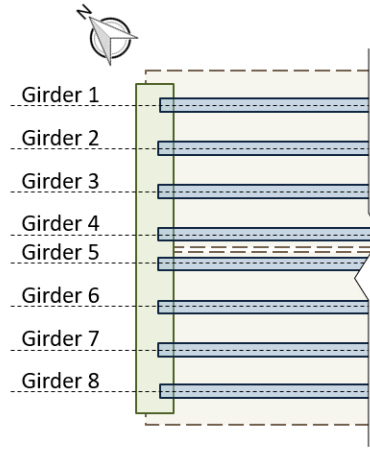


Figure 1.3.5: Schematic of Case Structure Typical Girder Layout with Numbered Girders

Substructure and Bearings

The concrete piers and abutments were constructed in 1952 and are all that remains of the original structure. They are supported by driven piles. Elastomeric bearing pads are installed on top of the piers and support the transverse box girders. Rocker bearings or pedestals are installed between the box girders and longitudinal girders at those locations which are in the center of continuous spans. Elastomeric bearings are installed between the box girder and the longitudinal girders at the remaining locations.



Figure 1.3.6: View of Case Structure Bearings

Condition

Visually, the deck appears to be in good condition, with no major cracking visible. Minor damage was observed in some regions of the center concrete barrier. The girders appeared in excellent condition. No major rusting was observed, and the girders appeared well maintained. The piers exhibited very little efflorescence and virtually no spalling. Repairs had been performed on several piers, where an embedded drainage pipe had rusted and caused a portion of concrete to spall off.

Table 1.3.1: NBI Details of Case Structure

Year Reconstructed	1986
Skew	0 degrees
Deck Width	76'6"
Maximum Span Length	140'0"
ADT	57410 (2013)
Deck Condition	6 (Satisfactory Condition)
Superstructure Condition	7 (Good Condition)
Substructure Condition	5 (Fair Condition)
Sufficiency Rating	70

Chapter 4: Preliminary Modeling of Test Structure

A 3D element-based model of a two-span continuous section of the viaduct was created based on the geometry and material specifications provided by construction documents. The specifics of this class of model are described in the following section.

Element-Level Method of Analysis

This type of model employs both one-dimensional (frame/beam elements) and two-dimensional elements (plate or shell elements) to model girders/diaphragms and the deck, respectively.

Beam elements have 2 nodes with 6 DOFs each. Plate/shell elements may have 3 (in the case of triangular elements), 4 (in the case of rectangular elements), or up to 9 (in the case of 9-node rectangular shells) nodes with up to 6 DOFs each. In an effort to remain consistent with the three-dimensional geometry of the structure, various link elements (to connect girders to the deck and diaphragm elements to the girders) and constraints (to simulate boundaries) are also employed. This model resolution is commonly termed “element level” and is the most common class of 3D FE models employed for constructed systems (Çatbaş et al., 2013b). The figure below shows a schematic illustrating how 3D geometry of the bridge is simulated using various elements and links.

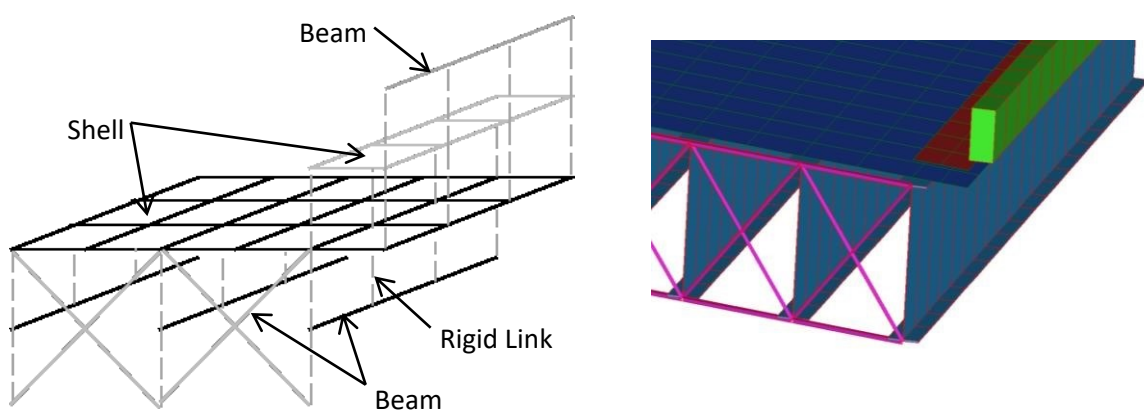


Figure 1.4.1: Schematic of Generic Element-level FEM Model

In this model type the girders are discretized into 1D beam elements and the cross-sections are considered through the definition of geometric constants (e.g. area, moment of inertia, etc.). While an element-level FE model can reasonably simulate most bridge responses, it is not without its shortcomings, specifically: (1) an inability to effectively simulate warping deformation of girders (associated with torsion), and (2) an inability to simulate localized stresses (i.e. stress concentrations) associated with geometric discontinuities. While these shortcomings may be critical in the case of modeling specific construction sequences for complex bridges (White, 2012) and advanced fatigue/fracture assessment, they are not relevant for the global behavior being investigated.

The two-span model included the entirety of the superstructure from the cross-girders to the concrete barriers. All elements were rigidly connected at coincident nodes unless otherwise specified. Full composite action was assumed and enforced by using rigid links to connect the girder nodes to the deck nodes. The image below shows a cross-section of the model and the reduction of 3D bridge elements to plate, beam and link elements.

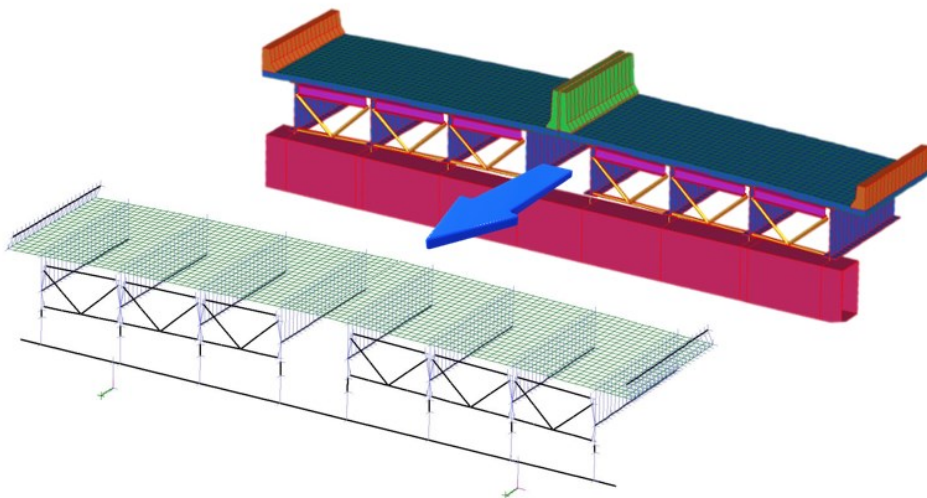


Figure 1.4.2: Illustration of Element-Level Representation of 3D Geometry

The concrete piers were initially included in the model, but sensitivity studies showed that these additional elements had little impact on the model behavior of interest. The piers were therefore reduced to nodal restraints at the location of the connection between cross-girder and pier. Boundary conditions were therefore applied to a node located at the bottom of the cross girder which was attached to the cross-girder element nodes with a rigid link. The following table summarizes the boundary conditions applied to the cross girders. Spring stiffness was assigned for rotation about the Z-axis to account for the stiffness provided by the elastomeric bearings.

Table 1.4.1: Cross-Girder Boundary Conditions (Nodal Restraints)

	DX	DY	DZ	RX	RY	RZ
@ East Piers	F	F	F	F	R	S
@ West Piers	R	F	F	F	R	S

F – fixed; R – released; S - spring



Bearings and Pedestals

The stringers were supported by elastomeric bearings, rocker bearings and pedestals. In all cases rigid links were used to connect the various elements at their nodes. Nodes were also placed at locations corresponding to the bottom surface of the stringers and the top surface of the cross-girder as illustrated in the following figure. An element (red) was subsequently placed between these nodes with attributes appropriate for the type of bearing/support.

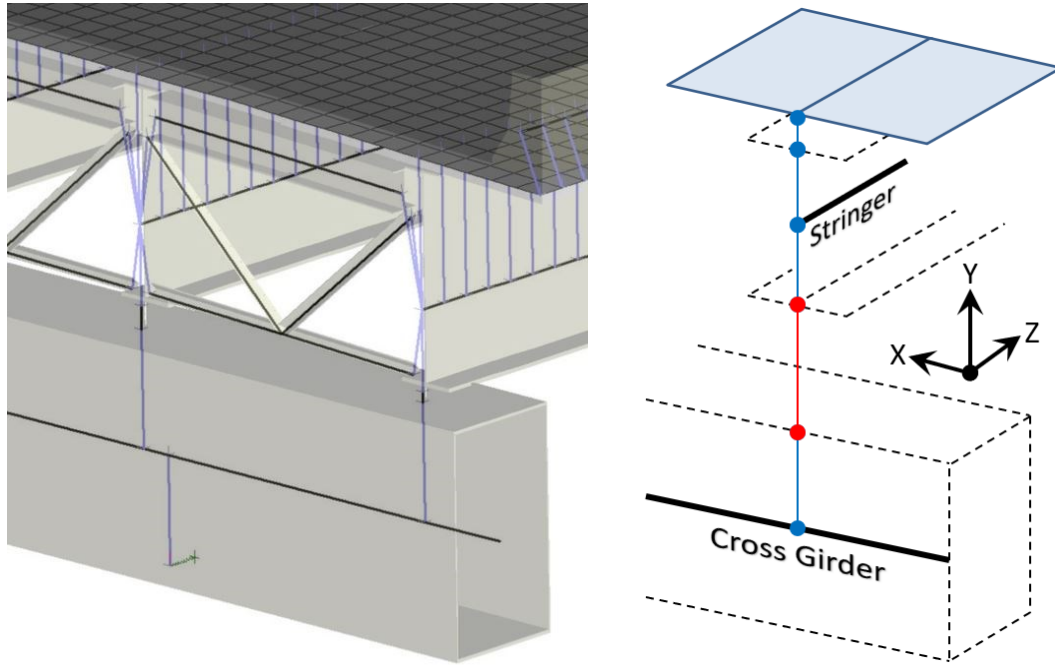


Figure 1.4.3: Illustration of FE Representation of Connectivity between Girders and Cross-Girders

For pedestals this element was simply a rigid link (XYZ-space). Links that were rigid in only the XY-plane (normal to bridge length) were used for rocker bearings thereby permitting longitudinal motion of the stringers while maintaining vertical rigidity and transverse stability. For elastomeric bearings, the same XY-plane rigid link was used in addition to a spring-damper element that spanned the same two nodes. The spring-damper element allowed the stiffness of the elastomeric to be included with its lateral stiffness parameter (axial and torsional stiffness values were set to zero).

Dynamic Characteristics of FE Model

A natural frequency analysis of the FE model was performed to extract the global mode shapes of the model and the corresponding frequencies. The first 8 modes are depicted in the following figures.

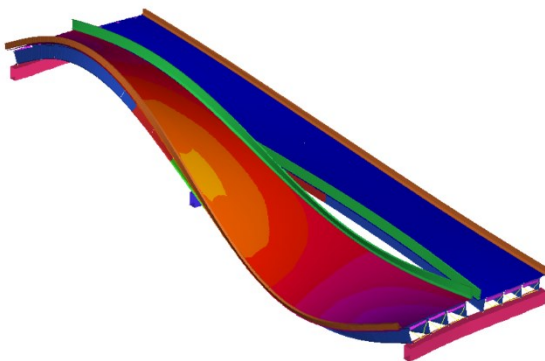


Figure 1.4.4: Apriori FEM Mode 1 – 2.37 Hz

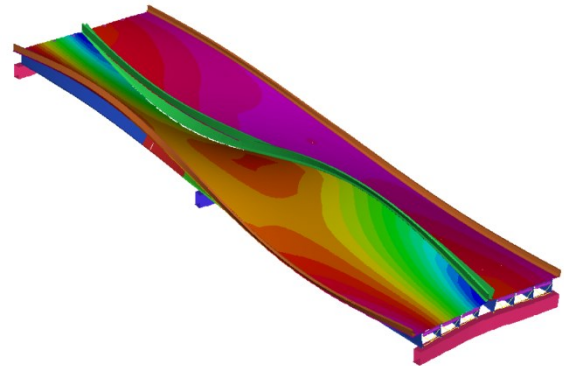


Figure 1.4.5: Apriori FEM Mode 2 – 2.73 Hz

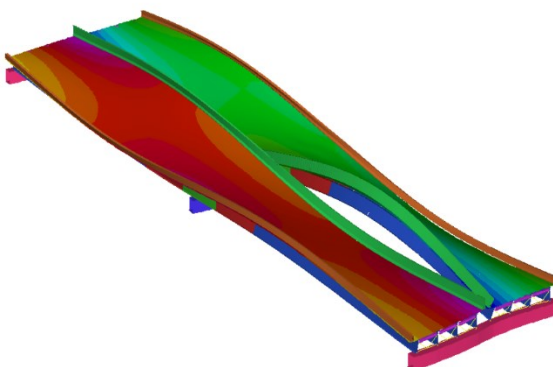


Figure 1.4.6: Apriori FEM Mode 3 – 3.22 Hz

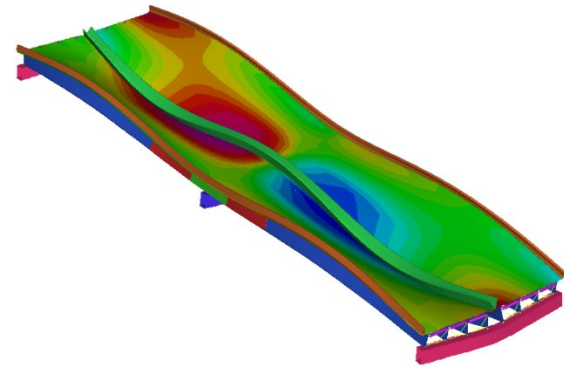


Figure 1.4.7: Apriori FEM Mode 4 – 3.71 Hz

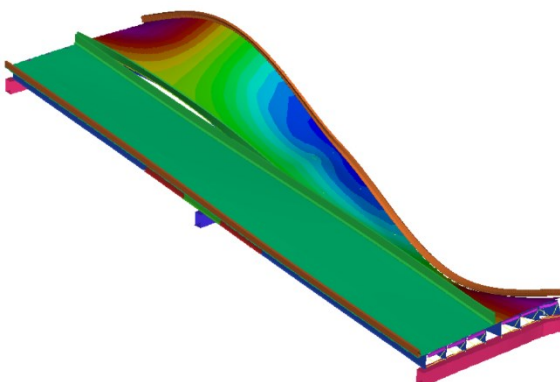


Figure 1.4.8: Apriori FEM Mode 5 – 3.77 Hz

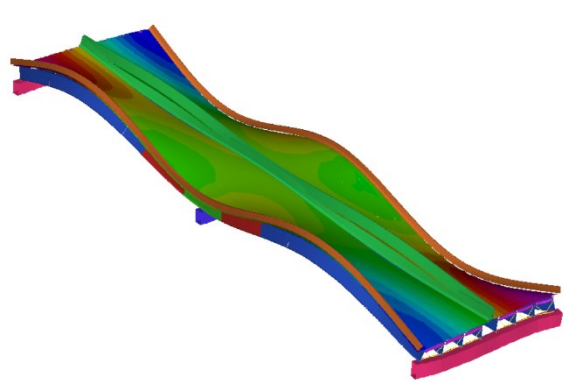


Figure 1.4.9: Apriori FEM Mode 6 – 4.22 Hz

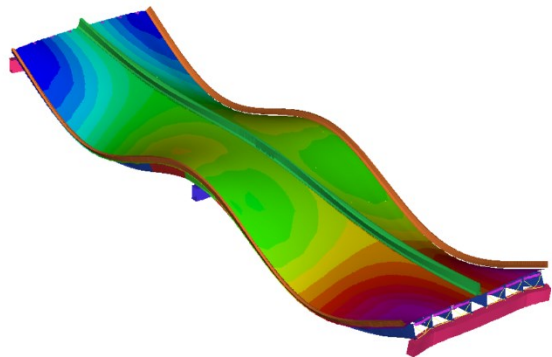


Figure 1.4.10: Apriori FEM Mode 7 – 4.25 Hz

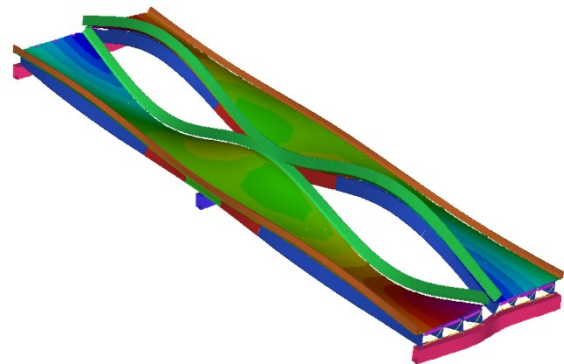


Figure 1.4.11: Apriori FEM Mode 8 – 4.58 Hz

As can be seen, the predicted modes of vibration are mostly bending and torsional modes as expected given the long-narrow geometry of the structure. These 8 modes of vibration accounted for 72% of mass participation (vertical translation) as reported by the FE software.

Conclusions

A 3D element-based model of spans 7 and 8 was created based on the geometry and material specifications provided by construction documents. This preliminary model exhibited 8 modes of vibration between 2 and 5 Hz.

Chapter 5: Phase 1 Testing

The purpose of the first phase of testing was to identify which portions of the structure were experiencing the greatest vibration and should receive further testing. Therefore, testing was planned and performed to achieve the following objectives.

1. Locate those spans which experience the largest vibrations
2. Identify in which direction the largest vibrations are occurring

Testing of the viaduct took place on July 7th and 8th of 2016.

Instrumentation Plan

The objectives of this test dictated that sensors be installed at several locations along the viaduct's length to facilitate comparison. Therefore, four locations were selected that were accessible and featured similar structural components. Furthermore, the major difference between different sections of this viaduct was the height of the piers. Sensors were therefore installed near or on the piers to examine their behavior under operational conditions.

Given these objectives and drivers, cross girders at piers 2, 3, 5 and 7 were instrumented with accelerometers. The accelerometers were positioned in the middle of the cross girders where maximum deformation was observed for several natural modes of vibration as predicted by the preliminary FE model. Accelerometers were also positioned at one end of the cross-girder to capture transverse (to bridge length) motion, as well as on the web over the piers to capture longitudinal motion. In this way motion of the cross-girder in the vertical, longitudinal and transverse directions could be captured and characterized.

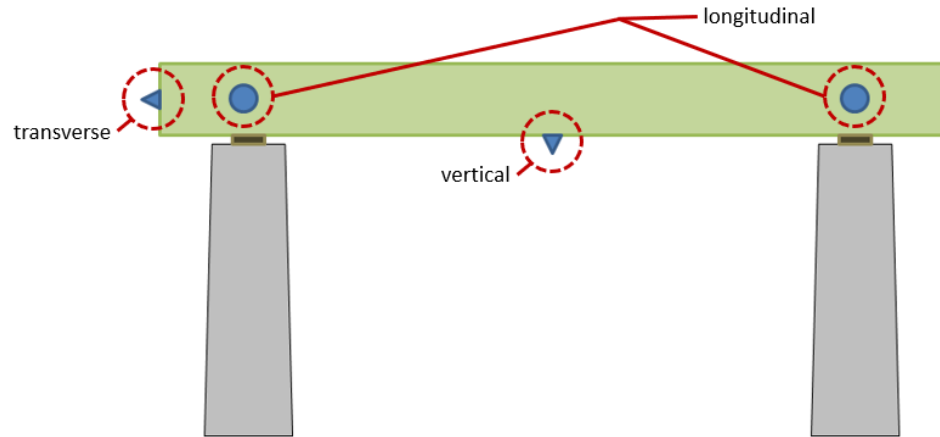


Figure 1.5.1: Schematic of Sensor Locations at a Given Pier Location

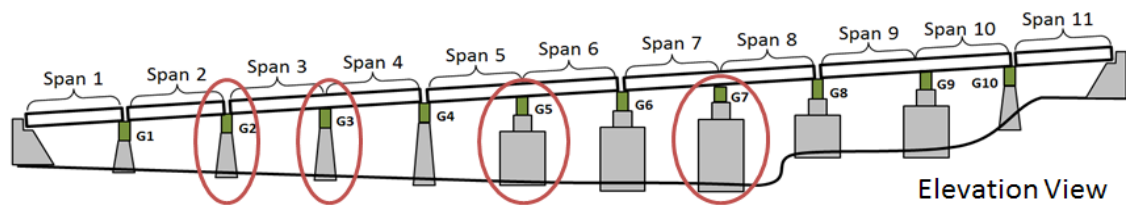


Figure 1.5.2: Schematic Showing Piers Chosen for Instrumentation

Equipment

A total of 16 (uniaxial) accelerometers were installed on the structure for this phase of testing.



Figure 1.5.3: Accelerometer (PCB 393A03) with Magnetic Base (PCB 080A54)

The sensor and data acquisition system (DAQ) model info are provided in the following table.

Detailed specifications can be found in the appendix.

Table 1.5.1: Testing Equipment Model Info

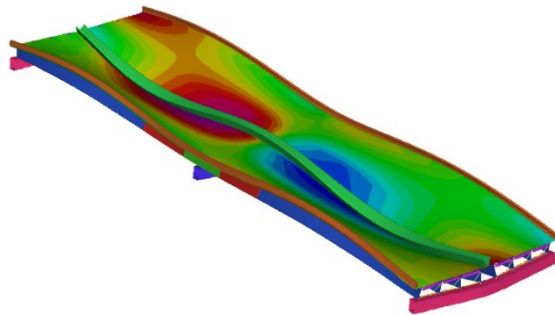
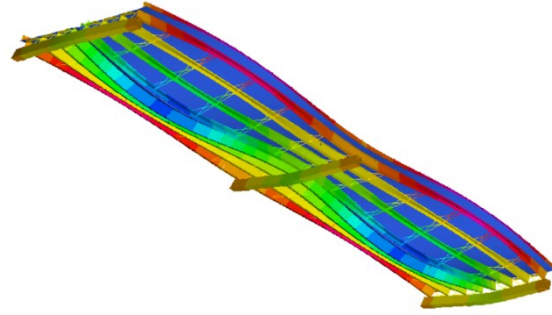
Item	Model No.	Description
Accelerometer	PCB Model 393A03	Ceramic Shear ICP® Accelerometer
DAQ Chassis	NI cRIO-9022	Embedded Real-Time Controller
DAQ I/O Modules	NI 9234	C Series Vibration Input Module

The DAQ was outfitted with 4 of the vibration input modules to provide the required 16 channels. The DAQ power was provided with a battery.

Test Activities

All accelerometers were attached to the steel structure with magnets. Cables were strain-relieved with hand clamps near their installation location to prevent the weight of the cable from pulling off the accelerometer and the motion of the cable from influencing the reading. Cables were subsequently run to the ground and to the data acquisition system.

The eight global modes predicted by the preliminary FE model were all under 5 Hz. The fourth mode depicted in the following figures results in the greatest deformation of the cross-girder. Therefore, the sampling rate should be assigned to capture this mode, at a minimum.

**Figure 1.5.4: Top View of Mode 4 (3.71 Hz)****Figure 1.5.5: Underside View of Mode 4 (3.71Hz)**

Since the global modes of vibration of interest were under 10 Hz, the sampling frequency should be at least 20 Hz according to the Nyquist Theorem to avoid signal aliasing. However, due to the uncertainty of the structure and its behavior, a sampling rate of 200 Hz was chosen. The higher sampling rate will provide enhanced frequency resolution when performing spectral analysis.

Sensors were installed on the morning of July 7th, 2016. Data was gathered continuously for several hours during normal operation of the bridge (i.e. no restrictions imposed on traffic) on the afternoon of July 7th. Daytime temperatures were steady near 90°F (32°C) with mostly cloudy skies and no precipitation. Sensors were removed from the bridge on July 8th.

Results and Interpretation

The resulting acceleration data was compared by examining and comparing time-histories for different cross-girders. All instrumented cross girders experienced similar levels of vertical and longitudinal acceleration, while the cross girder at pier 7 experienced much higher transverse acceleration. The transverse acceleration time history is shown below, while those for vertical and longitudinal acceleration are provided in the appendix.

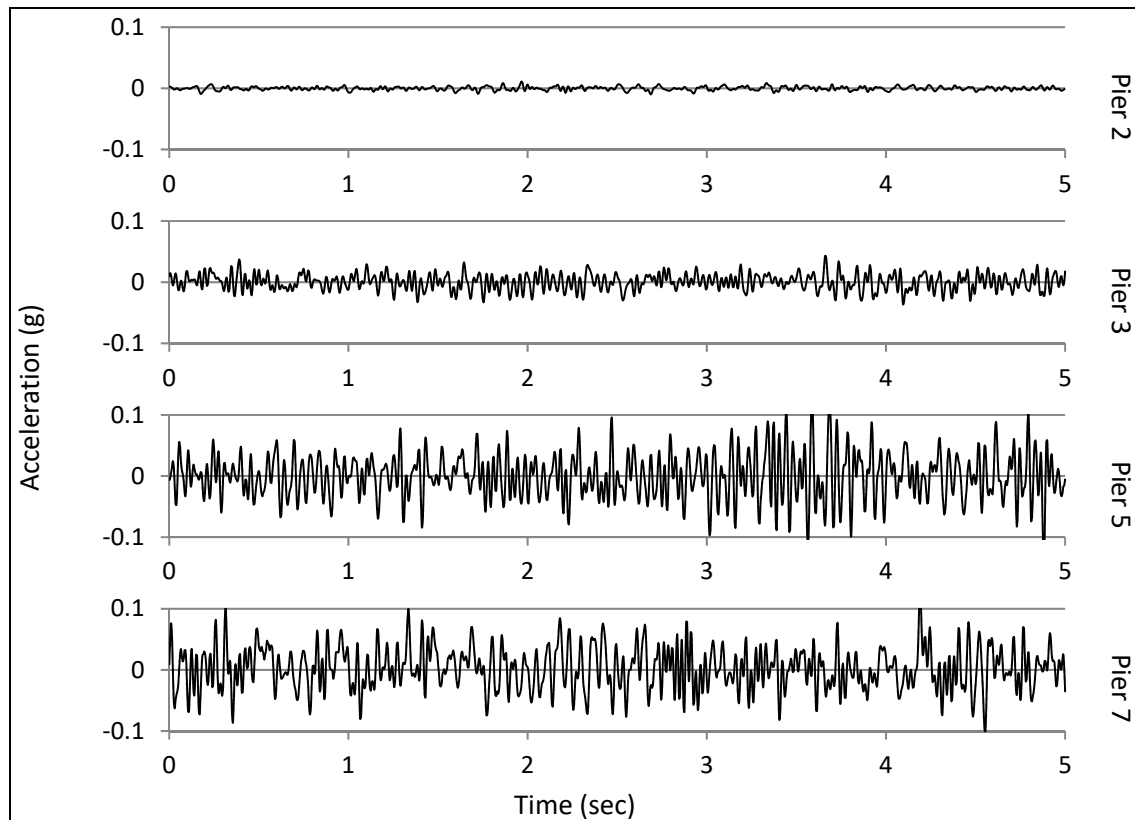


Figure 1.5.6: Transverse Acceleration Time Histories

To further compare acceleration the root-mean-square (RMS) was computed for each location over a period of 28 minutes. Because of the cyclic nature of structural acceleration that is nearly

symmetrical about the zero line, an average of the data would return a value very close to zero. It is for this reason that the RMS was employed. A comparison of the RMS values at different locations is compared in the following charts.

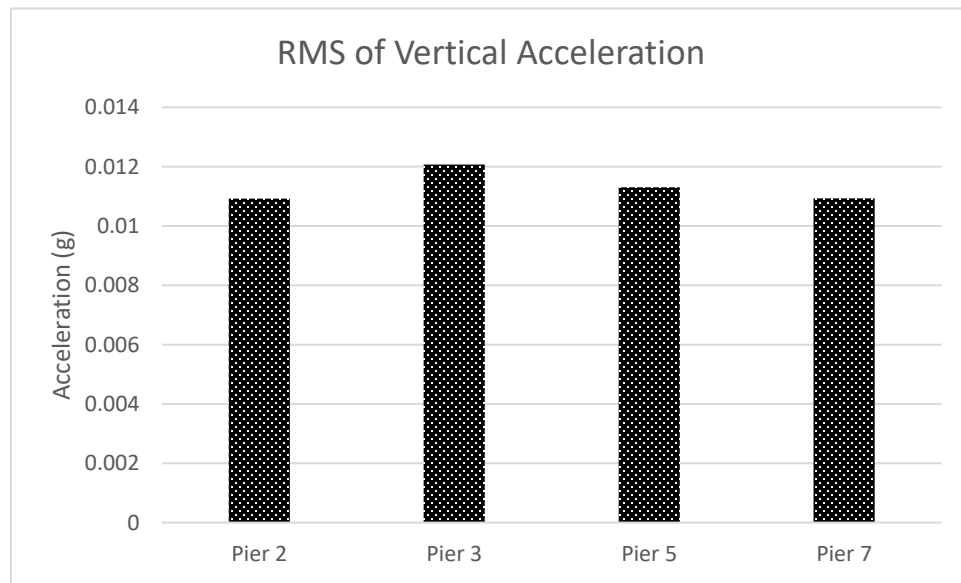


Figure 1.5.7: Comparison of Vertical Acceleration RMS for Different Piers

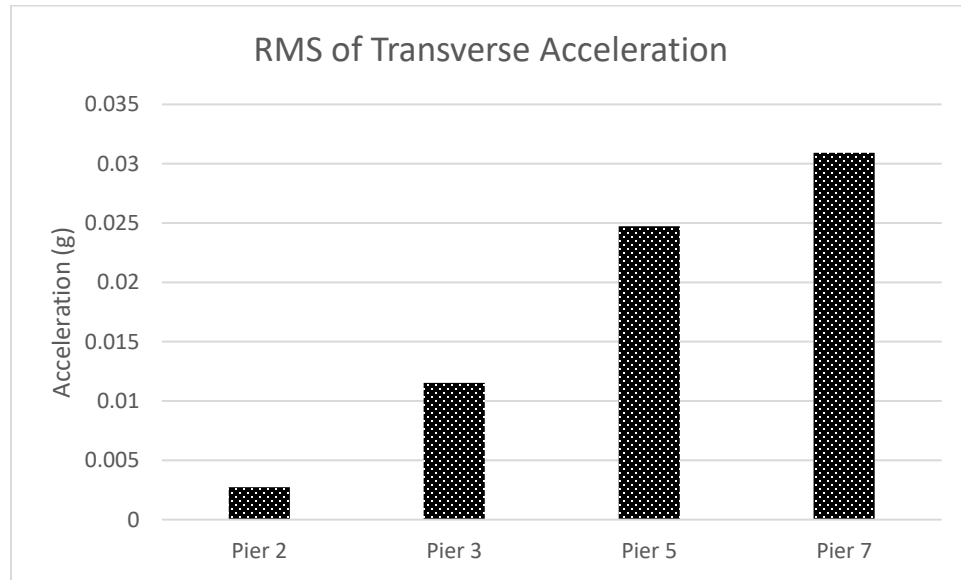


Figure 1.5.8: Comparison of Transverse Acceleration RMS for Different Piers

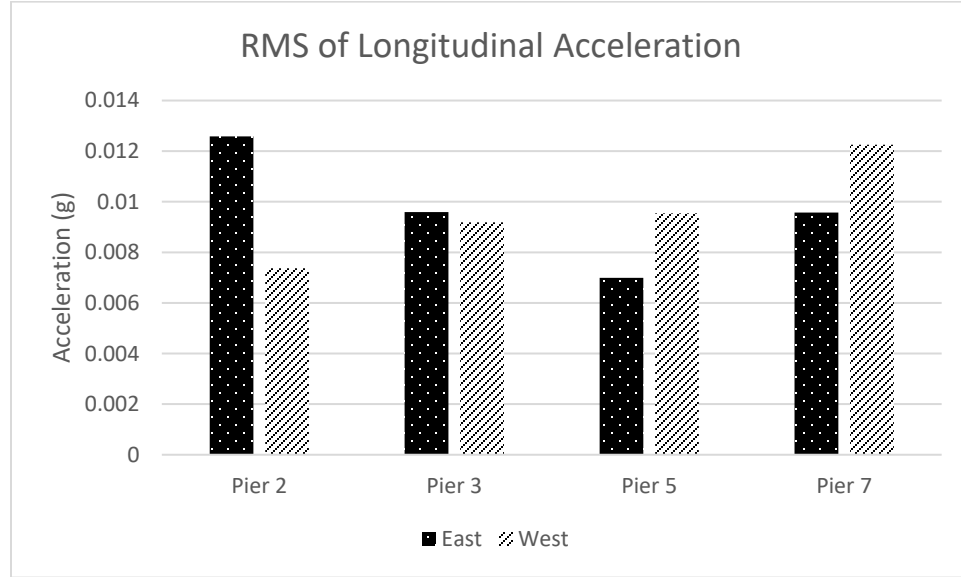


Figure 1.5.9: Comparison of Longitudinal Acceleration RMS for Different Piers

Since the performance of the bridge under vehicular loading is the principle concern of this study, and since that loading is applied almost exclusively in the vertical direction (centrifugal and braking forces are not considered in this study), it is the vertical response that should be most influential for deciding the region to perform further testing. However, as can be seen in the preceding RMS comparisons, the vertical acceleration is consistent between locations. While the longitudinal acceleration RMS does differ at different locations, the two sides (east and west) have dissimilar trends and therefore fail to identify a region of high excitation. Furthermore, while the RMS value for transverse acceleration clearly point to Pier 7 as experiencing the greatest excitation, it is uncertain that this direction of motion is indicative of the vibrations associated with dynamic amplification of vehicular loading. It can therefore be concluded that the bridge is experiencing similar levels of vibration across many or all of the spans.

Spans 7 and 8 were subsequently chosen for further testing. This decision was based on the available access to the superstructure as well as the evidence that span 7 may be experiencing

slightly higher vibrations. It was also hypothesized that the taller piers supporting spans 7 and 8 would provide greater flexibility thus permitting greater deformation and more vibration.

Test Conclusions

This phase of testing was intended to identify the regions of the structure that were experiencing the greatest vibrations. This was accomplished by instrumenting several cross-girders and piers with accelerometers and recording operational responses. The conclusions of this testing are as follows:

- All instrumented locations exhibited similar levels of vibration, especially in the vertical direction.
- Pier 7 exhibited higher transverse acceleration compared to other locations.

As a result of these findings and the available access to the underside of the structure, spans 7 and 8 were selected for further investigation in Phase 2 testing.

Chapter 6: Phase 2 Testing

Based on the observations and results from the first phase of testing, spans 7 and 8 were selected for further investigation. The purpose of this phase of testing was to characterize the superstructure using operational dynamic data and to quantify the dynamic amplification experienced by the bridge during typical traffic conditions. Therefore, testing was planned and performed to achieve the following objectives.

1. Identify the superstructure's global (operational) modes of vibration.
2. Capture operational vibrations and strains at critical locations and locations of maximum response under various traffic conditions.

Testing of spans 7 and 8 was performed on July 26th through the 29th of 2016.

Instrumentation Plan

The objectives of this test dictated that sensors be installed to capture maximum operational response as well as to uniquely identify the dominant global modes of vibration.

To capture a given mode shape of a structure, a sensor should be placed at or near the location of greatest deformation for that mode shape. For example, a first bending mode will experience the greatest deformation at midspan. Furthermore, a sufficient number of sensors should be spatially distributed such that the shape of the mode can be adequately characterized and distinguished from other modes.

The eight modes predicted by the preliminary FE model can be captured by locating sensors at the midspans of the exterior girders. Higher bending and torsional modes can be captured with sensors located at the quarter-spans of the exterior girders. Additional sensors in the interior of the bridge width facilitate the capture of butterfly modes. Given that the operational response is

a superposition of static and dynamic responses, it is expected that the maximum response of the stringers (acceleration and strain) would occur between 0.4L and 0.5L (midspan).

Therefore, sensor locations were chosen as depicted in the following figure. Additional sensors were located on the cross-girder to capture the shape of its deformation under operational loading as well as for the extracted mode shapes.

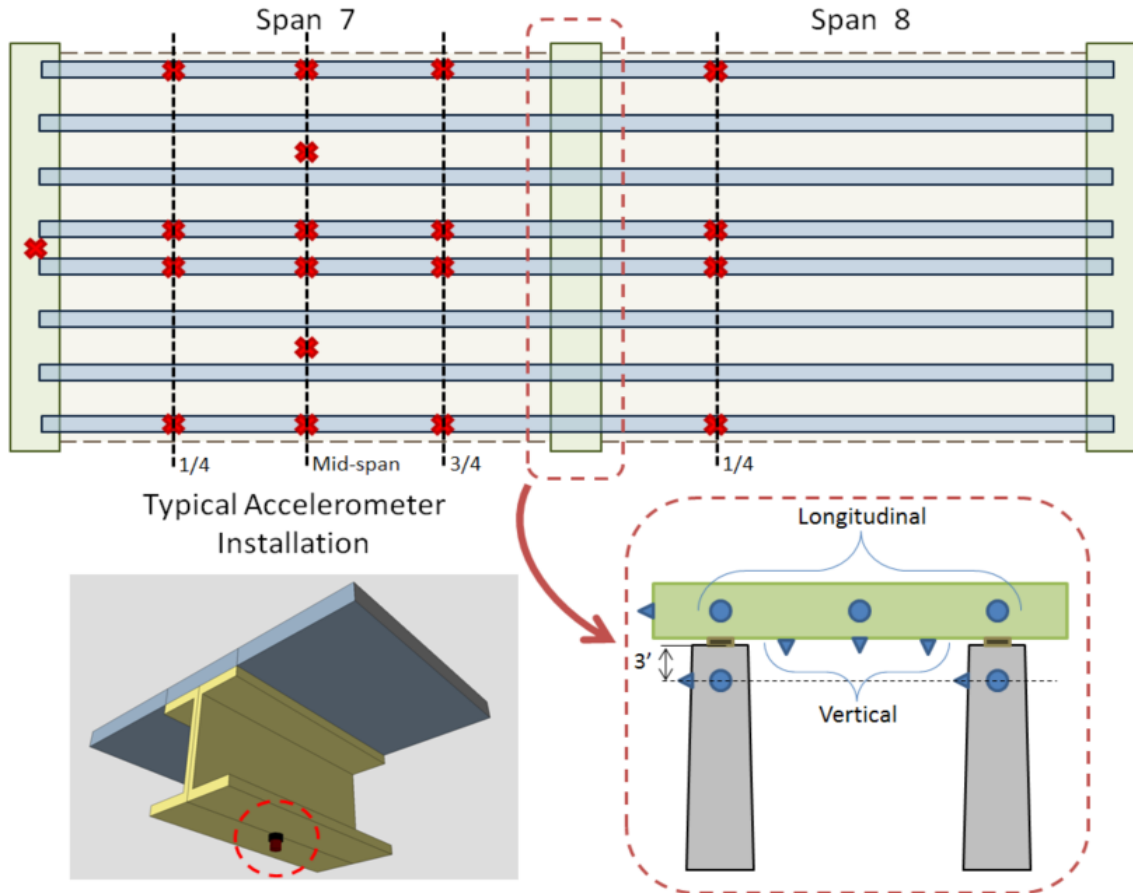


Figure 1.6.1: Accelerometer Installation Locations for Phase 2 Testing

A total of 30 accelerometers were installed on the chosen region of the viaduct (span 7 & 8).

Span 8 received far fewer sensors due to a utility line that impeded access to much of the span. However, accelerometers were able to be installed along the first quarter-span line and provide the necessary data to determine the relative phase between spans for a given mode shape.

Strain gauges were installed to provide information on the stress inducing deformation of the structure and the influence of vibrations on that deformation. Gauges were therefore installed at locations expected to experience the greatest strain (i.e. mid-span & negative moment region) as seen in the instrumentation layout provided below. A total of 12 strain gauges were installed.

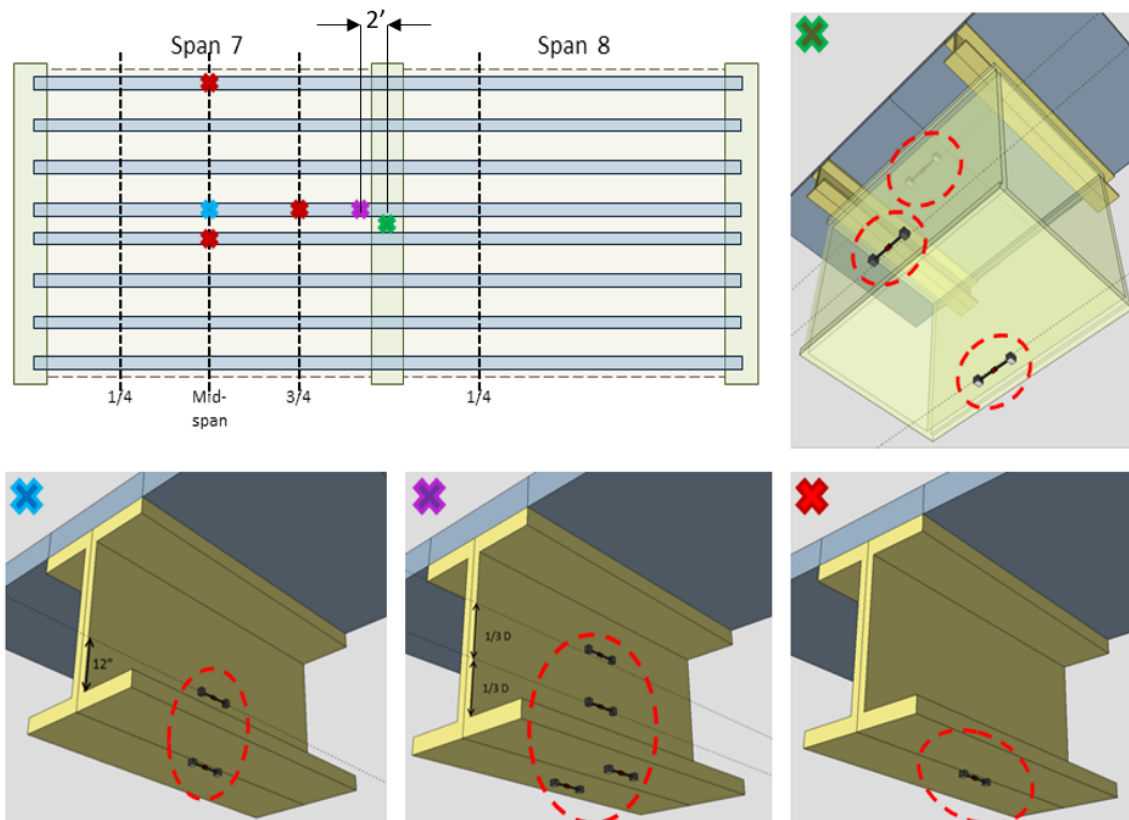


Figure 1.6.2: Strain Gauge Installation Locations for Phase 2 Testing

Equipment

All 30 accelerometers were sampled with a National Instruments (NI) CompactRIO. The 12 strain gauges were sampled with a Campbell Scientific Data Logger. The sensors and data acquisition systems were chosen based on their performance demonstrated in past tests. They have proven capable of capturing the range of responses expected for this structure and surviving the harsh

conditions that may be encountered in the field. The sensor and data acquisition system model info are provided in the following table. Detailed specifications can be found in the appendix.

Table 1.6.1: Phase 2 Testing Equipment Details

Item	Model No.	Description
Accelerometer	PCB Model 393A03	Ceramic Shear ICP® Accelerometer
NI DAQ Chassis	NI cRIO-9022	Embedded Real-Time Controller
NI DAQ I/O Modules	NI 9234	C Series Vibration Input Module
Strain Gauge	Geokon Model 4000	6" Vibrating-Wire Strain Gauge
Campbell DAQ	Campbell CR6	Measurement and Control Datalogger
Vibrating-Wire Analyzer	Campbell CDM-VW305	Vibrating-Wire Interface Module

The NI DAQ was outfitted with 8 of the vibration input modules to provide 32 vibration channels. Two of the vibrating-wire modules (CDM-VW305) were used with the Campbell DAQ to provide 16 vibrating-wire channels. Both DAQs were powered with batteries.

Test Activities

Access to the underside of the structure was provided with an articulating boom lift.



Figure 1.6.3: Photo Featuring Sensor Installation with Boom Lift

Accelerometers were attached to the steel superstructure with magnetic bases and attached to the concrete face of the piers with hot-glue (thermoplastic adhesive) after the surface had been cleaned with a steel-wire brush. Cables were clamped to the structure near the gauge to prevent the weight of the cable from damaging the gauge or affecting the readings. Cables were run on top of the girder bottom flanges to the central cross-girder before being run down to the ground where they were plugged into the DAQ.



Figure 1.6.4: Typical Accelerometer Installation on Steel Girder with Magnetic Base

Strain gauges were installed by epoxying the mounting blocks to the steel surface. The surface was first prepared by sanding off the paint until clean, bright steel was observed. The epoxy was allowed to cure for several hours before the gauges were locked into the mounting blocks. Tape was used to affix the gauges while the epoxy set. Cables were managed in the same manner as was done for the accelerometers.



Figure 1.6.5: Typical Strain Gauge Installation on Steel Girder with Epoxyed Mounting Blocks

Acceleration data was gathered at 200 Hz for a total of 14 hours to capture the behavior of the bridge under differing operational conditions (e.g. rush-hour vs free-flowing traffic). The sampling frequency was chosen using the same methodology provided in the documentation of the Phase 1 testing.

The Campbell DAQ was limited to 50 Hz sampling speed due to hardware limitations. Therefore, strain was sampled at 50 Hz for 12 hours and at 20 Hz over-night. The overnight sampling was performed at slower speeds to conserve battery power.

Accelerometers were installed on July 26th, 2016. Strain gauges were installed on July 27th. By 3:30 pm on July 27th, sensor installation was completed, and data recording commenced. Data was gathered for the remainder of the afternoon. At 7:45 pm, acquisition of vibration data was terminated, and the Campbell DAQ was set to sample the strain gauges overnight at 20 Hz before all personnel vacated the site. The Campbell DAQ continued to gather data until 5:00 am the following morning at which point the battery powering the DAQ had insufficient power to permit continued collection. At 7:00 am July 28th personnel arrived on site and reinstated

normal data collection (200 Hz for vibration; 50 Hz for strain). Data was collected until 3:00 pm at which time removal of accelerometers commenced. Sensor removal began on July 28th and was completed on July 29th. Paint was applied to areas that had been sanded.

Daytime temperatures routinely exceeded 90°F (32°C). Weather conditions for the four days of testing are summarized in the following table.

Table 1.6.2: Phase 2 Testing Weather Conditions

Date	Day Avg. Temp.	High Temp.	Conditions	%RH
July 26 th 2016	83°F (28°C)	92°F (33°C)	Mostly Cloudy	50%
July 27 th 2016	86°F (30°C)	94°F (34°C)	Partly Cloudy	40%
July 28 th 2016	85°F (29°C)	95°F (35°C)	Light Rain	90%
July 29 th 2016	81°F (27°C)	89°F (32°C)	Partly Cloudy	50%

Results & Interpretation

Characterization of vibrations with acceleration data

Peak acceleration levels remained consistent over the several hours of recorded data with frequent spikes suspected to correspond with heavy vehicle crossing events. One such event is depicted in the following plot.

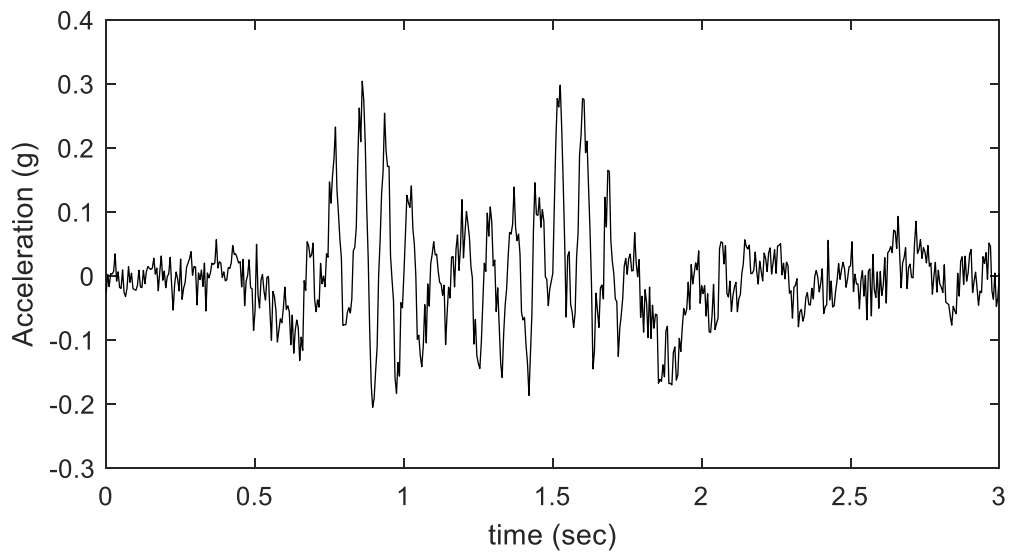


Figure 1.6.6: Event Acceleration Time History for Girder 5 at Middle of Span 7

The observed acceleration levels were higher than what was usually observed on multi-girder highway bridges. However, the magnitude of acceleration corresponds poorly with structural deformation or element stresses. This is because high-frequency acceleration contributes minimally to displacement. This is evident when considering the relationship between acceleration and displacement. The acceleration (\ddot{V}) over time (t) for a given frequency component can be described by the following sine function.

$$\text{Acceleration} = \ddot{V} = A * \sin(\omega t) \quad (4)$$

Where omega (ω) is the radial frequency ($2\pi f$), and A is the peak acceleration amplitude for the given frequency component.

Therefore, given that displacement is the double integral of acceleration ($V = \int \ddot{V} dt$), the displacement associated with a given frequency component is given by the following equation.

$$\text{Displacement} = -\frac{A}{\omega^2} * \sin(\omega t) = -\frac{\text{Acceleration}}{\omega^2} \quad (5)$$

It is evident from the previous equation that as the radial frequency increases, the displacement rapidly decreases.

To better judge the impact of acceleration on the amplitude of bridge displacement oscillations, the influence of high frequency content may be reduced by removing it with filtering techniques. This strategy is demonstrated with an elliptic filter.

While there are several filters which would accomplish this, the elliptic filter was chosen for its steep cut-off slope, resulting in greater reduction in content above the pass-band upper limit without compromising the pass-band content. The pass-band limit was chosen such that the major global modes of vibration were retained. Therefore, a filter was designed with an upper frequency cut-off of 20 Hz, a pass-band ripple of 0.5 decibels, and 40 decibels of stop-band attenuation. The frequency response of the resulting filter can be seen in the following figure.

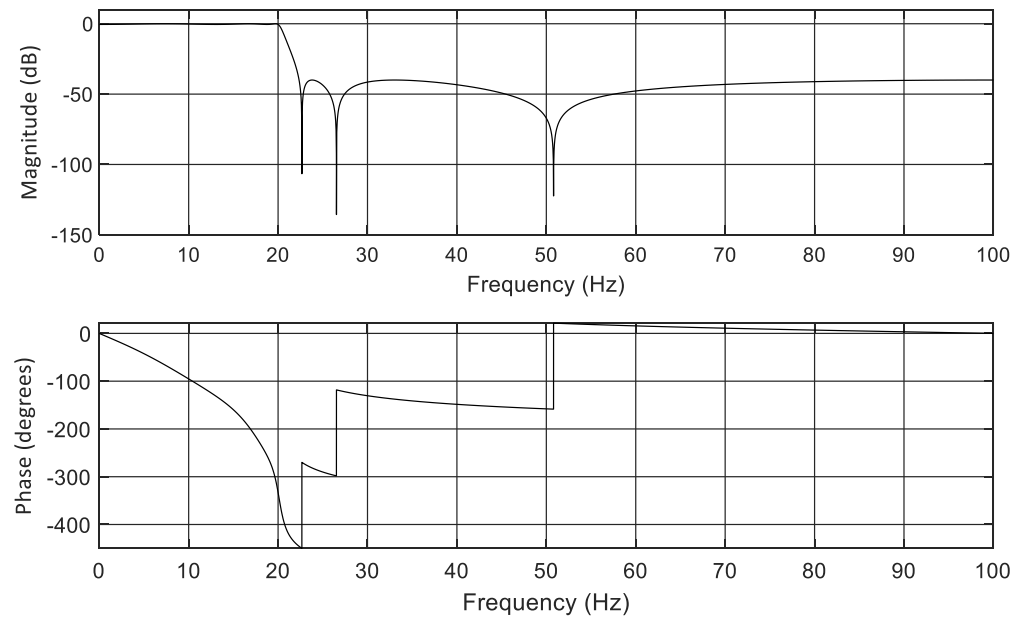


Figure 1.6.7: Frequency response of 6th order Elliptic filter

The above filter was applied to the acceleration time history. The same event depicted in Figure 1.6.6 is plotted below with the filter applied.

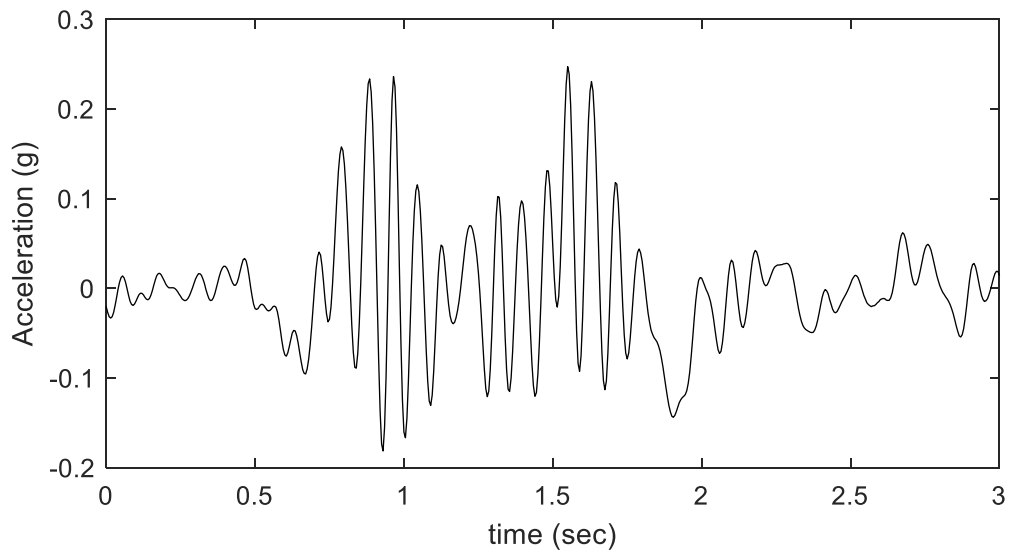


Figure 1.6.8: Filtered Event Acceleration Time History for Girder 5 at Middle of Span 7

As can be seen in the above plot, the filtering serves to reduce the peak acceleration but retains the nature of the signal. In spite of this reduction, the peak filtered acceleration still exceeds 0.2

g. The time-history of acceleration over a 4.5-hour period with the same filter applied is shown below for girder 5 at midspan.

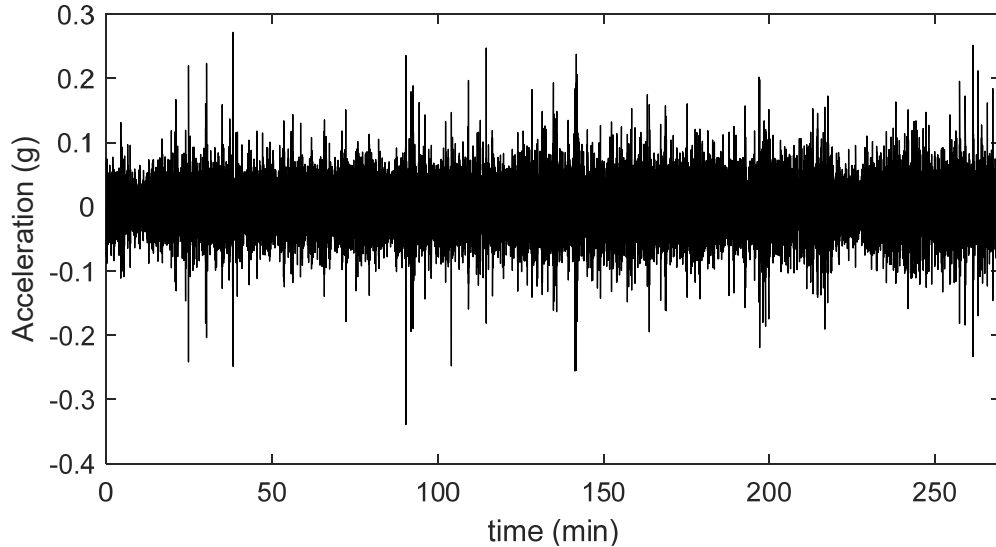


Figure 1.6.9: Filtered Acceleration Time History for Girder 5 at the Middle of Span 7

Over this period, multiple high acceleration events were recorded. The count of events that exceeded various thresholds are provided in the following plot.

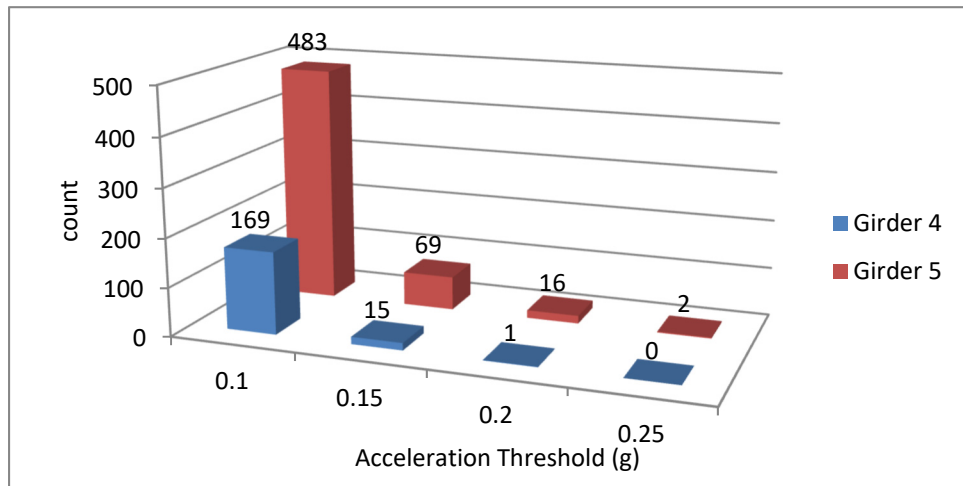


Figure 1.6.10: Count of Acceleration Exceedance Events over 4.5 Hours

Further characterization of the acceleration data may be performed with spectral analysis whereby the frequency content of the data is determined. The power spectral density (PSD) of

the data was estimated for several locations using Welch's overlapped segment averaging (100 second segment lengths with 25% overlap and a total record length of 4.5 hours). The PSD is better suited to the transient nature of the vibration data which contains a multitude of frequencies with time varying amplitude. The segmenting of the record tends to decrease the variance of the estimate but will also reduce the resolution of the periodogram. The chosen segment length and percent overlap results in a frequency resolution of 0.006 Hz which is more than adequate for the qualitative purposes of this analysis. The resulting frequency response is illustrated in the following plot and confirms that the majority of bridge motion occurs at low frequencies; between 2 and 4 Hz.

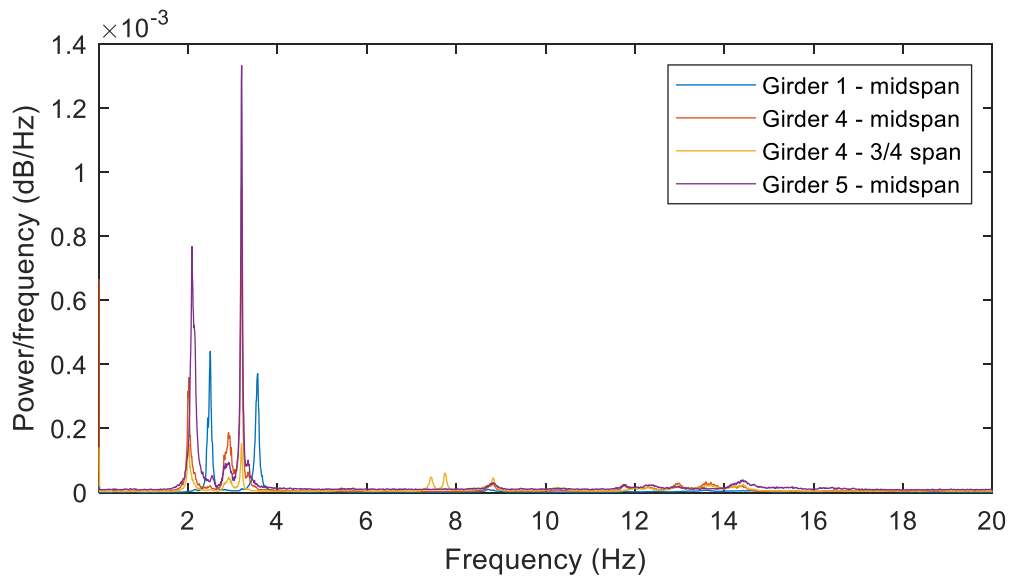


Figure 1.6.11: PSD Estimate of Girder Accelerations

As can be seen from the spectral analysis plot, most of the vibration being experienced by this superstructure under operational loading (i.e. traffic) is occurring at frequencies between 2 and 4 Hz.

To further assess the influence of bridge acceleration on deformation, the displacement is estimated using the “Omega Arithmetic” method. In this method, the acceleration is first

transformed into the frequency domain with an FFT, converted to displacement (by dividing by the radial frequency squared) and then transformed back to the time domain with an inverse FFT.

This method operates on the assumption that the signal is harmonic and that all frequency components were accurately captured. Therefore, the accuracy of this method is dependent of the ability of the data to be represented as a summation of harmonic functions. The recorded acceleration data is not harmonic, but rather transient due to the nature of the operational loading. Furthermore, the sensor sensitivity limits (i.e. 0.5 to 2000 Hz) prevent accurate capture of acceleration below 0.5 Hz. In order to assess the impact of these violations, a study was performed whereby an FE model was used to simulate a vehicle crossing and both acceleration and displacement were output. The acceleration record was then filtered to remove frequency content below 0.5 Hz, after which the "Omega" method of estimating displacement was performed. The estimated displacement is compared to the simulated displacement in the plot below.

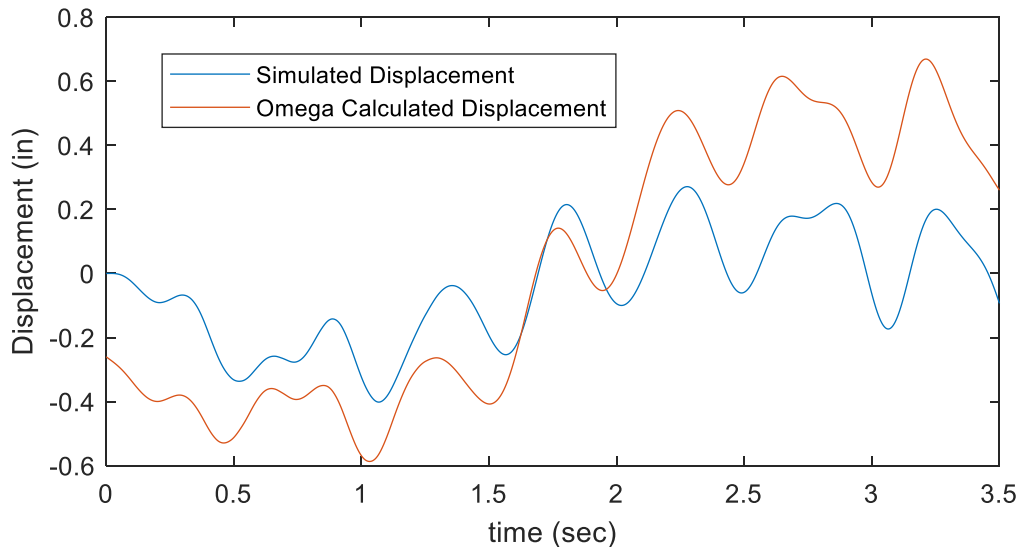


Figure 1.6.12: Performance of "Omega" Method for Data Without Low-Frequency Content

As can be seen from the above plot, the “Omega” method is unable to accurately estimate total displacement for this application. However, the method can still prove useful for estimating the deflection associated with bridge vibrations. To demonstrate this, the output displacement is filtered to remove frequency content below 1.5 Hz (below structure’s first natural frequency). This is compared to the displacement calculated with the “Omega” method, however, in this case the inverse FFT is performed on only a subset of the frequency components that excludes those components below 1.5 Hz. The resulting displacement time histories are compared in the following plot.

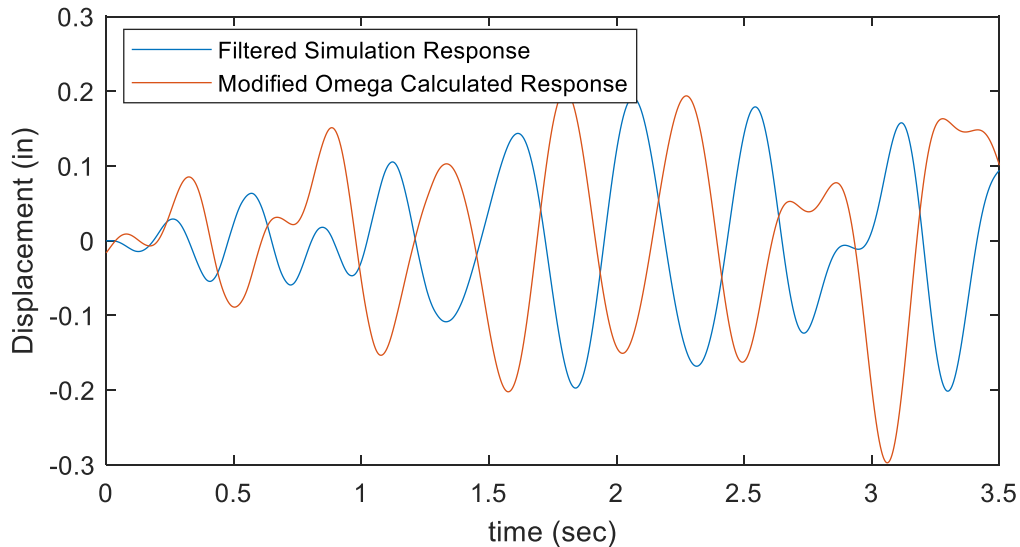


Figure 1.6.13: Performance of “Modified Omega” Method

While the modified “Omega” method is still inaccurate as evidenced by the previous plot, it still serves as a good estimate of the displacement associated with structural vibration. Therefore, the modified “Omega” method was performed on the acceleration data for the event presented earlier (Figure 1.6.6). The resulting displacement is plotted in the following figure. Note that this displacement estimate considers only frequency content between 1.5 and 20 Hz and thus only

represents a portion of the motion experienced by the bridge, but the motion that is associated with the bridge's major global modes of vibration.

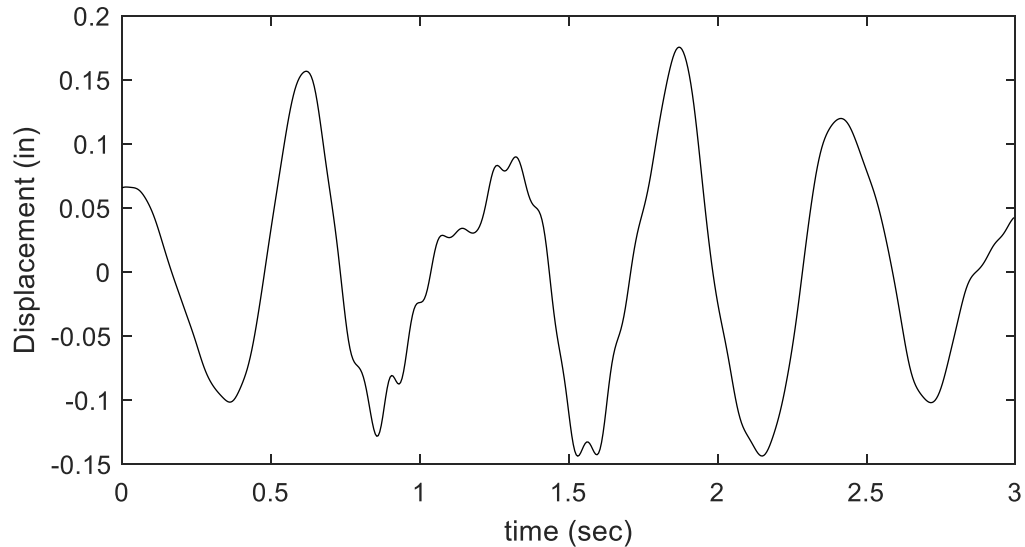


Figure 1.6.14: Displacement for Event as Estimated by “Omega Arithmetic” for Girder 5 at Middle of Span 7

The frequency components that made up the above displacement time history are described by the FFT and is plotted below.

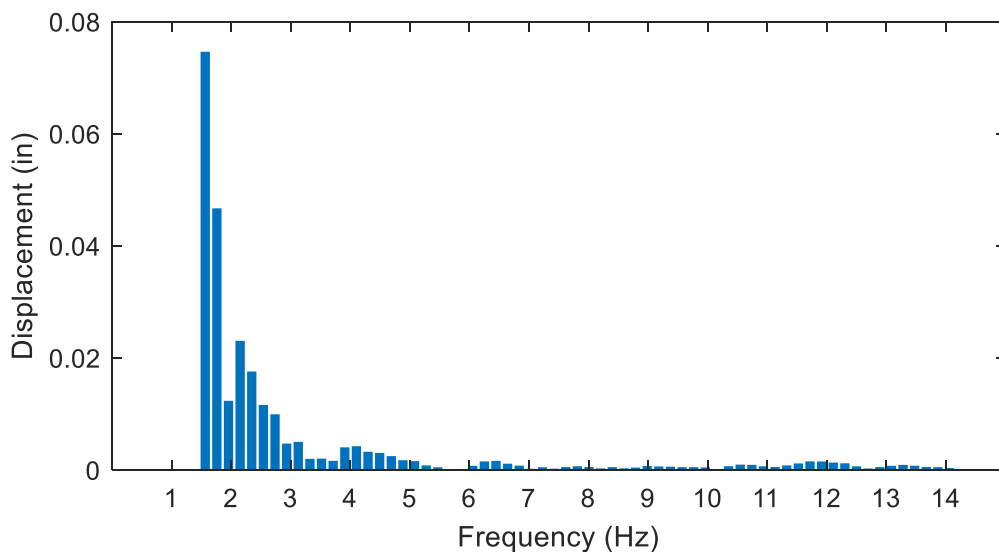


Figure 1.6.15: Parent FFT of Displacement Estimate by “Omega” Methods for Girder 5, Middle of Span 7

As can be seen in the preceding figure, the deformation of the structure associated with its vibration is roughly 0.15 in. and therefore is likely to significantly amplify the live-load demands. That amplification will be further quantified in the following section.

Quantifying dynamic amplification with dynamic strain data

The strain experienced by the bottom flange of select girders at midspan is provided in the following plot. As can be seen, these bottom flanges are frequently experiencing (tension) strains greater than $150 \mu\epsilon$ (micro-strain). This strain corresponds to approximately 4.5 ksi of stress for steel.

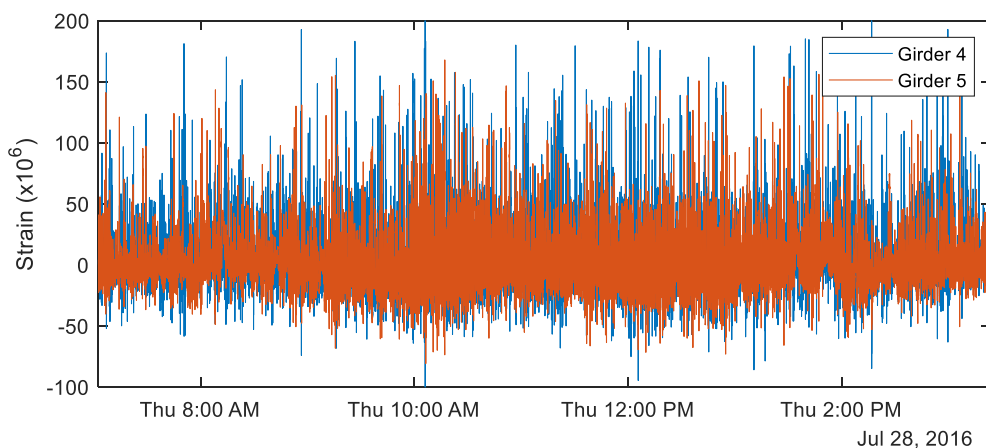


Figure 1.6.16: Strain Time History for Girders 4 and 5 at the Middle of Span 7

Girders 4 and 5 consistently experienced the highest strain levels. The number of events exceeding different thresholds over a 24-hour period for girders 4 and 5 (midspan, bottom-flange) is depicted in the following figure.

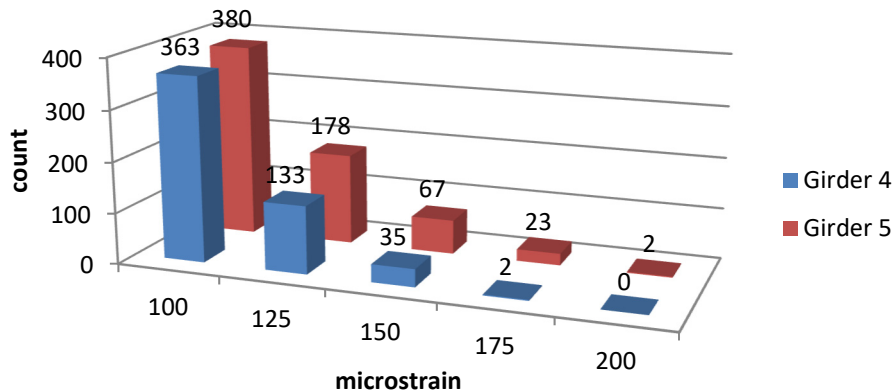


Figure 1.6.17: High-strain event occurrence count over 24 hours

One method of estimating dynamic amplification involves comparing raw responses to estimated static responses. The static responses are estimated by filtering out content associated with the bridge's vibration. This method can easily over-estimate amplification, especially when the data is too aggressively filtered, and if the loading is occurring at a frequency above the pass-band upper limit. Therefore, the pass-band upper limit should be chosen below the structure's lowest natural frequency.

A study was performed to assess the effectiveness of this method. In this study a vehicle crossing over the 3D FE model of the spans 7 and 8 was simulated at 960 in/sec (24.4 m/s) as well as at a crawl speed of 5 in/sec (0.13 m/s) to obtain the (quasi) static response. The dynamic response was filtered according to the method described above. A low-pass elliptic filter was applied with an upper pass-band limit of 1.5 Hz, a pass-band ripple of 0.5 decibels, and 40 decibels of stop-band attenuation. The upper pass-band limit was chosen such that it was less than the first natural frequency of 2 Hz. The frequency response of the resulting filter can be seen in the following figure.

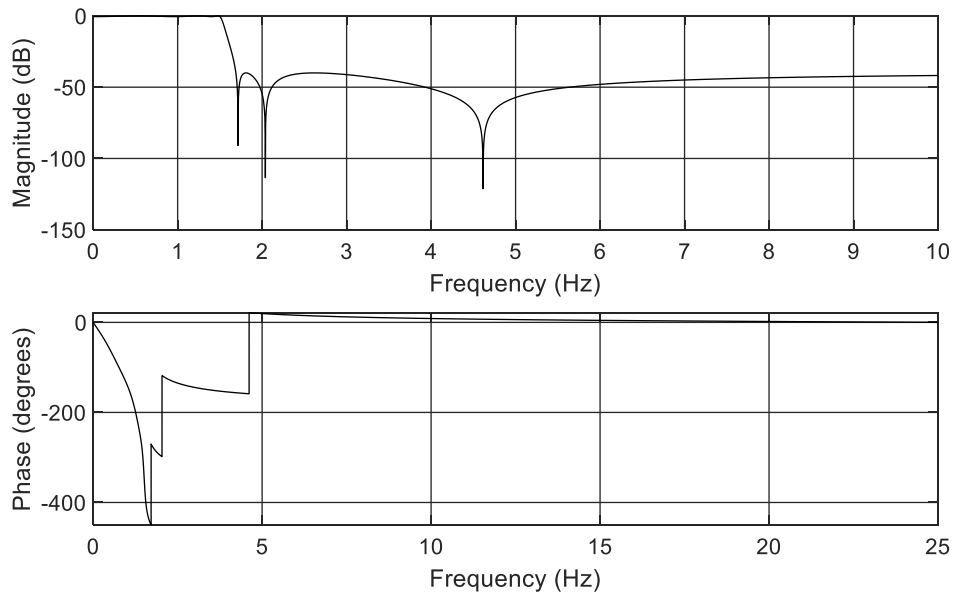


Figure 1.6.18: Frequency Response for Elliptic Filter (1.5 Hz Cutoff)

The moment at midspan of the girder beneath the vehicle path was the selected response. The FE software was not capable of outputting stress or strain in the element for this analysis, but since the model is linear, the stress and strain should be linearly related to the beam moment, and thus serves as an adequate substitute. The three data sets are compared in the following plot.

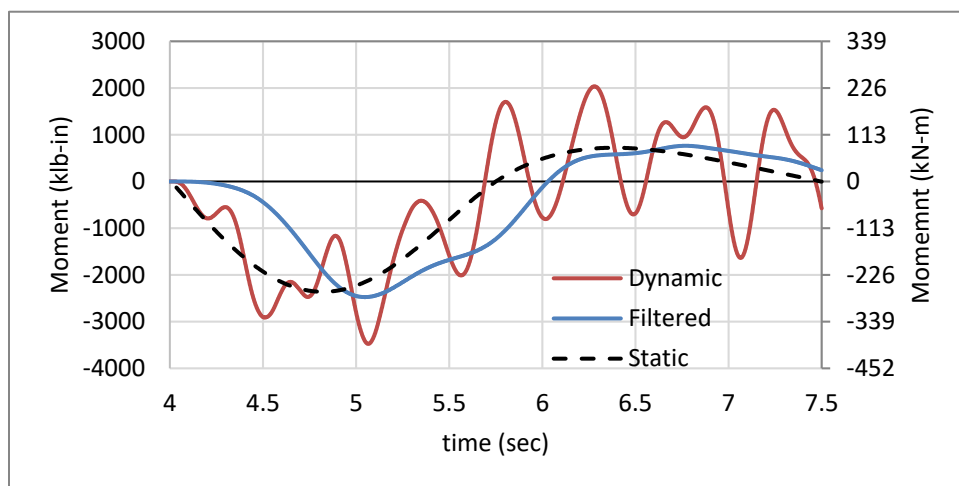


Figure 1.6.19: Comparison of Simulated Static Midspan Moment and Low-Pass Filtered Moment

The above plot shows that by applying a low-pass filter, a time shift occurs in the data. However, the amplitude of the filtered moment provides a good estimation of the static response.

The same process was performed with the experimental strain data. A low-pass elliptic filter was again applied with an upper pass-band limit of 1.5 Hz, a pass-band ripple of 0.5 decibels, and 40 decibels of stop-band attenuation. This filter effectively removes the dynamic component thereby providing an estimate of static response. The raw and filtered data are plotted below for an event that produced particularly high strains.

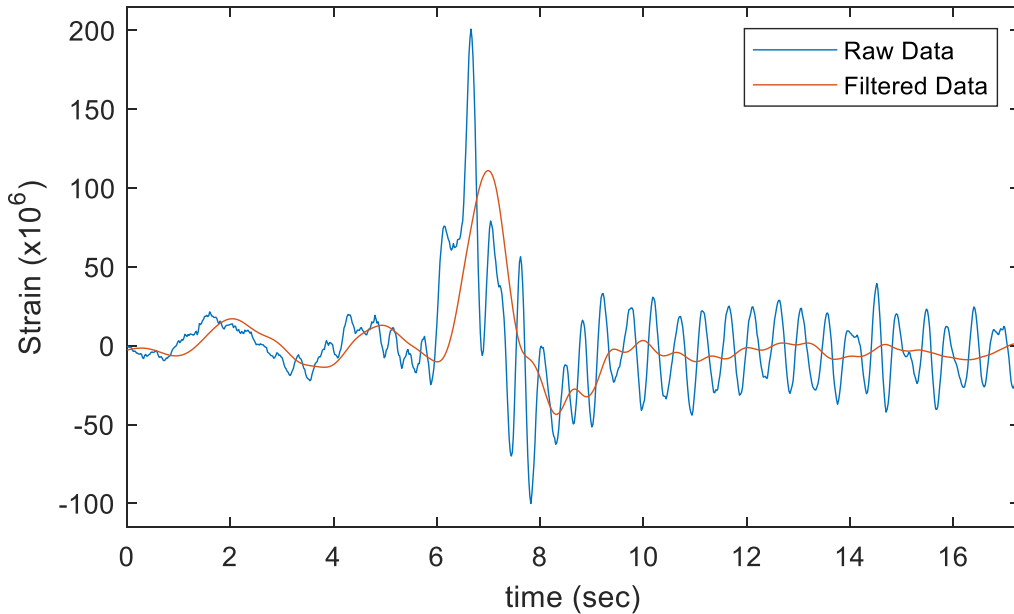


Figure 1.6.20: Filtered and Raw Strain for Girder 5 Bottom Flange at Middle of Span 7

The event featured in the above plot exhibits a dynamic amplification of almost 2.0.

Furthermore, this amplification is occurring at design-level load events.

The total response of the bridge is the sum of dead-load response and live-load response, including the dynamic component. Because the dynamic response of the bridge is dominated by mode 1, the live load response of the bridge (static and dynamic) can result in upward deflection of a span. Furthermore, because the deck was cast-in-place, it carries only superimposed dead-

load, which, for this bridge, consists of only the barriers. As a result, the dead-load stresses and strains in the deck are likely near zero. Therefore, any upward deflection of the bridge will result in net tension in the deck.

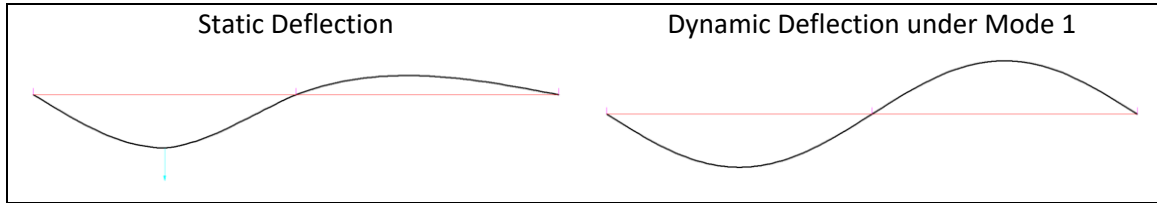


Figure 1.6.21: Live-Load Deflection Components for 2-Span Continuous Bridge

The magnitude of this tension strain may be extrapolated from the bottom flange and web strain readings assuming a linear strain profile for the cross-section. The measured and extrapolated strains for a typical large-strain event are provided in the following plot. Accordingly, the deck is routinely experiencing tension strain of $100 \mu\epsilon$ or greater in the “positive moment” region. Concrete strains of this magnitude are known to cause tension cracking (Leonhardt, 1988) and therefore may pose a threat to the continued performance of this structure.

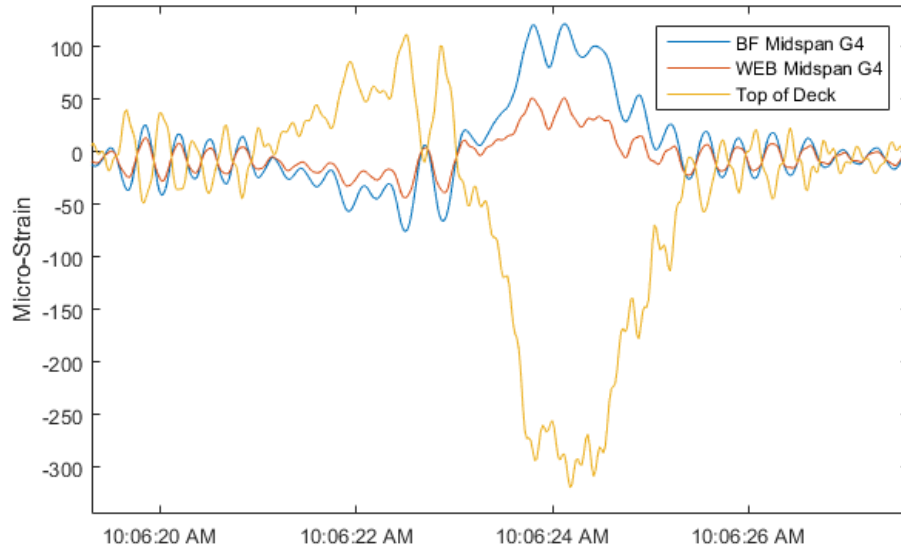


Figure 1.6.22: Extrapolated Strain in Top of Deck at Midspan over Girder 4

The strain for the bottom flange in the negative moment region (girder 4) is plotted for the same time period as shown in Figure 1.6.16. It can be observed that the bottom flange is frequently experiencing compressive strain over $50 \mu\epsilon$.

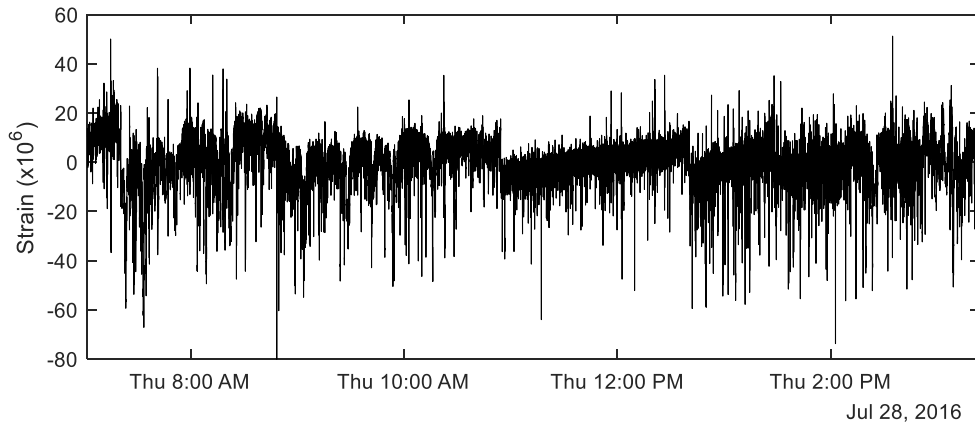


Figure 1.6.23: Strain Time History for Girder 4 Bottom Flange at 2' West of Cross-Girder 7 (Neg. Mom. Region)

Modal Parameter Estimation with Operational Response Data

From the field measurements, an $M \times N$ matrix is obtained, where M is the number of DOF that were instrumented, and N is the number of data points in the record. In order to examine the response for different frequencies, the data may be transformed into the frequency domain with the Fast Fourier Transform (FFT), which decomposes each response history into a sum of sinusoids. The number of discrete frequencies that are tested as part of a Fourier transform is directly proportional to the number of samples in the record (N) and equal to $N/2$. These frequency bins occur at intervals (Δf) equal to the sample rate of the data (f_s) divided by the number of samples (N).

Because the excitation of the bridge may be thought of as a random process, the response data (vibration) is also random and contains varied frequency content (i.e. vibration occurring at multiple frequencies simultaneously). While FFTs are quite capable at analyzing vibration when

there are a finite number of dominant frequency components, power spectral densities (PSD) are better suited to characterize random vibration signals.

The power spectrum of the data (PSD) may be estimated with a periodogram which multiplies the value of each frequency bin in an FFT (X_f) by its complex conjugate (\bar{X}_f). The result, which contains only real values, is then normalized by dividing it by the frequency bin width. This normalization effectively eliminates the dependency on bin width so that vibration levels may be compared in signals with differing lengths or sample rates. The periodogram can therefore be described by the following equation.

$$P_{xx}(f) = \frac{(X_f * \bar{X}_f)}{F_s/N} \quad (6)$$

Because the data set is finite, a modified periodogram is used which serves to reduce spectral leakage by windowing the time-domain signal prior to computing the FFT in order to smooth the signal at the edges of the window.

Welch's periodogram is an improved estimator of the PSD. Its method consists of dividing the time series data into (possibly overlapping) segments, computing a modified periodogram of each segment, and then averaging the PSD estimates. The result is Welch's PSD estimate. This method is especially useful for data in which the amplitude of different frequency components varies with time as is exhibited by operational acceleration data. A Hamming window was used for all PSD estimates using Welch's methods.

Because it is the goal of this analysis to obtain mode shapes of the structure, it is necessary to retain information about the relative phase of the responses at each location which will indicate the direction of deformation (i.e. is a given DOF deflecting upward or downward relative to other DOF). This is achieved by estimating the cross-power spectral density (CPSD). The

estimation is performed in same manner as the periodogram described above except the numerator is computed by multiplying the FFT value for one signal (X_f) by the complex conjugate of the FFT value from another signal (Y_f). In this case, both signals are response (output) records.

$$P_{xy}(f) = \frac{(X_f * \bar{Y}_f)}{F_s/N} \quad (7)$$

Since X and Y are complex, the CPSD estimate is also complex. Welch's methods were again employed to estimate the CPSD for each frequency line and with every signal such that P_{xy} was computed with X_f for each location (p) and with each location (q) serving as reference (Y_f), thereby producing a MxMxN matrix (H).

$$H_f = \begin{bmatrix} P_{xy_{11}} & \dots & P_{xy_{1q}} \\ \vdots & \ddots & \vdots \\ P_{xy_{p1}} & \dots & P_{xy_{pq}} \end{bmatrix}_f \quad (8)$$

Because the response data is from bridge motion, the responses are assumed to be directly related to the modal vectors (ψ) and the frequency response function (FRF) (H) is formally represented by the following equation (Allemang, 1999).

$$H_f = [\psi] * [\Lambda] * [L] \quad (9)$$

Where Λ contains temporal information and L is a function of input to the structure.

This representation of the FRF permits principle component analysis by Singular Value Decomposition (SVD). This algorithm decomposes a matrix (A) into three principle components: left singular vector (U), singular values (Σ), and right singular vector (V) according to the following equation.

$$A = [U] * [\Sigma] * [V]^T \quad (10)$$

Therefore, by performing SVD on the FRF matrix at each frequency line, spatial patterns in response may be extracted (U) and provide estimate of modal vectors (ψ) (shapes). The singular values (Σ), are proportional to the modal scaling of each corresponding mode and are plotted on a log scale as a function of frequency. Each peak of the singular values represents a frequency of resonance in the structure and the amplitude is directly related to the dominance of the corresponding mode shape at that frequency. At each frequency line, the left singular vector (U) is the approximate mode shape (ψ) of the response DOF, and the right singular vector (V) is the approximate modal participation vector (L) and represents the modal coefficients of the input at each DOF. In this case the input is unknown and thus only the left singular vector is used.

This process of identifying mode shapes with SVD is often referred to as the Complex Mode Indicator Function (CMIF). By including multiple columns of the FRF in the SVD (i.e. multiple records used as reference signals in the CPSD estimate), the CMIF can detect and decouple multiple modes within a frequency bandwidth.

The CMIF was leveraged to extract the first 18 operational modes of vibration and their corresponding frequencies. They all occur within a frequency range of 2 to 10 Hz. The singular values from the CMIF are plotted below with the peaks manually identified. The top two ranks dominate the total response and therefore are the only ranks from which peaks were chosen.

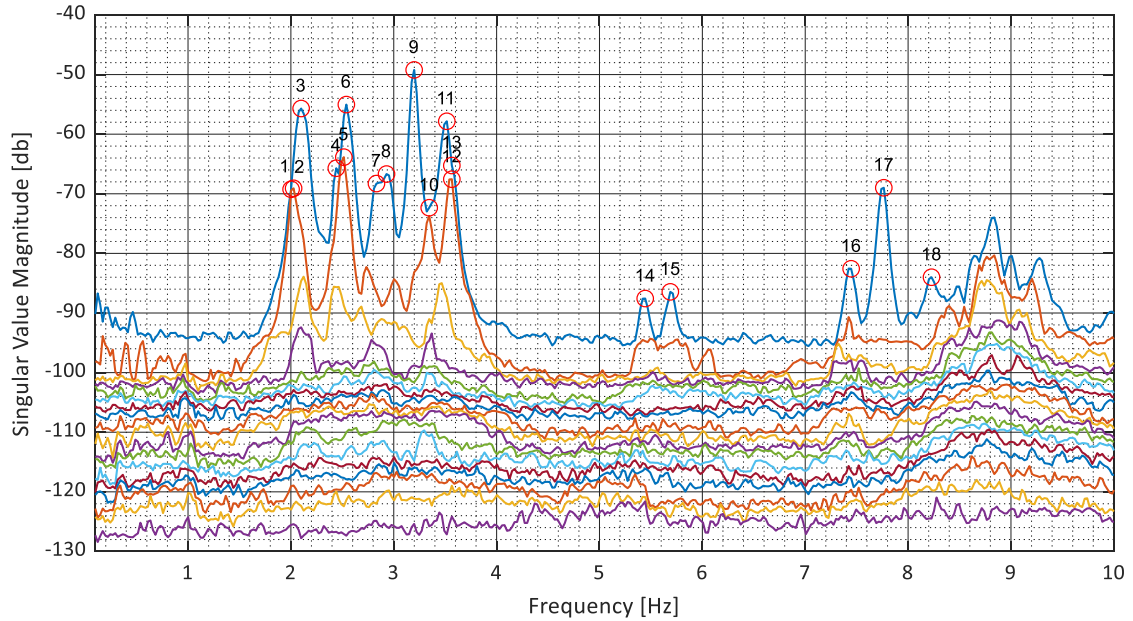


Figure 6.24: CMIF Singular Values with Peaks Identified

Due to the symmetric nature of the structure and the deck separation between the interior-most girders, many of the modes are quite similar in shape. Therefore, a representative few are plotted below while the remaining may be found in the appendix. The mode shapes and frequencies will be used for model calibration.

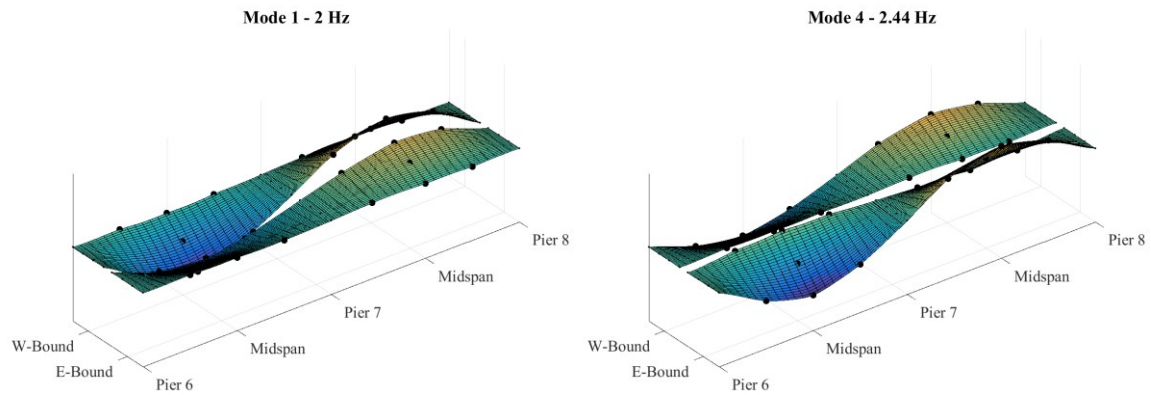


Figure 1.6.25: Experimental Mode 1 – 2.00 Hz

Figure 1.6.26: Experimental Mode 4 – 2.44 Hz

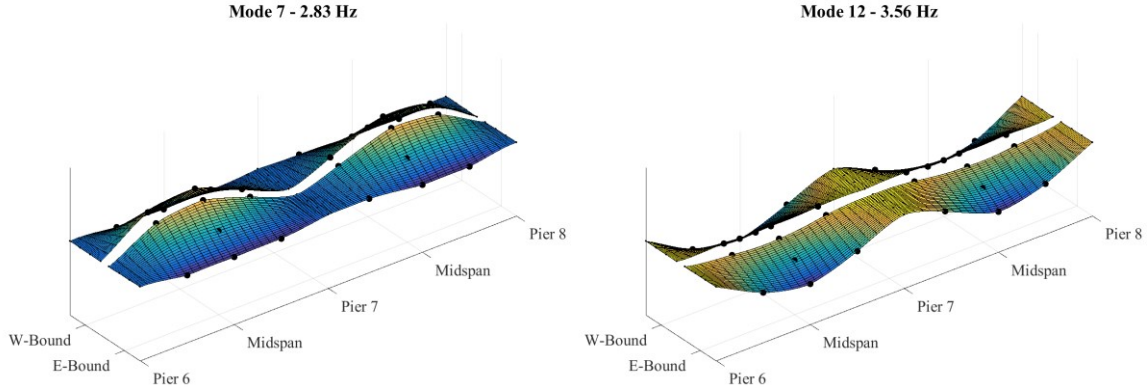


Figure 1.6.27: Experimental Mode 7 – 2.83 Hz

Figure 1.6.28: Experimental Mode 12 – 3.56 Hz

Model Validation

Any FE model will inherently have uncertainties. These are due to modeling decisions and assumptions made during the creation of the model such as material properties and connection fixity. The uncertainty of the model can be greatly reduced by comparing simulated responses to the measured responses of the real structure, and strategically adjusting the model until acceptable agreement is achieved. This process may be carried out automatically with optimization algorithms, or by manually adjusting model parameter values.

The model of spans 7 and 8 was manually calibrated using the mode shapes and frequencies obtained as part of operational monitoring. The initial model failed to predict the torsional deformation of the structure displayed by the experimental mode shapes. This suggested that those parameters which target the mass and stiffness of the exterior portions of the structure should be addressed in the calibration process.

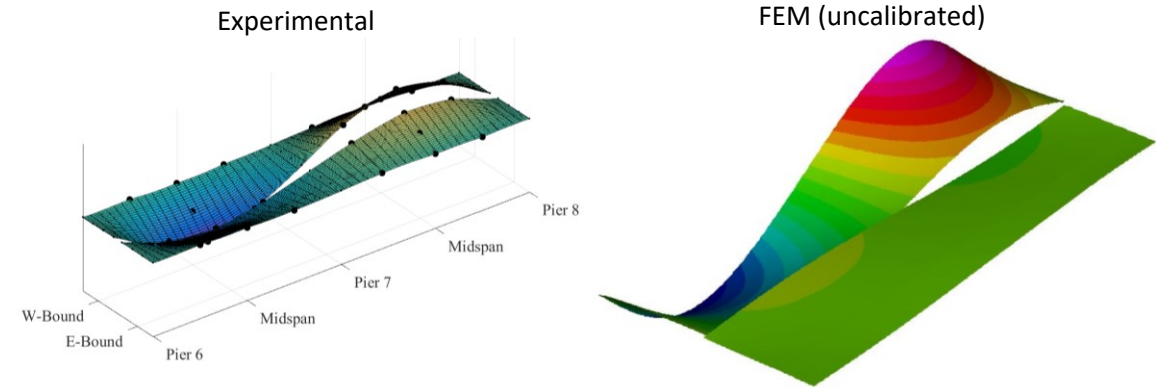


Figure 1.6.29: Comparison of Experimental and A-priori FEM Mode 1 Shape

The following model parameters were chosen to target the mass and stiffness of exterior bridge components.

- Stiffness of interior barriers (modulus of elasticity)
- Material density of interior barriers
- Material density of exterior barriers
- Continuity of exterior barriers over continuous support

Additionally, the lateral stiffness of stringer elastomeric bearings (spring-damper elements) was set arbitrarily high in the preliminary model to effectively restrain the elements from deforming in the transverse direction. The appropriate value for this parameter was not known and therefore represented a source of uncertainty in the model and was therefore added to the set of calibration parameters.

The objective of the calibration process was to minimize the difference between the predicted natural frequencies and the experimentally determined natural frequencies. However, because the structure was effectively two adjacent and identical bridges, there were many closely spaced modes that exhibited nearly identical shapes but with varying participation of the two sides. As a result, a subset consisting of 6 experimental mode shapes was chosen to be included in the

objective function. Those modes are illustrated in the following images. It was the goal of the calibration process to reduce the error of the FEM predicted frequencies for the selected set of modes to less than 10%.

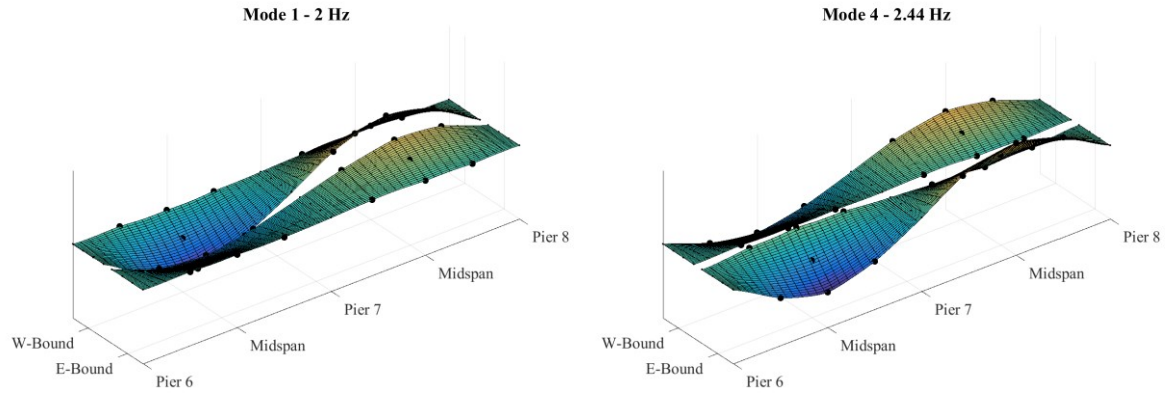


Figure 1.6.30: Experimental Mode 1 – 2.00 Hz

Figure 1.6.31: Experimental Mode 4 – 2.44 Hz

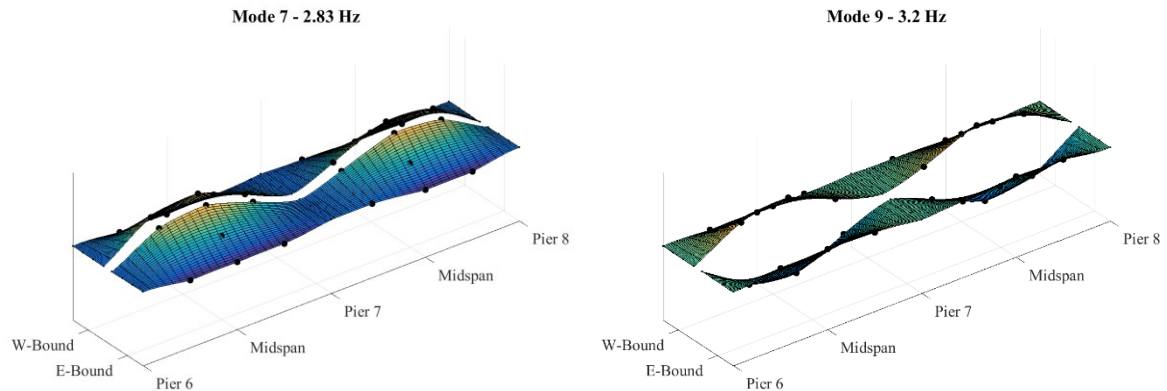


Figure 1.6.32: Experimental Mode 7 – 2.83 Hz

Figure 1.6.33: Experimental Mode 9 – 3.20 Hz

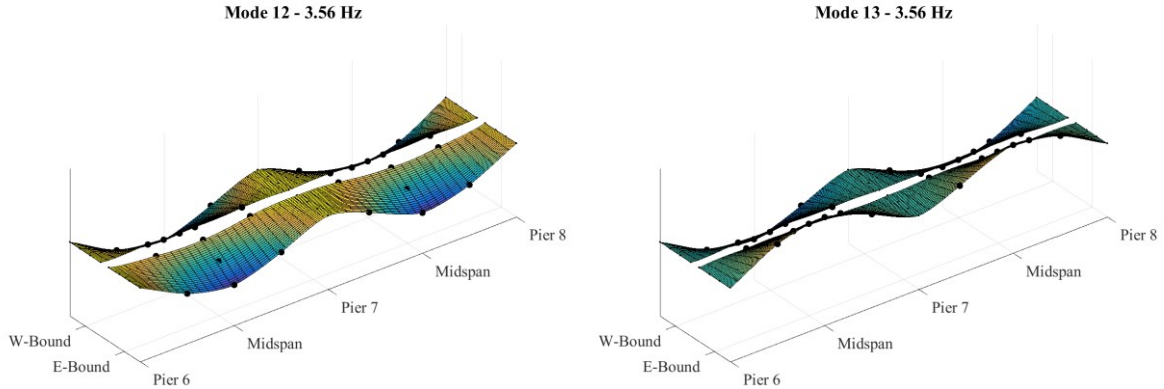


Figure 1.6.34: Experimental Mode 12 – 3.56 Hz

Figure 1.6.35: Experimental Mode 13 – 3.56 Hz

The first part of the calibration process consisted of reexamining the structure in the effort to identify any details that were missed or modeled improperly. Additional scrutiny of bridge photos revealed that the interior barriers appeared to be sawcut at regular intervals. This was implemented in the model by negating the stiffness of the interior barriers by setting the modulus of elasticity to a near zero value. Sawcuts were also observed in the exterior barriers over the continuous support. This was implemented by releasing the corresponding elements' moment and shear in all directions in that location.

The density of the barriers was next addressed since this parameter targeted the exterior of the structure and the uncertainty associated with the mass in those regions. Sources for additional mass included reinforcing bars in the barriers and thicker deck at the overhang. The density was increased by 20%.

The lateral stiffness of the bearing elements was adjusted in an effort to reduce the frequency of higher mode predictions. The lateral stiffness was reduced until the higher modes exhibited better agreement. The final value of the bearing element lateral stiffness is provided in the table below, along with the final values for all of the adjusted parameters as well as a few other uncertain parameters.

Table 1.6.3: Model Parameter Values

	Initial Values	Calibrated Values	units
E of Interior Barriers	3982736	5.0	lb/in ²
Density of Interior Barriers	0.086705	0.104047	lb/in ³
E of exterior barriers	3982736	3982736	lb/in ²
Density of Exterior Barriers	0.086705	0.104047	lb/in ³
Elastomeric bearing lateral stiffness	1E+09	4.0E+05	lb/in
E of deck concrete	4490369	4490369	lb/in ²

The natural frequencies of the calibrated model are compared in the table below.

Table 1.6.4: Frequency of Mode Shapes from Experimental Data and FEA

	Exp.	Prelim. FEM	% diff	FEM (cal.)	% diff
Mode 1	2.00	2.73	36.5%	2.00	<0.1%
Mode 2	2.03	2.37	16.7%	-	-
Mode 3	2.10	3.22	53.3%	2.02	-3.8%
Mode 4	2.44	-	-	2.28	-6.6%
Mode 5	2.51	-	-	-	-
Mode 6	2.54	3.77	48.4%	2.33	-8.3%
Mode 7	2.83	3.71	31.1%	3.06	8.1%
Mode 8	2.93	-	-	-	-
Mode 9	3.20	-	-	3.17	-0.9%
Mode 10	3.34	4.58	37.1%	-	-
Mode 11	3.52	-	-	-	-
Mode 12	3.56	4.25	19.4%	3.68	3.4%
Mode 13	3.56	-	-	3.68	3.4%

As can be seen the revisions yielded a model in close agreement with experimental data. The calibrated model can therefore be considered a reasonable digital representation of the structure. Experimental and FEM mode shapes for the six chosen modes are compared in the following figures. Additional FEM mode shapes can be found in the appendix.

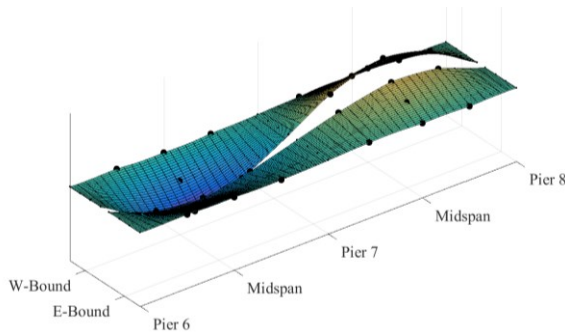


Figure 1.6.36: Experimental Mode 1 – 2.00 Hz

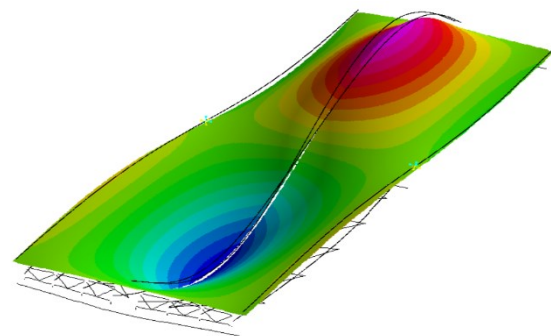


Figure 1.6.37: Updated FEM Mode 1 – 2.00 Hz

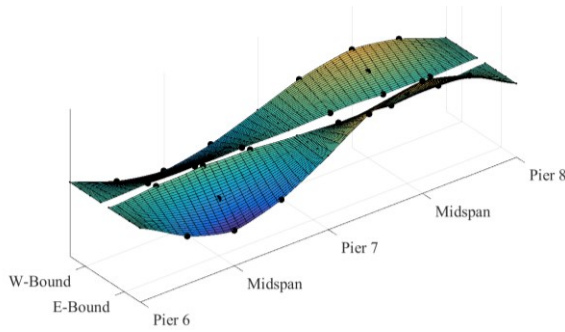


Figure 1.6.38: Experimental Mode 4 – 2.44 Hz

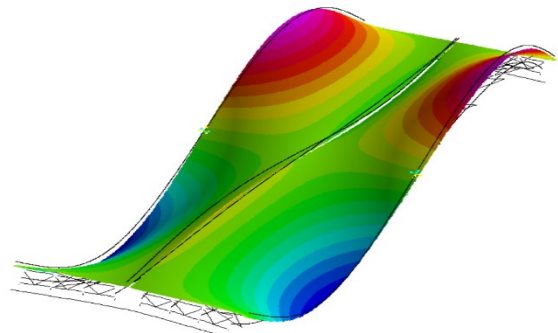


Figure 1.6.39: Updated FEM Mode 3 – 2.28 Hz

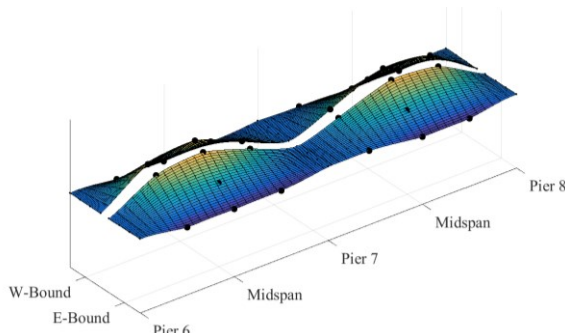


Figure 1.6.40: Experimental Mode 7 – 2.83 Hz

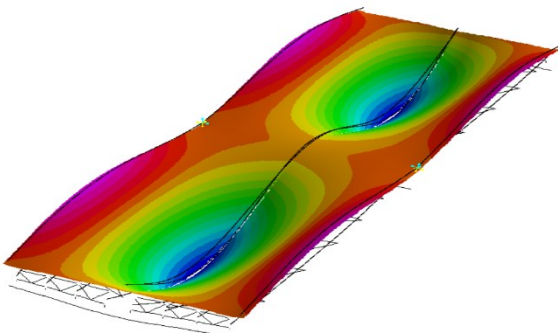


Figure 1.6.41: Updated FEM Mode 5 – 3.06 Hz

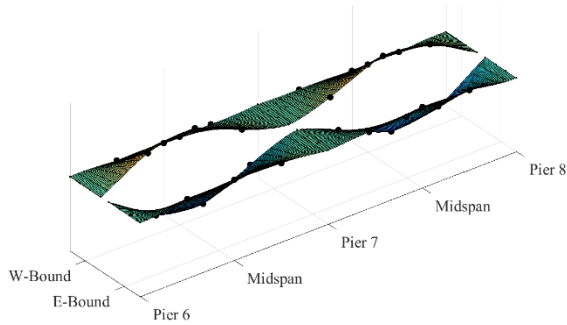


Figure 1.6.42: Experimental Mode 9 – 3.20 Hz

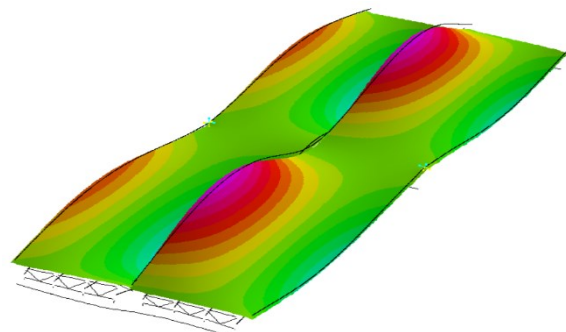


Figure 1.6.43: Updated FEM Mode 6 – 3.17 Hz

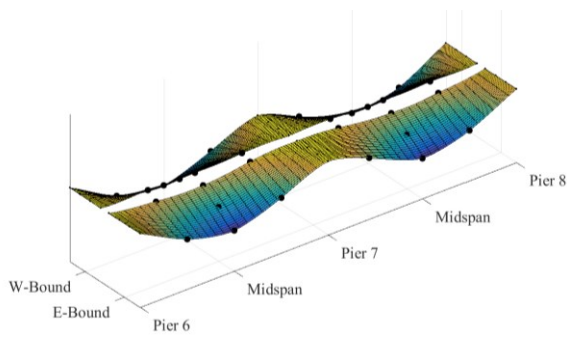


Figure 1.6.44: Experimental Mode 12 – 3.56 Hz

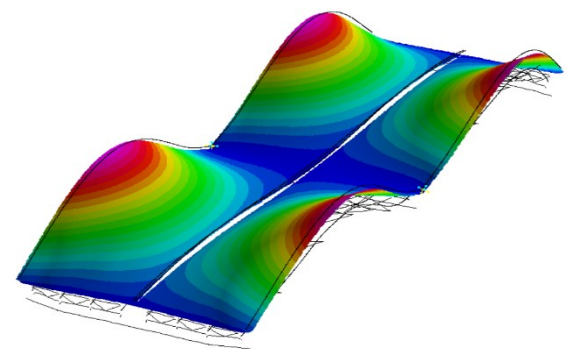


Figure 1.6.45: Updated FEM Mode 7 – 3.68 Hz

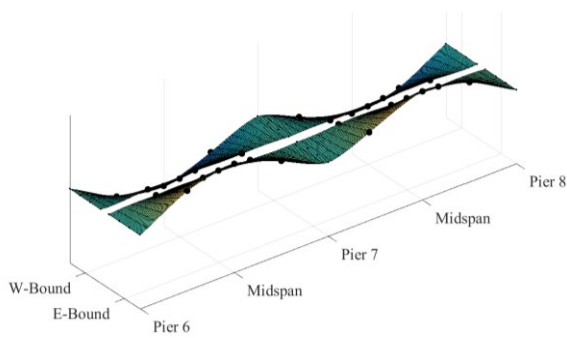


Figure 1.6.46: Experimental Mode 13 – 3.56 Hz

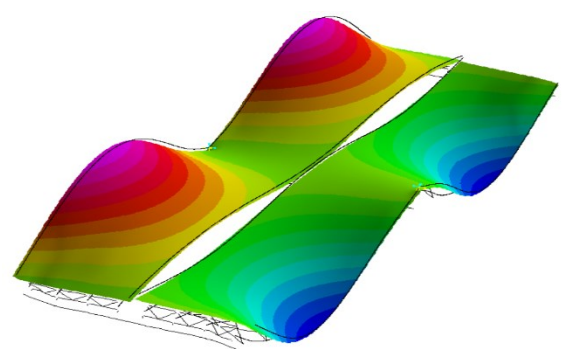


Figure 1.6.47: Update FEM Mode 8 – 3.68 Hz

Refined Load Rating

The calibrated model was used to assess the impact of observed dynamics on the bridge's ability to carry load and its continued performance by computing refined load ratings of the stringers (positive flexure) using the procedures provided in the *Manual for Bridge Evaluation* (MBE) (AASHTO, 2018).

Member capacity was computed using the equations provided in the LRFD standard specifications (AASHTO, 2014). The nominal moment capacity of the composite section was used for the positive moment region rating (0.4X span length). Dead load, superimposed dead load, and live load demands were computed using the FE model. Live loads were applied according to the AASHTO HL-93 live load model. The recommended impact factor of 1.33 was used as well as a value of 1.75, corresponding to the observed amplification. A more extensive description of rating through refined analysis is provided in the appendix.

Table 1.6.5: LRFD flexural ratings using refined analysis for 0.4 of span length

	IM = 0.33		IM = 0.75	
	Strength I	Service II	Strength I	Service II
Girder 4	1.60	1.73	1.21	1.32
Girder 5	1.86	1.98	1.41	1.50

Design vs. In Situ and Reserve Capacity

The stress associated with the live-load simulations that were performed for the above ratings was used to calculate the corresponding strain. The resulting strain is compared to the maximum recorded operational strain in the following table. The FE responses reported below include an impact factor of 0.33 but are otherwise unfactored.

Table 1.6.6: Operational vs Rating Bridge Responses (Midspan, Bottom-Flange)

	Stress (ksi)	Strain ($\times 10^6$)
FEM (HL-93 + IM)	11.8	407.6
Operational	6.1	209.6

As demonstrated by the load ratings and the strain comparison, this structure seems quite capable of withstanding the increased load levels resulting from dynamic amplification. This is no surprise as the structure was designed with a different methodology than the rating procedure resulting in reserve capacity.

The design utilized a single-line girder model which determines demands for the beams according to a distribution factor. That distribution factor was calculated according to equation provided by the bridge design specification which was based on numerous studies and is conservative. That equation from the bridge design specifications in use at the time this bridge was designed is provided below.

$$DF = S/5.5 \quad (11)$$

Where DF is the portion of load from a single wheel line that should be applied to the beam and S is the girder spacing in feet. In reality, the deck and diaphragms are much more effective at distributing load to adjacent beams than the distribution factor implies. For this structure, the design distribution factor was 0.91 (of total design load) while the FE rating analyses yielded a distribution factor of 0.79.

Furthermore, a different load model was used than is currently used for design and rating. At the time this bridge was designed, the HS-25 truck was the specified design load model rather than the current HL-93 model that was used for the load ratings. Furthermore, the construction documents indicate the structure was also analyzed for a 204 kip (907 kN) permit load which would produce much larger responses than the 90-kip (0.40 kN) HS-25 truck. It is likely this loading condition influenced the design of the structure and served to further increase its reserve capacity.

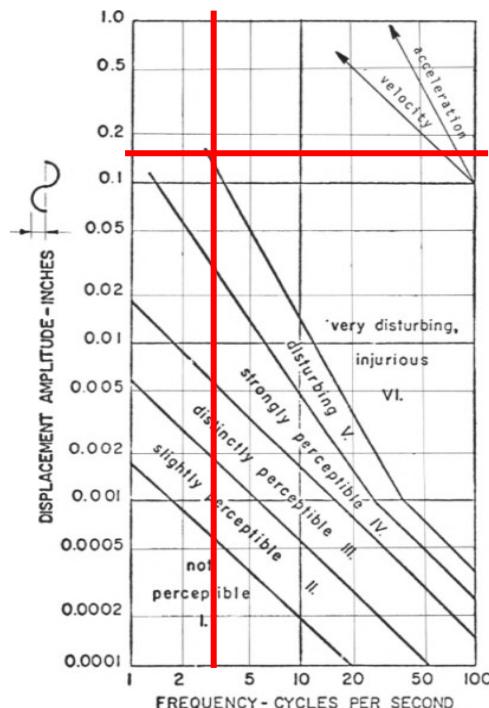
Additional differences include the live-load factors, which are compared in the following table.

Table 1.6.7: Live Load and Impact Factors

	Impact Factor	Live Load Factor
Design	0.189	1.667
Current	0.33	1.75

Human Comfort as a Service Limit State

With the displacements estimated from acceleration data, the vibrations may be assessed against human comfort criterion. Acceleration frequently exceeded 20% of gravity, which is above all of the annoyance thresholds established for floors (Allen and Rainer, 1976). Furthermore, the displacement associated with these vibrations was estimated to be 0.15 inches. According to criteria set forth by Reiher and Meister (1931) and illustrated in the following chart, this bridge motion would be classified as “very disturbing.” This confirms that the measured response is the same phenomenon being reported by motorists.

**Figure 1.6.48: Human Perception to Vibrations (Reiher and Meister, 1931)**

Test Conclusions

This phase of testing examined the operational responses of spans 7 and 8 by instrumenting multiple girders with strain gauges and accelerometers. The resulting strain data was used to estimate the operational dynamic amplification. The recorded acceleration was used to identify the operational mode shapes and frequencies which were subsequently leveraged for updating and validating the 3D element-level FE model. The results of this phase of testing are as follows:

- This structure is experiencing dynamic amplification in excess of 1.75.
- Refined load ratings revealed that due to design conservatism there is sufficient reserve capacity to handle the increased dynamic amplification.
- The structure's dominant operational modes of vibration are between 2 and 4 Hz.
- The calibrated FE model had parameter values (material properties, element connectivity, etc.) all within very reasonable bounds (i.e. there are no structural abnormalities contributing to the vibration issues).

This iteration of testing therefore concluded that although the bridge is experiencing large vibrations, it does not appear to pose a risk to the bridge's performance. However, the test results and simulations are unable to identify the cause of the vibrations.

Chapter 7: Phase 3 Testing

Previous testing revealed that vehicles were frequently exciting the mass of the structure. However, those tests failed to identify the mechanisms influential to large vibrations and dynamic amplification. A test was therefore designed to provide a more thorough understanding of the coupled behavior of bridge and vehicle by capturing the motion of the bridge and a vehicle synchronously. The objectives of this test were as follows:

- Record conditions resulting in large vibrations/amplification
- Record data that is appropriate for validating VBI models
- Characterize relationship between bridge responses and vehicle parameters
- Identify structural attributes that are influential to large vibrations
- Determine the influence of vehicle location (on the bridge) on vehicle response

Sensors were installed on the bridge on June 26th and 27th of 2017. Testing occurred on June 28th. Sensors were removed on the 29th.

Instrumentation Plan

While large vibrations were frequently observed and recorded for this structure, the nature of the traffic at the time of these recordings had thus far not been measured. It was therefore the broad objective of this test to measure the input that induces large vibrations in the bridge.

Rather than directly measure the force input to the structure, it was more practical to record the motion of a vehicle, and accelerometers served to best measure that motion. From the recorded acceleration, the force imparted by the vehicle could be calculated.

Accelerometers were also chosen for measuring bridge response. The large amplification observed in the previous test was a result of oscillations of 2 Hz and greater. The accelerometers are best able to capture motion in this frequency range.

Therefore, this phase of testing would require that sensors be installed on both the bridge as well as on a vehicle that was heavy enough to induce a measurable response in the bridge. Separate acquisition systems would be required for each, while still providing some means of synchronizing the gathered data. Therefore, NI cRIOs were again used; outfitted with a GPS module (NI-9467) which provided time-stamps with an accuracy of ± 100 ns. Synchronization between the multiple distributed DAQ systems is therefore achieved during processing based on time-stamp records.

Because it was desired to measure the relative excitation of different spans of the structure, multiple spans were chosen for instrumentation. Access to certain spans and the number of sensors available restricted the number of spans that could be practically instrumented. Therefore, spans 2, 3, 4, 7 and 8 were chosen for testing, providing data on one simply-supported span and two 2-span continuous sections. On each span sensors were spatially distributed to capture maximum responses as well as capture the first several modes of vibration as identified in the previous phase of testing.

The test vehicle consisted of a tandem dump truck (two rear axles) provided by the local DOT, that was loaded with crushed rock. The axle configuration and load level would provide concentrated force to the bridge and was therefore expected to induce response levels well above the noise thresholds of the sensors and hopefully also cause vibrations similar to those observed in the previous phase of testing. While it was intended that gauges be placed at the four corners of the truck body, this particular truck body was aluminum and therefore the mounting magnets were ineffective. The rear two magnets were able to be placed where intended thanks to steel hardware on the dump body. The front two sensors were attached to the vehicle chassis in-line with the front edge of the bucket. Cables were clamped to the vehicle

body and the DAQ was placed in the cab under the passenger's feet who operated the DAQ and recorded meta data.

A total of 36 accelerometers (PCB Model 393A03) were installed on the bridge. Another 4 accelerometers were attached to the dump truck bed so the "roll", "pitch" and "bounce" of the main mass of the vehicle could be captured. A total of 3 DAQ systems were employed. One was placed on the test truck; another was placed beneath span 3 and another beneath span 7. Video cameras were placed at the beginning and end of the bridge, as well as at an elevated position near span 2.

The following figures describe the locations of each sensor.

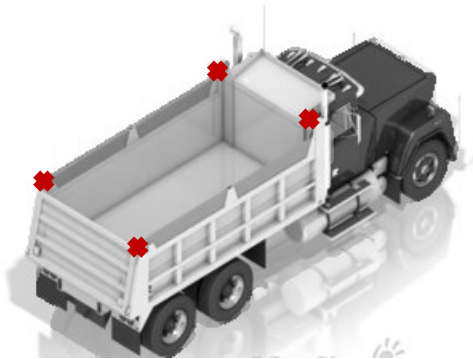


Figure 1.7.1: Test Truck Instrumentation Layout

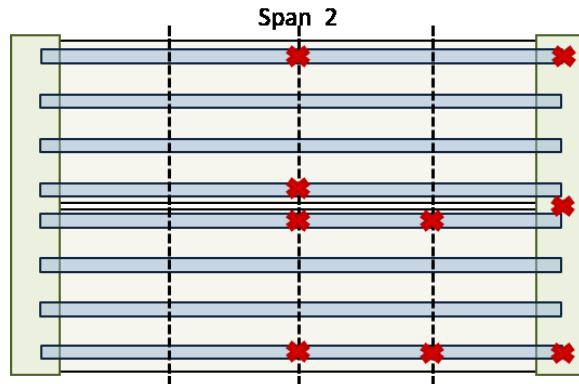


Figure 1.7.2: Span 2 Instrumentation Layout

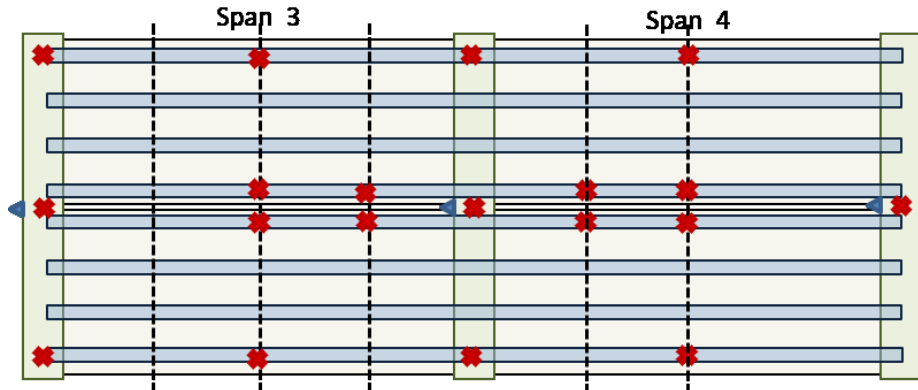


Figure 1.7.3: Spans 3 & 4 Instrumentation Layout

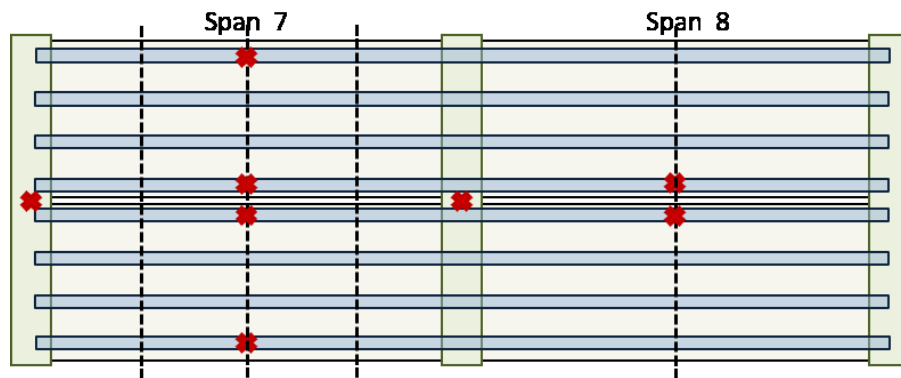


Figure 1.7.4: Spans 7 & 8 Instrumentation Layout

Equipment

All 36 accelerometers were sampled with National Instruments (NI) CompactRIOs. The sensors and data acquisition systems were chosen based on sampling rate and sensitivity requirements and the performance demonstrated in past tests. The sensors and data acquisition systems model info are provided in the following table. Detailed specifications can be found in the appendix.

Table 1.7.1: Phase 3 Test Equipment Model Specifications

Item	Model No.	Description
Accelerometer	PCB Model 393A03	Ceramic Shear ICP® Accelerometer
NI DAQ Chassis	NI cRIO-9022	Embedded Real-Time Controller
NI DAQ I/O Modules	NI-9234	C Series Vibration Input Module
NI DAQ GPS Module	NI-9467	GPS C-Series Synchronization Module
Truck Axle Scales	Intercomp LP600	Low-Profile Wheel Load Scales

The NI DAQ on the vehicle was outfitted with 2 of the vibration input modules to provide 8 vibration channels. The DAQ beneath span 3 had 7 vibration modules to provide 28 vibration channels and the DAQ beneath span 7 had 2 vibration modules to provide 8 vibration channels. All three also had a GPS synchronization module and were powered with batteries.

Test Activities

Access to the underside of the structure was provided with an articulating boom lift. Accelerometers were attached to the steel superstructure with magnetic bases. Cables were clamped to the structure near the gauge to prevent the weight of the cable from damaging the gauge or affecting the readings. Cables were run on top of the girder bottom flanges to the central cross-girder before being run down to the ground where they were plugged into the DAQ. Sensor installation required two days of work.

All 3 DAQs recorded data at 1652 Hz. This was the minimum sampling rate permitted when operating the DAQ's in the field-programmable gate array (FPGA) environment which was required when using the GPS synchronization modules. At a speed of 55 mph (24.4 m/s) this sampling rate would provide a data point for roughly every 1/2in. of vehicle travel. Furthermore, this sampling rate was sufficient for capturing the structure's global modes of vibration.

The dump truck was loaded to a total weight 61400 lbs. (2745 kg) at the DOT truckyard on the morning of testing. Truck weight was measured by measuring individual wheel weights with a wheel/axle scale (Intercomp LP600). The recorded weight at each wheel is summarized in the following table.

Table 1.7.2: Test Vehicle Wheel Weights

Wheel Location	Measured Weight
Passenger Front	6960 lb.
Passenger Middle	11680 lb.
Passenger Rear	12000 lb.
Driver Front	6500 lb.
Driver Middle	12180 lb.
Driver Rear	12080 lb.

**Figure 1.7.5: Photo of Test Truck**

The test truck traversed the bridge 14 times. Vehicle speed and lane position were varied between runs but kept consistent throughout a single pass. Traffic conditions varied from free-flowing to heavily congested. Crossing events were marked in the data files by a passenger in the test truck by tapping a designated accelerometer just before entering the bridge and just after exiting it. This would appear as a spike in the data allowing for visual identification or programmatically with threshold identification scripts. The following table summarizes the meta data for each run.

Table 1.7.3: Meta Data for Test Runs

Run #	Lane	Direction of Travel	Average Speed (mph)	Traffic Conditions
1	L	WB	60 – 30	Stopped near end of bridge
2	R	EB	35	Light
3	R	WB	42	Moderate
4	R	EB	25	Moderate
5	L	WB	40 – 0	Heavy with stop at end
6	L	EB	40	Light
7	L	WB	15	Heavy
8	L	EB	47	Light
9	L	WB	58	Light
10	R	EB	20	Light
11	R	WB	10	Moderate to light
12	L	EB	40	Light
13	R	WB	35	Light
14	R	EB	40	Light

The 14 runs took less than 2 hours. Accelerometers were removed from the test truck at the conclusion of testing. All sensors were removed from the structure the following day.

Profile Measurement

The profile was recorded using an Ames Engineering Model 8300 Portable Profiler at normal traffic speeds. Two passes were made on each lane. Both wheel lines of the profile were sampled at 1-inch intervals. The profiler specifications are provided in the following table.

Table 1.7.4: Ames Model 8300 Profiler Specifications

Laser Height Sensor Range	8 in
Laser Height Sensor Resolution	0.002 in
Elevation Sample Rate	16000 Hz
Horizontal Location Accuracy	0.05%
Horizontal Location Resolution	0.15 in

Results & Interpretation

Vehicle Response

The acceleration record for the vehicle is plotted below for run 6. This run was chosen because the truck maintained a consistent and relatively high speed and was accompanied by very little

other traffic, thereby isolating the effect of the test truck. From the following plot it is evident that the front accelerometers are experiencing much more acceleration than are the rear ones.

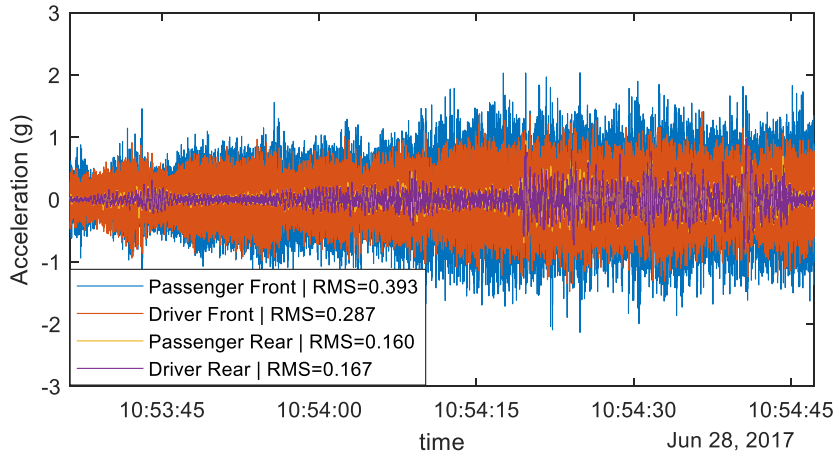


Figure 1.7.6: Truck Raw Acceleration Time History for Run 6

Spectral analysis of the signals revealed that the front sensors were experiencing much more high frequency vibration than the rear sensors. The following PSD estimate was performed with Welch's improved periodogram with (7) 10-second segments with 25% overlap providing a frequency resolution of 0.05 Hz. The same PSD estimate is plotted twice with different y-axis limits to better visualize high and low frequency content.

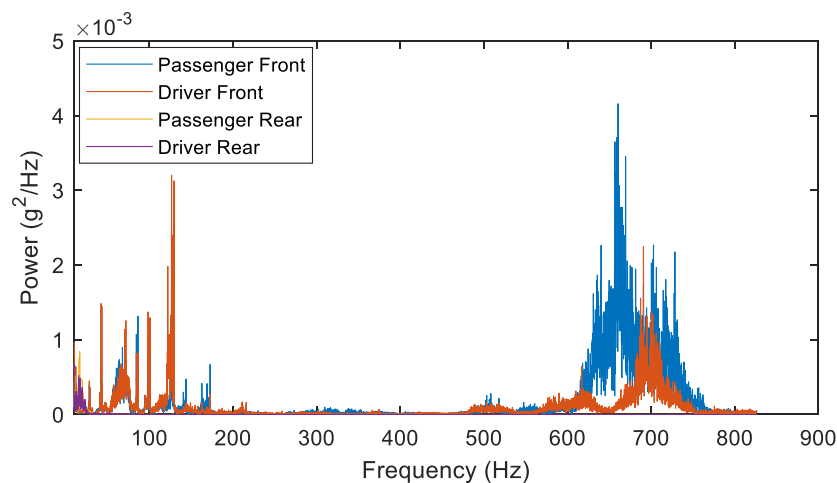


Figure 1.7.7: PSD Estimate of Test Truck Acceleration (Full Bandwidth)

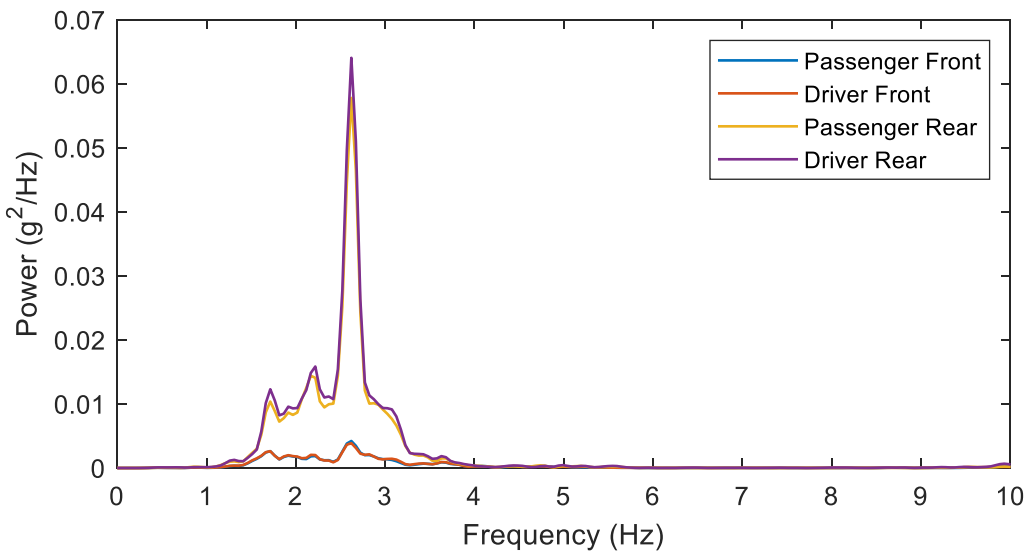


Figure 1.7.8: PSD Estimate of Test Truck Acceleration (<10 Hz)

It is likely that this high frequency content is due to banging/rattling of some part of the chassis.

Examination of the PSD estimate at low frequencies reveals that although the front sensors are experiencing higher acceleration, it is actually the rear sensors which are experiencing more low frequency vibrations as evidenced by Figure 1.7.8. To visualize and compare truck vibration in the time domain this high frequency content was removed with an elliptic low-pass filter. The filter was assigned a cut-off frequency of 20 Hz, a pass-band ripple of 0.5 decibels, and 40 decibels of stop-band attenuation. The frequency response function of the resulting low pass filter is provided in the following plots.

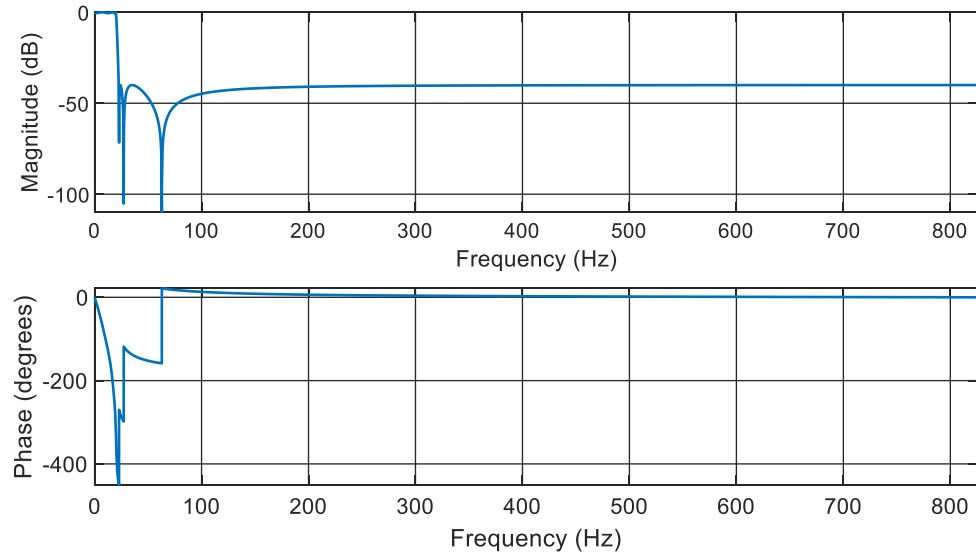


Figure 1.7.9: Frequency response of 6th order Elliptic filter

The above filter was applied to the truck acceleration time history for run 6. The resulting time history is plotted below.

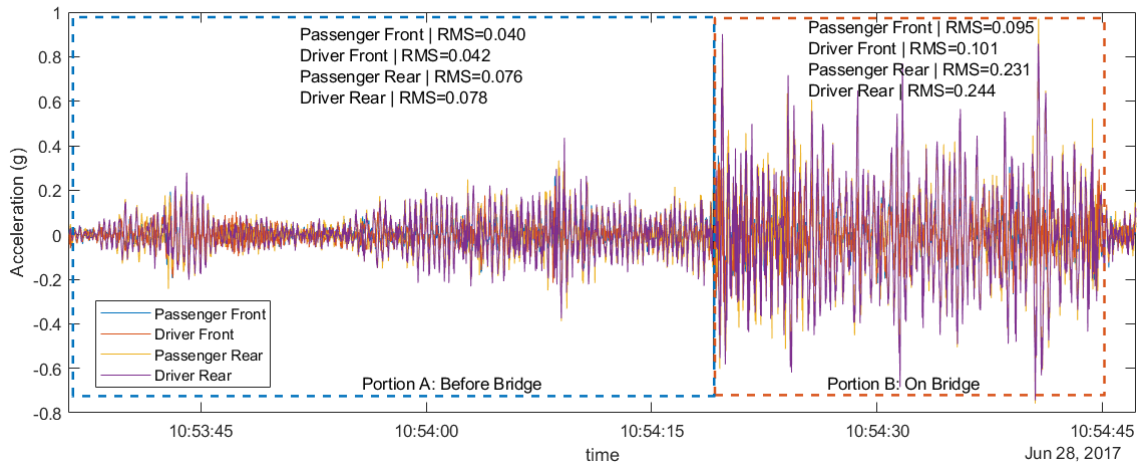


Figure 1.7.10: Filtered Truck Acceleration Time History (Before and On Bridge)

As can be seen in the previous plot, the truck's acceleration increases significantly after it enters the bridge. The boxes in the plot isolate the portions of data for the period before the truck enters the bridge (Portion A) and while the truck is on the bridge (Portion B). The time history of each portion is plotted below.

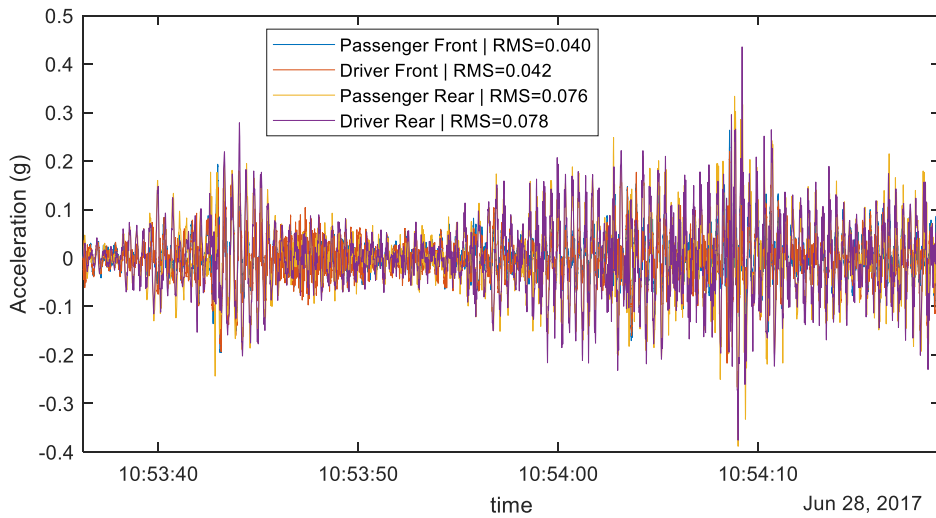


Figure 1.7.11: Filtered Truck Acceleration Time History for Period before Bridge (A)

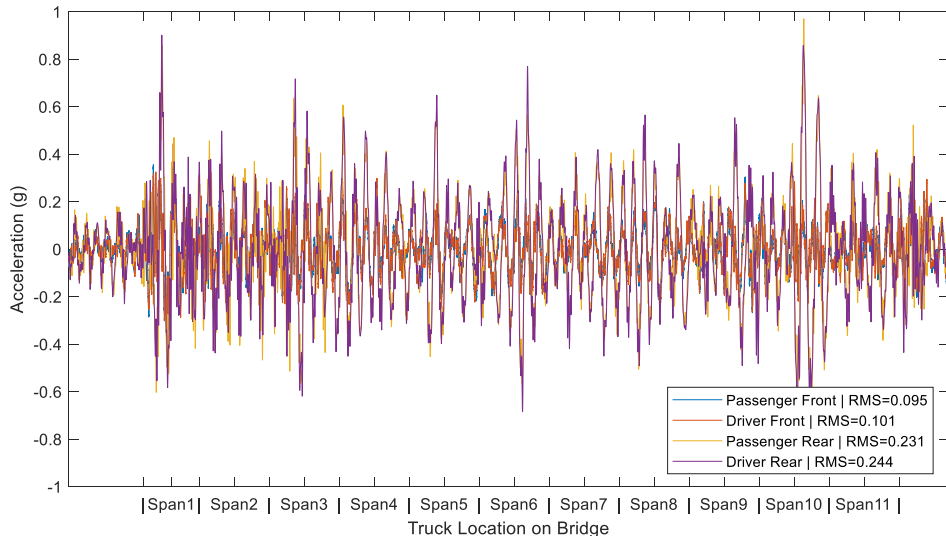


Figure 1.7.12: Filtered Truck Acceleration Time History for Period on Bridge (B)

The RMS for the truck accelerometers off and on the bridge (Portion A and B respectively) are summarized in the following table.

Table 1.7.5: RMS Values for (Run 6) Truck Acceleration Before and On Bridge

	Before Bridge (A)	On Bridge (B)	% Increase
Driver Front	0.042 g	0.101 g	140.0%
Driver Rear	0.078 g	0.244 g	213.2%
Passenger Front	0.040 g	0.095 g	134.8%
Passenger Rear	0.076 g	0.231 g	203.4%

Spectral analysis of each portion was performed to identify and compare the frequency content of the recorded vibrations. Because the two portions are of unequal length the PSD was estimated to facilitate comparison between the signals. Welch's periodogram was again used. Portion A was analyzed with (8) 5-second segments with 25% overlap. Portion B was analyzed with (4) 5-second segments with 25% overlap. Each estimate therefore has a frequency resolution of 0.1 Hz. The PSD estimates of the two portions are compared in the following plot.

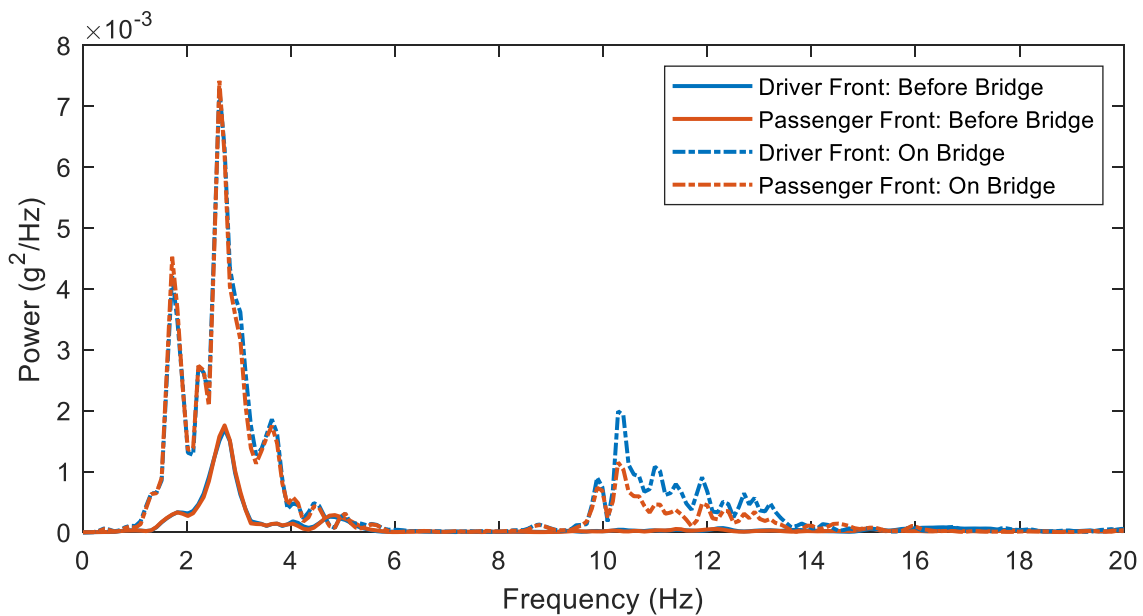


Figure 1.7.13: PSD Estimate for Acceleration from Front Sensors, On and Off Bridge

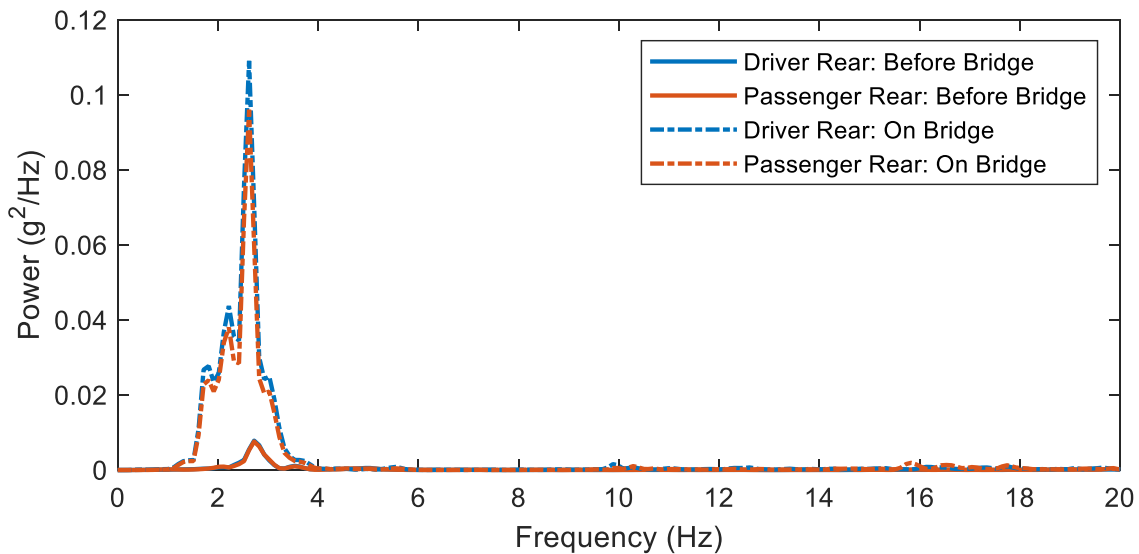


Figure 1.7.14: PSD Estimate for Acceleration from Rear Sensors, On and Off Bridge

It is clear from the above plots that the truck is experiencing much greater acceleration when it is on the bridge and it is occurring at frequencies between 1.5 and 5 Hz. Furthermore, the rear accelerometers are experiencing greater acceleration at these low frequencies than are the front accelerometers. This is likely because the front sensors are closer to the front suspension system with higher damping.

The PSD was also estimated with data that was recorded while the truck was traveling to the bridge site to eliminate the influence of bridge vibrations. Welch's improved PSD estimator was used with (4) 10-second segments with 25% overlap, providing a frequency resolution of 0.05 Hz.

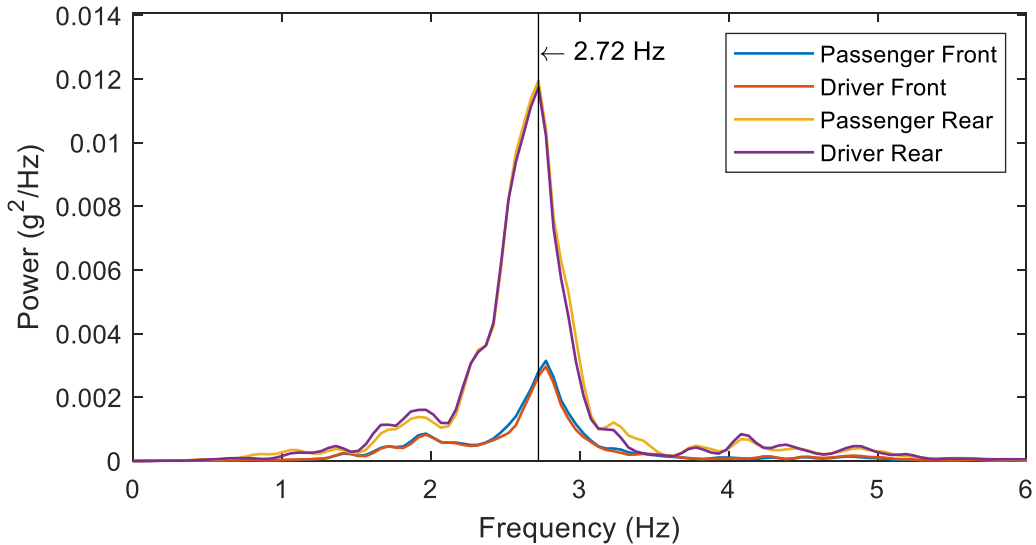


Figure 1.7.15: PSD Estimate from Truck Acceleration

The above frequency response suggests that the truck has a natural frequency of approximately 2.7 Hz. This assumes the vehicle was excited with white noise (uniform frequency content of input), but without knowledge of the profile experienced during this record, the character of the input cannot be known.

The Root-Mean-Square (RMS) of the filtered truck acceleration was computed for select runs over the time period when the truck was on the bridge. The values for the rear accelerometers were averaged and are plotted below versus vehicle speed (as reported by the truck passenger). Runs 1 and 5 were excluded from the following plot because the test truck was unable to maintain a consistent speed over the bridge. Runs 8 and 9 were also excluded due to corruption of the data files.

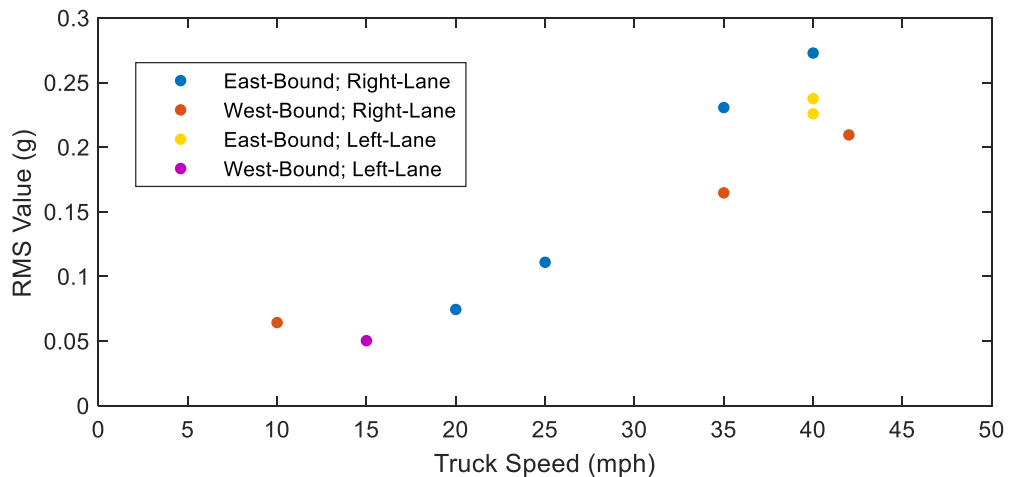


Figure 1.7.16: RMS of Filtered Truck Acceleration while on Bridge versus Truck Speed

The above plot strongly suggests that vehicle acceleration increases with an increase in its (horizontal) speed. Furthermore, the data provides no indication that the lane of travel had significant influence on the magnitude of truck acceleration.

Bridge Response

Acceleration time history for the bridge is plotted below for run 6. This run was chosen for examination because the truck maintained a consistent and relatively high speed and was accompanied by very little other traffic, thereby isolating the effect of the test truck. Girder 5 responses are displayed because run 6 occurred in the East-bound left lane which is located over girders 5 and 6 (Girder 6 was not instrumented). A low-pass filter was applied to remove content greater than 20 Hz to better visualize the vibration associated with bridge deformation.

Explanation and justification of this was provided in the previous phase of testing. It is evident in the following plots that the bridge is excited by the test truck.

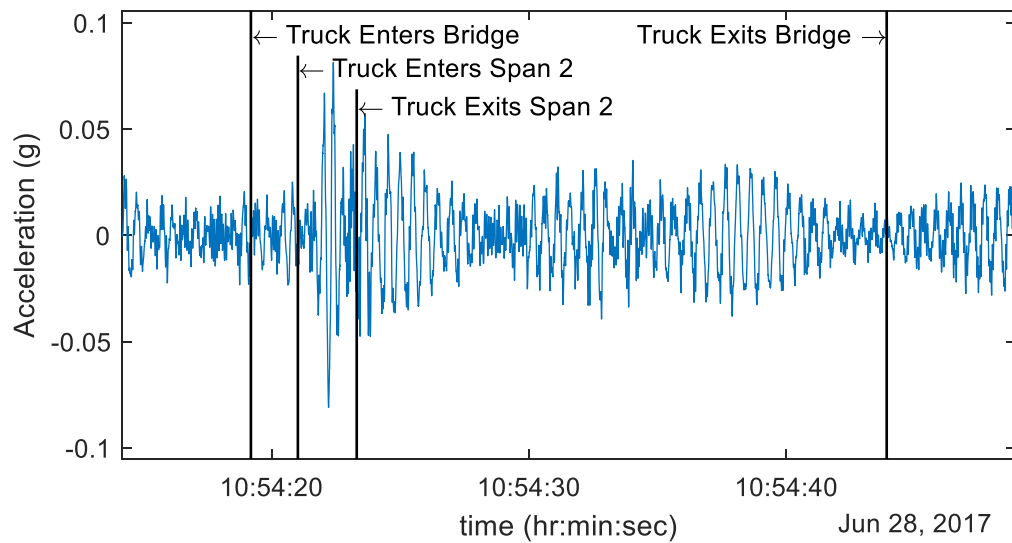


Figure 1.7.17: Acceleration Time History (Filtered) for Girder 5 at the Middle of Spans 2

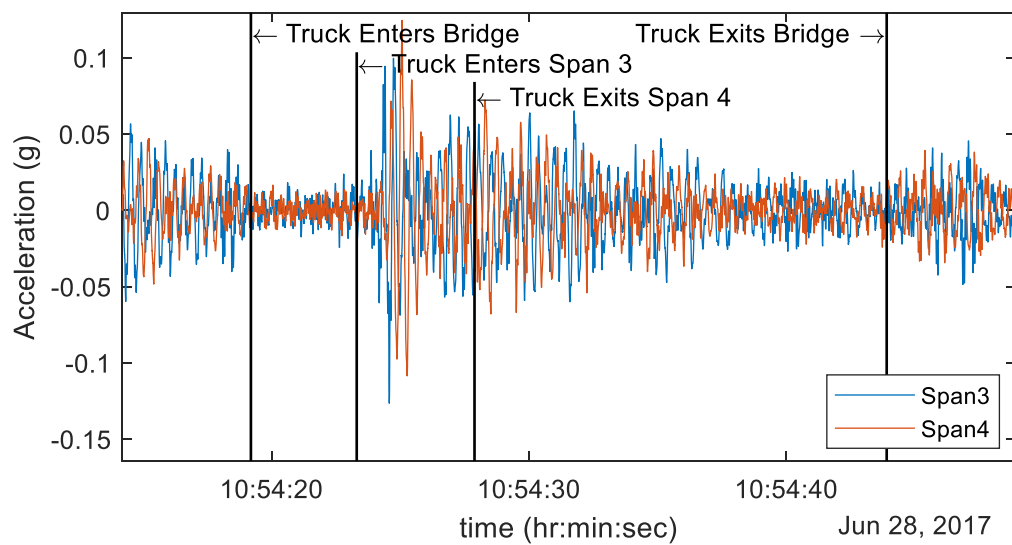


Figure 1.7.18: Acceleration Time History (Filtered) for Girder 5 at the Middle of Spans 3 & 4

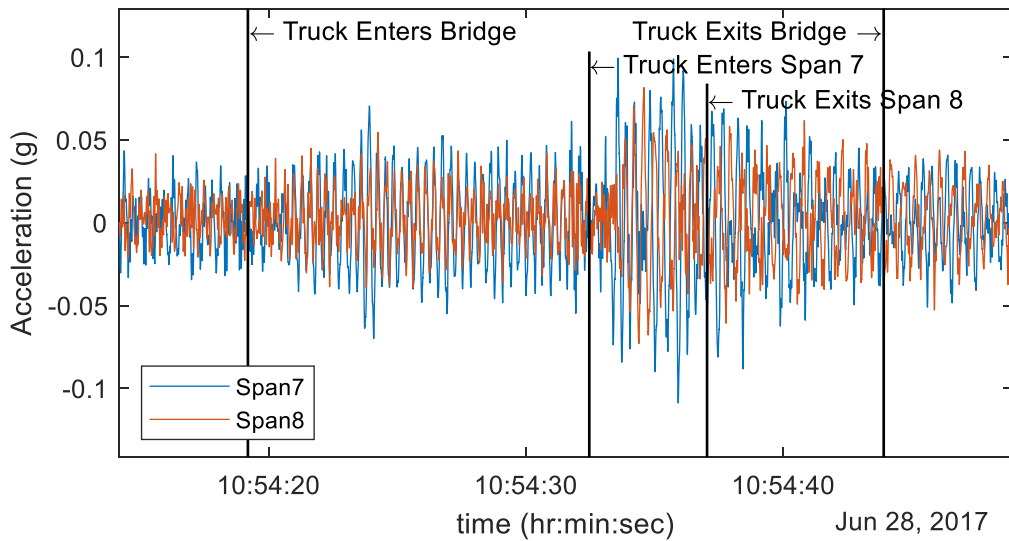


Figure 1.7.19: Acceleration Time History (Filtered) for Girder 5 at the Middle of Spans 7 & 8

The PSD was estimated for these acceleration time histories. In each case only a single segment was specified, defined by the period when the truck is on the span/s. Due to the short duration of these segments, the estimates have poor frequency resolution.

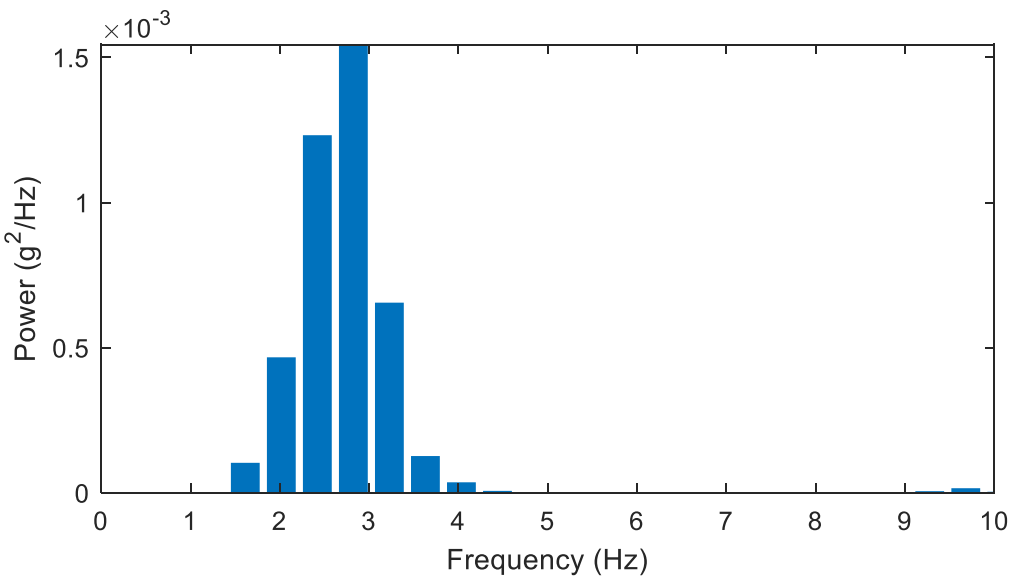


Figure 1.7.20: PSD Estimate for Acceleration of Girder 5 at the Middle of Span 2 over Period That Truck is on the Span

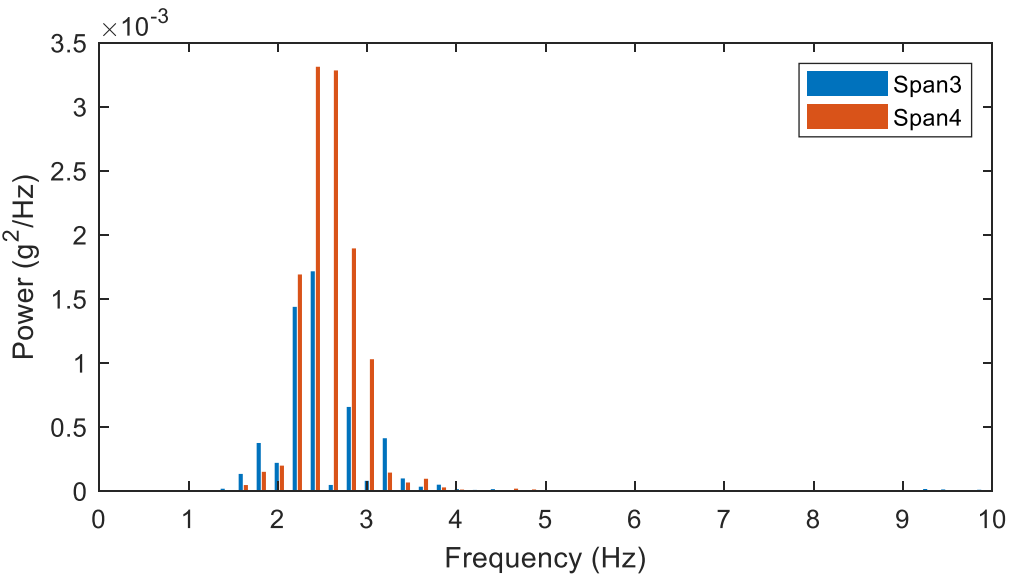


Figure 1.7.21: PSD Estimate for Acceleration of Girder 5 at the Middle of Spans 3 & 4 over Period the Truck is on the Spans

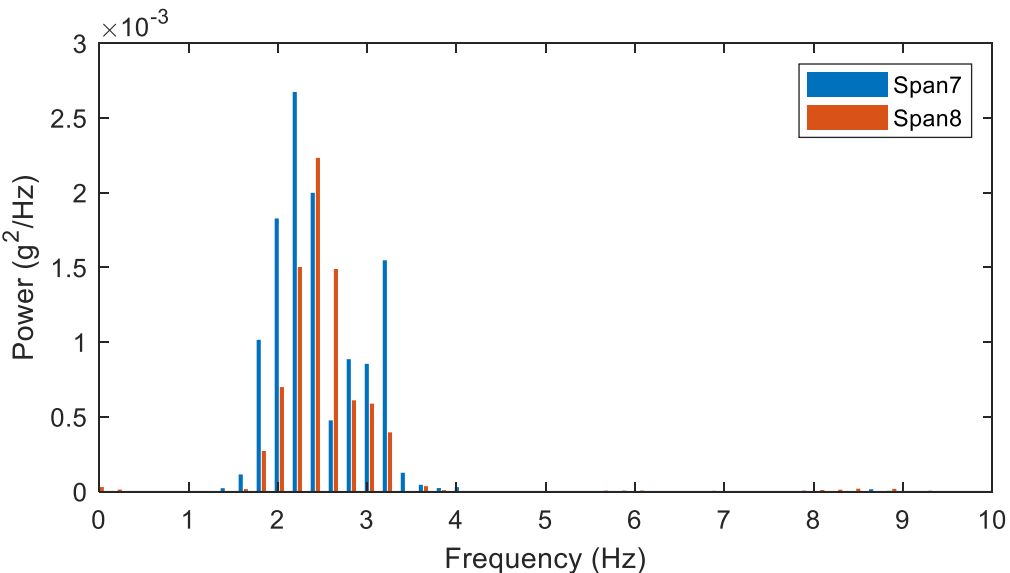


Figure 1.7.22: PSD Estimate for Acceleration of Girder 5 at the Middle of Spans 7 & 8 over Period the Truck is on the Spans

The above PSD estimates show that the truck is inducing vibrations in the bridge in the same frequency range as the bridge's natural frequencies (as determined in phase 2 testing). It is therefore reasonable to conclude that the truck is exciting the bridge's natural frequencies.

The acceleration of the structure for different runs is compared by plotting the RMS of the acceleration over the period that the truck is on the bridge.

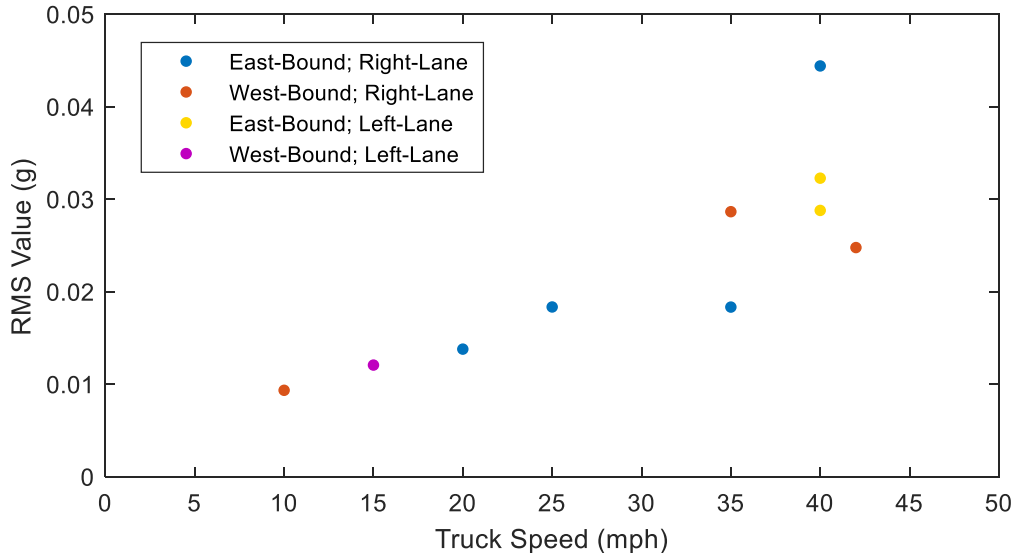


Figure 1.7.23: RMS of Filtered Midspan Acceleration of Span 2

The RMS values for the spans 3 and 4 were averaged in the following plot.

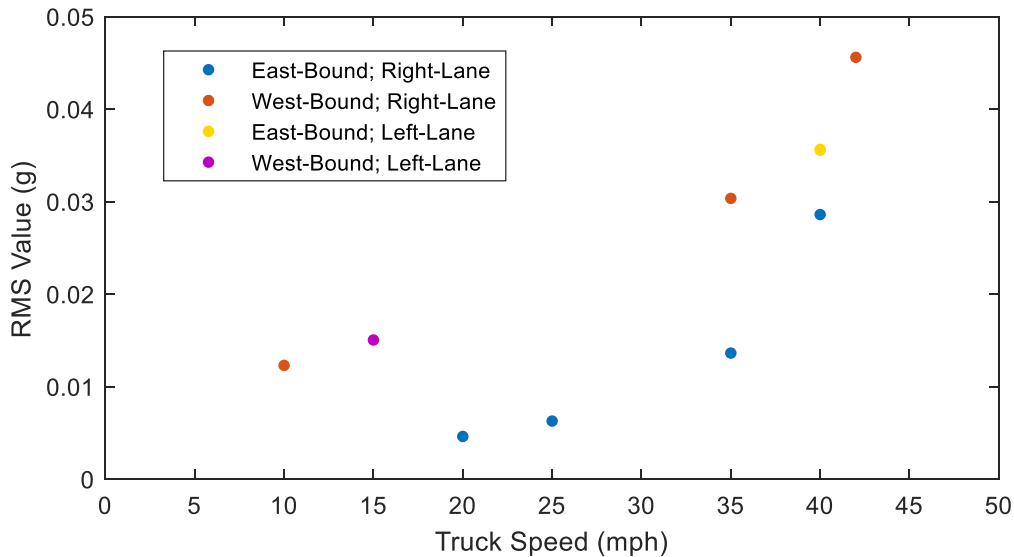


Figure 1.7.24: Average RMS Value for Filtered Midspan Acceleration of Spans 3 & 4

The above plots suggest that bridge acceleration increases with an increase in truck (horizontal) speed. The girder closest to the lane of travel was reported in the above RMS plots. The girders reported for each lane are summarized in the following plot.

Table 1.7.6: Girders Reported Corresponding to Lane of Travel

East-Bound Right-Lane	Girder 8
East-Bound Left-Lane	Girder 5
West-Bound Right-Lane	Girder 1
West-Bound Left-Lane	Girder 4

Test Conclusions

By capturing the motion of the bridge and test truck synchronously with accelerometers, this phase of testing demonstrated that a single truck is capable of inducing vibrations in the bridge that lead to dynamic amplification of bridge responses. Processing of the recorded data revealed the following:

- The acceleration of the truck increases immediately after entering the bridge as low frequency (1.5-4Hz) vibrations are excited.
- Similarly, the acceleration of the bridge increases very soon after the truck enters the respective span as low frequency (2-4Hz) vibrations are excited.
- The magnitude of vehicle vibrations increases with increased vehicle (horizontal) speed.
- The magnitude of bridge vibrations increases with increased vehicle (horizontal) speed.
- The lane and direction of travel of the truck does not have a significant influence on the magnitude of either vehicle or bridge vibrations.

Simulation is required to provide understanding of the mechanisms and influential parameters associated with dynamic amplification.

Chapter 8: VBI Model Validation

The three phases of testing provided valuable information on the behavior of the bridge and the ability of a truck to induce vibration in the bridge. However, the data was unable to identify the role of bridge or vehicle attributes in that behavior. It was therefore the goal of the simulation efforts presented in this section, to identify the bridge and vehicle attributes that were responsible for the observed bridge vibrations and dynamic amplification. It was therefore first necessary to develop a model that was capable of reproducing the responses observed in the field.

An FE software package was chosen (LUSAS) that was capable of simulating vehicle-bridge interaction. This required the ability to model the geometry and dynamics of the bridge as well as the dynamics of a vehicle traveling over the bridge model. A plate and eccentric-beam (PEB) modelling approach was employed to reduce model complexity in anticipation of computationally heavy simulations. The geometry and material properties were assigned to match those of the 3D FE model that had already been validated. The two-span model detailed in the following pages was replicated to produce a model of all 11 spans of the bridge.

Plate Eccentric-Beam Modeling

This class of model is much like a grillage model in that the vertical dimension of the bridge is flattened resulting in a 2D model. However, for a PEB model, the girders are offset from the deck plane. For the models used in this study, the offset was specified in the element attributes rather than physically relocating the beam nodes. In this way compatibility between the deck and girders was implicitly enforced at each node since they were coincident. The cross-girders, in contrast, were modeled at the elevation of their centroidal axis thereby allowing for correct

placement of boundary conditions and making it easier for a given box-girder to support adjacent discontinuous spans.

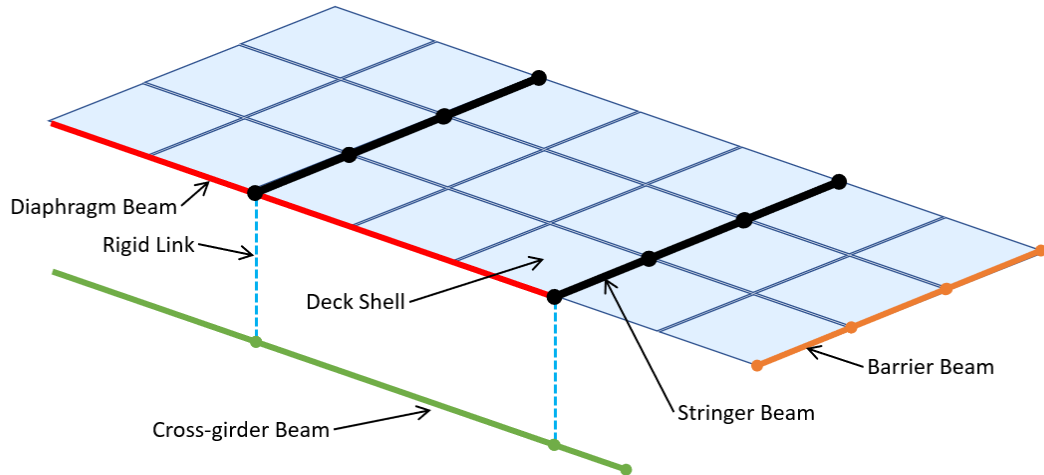


Figure 1.8.1: Schematic of Plate Eccentric-Beam FEM Model

The elevation of those elements which act compositely with the deck is important for accuracy, and while they were modeled on a single plane, the eccentricity of the elements was specified to effectively offset the elements to the correct elevation while maintaining the simplicity of the model. The image below shows the effective elevation of components when rendered with specified eccentricities.

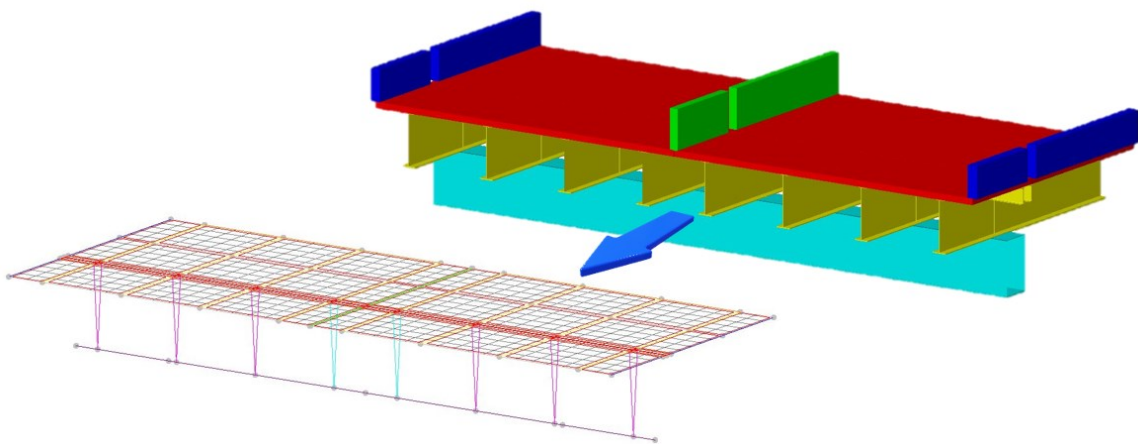


Figure 1.8.2: Plate Eccentric-Beam Representation and 3D Rendering with Assigned Eccentricities

Diaphragms

Due to the 2D nature of the model type, the chevron and x-framed diaphragms were represented with 2D beam elements coplanar with the deck and a 12 in offset below the deck centroidal plane. Care was taken to ensure the nodes of these diaphragm beam elements did not coincide with deck nodes except at girder intersections to prevent composite action between diaphragms and deck. The diaphragm beam elements were assigned section properties such that the diaphragm beams had stiffness equal to that of the X-framed bracing when loaded in a cantilever configuration. The following image displays the isolated diaphragms and the loading.

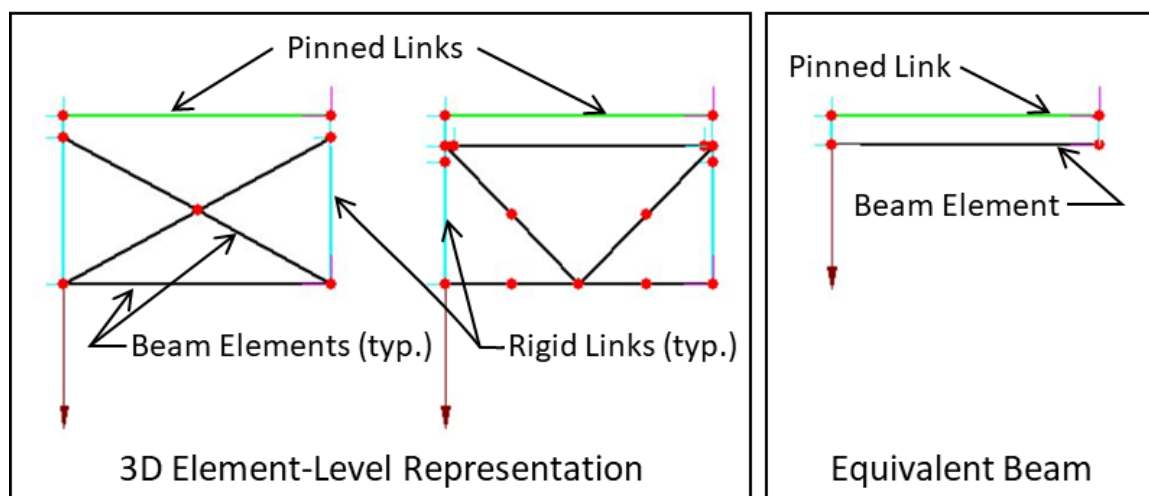


Figure 1.8.3: Diagram of FE Representation of Diaphragms

The right side of the diaphragms were restrained from translation at the top and bottom. "Pinned" links were created at the deck elevation to represent the axial restraint provided by the deck in the bridge system. The pinned links behave as a rigid bar with all rotations released at its ends. The pinned links were attached to the diaphragm elements with rigid links. The diaphragms were analyzed under two freedom conditions. In one, the free (loaded) side of the diaphragms were left unrestrained, while in the second freedom case, the rotation (about an

axis parallel to girder length and normal to the diaphragm plane) was restrained to represent the rotational restraint (torsional resistance) provided by a girder (in the bridge system). These two freedom conditions bound the nature of deformation imposed by the bridge (i.e. load applied to diaphragms by girders).

The area, moment of inertia, and shear area of the equivalent beam section were manually adjusted until the reported beam displacements matched those of the X-frame. Ultimately, the X-frame responses were chosen for updating the equivalent beam section properties because these diaphragms are located in the interior of spans and therefore have greater influence on the global deformation and behavior of the bridge. In contrast, the chevron diaphragms are located at the ends of the spans where deformation is already restrained by boundary conditions.

The following table compares the displacements at the location of load application for the three diaphragm types.

Table 1.8.1: Displacement Comparison for Different Representations of Diaphragms

	X-Frame	Chevron	Beam	% diff from X-Frame
Unrestrained	-4.28E-06	-3.95E-06	-4.27E-06	-0.12%
Rotation Restrained	-3.87E-06	-3.19E-06	-3.87E-06	-0.04%

The following table summarizes the section properties of the equivalent diaphragm beam that resulted in the displacements as reported in the preceding table. The element was assigned steel material properties ($E = 29 \times 10^6$ psi).

Table 1.8.2: Diaphragm Equivalent Beam Element Section Properties

Area	200	in ²
Moment of Inertia (I11)	1500	in ⁴
Shear Area (A1)	4.8	in ²
Shear Area (A2)	8.5	in ²

Bearings and Pedestals

Beam elements with very high stiffness and zero density (weightless) were used in place of rigid links to connect the cross-girder beam nodes to the stringer nodes since LUSAS does not include rigid links in their element library. The elements were therefore assigned section properties as summarized in the following table.

Table 1.8.3: Pedestal Beam Element Attributes

Cross-Sectional Area	1000	in ²
Moments of Inertia (I11&I22)	87000	in ⁴
Torsional Constant	148000	in ⁴
Shear Areas (A1&A2)	850	in ²
Modulus of Elasticity (E)	2.9E7	lb/in ²

These beam elements had all rotation released at the top end. The following table summarizes the additional translational releases assigned. Girders 4 & 5 were also restrained transversely to represent what is commonly referred to as an alignment bearing.

Table 1.8.4: Pedestal Element End Releases (Translational)

	TX	TY	TZ
Fixed (Pedestals)	F	F	F
Expansion (Elastomeric)	R	F	R
Expansion (Alignment)	F	F	R



F – fixed; R – released

The cross-girders were assigned boundary conditions by applying restraint to two nodes.

Translation was restrained in all three principle directions as well as rotation about the girder's length. The rotational restraint was necessary to maintain stability and accurately represent the bolted connection between pier and box-girder. The following table summarizes the restraint applied to the nodes at either end of the cross-girder.

Table 1.8.5: Cross-Girder Boundary Node Restraints

	DX	DY	DZ	RX	RY	RZ
@ East Piers	F	F	F	F	R	R
@ West Piers	R	F	F	F	R	R

F – fixed; R – released



Mesh Size

The beam and deck elements were discretized to achieve an element length of 2 feet. The influence of this mesh size was assessed by comparing model output with a smaller mesh size (1 ft.). The model was analyzed under self-weight (dead load), with a 1000 lb. point load at the middle of span 7, directly over girder 5, and for natural frequencies (eigenvalue analysis). Responses were reported for girder 5 at the middle of span 7 for the dead-load and the point load analysis. The results are summarized in the following table.

Table 1.8.6: Influence of Mesh Size on Model Responses

	2ft. Mesh	1ft. Mesh	% diff.
Dead Load Moment (lb-in) (Midspan of Girder 5)	-1.00E+05	-9.97E+04	-0.44%
Point Load Moment (lb-in) (Midspan of Girder 5)	-9.92E+06	-9.90E+06	-0.22%
Mode 1 Natural Frequency (Hz)	1.97963	1.98356	0.20%
Mode 2 Natural Frequency (Hz)	2.05164	2.05561	0.19%
Mode 3 Natural Frequency (Hz)	2.20942	2.20721	-0.10%
Mode 4 Natural Frequency (Hz)	2.22945	2.22757	-0.08%

The results provided in the above table show that the 2-ft. mesh provides sufficient accuracy for the types of global responses that this model will be used to predict.

Bridge Model Validation

An initial comparison of experimental and model predicted mode shapes revealed that the predicted first bending mode had significantly higher deflection along the exterior of the bridge compared to the experimental results.

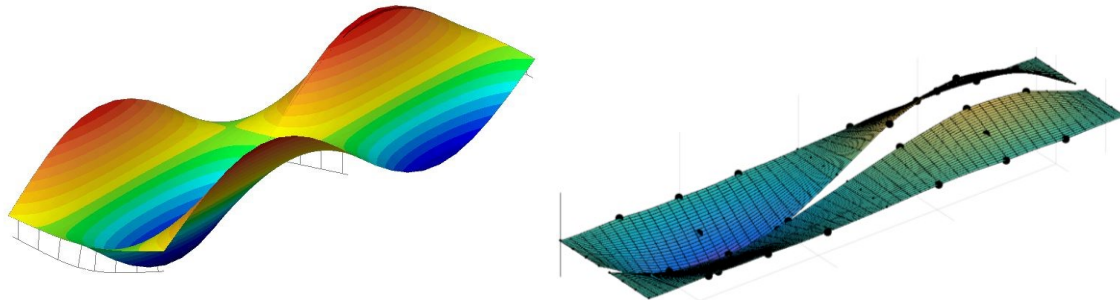


Figure 1.8.4: LUSAS FEM Mode 1 – 1.98 Hz

Figure 1.8.5: Experimental Mode 1 – 2.00 Hz

The discrepancy suggested that the exterior regions of the bridge had less mass/greater stiffness, or the center region had greater mass/decreased stiffness. The barriers are the major components that differ for these two regions, therefore these were the first to receive further scrutiny.

Upon re-examination of construction documents and pictures of the bridge it became clear that the center barriers had saw cuts at approximately every twelve feet. These cuts were represented by releasing rotations and longitudinal translation at beam ends (approximately every 12 feet). Alternatively, the stiffness of the barriers could be set nominally low; however, this method tended to create unrealistic local modes of vibration. The exterior barriers were released over the central supports, as they appeared to be discontinuous at this point in pictures. These releases consisted of all three principle rotations, along with translation in the transverse and longitudinal directions (global).

Additional discrepancy was observed for the analytical 3rd mode (Figure 1.8.6), for which the predicted frequency was nearly 0.4 Hertz lower than that determined experimentally.

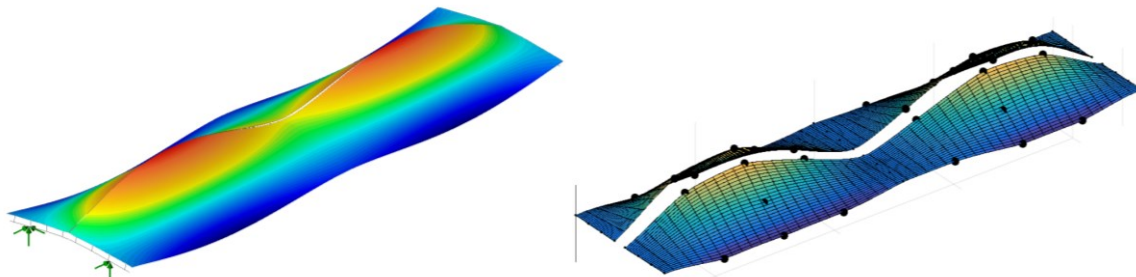


Figure 1.8.6: LUSAS FEM Mode 3 – 2.45 Hz

Figure 1.8.7: Experimental Mode 7 – 2.83 Hz

To resolve this discrepancy, those components that experienced significant curvature were examined first, especially those that experienced relatively little curvature in other modes. The moment of inertia of the I-girders in the negative moment region was checked and found to be consistent with the drawings as well as have little impact on the frequency of the mode.

The central box girder displayed significant deformation for this mode and was the next component to be investigated. The mode was found to be sensitive to its stiffness by studying the effects of altering its moment of inertia. However, as there was a high degree of confidence in the girder's section properties, the boundary conditions of the box girder were ultimately chosen for modification. The box-girder supports were already represented with fixed translational degrees of freedom as well as rotation about the transverse axis. Rotation about the longitudinal axis was restrained by specifying a spring stiffness of 5×10^{10} lb.-in./rad. This value was determined through incremental adjustment until the predicted frequencies were within 10% of those determined experimentally.

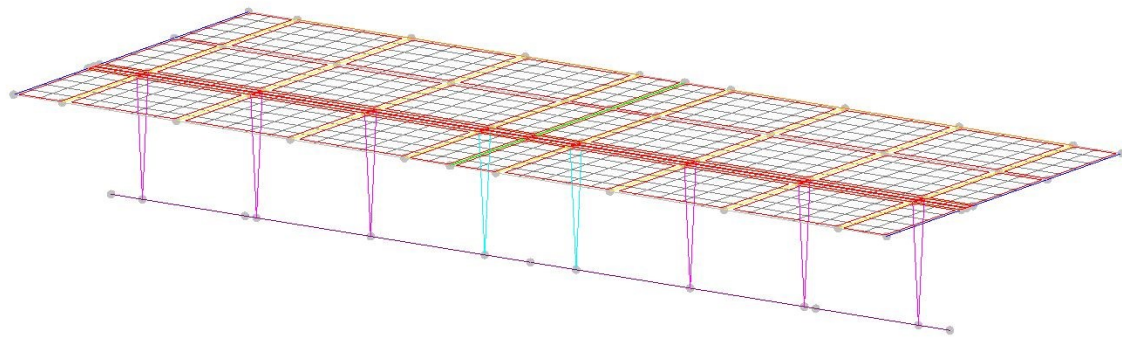
With the aforementioned adjustments completed, the natural frequency results of the FE model differed from the experimental results by no more than 2 percent as can be seen in the summary table below. The corresponding shapes may be found in the appendix.

Table 1.8.7: Comparison of Experimental and FE (LUSAS) Mode Shape Frequencies

	Exp.	LUSAS FEM	% diff
Mode 1	2.00	2.033	1.5%
Mode 2	2.03	-	-
Mode 3	2.10	2.072	1.4%
Mode 4	2.44	2.493	2.0%
Mode 5	2.51	-	-
Mode 6	2.54	2.496	1.6%
Mode 7	2.83	2.821	0.4%
Mode 8	2.93	-	-
Mode 9	3.20	3.137	1.9%
Mode 10	3.34	-	-
Mode 11	3.52	-	-
Mode 12	3.56	3.628	2.0%
Mode 13	3.56	3.629	2.0%

Full Model

Once the two-span model was satisfactorily modeled, a more comprehensive model was constructed that included all eleven spans of the viaduct. Deck elements were left separated by $\frac{1}{2}$ " where discontinuous spans met. Furthermore, by utilizing adjacent "pedestal" elements, the box-girder element could support the two different spans without forcing continuity between their components (deck and girders).

**Figure 1.8.8: Connectivity at discontinuous joints**

Vehicle Modeling

The vehicle model was developed from the experimental data. A model form of minimal complexity was initially chosen consisting of a single sprung mass. The reduction of the truck to a SDOF system collapses the spatial distribution of wheel loads to a single point load. Furthermore, the SDOF system can have only a single mode shape, while the vehicle will exhibit at least three dominant vertical modes (roll, pitch, and bounce). More complex models would be employed should this SDOF representation fail to provide results comparable to experimental results.

The mass of the truck (m_s) was assigned based on the total measured weight of the test truck.

The acceleration data of the truck was processed using spectral analysis methods and the suspected frequency of the first mode of vibration was identified as detailed in the previous section. Using the relationship for the frequency (f) of a single degree-of-freedom system, the stiffness of the suspension (k_s) was estimated according to the following equation.

$$k_s = \omega^2 * m_s = (2\pi f)^2 * m_s \quad (12)$$

According to the PSD estimate of truck acceleration records (Figure 1.7.15), the first mode of vibration occurs near 2.7 Hz. Assuming, 45 kips of the truck weight are carried by the suspension, the suspension stiffness is computed to be 36 kip/in.

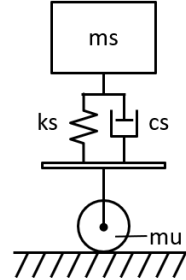
The damping coefficient (c_s) was an uncertain parameter as it could not be reliably determined from the gathered experimental data. Furthermore, damping values vary widely for different vehicles and suspension types. This parameter would be examined as a variable during the model validation phase. A reasonable initial value was assigned to achieve 10% of critical damping. The coefficient value was calculated with the following equation.

$$c_s = 0.10 * 2\sqrt{k_s m_s} \quad (13)$$

The initial vehicle model parameter values are summarized in the following table.

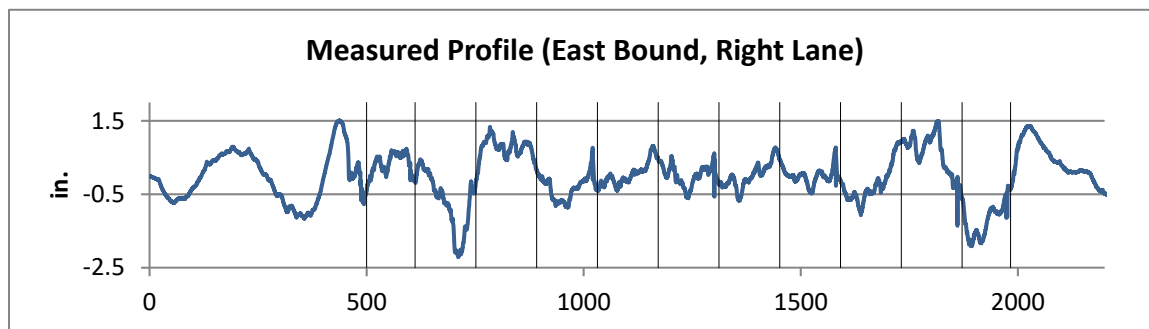
Table 1.8.8: Parameter Values for Initial Vehicle Model

	Value	Units
ks	36000	lb/in
cs	410 (10%)	lb-s/in
ms	116.55	lb-s ² /in
mu	0	lb-s ² /in



Profile Consideration

Initial simulations did not include any roadway profile and therefore inherently assumed a perfectly smooth profile. It very soon became clear that neglecting the roadway profile in the simulations greatly under-predicts the bridge responses. The in-situ roadway profile was subsequently measured for implementation in further simulations.

**Figure 1.8.9: Measured Profile**

Profile measurements were converted to csv files, each of which contained an array of distances and an array of corresponding elevations for right and left wheel lines using the ProVAL software. MATLAB was then used to prepare the profile data so that it could be directly imported into the LUSAS software for simulation. A custom MATLAB script made the following changes to the data:

- Profile is trimmed to a specified distance before the beginning of the bridge.

- Distance values are converted to inches and made to start from 0 at the beginning of the profile.
- The profile elevation values, over a specified distance from the profile start, are windowed with a simple ramp (linear) function to avoid any initial jumps in elevation at the start of the profile.
- New distance and elevation arrays are saved to a text file.

The ramp in the profile data prevents the large initial energy input that would result from a sudden step in the profile at the first elevation point. A ramp of 20 feet was specified. The profile was trimmed such that it began 500 feet before the beginning of the bridge to induce initial vehicle conditions (displacement and velocity).

Simulations were performed with the measured profiles. The vertical acceleration at mid-span of span 3 from simulation with above measured profile is plotted below and compared with the results from simulation with no profile. These results provide clear indication that the profile has a great influence on vehicle-bridge interaction. These results are consistent with the conclusions of previous studies (Deng and Cai, 2010; Huang et al., 1995, 1992; Kwasniewski et al., 2006b).

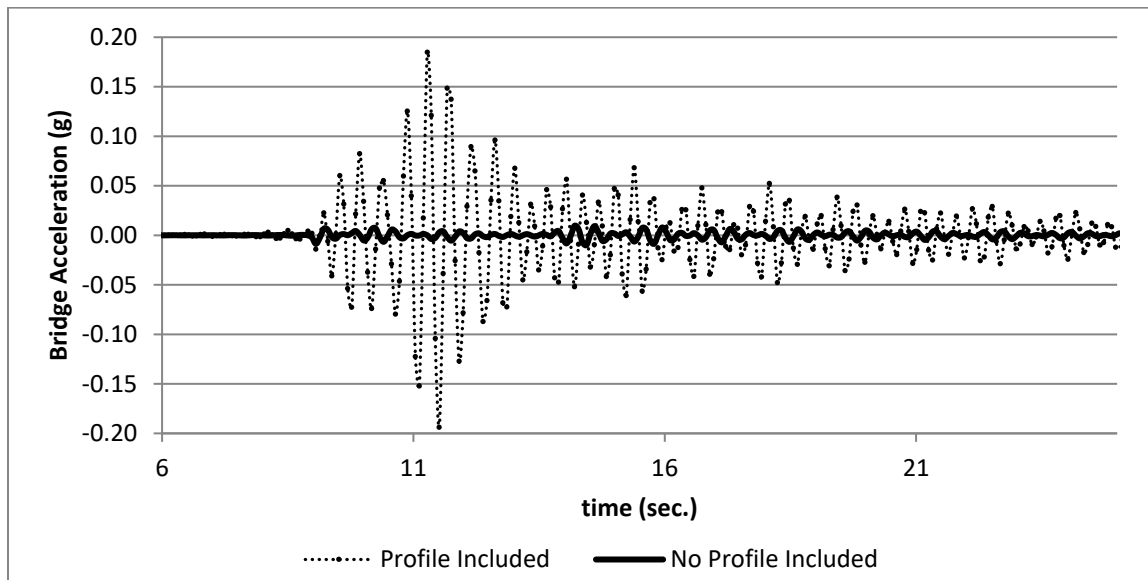


Figure 1.8.10: Comparison of span 3 midspan acceleration for simulations with and without a profile included

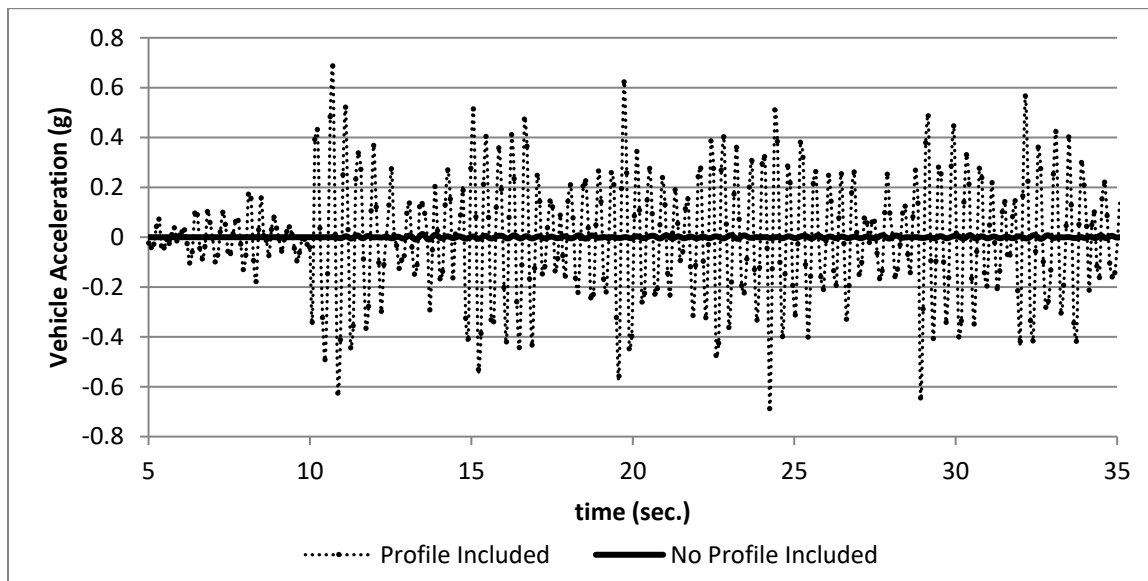


Figure 1.8.11: Comparison of truck vertical acceleration for simulations with and without a profile included

Validation of VBI Simulation Methods

In an effort to validate the bridge and vehicle model and the overall VBI modeling methods, the mass, stiffness and damping of the vehicle model were adjusted. Damping ratios of 5, 7, 10 and 20 percent were investigated. Mass and stiffness were increased (while maintaining 2.9 Hz

frequency) but they were ultimately bounded by the field measurements, and therefore, were relatively certain parameters. Suspension stiffness had minimal effect on truck acceleration, while decreased damping significantly increased truck acceleration. A truck model with the parameters listed in following table ultimately resulted truck acceleration that best matched the experimental data. Structural damping of 2% was assigned for all included modes.

Table 1.8.9: SDOF Vehicle Model Final Parameter Values

	Value	Units	
ks	30000	lb/in	
cs	241 (7%)	lb-s/in	
ms	98.42	lb-s ² /in	
mu	20.72	lb-s ² /in	

Simulations of run 14 were performed with the path of travel located in center of the right lane of the east-bound side and the measured profile of the right wheel line for that lane. Vehicle speed was set to 715 in/sec (18.2 m/s).

Simulations of run 3 were performed with the path of travel located in the center of the right lane of the west-bound side and the measured profile of the right wheel line for that lane. Vehicle speed was set to 740 in/sec (18.8 m/s).

The error between the simulated and measured acceleration time histories is quantified in the following section for bridge and vehicle acceleration for runs 3 and 14. These runs were chosen because they had very little accompanying traffic, were performed at relatively constant speed over the duration of the bridge crossing and provide responses for the two different sides of the bridge. Furthermore, these runs featured large bridge and vehicle responses and are thus likely to contain the least amount of influence from unmeasured loading sources (e.g. other traffic).

The bridge responses are reported at midspan for the instrumented girders that were closest to

the lane of travel for the given run. These locations correspond to the regions that experience the greatest vertical deformation.

Time History Comparison

The recorded and simulated vehicle acceleration time histories for run 14 are plotted in the following image.

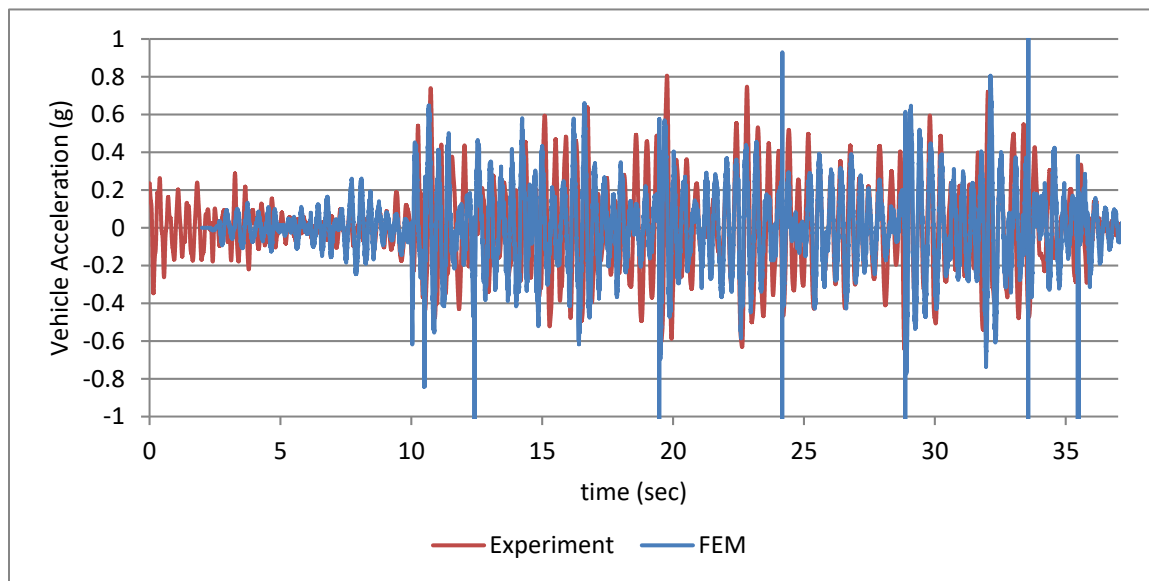


Figure 1.8.12: Experiment vs Simulation for Vehicle Acceleration for Run 14 over Bridge (Raw Data)

Although the two signals in the above plot appear similar, the degree to which the two signals match must be quantified. The process employed to quantify the discrepancy between two data sets is demonstrated in the following pages.

The experimental data was sampled at 1652 Hz, while the simulations were performed with a time-step of 0.002 seconds (500 Hz). Therefore, the experimental data has far more data points over a given period of time than the simulated data. The experimental data set must therefore be decimated to provide data points that correspond to each time step of the simulated data.

The experimental data is filtered prior to decimation to remove high frequency content that (1) is not included in the simulated data (due to specified time-step size and the included modes)

and (2) does not appreciably contribute to structural deformation (in the case of structural response) or contact force (in the case of vehicle response). The second reason is also applicable to the simulated data which is therefore also filtered to remove high frequency. An elliptic low-pass filter with a 10 Hz cut-off frequency, 0.5 decibels pass-band ripple, and 40 decibels stop-band attenuation was applied to both the experimental and analytical data. The filtered and decimated experimental data is plotted below for the truck acceleration (run 14).

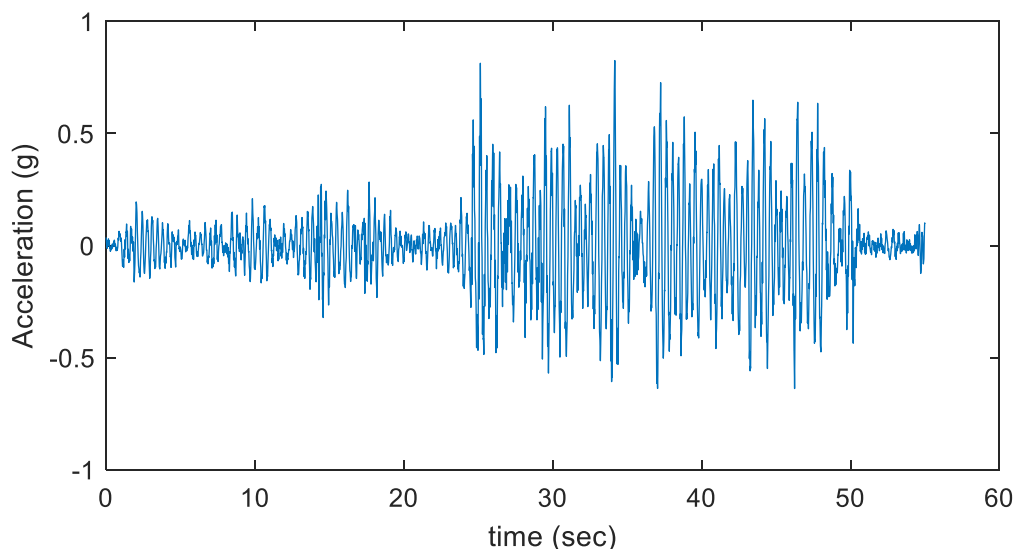


Figure 1.8.13: Filtered Experimental Vehicle Acceleration for Run 14 over Bridge

The two data sets were aligned by computing the cross-correlation of the two signals across a range of lags. The lag corresponding to the maximum cross-correlation value is taken as the shift required to align the two signals. The aligned experimental and analytical data are provided in the following plot.

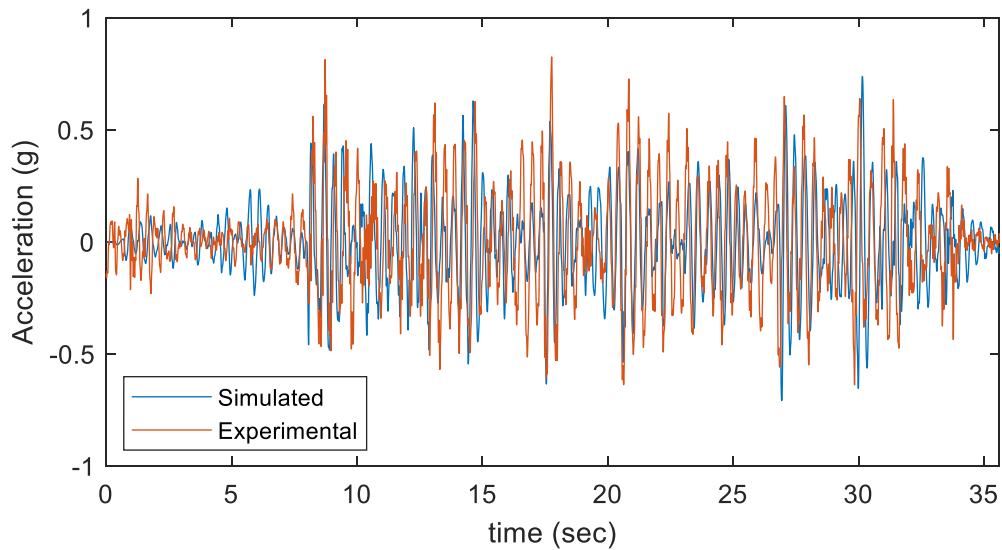


Figure 1.8.14: Experiment vs Simulation for Vehicle Acceleration for Run 14 over Bridge (Filtered and Decimated)

The mean-absolute-error between the filtered, decimated and aligned signals was computed according to the following equation.

$$MAE = \frac{1}{n} \sum_{i=1}^n |Y_i - \hat{Y}_i| \quad (14)$$

Where Y is the experimental data set and \hat{Y} is the simulated data set and n is the number of data points.

The MAE is also expressed as a percentage of the maximum filtered experimental response and was calculated according to the following equation.

$$\%MAE = \frac{MAE}{\max(Y)} \quad (15)$$

The resulting error for the filtered, decimated and aligned data plotted in Figure 1.8.14 above was 0.188 (g) (22.8%). While the plots appear very similar, slight differences in phases result in relatively large errors between individual data points. These differences can be attributed to inaccuracies of the vehicle model and especially the difference between the vehicle speed in simulations and the actual vehicle speed during the experiment. To better estimate the error

associated with the magnitude of the predicted response while discounting the error due to phase difference, the analytical data is mapped to the experimental data with the dynamic time warping (DTW) algorithm. The resulting experimental and analytical data is plotted in the following figure.

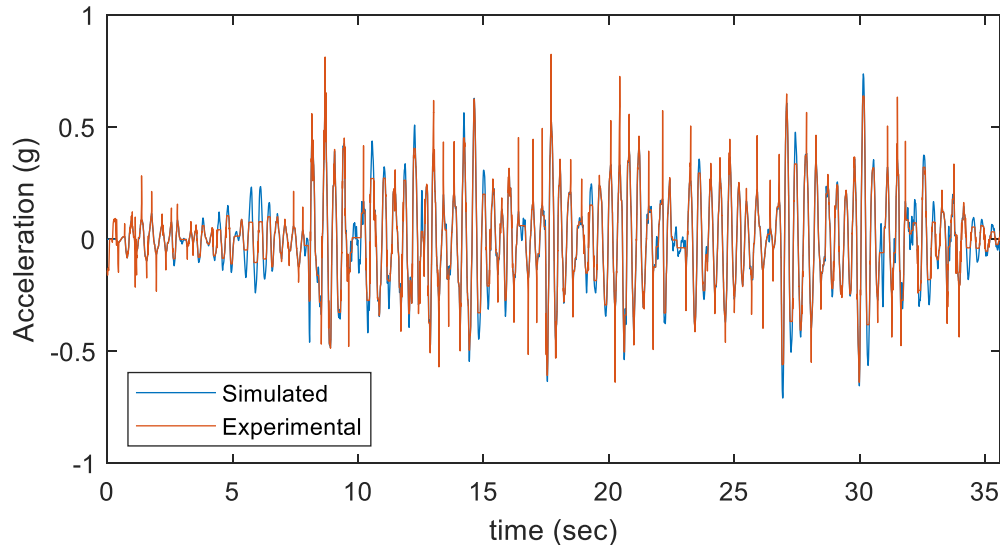


Figure 1.8.15: “Warped” Experimental and Simulated Truck Acceleration from DTW

The mean-squared-error between these “warped” signals was computed according to equation (14) and was found to be 0.029 (g) or 3.53% of the maximum filtered experimental acceleration (0.825 g).

The mean-absolute-error (MAE) of the filtered, aligned and decimated data and the MAE of the “warped” data are provided in the following table for runs 3 and 14.

Table 1.8.10: Mean Absolute Errors for Experiment vs Simulation

	Run 3				Run 14			
	MAE (g)	%MAE	MAE_DTW (g)	% MAE_DTW	MAE (g)	% MAE	MAE_DTW (g)	% MAE_DTW
Truck (Avg. Rear)	0.1443	15.43%	0.0224	2.40%	0.188	22.83%	0.029	3.53%
Span 2	0.0077	10.24%	0.0031	4.14%	0.051	37.31%	0.008	5.51%
Span 3	0.0136	11.58%	0.0049	4.13%	0.025	15.12%	0.007	4.18%
Span 4	0.0142	13.49%	0.0049	4.67%	-	-	-	-
Span 7	0.0173	24.59%	0.0056	7.97%	0.052	51.73%	0.006	6.12%

Span 4 errors are not provided in the above table because the corresponding sensor did not function properly and resulting data was unreliable.

The experimental and simulated acceleration were also compared based on maximum values.

The percent difference between the maximum values of the filtered experimental and simulated acceleration records were computed over the period for which the truck was on the bridge. The errors are also expressed as a percentage of the maximum experimental response. These errors are summarized in the following table.

Table 1.8.11: Error of Maximum Responses for Experiment vs Simulation

	Run 3			Run 14		
	Max Exp.	Max Sim.	%Diff.	Max Exp.	Max Sim.	%Diff.
Truck (Avg. Rear)	0.9352	0.6345	-32.15%	0.825	0.738	-10.58%
Span 2	0.0750	0.0890	18.58%	0.137	0.210	53.61%
Span 3	0.1177	0.1190	1.09%	0.162	0.225	38.31%
Span 4	0.1055	0.1230	16.68%	-	-	-
Span 7	0.0705	0.0926	31.48%	0.100	0.168	68.84%

It should be noted that the bridge remained open to traffic during testing and therefore the experimental bridge responses include the effect of additional vehicles that could not be considered in the FE simulations. Therefore, some disagreement is expected between experimental and simulated data. However, the mean-absolute-errors and maximum percent differences summarized in the preceding tables provide a quantitative measure of FE model's

ability to simulate vehicle crossings over the bridge and the resulting bridge and vehicle responses.

The filtered and aligned experimental and simulated data for run 14 is plotted for spans 2, 3, and 7 in the following figures.

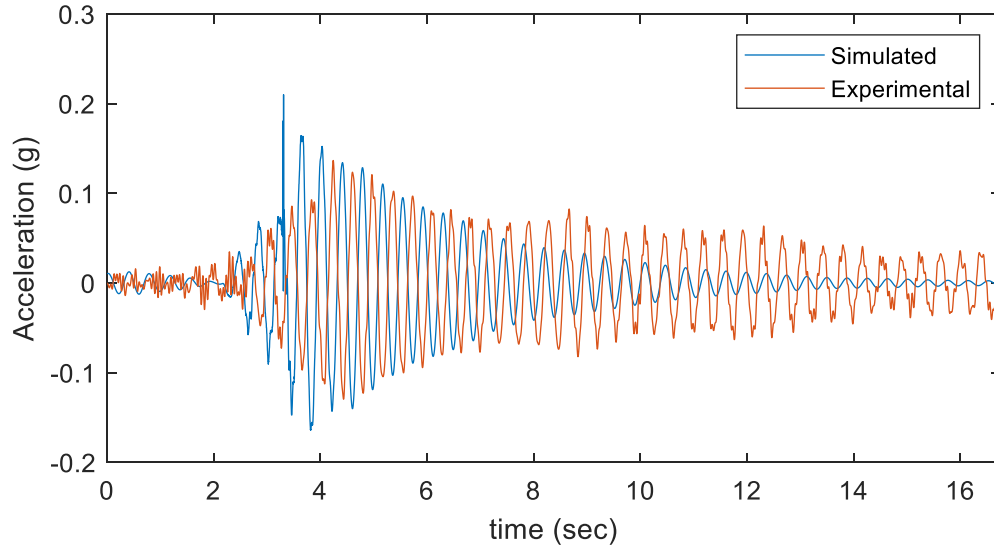


Figure 1.8.16: Experiment vs Simulation for Span 2 Midspan Acceleration of Girder 8 for Run 14 (Filtered and Decimated)

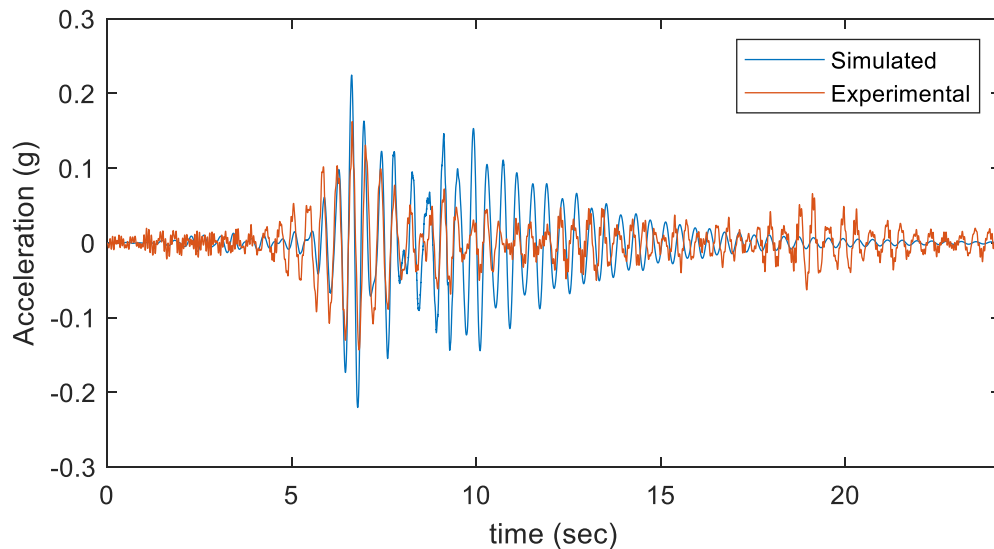


Figure 1.8.17: Experiment vs Simulation for Span 3 Midspan Acceleration of Girder 8 for Run 14 (Filtered and Decimated)

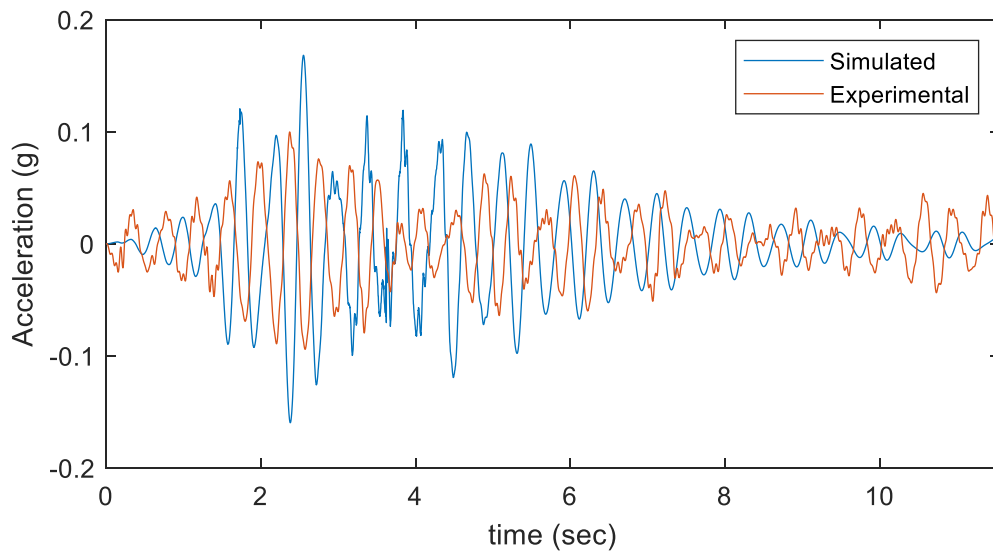


Figure 1.8.18: Experiment vs Simulation for Span 7 Midspan Acceleration of Girder 8 for Run 14 (Filtered and Decimated)

The filtered and aligned experimental and simulated data for run 3 is plotted for the test vehicle and spans 2, 3, 4 and 7 in the following figures.

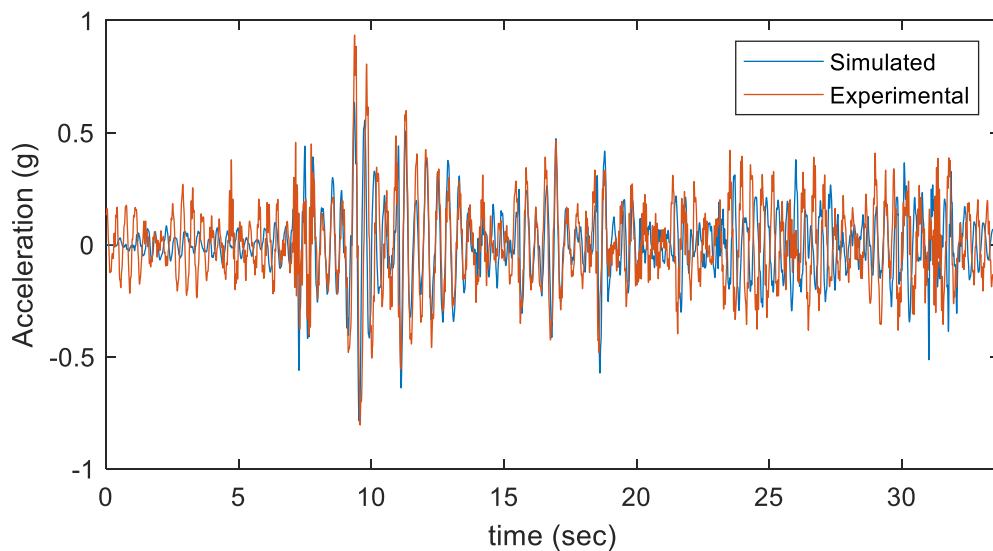


Figure 1.8.19: Experiment vs Simulation for Vehicle Acceleration for Run 3 over Bridge (Filtered and Decimated)

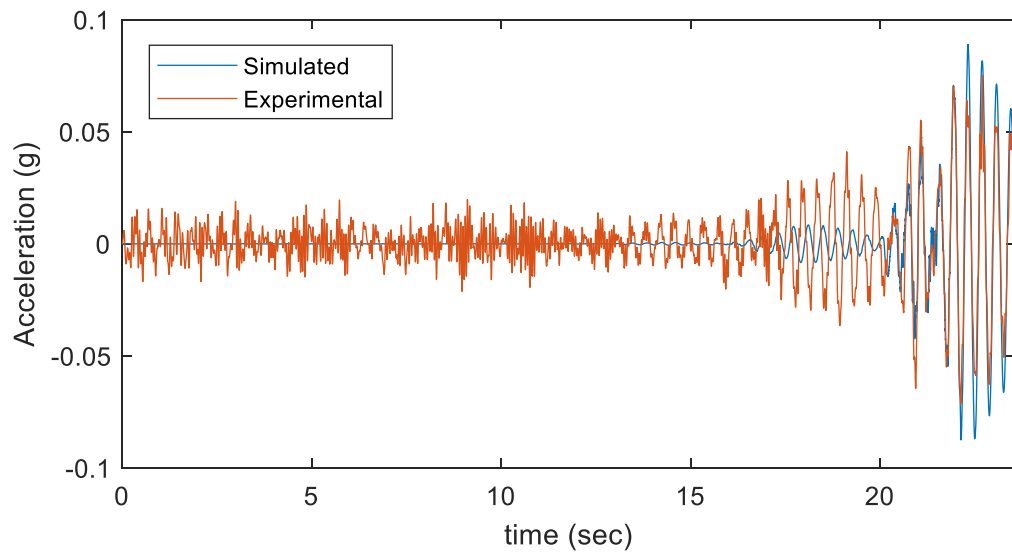


Figure 1.8.20: Experiment vs Simulation for Span 2 Midspan Acceleration of Girder 8 for Run 3 (Filtered and Decimated)

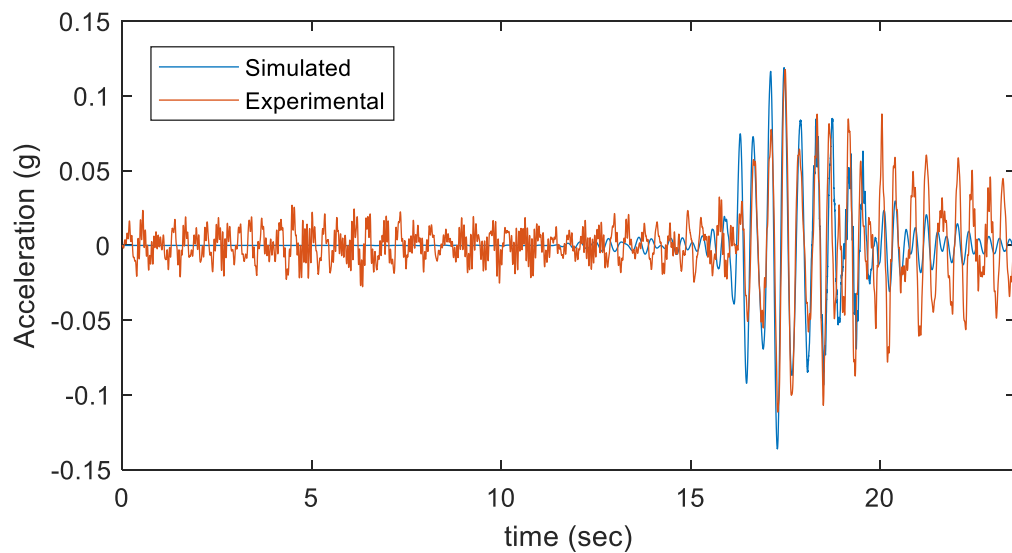


Figure 1.8.21: Experiment vs Simulation for Span 3 Midspan Acceleration of Girder 8 for Run 3 (Filtered and Decimated)

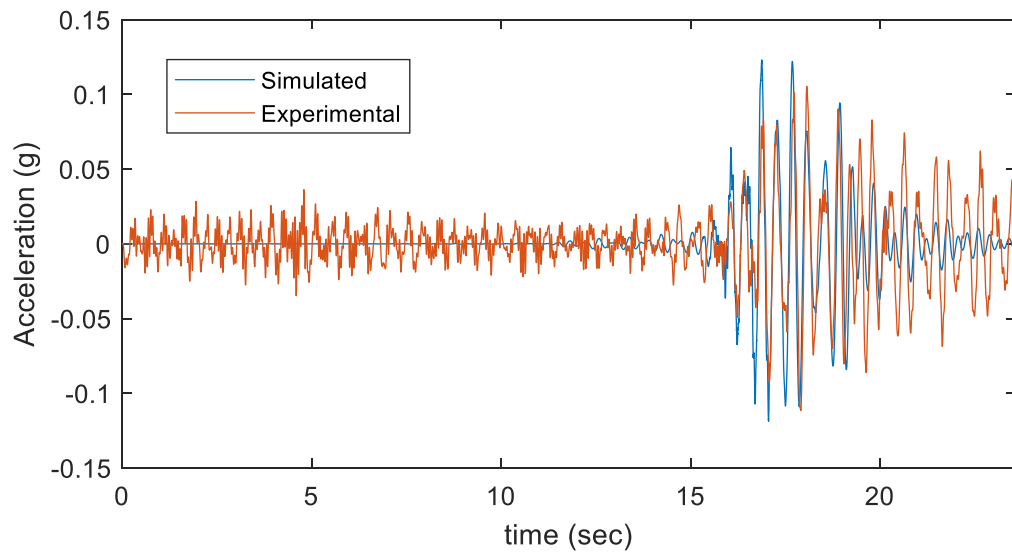


Figure 1.8.22: Experiment vs Simulation for Span 4 Midspan Acceleration of Girder 8 for Run 3 (Filtered and Decimated)

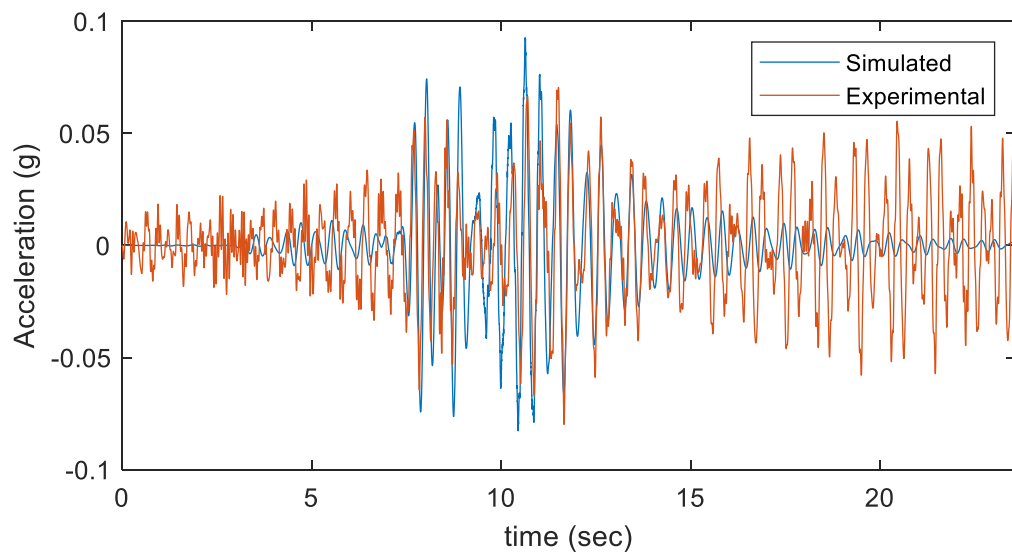


Figure 1.8.23: Experiment vs Simulation for Span 7 Midspan Acceleration of Girder 8 for Run 3 (Filtered and Decimated)

Simulated Amplification

The simulation of run 14 as detailed in the previous section was repeated for the purposes of predicting dynamic amplification. Both midspan displacement and moment were recorded for a vehicle crossing and amplification was computed as the ratio of dynamic response to maximum (quasi) static response.

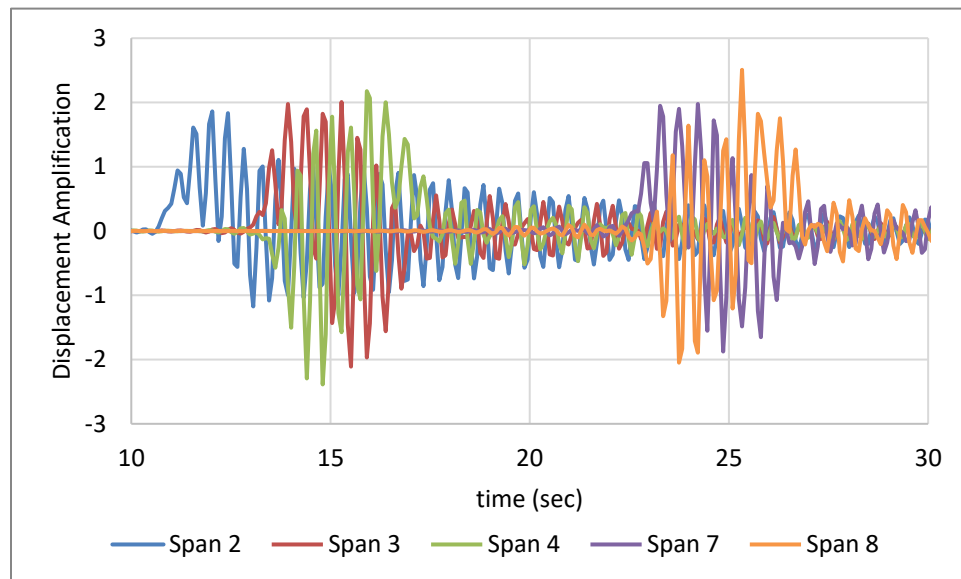


Figure 1.8.24: Simulated Bridge Midspan Displacement Amplification Time History

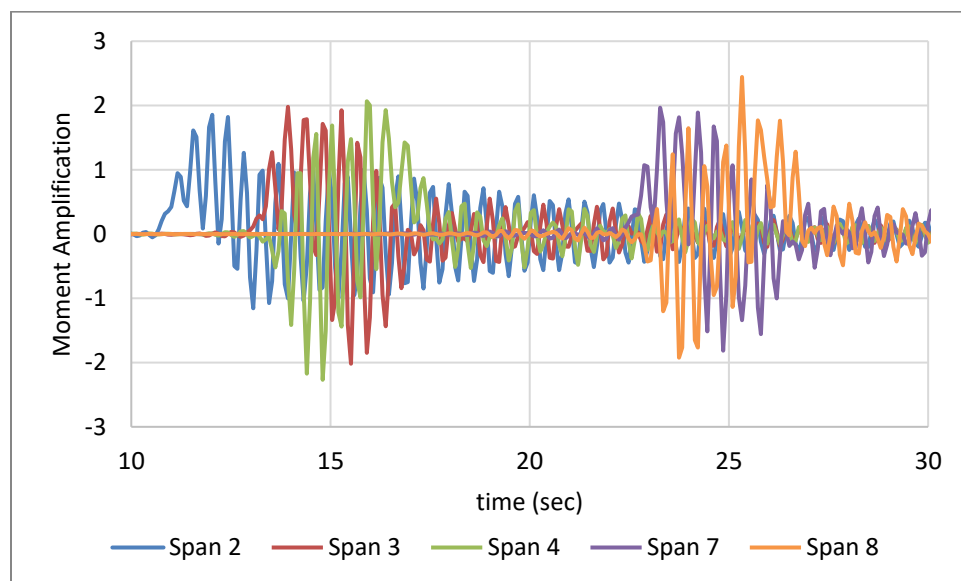


Figure 1.8.25: Simulated Bridge Midspan Moment Amplification Time History

The simulations were subsequently repeated for different vehicle speeds. The resulting variation in displacement amplification at the midspan of the exterior girder (8) is illustrated in the following plot.

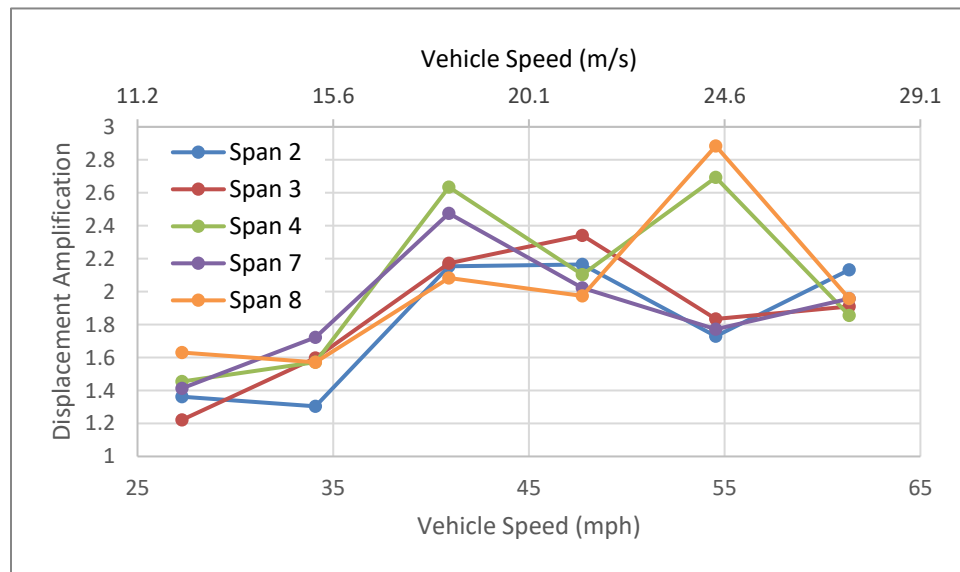


Figure 1.8.26: Maximum Displacement Amplification for Varying Speeds

Simulation Conclusions

The bridge and vehicle responses recorded during Phase 3 testing were leveraged to validate FE simulations of a vehicle (sprung-mass) traversing the bridge model. The conclusions of this validation process are as follows:

- A validated 3D FE model is capable of simulating bridge-vehicle interaction if roadway profile is included and accurately positioned on the model.
- A single degree-of-freedom vehicle model is adequate for simulating VBI and provides a conservative estimate of bridge response.
- Simulation results suggest that this structure may experience dynamic amplification even greater than observed, especially at higher speeds.

Chapter 9: Part 1 Summary and Conclusions

As a result of the tests performed on the case structure and the simulation studies with the validated model the following may be concluded.

- The high vibration levels are occurring on all spans (that were instrumented).
- These vibrations may be principally attributed to the bridge deck roadway profile.
- The vehicle is excited by the bridge deck profile, which in-turn excites the bridge.
- The high dynamic amplification does not seem to pose a risk to the structure's performance (at strength or service limit states).
- The bridge exhibits dynamic amplification in excess of 1.75 even under heavy vehicles (compared to AASHTO recommended 1.33).
- The bridge is experiencing motion that exceeds human comfort criterion.

Part 2: Estimating Dynamic Amplification

As vehicle loading continues to increase and while engineers design bridges more flexible and closer to the margins, the reserve capacities of structures are reduced. The reduction in conservatism can only be justified if the assumptions inherent to our design and evaluation methodologies are made more certain. The structure presented in the first part of this paper indicated that the dynamic amplification assumptions in the current live-load model are inaccurate and can be unconservative. These inadequacies have also been documented in other cases (Billing, 1984; Billing and Green, 1984; Cantieni, 1983; Kwasniewski et al., 2006b).

Therefore, it is necessary to utilize more accurate means of estimating or predicting dynamic amplification. The suitability of a given method is dependent on the application. In the case of existing structures, the in-situ behavior may be recorded, but the as-constructed dimensions and material properties may not be documented. During design, the in-situ behavior or attributes are not known, but the expected form of the structure is fully documented. It is therefore the objective of this part to identify and develop methods of predicting or estimating dynamic amplification that are suitable for the different applications.

Furthermore, these methods should be simple enough that they can be implemented by the typical practicing engineer. The simplicity of a method will undoubtedly come at the expense of accuracy. Therefore, a balance must be struck between accuracy and simplicity that is appropriate for the application. While this decision is ultimately left to the engineer, the following sections will demonstrate the tradeoff by presenting several methods of varying complexity for estimating dynamic amplification.

There are two widely used factors for expressing dynamic amplification. They are referred to as impact factor (IM) and dynamic amplification factor (DAF) and are defined by the following equations:

$$IM = \frac{Dynamic\ Response - Static\ Response}{Static\ Response} \quad (16)$$

$$DAF = \frac{Dynamic\ Response}{Static\ Response} \quad (17)$$

Therefore, the IM is just $DAF - 1$. The total live load response can be computed by the following:

$$LL = (1 + IM) * R_{sta} \quad \text{or} \quad LL = DAF * R_{sta} \quad (18)$$

Where R_{sta} is the static load effect which is amplified by $(1 + IM)$ or the DAF.

In this paper the dynamic amplification factor will be computed according to equation (17). The responses used in computing the factor may be any structural response, experimentally recorded or obtained through analysis.

This part summarizes the various methods of predicting dynamic amplification using both experimental and analytical methods. These methods are time-consuming to perform and require considerable expertise. Therefore, a simplified model is proposed that reduces the bridge to a single degree-of-freedom using generalized coordinates and reduces the vehicle to a single sprung-mass. The ability of this model to predict dynamic amplification is assessed by comparing its predictions to those obtained from 3D FE models. The simplified model as well as the 3D FE models are further used to investigate the parameters that are influential to dynamic amplification.

Chapter 10: Components of Vehicle Bridge Interaction

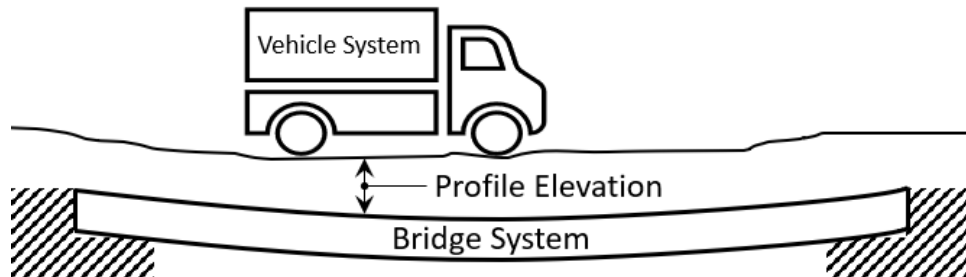


Figure 2.10.1: Schematic of Combined Vehicle and Bridge Systems

The excitation of the vehicle-bridge system is due to the contact force between the vehicle tire and roadway surface. This contact force is dependent on the difference in vertical position of the bridge roadway surface and the vehicle body which is equal to the deformation of the suspension system assuming the tires remain in contact with the bridge surface. The bridge surface elevation is the combination of bridge motion at the vehicle position and elevation added by the profile. It therefore follows that any model of vehicle-bridge interaction, in order to capture all of the primary mechanisms that give rise to dynamic amplification, should include the following:

- The mass of bridge excited by the vehicle-induced forces
- The stiffness of the bridge
- The mass of the vehicle
- The suspension characteristics of the vehicle
- The vehicle velocity
- The roadway profile accurately positioned on bridge

This last element, an accurately positioned profile, is critical. The effect of a profile feature (bump) is partially dependent on the location of the feature, therefore an accurate model must

also include longitudinal (along path of travel) bridge geometry (e.g. span length). This is demonstrated in Chapter 15.

There are many different methods of representing all of these elements in a model, but the success of a model is ultimately judged by its ability to reliably estimate the response of interest. For this study, that response of interest is the amplification of peak bridge responses during live load events (vehicle-crossing). The following sections will present several model types of varying complexity, document their construction, and demonstrate their ability to predict dynamic amplification.

Chapter 11 provides methods of estimating dynamic amplification of existing structures with field testing. Chapter 12 provides an analytical approach to estimating dynamic amplification using finite element analysis. Both approaches are demonstrated in the Part 1 case study.

Chapter 13 details the development and performance of a simplified model for estimating dynamic amplification. Chapter 14 demonstrates the shortcomings of common profile roughness metrics in predicting dynamic amplification. Chapter 15 examines the parameters influential to dynamic amplification through simulation studies.

Chapter 11: In-Situ Measurement

There is no substitute for directly measuring a phenomenon. This section provides guidance on methods of directly measuring the dynamic amplification being experienced by a bridge that is in-service.

Strain vs. Displacement

Within the relevant literature it is not uncommon for experimentally derived dynamic amplification factors to be reported for both displacement and strain (or stress). The amplification factors are almost always greater for displacement than those for stress or strain. If a bridge behaves linearly then its response should be linear (i.e. an increase in load by a factor X will result in an increase in response by the same factor, X) regardless of whether the response in question is global (e.g. displacement) or local (e.g. stress, strain). This is not the case with dynamic amplification factors because of a violation of the key assumption that the measured response is due solely to the applied load.

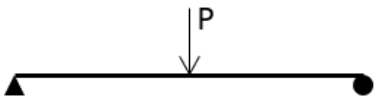
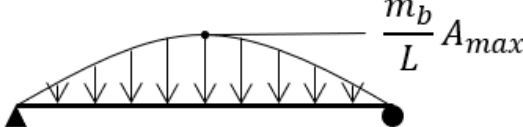
Dynamic amplification factors assume that the bridge response is due to a vehicle which applies a force equal to its weight increased by a factor to account for its dynamic motion (i.e. an acceleration greater than gravity). If this assumption were true, dynamic amplification factors would be equal for the various response quantities.

However, the bridge response is actually due to a force applied by the vehicle as well as inertial forces that develop due to the acceleration of the mass of the bridge as it is excited by the crossing vehicle (or other excitation sources).

Therefore, the bridge response is the sum of the responses due to these two inputs. To demonstrate this, consider a simply supported beam with a point load placed at midspan. The beam displacement and stress at midspan due to the point load (P) at midspan ($L/2$) is as

described by the equations provided in the following table, where E is the modulus of elasticity of the beam material, I is beam section's moment of inertia and y is the distance from the beam section's neutral axis.

Table 2.11.1: Displacement and Stress Equations for Point Load and Sinusoidal Distributed Load

	Point Force	Distributed (Inertial) Force
Loading		
Displacement	$\Delta = \frac{PL^3}{48EI}$ (19)	$\Delta = \frac{m_b L^3 A_{max}}{\pi^4 EI}$ (20)
Stress	$\sigma = \frac{PLy}{4I}$ (21)	$\sigma = \frac{m_b L A_{max} y}{\pi^2 I}$ (22)

A beam oscillating under its first mode deforms according to a sinusoidal shape with a maximum acceleration (A_{max}) at midspan. Therefore, the maximum acceleration at any point (x) along the beam length (L) can be described by the following equation:

$$u''_{max}(x) = A_{max} \sin\left(\frac{\pi}{L}x\right) \quad (23)$$

If the mass of the beam (m_b) is uniformly distributed along its length, the equivalent distributed static force (f_s) induced by the oscillating bridge mass can be described with the following equation.

$$f_s(x) = \frac{m_b}{L} A_{max} \sin\left(\frac{\pi}{L}x\right) \quad (24)$$

This equation takes the form of the Newton's second law of motion: $F = ma$.

The beam displacement and stress at midspan due to this distributed force can then be calculated using statics and the relationship between moment and curvature to produce the equations listed in the preceding table.

Therefore, the total response would be the sum of the two components, and the amplification factors can be described with the following equations, where the dynamic vehicle force is the product of the vehicle force amplification (A_v) and its weight (P):

$$DAF = \frac{\text{Total Bridge Response}}{\text{Bridge Response to Static Vehicle}} \quad (25)$$

$$DAF_{disp} = \frac{\frac{A_v PL^3}{48EI} + \frac{m_b L^3 A_{max}}{\pi^4 EI}}{\frac{PL^3}{48EI}} = A_v + \frac{48m_b A_{max}}{P\pi^4} \quad (26)$$

$$DAF_{stress} = \frac{\left(\frac{A_v PLy}{4I} + \frac{m_b LA_{max}y}{\pi^2 I}\right)}{\frac{PLy}{4I}} = A_v + \frac{4m_b A_{max}}{P\pi^2} \quad (27)$$

It can be deduced from the above equations that if vehicle amplification factors are to be used, an additional response due to the excitation of the bridge mass must be accounted for by including the second term in the above equations. Furthermore, these equations show that the amplification factor for displacement and stress will be different, and the amplification in excess of the vehicle amplification (second term) is greater for displacement than stress (or strain or moment). The additional amplification due to bridge inertial forces (only first mode considered) is plotted below for different ratios of bridge inertial force ($m_b * A_{max}$) to vehicle weight (P).

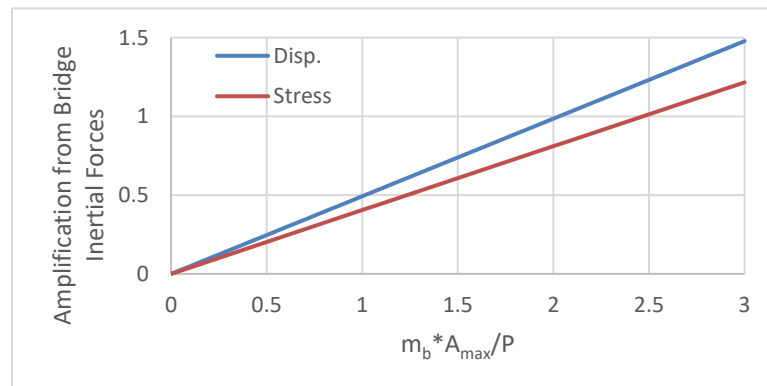


Figure 2.11.1: Additional Amplification as a Function of Bridge Inertial Force

The ratio of the additional amplification due to bridge inertial forces is calculated below.

$$\frac{\frac{48mA_{max}}{P\pi^4}}{\frac{4mA_{max}}{P\pi^2}} = \frac{12}{\pi^2} \approx 1.2 \quad (28)$$

The results of equation (28) and the previous plot demonstrate that, regardless of bridge or vehicle, the experimental amplification factor for displacement will always be greater than that for stress or moment as long as the bridge is exhibiting some oscillation. It should be noted that these calculations included only the first mode. If more modes were to be included, the equations for amplification factors would take the following form:

$$A_{disp} = A_v + \frac{48m}{P} \sum_{n=1,3,5,\dots}^{\infty} A_{max,n} \left(\frac{n}{\pi}\right)^4 \quad (29)$$

$$A_{stress} = A_v + \frac{4m}{P} \sum_{n=1,3,5,\dots}^{\infty} A_{max,n} \left(\frac{n}{\pi}\right)^2 \quad (30)$$

The ratio of additional amplification can again be computed.

$$\frac{\left(\frac{48m}{P} \sum_{n=1,3,5,\dots}^{\infty} A_{max,n} \left(\frac{n}{\pi}\right)^4\right)}{\frac{4m}{P} \sum_{n=1,3,5,\dots}^{\infty} A_{max,n} \left(\frac{n}{\pi}\right)^2} = 12 * \frac{\sum_{n=1,3,5,\dots}^{\infty} A_{max,n} \left(\frac{n}{\pi}\right)^4}{\sum_{n=1,3,5,\dots}^{\infty} A_{max,n} \left(\frac{n}{\pi}\right)^2} \quad (31)$$

Additionally, these results are limited to midspan responses. Amplification factors at other locations can be computed in a similar manner, using equations for displacement or stress at other locations. This derivation considers only a simply supported beam and a point load, but the results are still representative of the phenomenon occurring in real structures as long as the following conditions remain true:

- The vibration of a bridge takes a shape that can be described by a shape function that is a summation of sines.
- The vehicle force is applied to a small area of the bridge and can be reasonably approximated as a point load.

In summary, amplification factors determined with displacement will be greater than those determined from strain (or stress or moment) due to the distribution of load from the mass loading that is ignored in static analysis. As bridge oscillation increases, the difference between the two factors also increases. Therefore, experimentally determined displacement amplification factors are a more conservative measure of dynamic amplification, but strain amplification factors remain adequate since strain responses more directly measure the stress experienced by the bridge.

Operational Monitoring

Often operational monitoring, whereby bridge response is recorded during normal operation, is cost-effective (since it is least disturbing to traffic) and provides responses under typical loading conditions. Bridge members should be instrumented at “governing” locations (i.e. expected to experience the largest responses or suspected to have the least reserve capacity). Sensors should be carefully selected based on required response, range, frequency, accuracy, etc. This study is principally interested in material level responses (i.e. stress). Strain is directly related to stress (for linear material) and thus strain gauges are preferred for measuring dynamic amplification. Displacement gauges can also be used but may overestimate amplification when the resulting factors are employed within static analysis that ignores the mass forces associated with the vibrating bridge (as discussed in the previous section). Acceleration gauges may be used to estimate displacement if they remain accurate at frequencies near zero. This requirement is true of any gauge chosen but is more likely to be an issue with AC-coupled, piezoelectric accelerometers.

The process of determining dynamic amplification from operational responses has been already detailed by other researchers. Regardless of the exact method used, the data is filtered to

remove high frequency content leaving behind an estimate of the content associated with quasi-static loading. The dynamic amplification is then estimated by computing the ratio of the maximum of the original data to the maximum of the filtered data. Multiple vehicle events should be examined as the degree of dynamic amplification may vary significantly for different vehicles. A demonstration of this process as well as the error that results from substituting filtered response for static response can be found in the case study presented in Part 1.

The filter parameters should be selected such that the pass-band upper limit is less than the first natural frequency but greater than the frequency of loading. In reality, some loading events occur at higher frequencies than the first natural frequency of the structure. In these cases, the filtered response under-estimates static response, subsequently resulting in an over-estimation of amplification. This problem is mitigated by the large mass of the bridge which resists rapid motion but is always an inherent source of error when estimating static response from operational responses. Furthermore, it is unlikely that a “worst-case” scenario will occur during the record interval and thus the estimated amplification can be non-conservative but can be appropriate for operational limit states and is a valuable approximation for assessing in-service performance.

Load Testing

The static response of the bridge can be measured directly when the load is applied statically during a load test in which the bridge is closed to other traffic. Responses should be recorded for the test-vehicle (loaded truck) motionless as well as travelling over the bridge at speeds corresponding to minimum, typical, and maximum traffic speeds. Dynamic amplification computed from the resulting static and dynamic responses will be accurate for that specific test-vehicle but is not guaranteed to remain conservative for all loading events. A bridge’s

performance in design or evaluation is measured by its ability to carry limit-state loads. Test-vehicles should therefore be loaded to a weight similar to the legal load limit. When possible, test-vehicles should also be chosen with a body-bounce natural frequency similar to that of the first-bending mode of vibration of the bridge as this will result in the greatest dynamic amplification (demonstrated in Chapter 15).

The test-vehicle should be placed at locations that produce maximum response or made to “crawl” at speeds low enough to maintain “quasi-static” conditions for the static portion of the load test. The dynamic load test should occur at various speeds and along all paths of travel. The test vehicle must begin a significant distance from the start of the bridge to account for vehicle motion resulting from traversing the approach roadway. The test-vehicle should maintain the set speed over the approach and bridge roadway. An approach length of 100 meters is common and shown in Chapter 15 to be adequate for vehicles with 10% damping.

Profile Measurement

In some cases, it becomes necessary to simulate the bridge response to moving vehicles. Any simulations of vehicle-bridge interaction must include bridge deck profile. The roadway profile was shown to be highly influential to bridge response in Part 1 as well as in numerous other studies (Deng and Cai, 2010; Huang et al., 1995; Kim et al., 2007; Wang and Huang, 1992). The profile should contain paired position and elevation information along the entire length of the bridge and approach roadway for every reasonable path of travel. Elevation data may be recorded along a single line or along multiple wheel lines. The spatial resolution should be set small enough to capture all features of interest. Since the bridge is most sensitive to loading near its own natural frequencies, and harmonic profile features induce loading at frequencies equal to the vehicle speed divided by the feature wavelength, the spatial sampling should be

such that the distance between samples is no more than half the feature length that induces vibrations at the structure's highest frequency (f_{max}) that appreciably contributes to bridge deformation when a vehicle is traveling at a minimum (reasonable) speed (v_{min}). Therefore, the following equation may be used to compute the maximum spacing between samples (S_{max}).

$$S_{max} = \frac{v_{min}}{2f_{max}} \quad (32)$$

For a typical highway bridge the maximum contributing natural frequency is likely less than 15 Hz while vehicle speeds can be expected to exceed 20 mph (32 kph). Therefore, according to the above equation, profile measurements should be taken at least every 10 inches (25 cm). Commercial profilographs have sampling intervals on the order of one inch and thus can be expected to produce adequate profile measurements.

Conclusions

This chapter presented experimental methods of estimating dynamic amplification. These included operational monitoring and load testing. Measurement of the in-situ roadway profile is also addressed as it is a very influential parameter to dynamic amplification and will likely need to be measured if a structure is suspected to be experiencing large dynamic amplification. The conclusions of this chapter are as follows.

- Amplification factors determined from displacement measurements will be greater (more conservative) than those determined from strain measurements.
- Dynamic amplification may be determined from recorded operational responses through the use of filtering techniques.
- Live-load testing is better able to capture static responses, but dynamic responses may not be representative of worst-case scenarios. Dynamic amplification estimates may therefore be underestimated.

- Profile measurement of the bridge roadway should be performed with a longitudinal resolution of 10 inches or less and include the approach roadway.

Chapter 12: Model-Based Simulation

There are often scenarios in which it is impractical or even impossible to implement certain loading events or measure certain responses. Furthermore, measurements alone generally cannot be used to identify the importance of the various mechanisms. Therefore, when it is the goal to identify the role of bridge components and mechanisms in observed responses or assess the suitability of proposed mitigation strategies (adding damping sources, changing the profile, adding stiffness, etc.) an analytical model is required. The selection and construction of a suitable model for these simulations is critical to reliable predictions.

Common Structural Model Classes

Single-Line Girder Model

This method of modeling is the most basic and commonly used approach for the design and performance evaluation of common bridge types within the U.S. This approach approximates structural phenomena through various equations to estimate the equivalent demands that a single girder within the structural system will experience. This approach has been shown to under-estimate stiffness, but is generally conservative for the computation of static dead-load and live-load demands (Romano et al., 2017). While this model type is simple and very easy to implement, it is unable to simulate dynamic loading or represent transverse distribution of mass or stiffness.

2D Grid Model

The 2D grid method borrows assumptions from the classical “plane grid” analysis method and is sometimes referred to as a grillage model. The girders and diaphragms are modeled as beam elements having three degrees of freedom (DOF) per node (two rotational and one translational DOF), with no depth information being explicitly represented. The two rotational degrees of

freedom capture each girders' major axis bending and torsional response. The single translational degree of freedom captures the vertical displacements of the girder.

With this method, all of the girders, diaphragms, and bearings are located at the same theoretical elevation in the model. Such models only permit the computation of vertical displacements and rotations within the plane of the bridge model.

2D Frame Model

Similar to the 2D grid model, the 2D frame method of analysis ignores depth information. However, in this approach, the beam elements are equipped with six degrees of freedom at each node, three translational and three rotational. According to White et al. (2012), if there is no coupling between the degrees of freedom for the conventional 2D-grid and the three additional degrees of freedom, 2D-frame models provide no additional information beyond the ordinary 2D-grid solutions. Therefore, for vertical loading of a structure with no appreciable slope, this class of model performs no better than a 2D grid model.

Plate Eccentric-Beam Model

Similar to the 2D frame model, the plate eccentric-beam (PEB) model places the model elements in a single plane. However, for a PEB model, the girders are assigned an offset from the deck plane. This provides a more accurate representation of the composite (girder-deck) section and its stiffness. This model type provides better accuracy than 2D-grid or 2D-plane models while maintaining similar levels of simplicity and is suited to prismatic multi-girder bridges.

Element-Level Model

This type of model employs both one-dimensional (frame/beam elements) and two-dimensional elements (plate or shell elements) to model girders/diaphragms and the deck, respectively. Beam elements have either 2 or 3 nodes with 6 DOFs each. Plate/shell elements may have 3 (in the case of triangular elements), 4 (in the case of rectangular elements), or up to 9 (in the case

of 9-node rectangular shells) nodes with up to 6 DOFs each. In an effort to remain consistent with the three-dimensional geometry of the structure, various link elements (to connect girders to the deck and diaphragm elements to the girders) and constraints (to simulate boundaries) are also employed. This model resolution is commonly termed “element-level” and is the most common class of 3D FE models employed for constructed systems (Çatbaş et al., 2013b). This class of model is particularly well suited to structures with complex geometry as the elements can be accurately positioned in the model.

While an element-level FE model can reasonably simulate most bridge responses, it is unable to effectively simulate warping deformation of girders (associated with torsion) or stress concentrations associated with geometric discontinuities. While these shortcomings may be critical in the case of modeling specific construction sequences for complex bridges (White, 2012) and advanced fatigue/fracture assessment, they are not relevant for the global responses induced by VBI and considered for dynamic amplification.

Shell Element Method of Analysis

The most significant distinction between element-level and shell element models of multi-girder bridges is that the beams in shell element models are discretized vertically, laterally, and longitudinally using shell elements. This method of modeling girders allows for the accurate simulation of warping of the girders due to torsion. Computation, model construction, and result extraction activities however, are more time consuming and more difficult than with element level models.

Vehicle Model

While there are many different methods of modeling a vehicle, the simplest method is to reduce the vehicle to a SDOF system, thereby collapsing the spatial distribution of wheel loads to a single point load. This method is conservative for predicting bridge responses and was shown in

Part 1 to perform adequately for the purposes of simulating dynamic bridge response and estimating dynamic amplification.

The vehicle can be modeled after a real vehicle by assigning equivalent mass (weight) and by setting suspension characteristics that produce a natural frequency equal to the vehicle's body-bounce natural frequencies. If there is no reference vehicle, a worst-case vehicle model may be created that has a mass equal to the legal limit, low damping (e.g. 10%), and a suspension stiffness that results in a body-bounce frequency 10-20% greater than the bridge's first-bending natural frequency (as demonstrated in Chapter 15).

Model Selection and Implementation for Simulating VBI

Simulation of VBI for predicting dynamic amplification should be performed with a model that is capable of capturing the dynamics of the structure. This requires a model that is geometrically consistent with the real structure such that the mass and stiffness can be accurately modeled and spatially distributed. In most cases, either a 3D element-level model or PEB model can represent all mechanisms and features that are a part of vehicle-bridge interaction and influence dynamic amplification.

It is not the aim of this paper to provide guidance on constructing and validating FE models. The exact methods of model construction and analysis are dependent on the FE software package employed. The selected FE software should be capable of simulating moving sprung masses over a specified profile and bridge model. The model should be constructed using best practices, error-screened, and validated with experimental data whenever possible. Validation with dynamic data (e.g. frequencies and mode shapes) is preferable and ensures the model dynamics match those of the structure. The model should have at least the first natural frequency matching that of the real structure.

Static responses can be simulated with vehicle at a crawl-speed (i.e. <1mph) or with a static linear analysis of the vehicle placed in locations that produce maximum response. Simulated responses should be recorded at governing locations (maximum response or particular vulnerability). Dynamic amplification can be computed for a given location as the ratio of maximum dynamic response to maximum static response.

The case study provided in the first part of this document demonstrates the process of estimating dynamic amplification with FE analysis.

Conclusions

This chapter reviewed common structural model types and made recommendations on vehicle and bridge model forms for the simulation of VBI. These recommendations can be summarized as follows:

- Models should be able to represent bridge mass and stiffness, vehicle suspension characteristics, and bridge roadway profile.
- 3D FE models are recommended when possible because they are capable of accurately representing the 3D nature of bridge dynamic behavior.
- Vehicle models can be represented as a single-sprung mass as demonstrated in Part 1.

Chapter 13: Simplified Model Formulation

Although 3D FE analysis is capable of accurately simulating vehicle-bridge interaction and estimating dynamic amplification, it is often impractical for current engineering practice due to the required time and expertise or the limitations of available FE software. It is therefore advantageous to develop models that require minimal time and expertise while still providing accurate estimates of dynamic amplification.

Description

The following pages present a model type that includes all of the mechanisms involved with vehicle and bridge motion as listed in Chapter 10. The model reduces the bridge to a generalized single degree-of-freedom (SDF) system for which its deformation at any point along the bridge's length is defined by a shape function. The vehicle is also represented as a single sprung mass and is coupled to the bridge degree-of-freedom. The equations of motion for this generalized SDF system are relatively simple and are used to develop state-space equations that define the vertical position of both bridge and vehicle. The following image illustrates the model components.

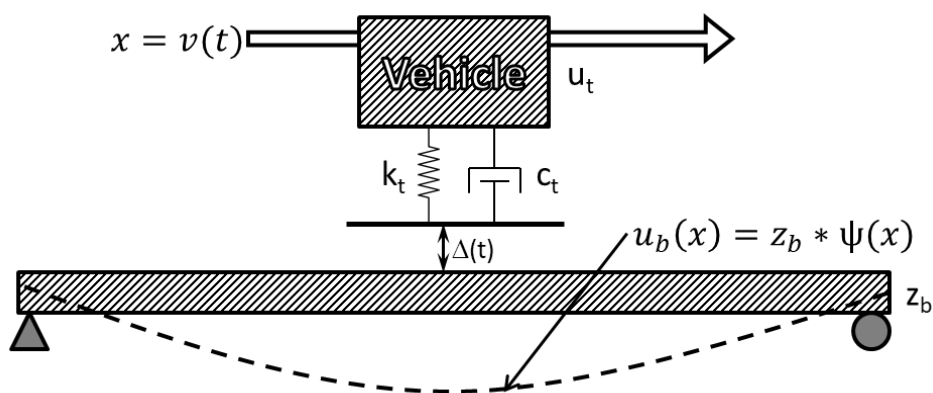


Figure 2.13.1: Diagram of Simplified 2-DOF Model

Models of this form were developed for single-span bridges and for 2-span continuous bridges with equal span lengths. Although these models include every mechanism that plays a role in dynamic amplification they have several inherent limitations:

- 1) A half-sine wave ($\Psi(x) = \sin\left(\frac{\pi x}{L}\right)$) was chosen for the shape function that generalizes the distributed system by defining the shape of the beam deformation. While this shape function accurately describes the deformation associated with the first-bending mode of vibration, it is incorrect for point loading (or any other loading). For a single-span beam subject to a point load at midspan, the error due to this shape function is 1.45%, while, for a two-span continuous beam, the error is 31% (for midspan displacement predictions).
- 2) The error is further exacerbated when the load is not at midspan as the shape function is symmetric about midspan.
- 3) The single shape function only accounts for the bridge's first mode of vibration.
- 4) By modeling the bridge as a single beam, the lateral distribution of mass and stiffness is neglected, much like the single-line girder model.

While these limitations leave the models much less capable than a full 3D FE model, they prove useful for estimating dynamic amplification and require a fraction of the time investment and computing power.

Single Span

This state-space model is developed from the equations of motion for a single sprung mass traveling over a simple-supported beam with distributed mass and stiffness. The beam is reduced to a single degree-of-freedom by generalizing its displacement according to a shape function. A sinusoidal shape function was chosen to capture the excitement of the beam's first

mode of vibration (1st bending). The beam has a uniform stiffness parameter (EI), uniform mass distribution (m_b/L), and a span length of L . Mass proportional damping of the beam is included. The vehicle is reduced to a single point mass (m_t) with specified spring stiffness (k_t), viscous damping coefficient (c_t), and traveling at a specified velocity (v).

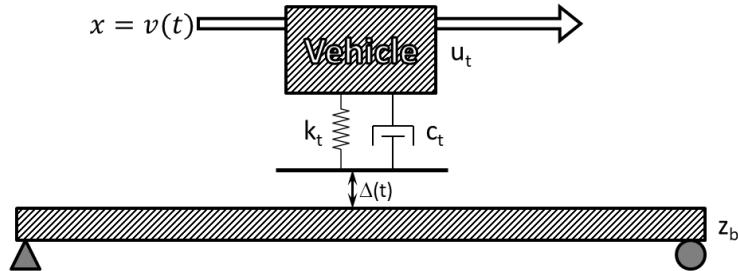


Figure 2.13.2: Diagram of Single-Span 2-DOF Model

Assumed deformation shape function

The beam is assumed to deform with a half sine function (i.e. wavelength is twice the length of the span). That function is described by the following equation.

$$\psi(x) = \sin\left(\frac{\pi x}{L}\right) \text{ for } 0 \leq x \leq L \quad (33)$$

Therefore, the deflection (u_b) and velocity (\dot{u}_b) of the beam at the vehicle's location at time (t) is related to the generalized coordinate (z_b) by the following equations.

$$u_b = z_b \sin\left(\frac{\pi v t}{L}\right) \quad (34)$$

$$\dot{u}_b = \dot{z}_b \sin\left(\frac{\pi v t}{L}\right) \quad (35)$$

Generalized mass, stiffness and damping

The generalized mass (\tilde{m}) and stiffness (\tilde{k}) properties for the beam can be calculated as follows.

$$\tilde{m} = \int_0^L \frac{m_b}{L} \psi(x)^2 dx = \frac{m_b}{2} \quad (36)$$

$$\tilde{k} = \int_0^L EI(x) \psi''(x)^2 dx = \frac{\pi^4 EI}{2L^3} \quad (37)$$

The theoretical midspan displacement (due only to bending) of a single-span beam due to a point load (P) at midspan (Δ_{theor}) is given by the following equation.

$$\Delta_{theor} = \frac{PL^3}{48EI} \quad (38)$$

Therefore, the error associated with the chosen shape function for a point load (P) at midspan may be calculated as follows.

$$Err = \frac{\frac{P}{\tilde{k}} - \Delta_{theor}}{\Delta_{theor}} = \frac{\left(\frac{2PL^3}{\pi^4 EI} - \frac{PL^3}{48EI}\right)}{\frac{PL^3}{48EI}} = 2 * \frac{48}{\pi^4} - 1 = -0.0145 \quad (39)$$

The generalized damping property (\tilde{c}) is defined by the following equation for mass proportional damping.

$$\tilde{c} = a * \tilde{m} \quad (40)$$

Where a is the mass-proportional damping coefficient. The damping ratio is defined by the following equation.

$$\zeta = \frac{\tilde{c}}{2\tilde{m}\omega_n} \quad (41)$$

Where ω_n is the radial natural frequency of the beam (first mode). Thus, the damping coefficient (a) may be determined based on a specified damping ratio (ζ) using the following equation.

$$a = 2\zeta\omega_n \quad (42)$$

By substitution, the generalized damping property may be expressed as follows.

$$\tilde{c} = a * \tilde{m} = 2\zeta\omega_n * \frac{m_b}{2} = \zeta\omega_n m_b \quad (43)$$

Force transformation

The force applied by the vehicle mass (p_0) must also be generalized. The force is described as a function of time and position as follows:

$$p(x, t) = \begin{cases} p_0\delta(x - vt) & 0 \leq t \leq t_d \\ 0 & t > t_d \end{cases} \quad (44)$$

Where $\delta(x - vt)$ is the Dirac delta function centered at $x = vt$, and $t_d = L/v$. The generalized force (\tilde{p}) is therefore calculated as follows for $0 \leq t \leq t_d$.

$$\tilde{p}(t) = \int_0^L p(x, t)\psi(x)dx = \int_0^L p_0\delta(x - vt)\sin\left(\frac{\pi x}{L}\right)dx = p_0 \sin\left(\frac{\pi vt}{L}\right) \quad (45)$$

The force (p_0) applied by the vehicle is calculated based on the relative vertical motion of bridge and vehicle, including profile elevation, as shown below.

$$p_0 = k_t * (u_t - u_b - \Delta) + c_t(\dot{u}_t - \dot{u}_b - \dot{\Delta}) \quad (46)$$

Where u_t is the vertical position of the vehicle, u_b is the vertical position of the bridge at the vehicle location and Δ is the profile elevation at the vehicle location. Single dot notation indicates the first derivative (with respect to time) and therefore \dot{u}_t is the vertical velocity of the vehicle, \dot{u}_b is the vertical velocity of the bridge at the vehicle location and $\dot{\Delta}$ is the rate of change in profile elevation.

Equations of motion when the vehicle is on the bridge

The equations of motion of the generalized beam and moving vehicle may therefore be composed as follows for $0 \leq t \leq t_d$.

$$\text{Vehicle DOF: } m_t \ddot{u}_t + c_t (\dot{u}_t - \dot{u}_b - \dot{\Delta}) + k_t (u_t - u_b - \Delta) + m_t g = 0 \quad (47)$$

$$\text{Beam DOF: } \tilde{m} \ddot{z}_b + \tilde{c} \dot{z}_b + \tilde{k} z_b + [k_t (u_b - u_t + \Delta) + c_t (\dot{u}_b - \dot{u}_t + \dot{\Delta})] * \sin\left(\frac{\pi v t}{L}\right) = 0 \quad (48)$$

Double-dot notation is used in the preceding equations to indicate the second derivative and therefore \ddot{u}_t is the vertical acceleration of the vehicle and \ddot{z}_b is the acceleration of the generalized bridge coordinate (z_b).

State Space

The states of this system (z_1, z_2, z_3 & z_4) are therefore defined as follows:

$$z_1 = \dot{z}_b; z_2 = z_b; z_3 = \dot{u}_t; z_4 = u_t \quad (49)$$

The profile elevation and velocity are assigned to matrix U with elements (u_1 & u_2):

$$u_1 = \dot{\Delta}; u_2 = \Delta \quad (50)$$

The equations of motion are reorganized in terms of the defined states as follows.

$$Z = \begin{bmatrix} Z_1 \\ Z_2 \\ Z_3 \\ Z_4 \end{bmatrix}; \dot{Z} = \begin{bmatrix} \dot{Z}_1 \\ \dot{Z}_2 \\ \dot{Z}_3 \\ \dot{Z}_4 \end{bmatrix} \quad (51)$$

$$\dot{Z} = AZ + BU + F \quad (52)$$

$$A = \begin{bmatrix} -\frac{2c_t}{m_b} \sin^2 \frac{\pi v t}{L} - \zeta \omega_n & -\frac{\pi^4 EI}{L^3 m_b} - \frac{2k_t}{m_b} \sin^2 \frac{\pi v t}{L} & \frac{2c_t}{m_b} \sin \frac{\pi v t}{L} & \frac{2k_t}{m_b} \sin \frac{\pi v t}{L} \\ 1 & 0 & 0 & 0 \\ \frac{c_t}{m_t} \sin \frac{\pi v t}{L} & \frac{k_t}{m_t} \sin \frac{\pi v t}{L} & -\frac{c_t}{m_t} & -\frac{k_t}{m_t} \\ 0 & 0 & 1 & 0 \end{bmatrix} \quad (53)$$

$$B = \begin{bmatrix} -\frac{2c_t}{m_b} \sin \frac{\pi v t}{L} & -\frac{2k_t}{m_b} \sin \frac{\pi v t}{L} \\ 0 & 0 \\ \frac{c_t}{m_t} & \frac{k_t}{m_t} \\ 0 & 0 \end{bmatrix} \quad (54)$$

$$F = \begin{bmatrix} 0 \\ 0 \\ -g \\ 0 \end{bmatrix} \quad (55)$$

When the vehicle is off the bridge, the bridge experiences free vibration and the vehicle's motion is independent of the bridge motion. The state-space matrices for this condition are provided as follows.

$$A = \begin{bmatrix} -\zeta \omega_n & -\frac{\pi^4 EI}{L^3 m_b} & 0 & 0 \\ 1 & 0 & 0 & 0 \\ 0 & 0 & -\frac{c_t}{m_t} & -\frac{k_t}{m_t} \\ 0 & 0 & 1 & 0 \end{bmatrix} \quad (56)$$

$$B = \begin{bmatrix} 0 & 0 \\ 0 & 0 \\ \frac{c_t}{m_t} & \frac{k_t}{m_t} \\ 0 & 0 \end{bmatrix} \quad (57)$$

$$F = \begin{bmatrix} 0 \\ 0 \\ -g \\ 0 \end{bmatrix} \quad (58)$$

Two-span Continuous

This state-space model is developed from the equations of motion for a single sprung mass traveling over a 2-span continuous beam with distributed mass and stiffness. The beam is reduced to a single degree-of-freedom by generalizing its displacement according to a shape function. A sinusoidal shape function was chosen to capture the excitement of the beam's first mode of vibration (1st bending). The beam has a uniform stiffness parameter (EI), uniform mass distribution (m_b/L), and equal span lengths (L). Mass proportional damping of the beam is included. The vehicle is reduced to a single point mass (m_t) with specified spring stiffness (k_t), viscous damping coefficient (c_t), and traveling at a specified velocity (v).

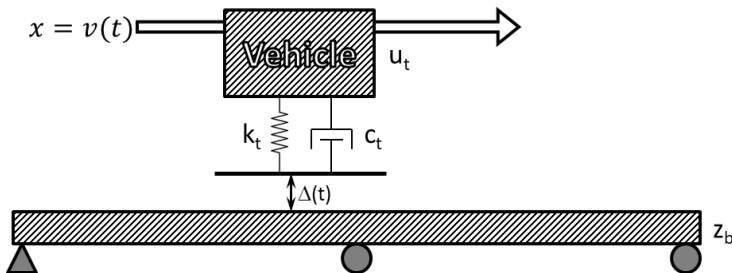


Figure 2.13.3: Diagram of 2-Span 2-DOF Model

Assumed deformation shape function

The beam is assumed to deform with a sine function (i.e. wavelength is twice the length of a single span). That function is described as follows.

$$\psi(x) = \sin\left(\frac{\pi x}{L}\right) \text{ for } 0 \leq x \leq 2L \quad (59)$$

Therefore, the deflection (u_b) and velocity (\dot{u}_b) of the beam at the vehicle's location at time (t) is related to the generalized coordinate (z_b) by the following equations.

$$u_b = z_b \sin\left(\frac{\pi v t}{L}\right) \quad (60)$$

$$\dot{u}_b = \dot{z}_b \sin\left(\frac{\pi v t}{L}\right) \quad (61)$$

Generalized mass, stiffness and damping

The generalized mass (\tilde{m}) and stiffness (\tilde{k}) properties for the beam are calculated as follows.

$$\tilde{m} = \int_0^{2L} \frac{m_b}{L} \psi(x)^2 dx = m_b \quad (62)$$

$$\tilde{k} = \int_0^{2L} EI(x) \psi''(x)^2 dx = \frac{\pi^4 EI}{L^3} \quad (63)$$

The theoretical midspan displacement (due only to bending) of a two-span continuous beam

due to a point load (P) at midspan (Δ_{theor}) is given by the following equation.

$$\Delta_{theor} = \frac{23PL^3}{1536EI} \quad (64)$$

Therefore, the error associated with the chosen shape function for a point load (P) at midspan may be calculated as follows.

$$Err = \frac{\frac{P}{\tilde{k}} - \Delta_{theor}}{\Delta_{theor}} = \frac{\left(\frac{PL^3}{\pi^4 EI} - \frac{23PL^3}{1536EI}\right)}{\frac{23PL^3}{1536EI}} = \frac{1536}{23\pi^4} - 1 = -0.3144 \quad (65)$$

The generalized damping property (\tilde{c}) is derived in the same manner as was done for the single-span model.

$$\tilde{c} = a * \tilde{m} = a * m_b = 2\zeta\omega_n m_b \quad (66)$$

Force transformation

The force applied by the vehicle mass (p_0) must also be generalized. The force is described as a function of time and position as follows:

$$p(x, t) = \begin{cases} p_0 \delta(x - vt) & 0 \leq t \leq t_d \\ 0 & t > t_d \end{cases} \quad (67)$$

Where $\delta(x - vt)$ is the Dirac delta function centered at $x = vt$, and $t_d = 2L/v$. The generalized force (\tilde{p}) is therefore calculated as follows for $0 \leq t \leq t_d$.

$$\tilde{p}(t) = \int_0^{2L} p(x, t) \psi(x) dx = \int_0^{2L} p_0 \delta(x - vt) \sin\left(\frac{\pi x}{L}\right) dx = p_0 \sin\left(\frac{\pi v t}{L}\right) \quad (68)$$

The force (p_0) applied by the vehicle is calculated based on the relative vertical motion of bridge and vehicle, including profile elevation, as shown below.

$$p_0 = k_t * (u_t - u_b - \Delta) + c_t(\dot{u}_t - \dot{u}_b - \dot{\Delta}) \quad (69)$$

Where u_t is the vertical position of the vehicle, u_b is the vertical position of the bridge at the vehicle location and Δ is the profile elevation at the vehicle location. Single dot notation indicates the first derivative (with respect to time) and therefore \dot{u}_t is the vertical velocity of the vehicle, \dot{u}_b is the vertical velocity of the bridge at the vehicle location and $\dot{\Delta}$ is the rate of change in profile elevation.

Equations of motion for when vehicle is on bridge

The equations of motion of the generalized beam and moving vehicle may therefore be composed as follows for $0 \leq t \leq t_d$.

$$\text{Vehicle DOF: } m_t \ddot{u}_t + c_t (\dot{u}_t - \dot{u}_b - \dot{\Delta}) + k_t (u_t - u_b - \Delta) + m_t g = 0 \quad (70)$$

$$\text{Beam DOF: } \tilde{m} \ddot{z}_b + \tilde{c} \dot{z}_b + \tilde{k} z_b + [k_t (u_b - u_t + \Delta) + c_t (\dot{u}_b - \dot{u}_t + \dot{\Delta})] * \sin\left(\frac{\pi v t}{L}\right) = 0 \quad (71)$$

Double-dot notation is used in the preceding equations to indicate the second derivative and therefore \ddot{u}_t is the vertical acceleration of the vehicle and \ddot{z}_b is the acceleration of the generalized bridge coordinate (z_b).

State Space

The states of this system (z_1, z_2, z_3 & z_4) may therefore be defined as follows:

$$z_1 = \dot{z}_b; z_2 = z_b; z_3 = \dot{u}_t; z_4 = u_t \quad (72)$$

The profile elevation and velocity are assigned to matrix U with elements (u_1 & u_2):

$$u_1 = \dot{\Delta}; u_2 = \Delta \quad (73)$$

The equations of motion are reorganized in terms of the defined states as follows.

$$Z = \begin{bmatrix} Z_1 \\ Z_2 \\ Z_3 \\ Z_4 \end{bmatrix}; \dot{Z} = \begin{bmatrix} \dot{Z}_1 \\ \dot{Z}_2 \\ \dot{Z}_3 \\ \dot{Z}_4 \end{bmatrix} \quad (74)$$

$$\dot{Z} = AZ + BU + F \quad (75)$$

$$A = \begin{bmatrix} -\frac{c_t}{m_b} \sin^2 \frac{\pi v t}{L} - 2\zeta\omega_n & -\frac{\pi^4 EI}{L^3 m_b} - \frac{k_t}{m_b} \sin^2 \frac{\pi v t}{L} & \frac{c_t}{m_b} \sin \frac{\pi v t}{L} & \frac{k_t}{m_b} \sin \frac{\pi v t}{L} \\ 1 & 0 & 0 & 0 \\ \frac{c_t}{m_t} \sin \frac{\pi v t}{L} & \frac{k_t}{m_t} \sin \frac{\pi v t}{L} & -\frac{c_t}{m_t} & -\frac{k_t}{m_t} \\ 0 & 0 & 1 & 0 \end{bmatrix} \quad (76)$$

$$B = \begin{bmatrix} -\frac{c_t}{m_b} \sin \frac{\pi v t}{L} & -\frac{k_t}{m_b} \sin \frac{\pi v t}{L} \\ 0 & 0 \\ \frac{c_t}{m_t} & \frac{k_t}{m_t} \\ 0 & 0 \end{bmatrix} \quad (77)$$

$$F = \begin{bmatrix} 0 \\ 0 \\ -g \\ 0 \end{bmatrix} \quad (78)$$

When the vehicle is off the bridge, the bridge experiences free vibration and the vehicle's motion is independent of the bridge motion. The state-space matrices for this condition are provided as follows.

$$A = \begin{bmatrix} -2\zeta\omega_n & -\frac{\pi^4 EI}{L^3 m_b} & 0 & 0 \\ 1 & 0 & 0 & 0 \\ 0 & 0 & -\frac{c_t}{m_t} & -\frac{k_t}{m_t} \\ 0 & 0 & 1 & 0 \end{bmatrix} \quad (79)$$

$$B = \begin{bmatrix} 0 & 0 \\ 0 & 0 \\ \frac{c_t}{m_t} & \frac{k_t}{m_t} \\ 0 & 0 \end{bmatrix} \quad (80)$$

$$F = \begin{bmatrix} 0 \\ 0 \\ -g \\ 0 \end{bmatrix} \quad (81)$$

Implementation

The first step in determining the appropriate parameters for defining the state-space model is to define a beam that can approximate bridge response due to a vehicle traveling along specified path of travel. The distributed stiffness (EI) can be approximated by first determining the stiffness of the bridge to a point load at midspan along the path of travel. This stiffness value (K_{mid}) may be determined experimentally or with a refined FE model. The appropriate EI value is subsequently calculated using the generalized stiffness evaluated for a unit load at midspan. Stiffness is assumed to be uniformly distributed (i.e. EI is constant along the length of the beam). The following equations describe that calculation for single-span and two-span models.

$$\text{Single Span: } EI = K_{mid} * \frac{2L^3}{\pi^4} \quad (82)$$

$$\text{Two-Span: } EI = K_{mid} * \frac{L^3}{\pi^4} \quad (83)$$

Once the distributed stiffness of the beam is determined, the distributed mass of the beam may be calculated such that the beam has a first-bending natural frequency (ω_n in rad/sec) equal to that of the bridge. Mass was assumed to be uniformly distributed along the length of the beam for the models presented herein. The total equivalent beam mass (m_b) may therefore be calculated with the following equation.

$$m_b = \frac{EI\pi^4}{\omega_n^2 L^3} \quad (84)$$

The vehicle is also reduced to a single degree-of-freedom based on known mass (m_v) and natural frequency (ω_v) as described for FE simulations. The suspension spring stiffness (k_v) may be calculated according to the following equation.

$$k_v = \omega_v^2 * m_v \quad (85)$$

The profile should be measured and provided in the form of sequential distance and elevation measurements. The distance values should be monotonically increasing.

With all parameter values obtained and assigned, the scenario may be simulated by stepping through each time increment, solving each “state” in-turn. This is easily accomplished programmatically with a loop. The corresponding computer code is available upon request.

While the state-space model directly computes bridge displacement, the amplification (and other response quantities) is easily computed and is the quantity reported in many of the supporting figures. The assumed shape functions are unable to accurately predict displacement due to a point load (especially in the case of two-span continuous models) as previously discussed. Furthermore, the simplified models reduce the bridge to a single beam, neglecting the change in transverse load distribution as the load changes position on the bridge. By computing the amplification (normalizing displacement responses by static deflection), the resulting errors, as well as any errors in computing equivalent stiffness and mass, are mitigated.

Therefore, structural responses (e.g. displacement) should not be interpreted directly from these simplified models. Rather these models are intended to only predict the amplification of responses.

Validation

The models previously described were implemented in MATLAB. The models were error screened by first comparing output to that from FE models of corresponding beams (with only the first mode included). These FE beam models consisted of a single beam with minimal constraints. The FE beam models were assigned parameters matching those implemented in the state-space model. Simulations were performed for which a single sprung mass traversed the beams at 720 in/sec over an artificial profile created using ISO 8608 methods ($C_{10} = 300E-6$; $w = -2$).

The bridge and vehicle models were assigned the parameters as provided in the following table. These bridge and vehicle parameters were roughly based on the case structure presented in Part 1 such that reasonably large responses would be produced. Single span and 2-span models were assigned the same parameter values.

Table 2.13.1: Beam and Sprung Mass Parameter Values for Validation Simulations

Span Length (L)	100	ft
Distributed Mass (m_b/L)	4.6	kip/ft
Distributed Stiffness (EI)	7.5×10^{12}	lb-in ²
Vehicle Mass (m_t)	100	sling
Vehicle Suspension Stiffness (k_t)	63.1655×10^3	lb/in
Vehicle Damping Ratio (ζ)	10%	

Simulations were performed with a time-step of 0.0014 sec. This time-step (Δt) was assigned based on the 1 in. spatial resolution (Δ_d) of the profile data and the vehicle speed (v) according to the following equation.

$$\Delta t = \frac{\Delta_d}{v} \quad (86)$$

This time-step size was evaluated with FE simulations. The FE simulations with the single-span beam model were performed with a time-step size of 0.0015 seconds and 0.003 seconds. The absolute difference between the midspan displacement predicted by the two simulations is

plotted as a percent of the minimum displacement (maximum downward displacement) as predicted by the simulation with 0.0015 time-step.

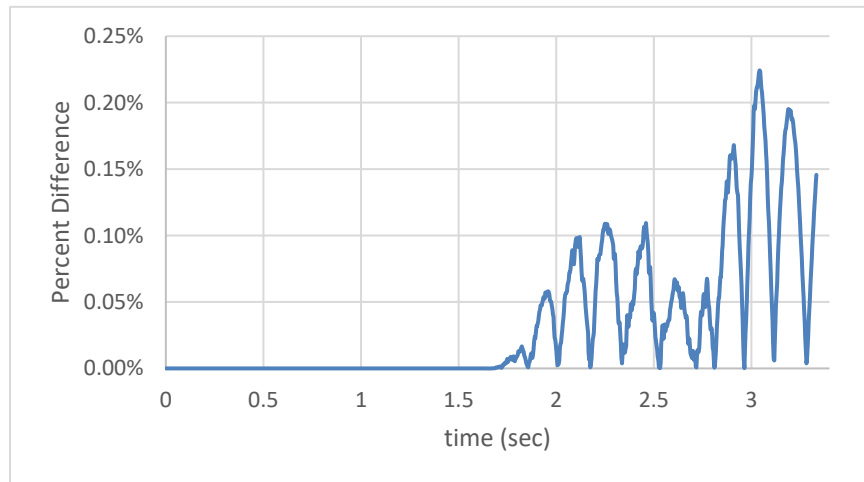


Figure 2.13.4: Difference between FEM Predicted Midspan Displacement with Varied Time-Step Size

The maximum absolute difference and mean of the absolute differences between the simulation results for the two different step sizes is summarized in the following table.

Table 2.13.2: Difference between FEM Predicted Midspan Displacement with Varied Time-Step Size

	Max Diff	Max % Diff	MAE	%MAE
FEM $\Delta t=0.0015$ vs $\Delta t=0.003$	0.001056	0.22%	0.000308	0.07%

The difference between the simulated responses illustrated in the preceding plot and table confirms that the chosen time-step size is adequately small, and the solution has converged.

Comparison of state-space model responses are compared to the responses predicted by the FE beam models in following plots. The FE model solutions included only the first mode of vibration to provide a more direct comparison with the state-space model. Some error was expected (and observed) because the state-space models are still an approximate representation of beam behavior. That error was more pronounced for models of two-span continuous beams.

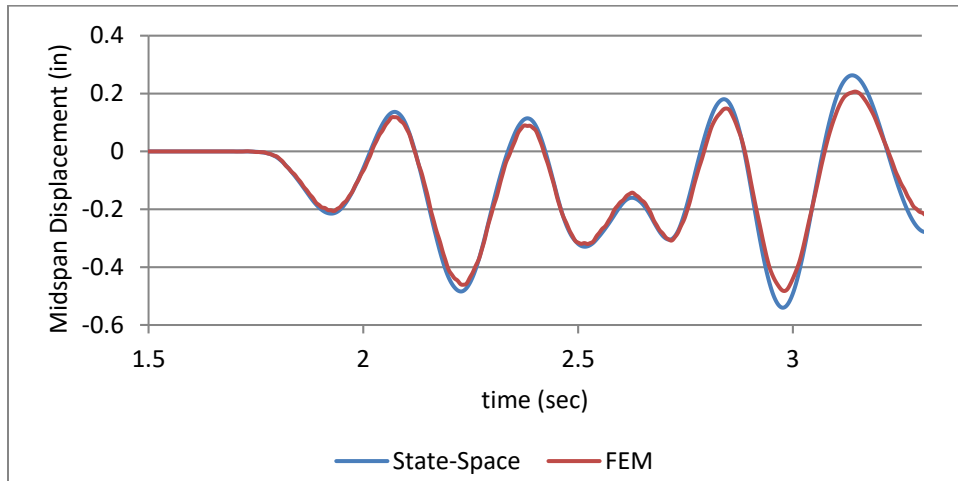


Figure 2.13.5: Comparison of Single-Span Beam Model Displacement Simulations

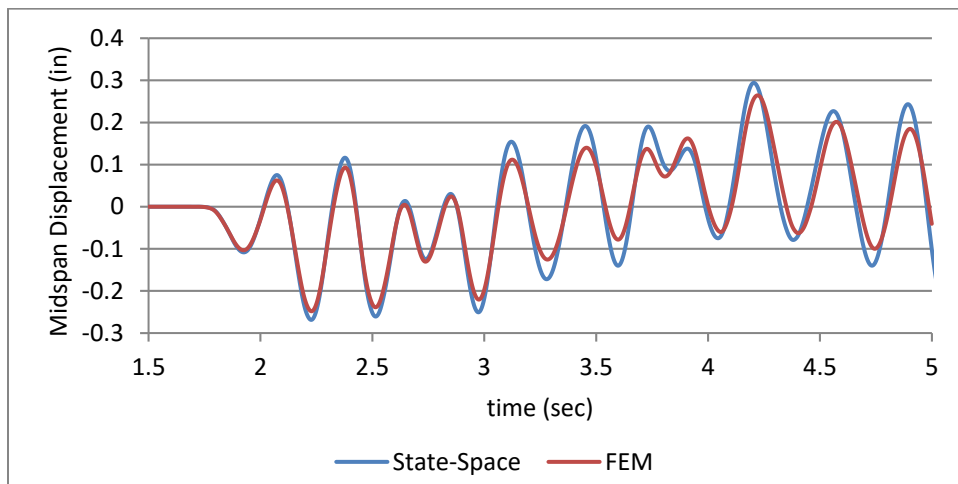


Figure 2.13.6: Comparison of 2-Span Beam Model Displacement Simulations

The errors between the state-space and FEM beam models were quantified by computing the difference between maximum displacements (downward) as well as the mean-absolute-error. These were also expressed as a percent of the maximum displacement (downward) as predicted by the FE model. Those errors are summarized in the following table.

Table 2.13.3: Differences between FEM and State-Space Displacement Predictions

	State-Space Max Disp.	FEM Max Disp.	% Diff.	MAE	%MAE
Single-Span	-0.54011	-0.47087	14.70%	0.023058	4.90%
2-Span	-0.26863	-0.24819	8.24%	0.024253	9.77%

The disagreement evident in the preceding plots and table may be contributed to the simplicity of the state-space model compared to the FE model. In reducing the beam to a single degree-of-freedom, the state-space model assumes all deformation occurs according the specified shape function. While this function is accurate for the first mode of vibration, it is less adequate at describing the deformation due to concentrated loading as presented by the moving sprung mass. This assumption also ignores contribution from other modes. Higher modes were not included in the FE simulations presented in the preceding plots to provide a more direct comparison, but they do contribute to responses, especially those modes with low frequencies.

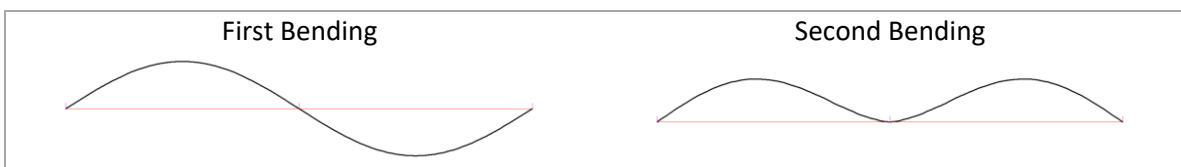


Figure 2.13.7: First Two Mode Shapes for 2-Span Continuous Beam

Due to the nature of two-span continuous bridges, the second bending mode (illustrated in the above image) is likely to occur at a frequency near to that of the first-bending mode. Thus, simulations that only consider the first mode will suffer greater inaccuracy when performed for two-span continuous bridges. The following plot compares the FE simulation of the two-span beam model with only the first mode included, and with the first five modes included.

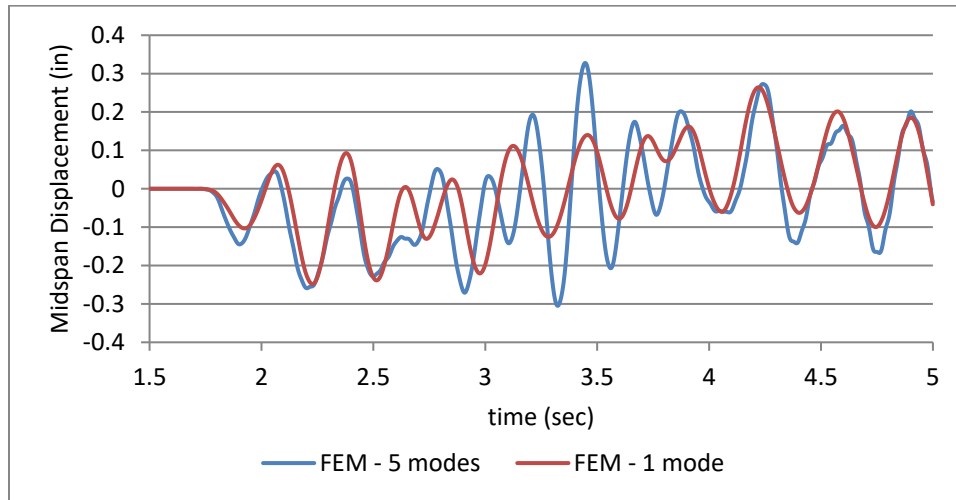


Figure 2.13.8: FEM Displacement Predictions with 1 Mode and 5 Modes for 2-span Continuous Beam

The differences between the FEM simulations with the first 5 modes included and just the first mode included were quantified by computing the difference between maximum displacements (downward) as well as the mean-absolute-error. These were also expressed as a percent of the maximum displacement (downward) as predicted by the simulation with the first 5 modes included. Those differences are summarized in the following table.

Table 2.13.4: Differences between FEM Displacement Predictions with 1 Mode and 5 Modes

1 Mode Max Disp.	5 Modes Max Disp.	% Diff.	MAE	%MAE
-0.2482	-0.3048	18.58%	0.0673	22.09%

The above plot illustrates the inadequacy of a two-span model that includes only the first mode of vibration. However, the purpose of the simplified model proposed herein is to estimate dynamic amplification rather than accurately predict displacement. The ability of the model to perform in this regard is next investigated.

Performance Assessment

It is always preferable to measure a model against ground truth values, which in this case would be the dynamic amplification as recorded on an actual structure. However, the number of sample structures that have been instrumented for the determination of dynamic amplification

and have also had their profile measured is very limited. There are simply too few samples from real structures to adequately assess the performance of the state-space models. As a result, the performance of the state-space models was evaluated by comparing the dynamic amplification predicted by the model to that predicted by a 3D FE model.

Bridge Models

A total of six test-case models were created with varied geometry and stiffness while remaining representative of real structures. This was accomplished by basing the models on existing bridges. These bridges have varying length, width and skew. Furthermore, the dynamics of the bridges had been determined from previous field tests and have first natural frequencies ranging from 2 to 10 Hz. A single-span model and a two-span continuous model were created based on each of the three case structures. The plate eccentric-beam model type was employed for these FE models as described in Chapter 12 and in Part 1.

Road profiles were assigned to a line that defined the vehicle path of travel. The deck width of some models was great enough to accommodate multiple lanes and therefore multiple paths of travel were defined. Each vehicle path included an approach length of 320 feet. This approach length is more than sufficient to account for the vehicle's initial conditions (demonstrated in Chapter 15).

Linear transient dynamic analyses of the moving mass were performed using LUSAS' IMDPlus. This product option features several Interactive Modal Dynamics techniques; the relevant portion is described below.

An IMDPlus analysis uses conventional eigenvalue analyses to obtain the undamped modes of vibration for a structure over the frequency range of interest. The modal response in the form of frequencies, participation factors

and eigenvectors, together with the moving mass vehicle loads, enable IMDPlus to compute the dynamic response for each mode of vibration. The assumption of linear structural behavior allows the IMDPlus facility to utilize linear superposition methods to calculate the total response of the structure from each of the contributing frequencies.

The simulation assumptions and limitations inherent to this solver are as follows.

- The system is linear in terms of geometry, material properties and boundary conditions.
- There is no cross-coupling of modes caused by the damping matrix. This is reasonable for all but the most highly damped structures or applications.
- Critical Damping ratios of 100% or more are not permitted due to the solution of the time domain response of the structure using either the Hilber–Hughes–Taylor (HHT) method or Duhamel’s Integral.
- There is no loss of contact between the unsprung masses (wheels) of the spring-mass systems and the structure at any time during the analysis
- Only vertical motion of the spring-mass systems is considered in a moving mass analysis.
- Mass of the spring-mass systems are not included in the eigenvalue solution

140ft. Bridge

The 140 ft span models were based on the geometry of the bridge presented in Part 1—a multi-girder highway bridge with steel plate girders. Simple beam elements were used in place of the cross-frame diaphragms that existed on the actual bridge. These beam elements were assigned equivalent stiffness as detailed in Part 1.

The first natural frequency of the models was 2.08 Hz. The path of travel was defined over the first interior girder. The midspan displacements of that girder due to twin point loads totaling 1

lb., spaced 6' apart at midspan on the vehicle path are given below. These values were used to compute equivalent EI values for implementing the state-space models as described previously.

Table 2.13.5: Midspan Stiffness Values for 140 ft. Bridge Models

1-span			2-span		
	in/lb	lb/in		in/lb	lb/in
Path 1, Girder 2	-4.49887E-6	222278	Path 1, Girder 2	-4.04871E-6	246992

100ft. Bridge

This set of bridges was created based on a 2-lane bridge in Maryland with structure number [80053010](#): a continuous bridge with two spans with a length of 100 feet and with (5) AASHTO Type IV girders spaced at 99 in. Cast-in-place concrete diaphragms are located at the center of each span and at the ends of the spans. They extended to the bottom of the girder webs and were modeled with a rectangular section (37"x9"). The deck is 9.5" thick; no sidewalks are present; 4' tall by 2' wide concrete barriers are placed along either side.

The first natural frequency of the models is 3.99 Hz. Three paths were defined on this model for simulations. Their locations are at 4', 10.5' and 16.5' from the exterior girder. The midspan displacements of the girder closest to each path due to twin point loads totaling 1 lb., spaced 6' apart at midspan on the vehicle path are given below.

Table 2.13.6: Midspan Stiffness Values for 100 ft. Bridge Models

1-span			2-span		
	in/lb	lb/in		in/lb	lb/in
Path 1, Girder 1	-2.00994E-6	497527	Path 1, Girder 2	-1.49518E-6	668815
Path 2, Girder 2	-1.56329E-6	639676	Path 2, Girder 3	-1.21648E-6	822043
Path 3, Girder 3	-1.49866E-6	667262	Path 3, Girder 3	-1.19393E-6	837570

40 ft. Span

This set of bridges was based on a 2-span simply supported bridge located in Maryland with structure number: [70042010](#). The bridge features a 15-degree skew, (7) wide-flange (rolled) steel girders (W30X108) spaced at 84 in., channel diaphragms (15C33.9) and concrete barriers modeled with a rectangular section (32"x19"). The deck is 8.5" thick and the barriers are 32" tall

by 19" wide; there is no sidewalk. The skew of the models was increased to 16 degrees for ease of modeling.

The first natural frequency of the models is 9.95 Hz. The simulations were performed with 10 global modes included. Path 1 was located over the first interior girder and path 2 was located 16' (transversely) from the exterior girder. The midspan displacements of the girder closest to each path due to twin point loads totaling 1 lb., spaced 6' apart at midspan on the vehicle path are given below.

Table 2.13.7: Midspan Stiffness Values for 40 ft. Bridge Models

1-span			2-span		
	in/lb	lb/in		in/lb	lb/in
Path 1, Girder 2	-1.70148E-6	587723	Path 1, Girder 2	-1.38695E-6	721006
Path 2, Girder 3	-1.90733E-6	524293	Path 2, Girder 3	-1.51232E-6	661235

State-Space Parameters

The 2-DOF state-space models were implemented in the manner described in earlier in this chapter. The model input parameters included:

- Span length
- Number of Spans
- Bridge Mass
- EI
- Bridge Damping Ratio
- Vehicle Mass
- Vehicle Spring Stiffness
- Vehicle Damping Coefficient
- Vehicle Velocity

The bridge related parameters were defined that corresponded to each FE model and vehicle path, totaling 12 cases. The EI value was calculated based on the midspan stiffness values determined from the FE models (equations (82) & (83)). The mass values were then calculated to achieve a natural frequency that matched the FE models (equation (84)). A structural damping ratio of 1% was assigned for all models. The state-space beam model parameters are summarized in the following table.

Table 2.13.8: State-Space Beam Parameters

	Span Length (ft)	Number of Spans	1st Nat. Freq. (Hz)	Path	K_{mid} (lb/in)	EI (lb-in ²)	Mass per Span (slinch)
1	40	1	9.95	1	587723	1.354E+12	305.16
2				2	524293	1.208E+12	272.22
3		2	9.98	1	721006	8.186E+11	183.37
4				2	661235	7.507E+11	168.16
5	100	1	3.99	1	497527	1.791E+13	1606.46
6				2	639676	2.303E+13	2065.44
7				3	667262	2.402E+13	2154.51
8		2	3.99	1	668815	1.186E+13	1064.14
9				2	822043	1.458E+13	1307.94
10				3	837570	1.486E+13	1332.65
11	140	1	2.08	1	222278	2.196E+13	2641.00
12		2	2.08	1	246992	1.202E+13	1446.09

The vehicle parameter values matched those assigned in the FE models.

Vehicle Models

For each model, a corresponding vehicle model was created with a natural frequency just slightly above the first natural frequency of the bridge. Vehicle models consisted of a single sprung mass with viscous damping (10%). The following table details the parameters for each vehicle model.

Table 2.13.9: SDOF Vehicle Model Parameters

	40 ft span	100 ft span	140 ft span	
Mass	200.00	200.00	200.00	sinch
Spring Stiffness	8.7929E+05	1.6150E+05	4.9846E+04	lb/in
Damping Coefficient	2652.23 (10%)	1136.67 (10%)	631.48 (10%)	lb-s/in
Damped Natural Frequency	10.5	4.5	2.5	Hz

A vehicle model was also created that was used in analyses across all models. This vehicle model was a single sprung mass with a natural frequency of 2.8 Hz. The parameters were as listed below.

Table 2.13.10: 2.8 Hz SDOF Vehicle Model Parameters

Mass	200	sinch
Spring Stiffness	61902.2	lb/in
Damping Coefficient	1407.43 (20%)	lb-s/in

Profiles

A total of 15 profiles were evaluated. Three of the profiles were obtained from the profiles recorded from the case study bridge. Another twelve were artificial and generated using the methods defined by the ISO 8608 standards. This standard defines a roughness metric, but also describes the process whereby the profile is defined by frequency content and is generated through the summation of sine functions with amplitudes set according to PSD parameters. These parameters, defined by the standard, include a waviness value (w) and the amplitude of the PSD function at a spatial wavelength equal to 10 meters (C_{10}). The PSD amplitude of each frequency band is therefore assigned according to the following equation.

$$G_d = C_{10} * (10n)^{-w} \quad (87)$$

The profiles were created using the following parameter set:

Table 2.13.11: Profile Parameters for Performance Assessment Study

Waviness	{2, 3, 4}
$C_{10} (*10^{-6})$	{300, 600}

Full factorial sampling of the above parameter sets yields 6 profiles, however, each profile generation was performed twice with different phase angles (reseeded random number

generator for random uniform distribution). Therefore, a total of 15 test case profiles are examined (3 real profiles, 12 artificially generated). Each profile was created with a length such that it could fully cover the longest vehicle path, including approach. Since the longest test-case bridge was 280 feet long with a 320-foot long approach, a minimum profile length of 600 feet was required. The test-case profiles were therefore created with a total length of 650 feet.

Simulation Decisions

LUSAS FE

The simulation process consisted of following steps.

1. Eigenvalue analysis to obtain undamped natural modes of vibration
2. Incremental unit load analysis along vehicle path of travel
3. Calculation of the equivalent modal forces for each of these distinct locations
4. Definition of moving-mass solver parameters
5. Selection of desired response quantities
6. Moving mass analysis

The decisions made in these steps are as follows.

Table 2.13.12: Moving Mass Simulation Decisions

Decision	Selection	Units	Step
Number of modes to solve for/include	15		1, 4
Incremental distance along load-path	6	inches	2
Time integration scheme	Hilber Hughes Taylor (HHT)		4
Profile interpolation method	Linear		4
Structural damping	1%		4
Vehicle speed	720	in/sec	4
Solution time-step	0.0015	sec	4

Vertical displacement of midspan nodes was selected for analysis output. The amplification for any given run is then computed according to the following equation.

$$DAF = \delta_{max}/\delta_{static} \quad (88)$$

Where δ_{max} is the maximum downward deflection and δ_{static} is the maximum static deflection reported when the moving mass is analyzed at 5 in/sec.

State-Space

The appropriate parameters (as described in a preceding section) were assigned to the state-space model using custom MATLAB scripts and functions. The scripts subsequently looped through all the cases, performing simulation for each. Beam and sprung mass position and velocity time histories were output as well as contact force. The displacement amplification was computed according to the following equation.

$$DAF = \delta_{max}/\delta_{static} \quad (89)$$

Where δ_{max} is the minimum (maximum downward) displacement of the beam DOF over the time period for which the vehicle was on the span. For 2-span models, the displacement of the second span was reported as the minimum displacement of the beam DOF over the time period for which the vehicle was on the second span multiplied by a factor of -1, which is consistent with the assumed shape function. The static displacement (δ_{static}) is the maximum static deflection according to the generalized stiffness parameter and calculated with the following equations.

$$\text{Single Span: } \delta_{static} = \frac{2P_{veh}L^3}{\pi^2 EI} \quad (90)$$

$$\text{Two-Span: } \delta_{static} = \frac{P_{veh}L^3}{\pi^4 EI} \quad (91)$$

Where P_{veh} is the static weight of the vehicle.

The IRI of each profile over each span was also computed for comparison. These computations were also performed with a state-space model based on the golden-car model and benchmarked against FHWA's profile analysis program: ProVAL.

Results

The four parameter categories (i.e. bridge, path of travel, vehicle, and profile) were sampled to obtain a total of 239 different scenarios. Each scenario was simulated with a detailed 3D FE model and with a state-space model. The predicted amplification is compared in the plots below.

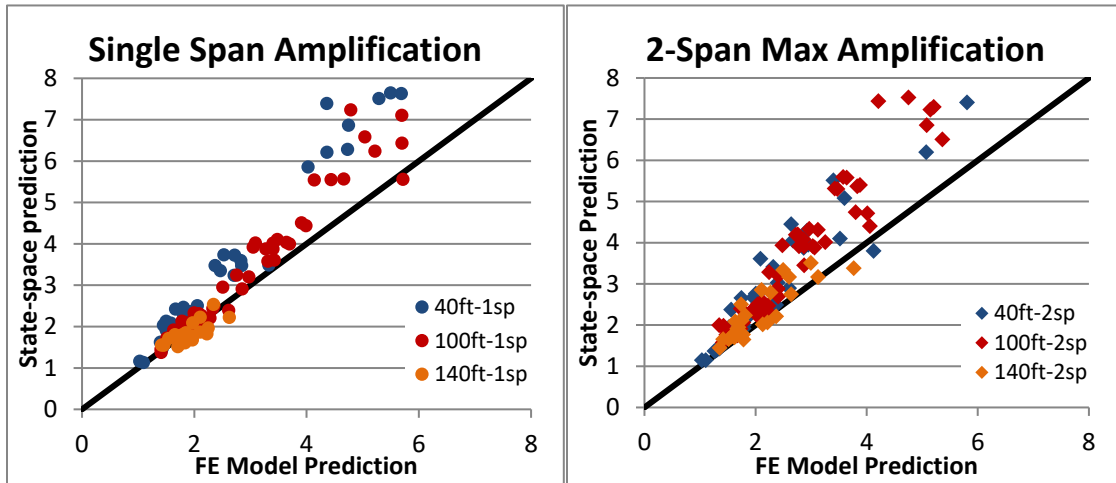


Figure 2.13.9: Performance of 2DOF State-Space Models for Predicting Dynamic Amplification

The R^2 value (coefficient of determination) for single-span state-space model predictions is 0.948, while that for the two-span state space model predictions is 0.913. It can be observed from the previous plots that the state-space models are more conservative for scenarios that result in high levels of amplification, but more accurate at lower amplification levels. This is because the simplified state-space model overestimates the dynamic response due to the manner in which loading and deformation is generalized by the shape functions used in the simplified state-space models. Furthermore, in reducing the width of the bridge to an equivalent beam, the simplified model underestimates the mass that resists the force imposed by the vehicle, resulting in a model that is more easily excited by the moving vehicle mass and thus overestimates dynamic response of the bridge.

It is not expected that dynamic amplification will reach such high values on real structures since the values were obtained from simulations with unrealistically rough artificial profiles and assumed the vehicle tires did not lose contact with the roadway surface. While this is not representative of reality, these simulations were intended to examine the performance of the simplified models compared to 3D FE models. It was therefore important to compare the model types across a wide range of response levels. The suitability of a 3D element-level model for predicting dynamic amplification is demonstrated in Part 1.

Therefore, while the simulated responses are not representative of the range of dynamic amplification that would be expected on real structures, they still serve to demonstrate the performance of the state-space models.

Vehicle Dynamics and Bridge Vulnerability

In the following plot the dynamic amplification data points are grouped by the type of vehicle used in the analysis where the “matching vehicle” corresponds to the vehicles that have natural frequencies close to the bridge’s first natural frequency and “non-matching vehicle” corresponds to the 2.8 Hz vehicle. The data points associated with the 140 ft bridges have been omitted since the 2.8 Hz vehicle’s natural frequency is close to the natural frequencies (2.08 Hz) of those bridges.

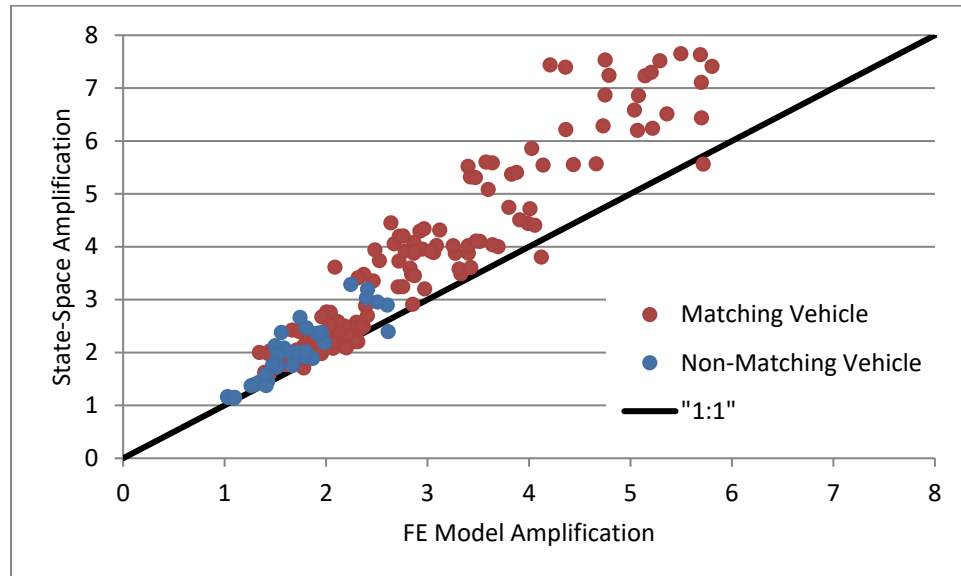


Figure 2.13.10: Performance of 2DOF State-Space Model Grouped by Vehicle

As can be seen, the bridges with higher first natural frequencies fail to be excited by the non-matching (2.8 Hz) vehicle. Furthermore, it is postulated that fully loaded trucks most often have first natural frequencies less than 4 Hz, and thus bridges with high first natural frequencies have reduced vulnerability to dynamic amplification.

Conclusions

This chapter introduced two simplified models (single-span and 2-span continuous) that reduce the bridge to a single degree of freedom with generalized coordinates according to shape functions that describe the first mode of bending for a beam. The performance of these simplified models was assessed by comparing predicted amplification factors to those predicted by 3D FE models. The simplified models were found to perform relatively well and yield conservative estimates of amplification factors.

Chapter 14: IRI & Other Vehicle-Only Models

There are several methods already widely used to assess the roughness of roadway profiles. The International Roughness Index (IRI) is the most complex and simulates a specific vehicle (golden quarter-car) traveling over the profile. Other metrics ignore the vehicle and deal only with the profile data. The ISO 8608 parameters, for example, describe the spatial frequency content of the profile. However, all of these roughness metrics fail to consider the bridge or the position of the profile. Studies were performed to examine if these metrics had any ability to predict dynamic amplification.

ISO 8608 parameters describe the spatial frequency content of the profile. Studies presented in Chapter 15 show that the spatial frequency of the profile content does influence dynamic amplification. However, the ISO parameters ignore any transient features and ignore the phase angle distribution and therefore are inadequate for predicting dynamic amplification (also demonstrated in Chapter 15). The inadequacy is further demonstrated by the supplied correlation plot.

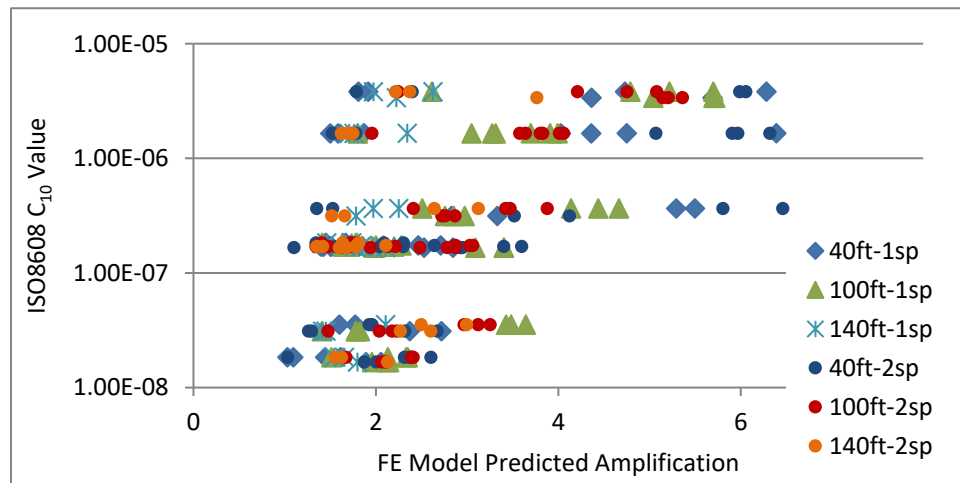


Figure 2.14.1: Performance on ISO 8608 Parameters for Predicting Dynamic Amplification

The IRI includes the vehicle in its model and may be expected to demonstrate better ability to predict dynamic amplification. However, the following correlation plot shows that the IRI cannot reliably predict dynamic amplification. The plot also reveals that while profiles with high IRI may not always result in high dynamic amplification, bridges with high dynamic amplification have high profile IRI values. This provides further evidence to encourage and mandate a smooth deck surface.

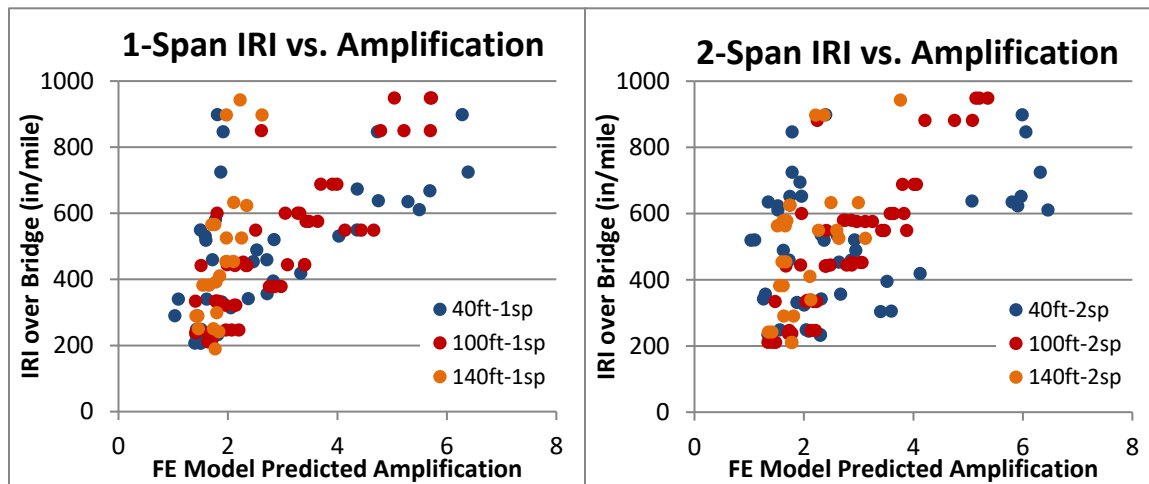


Figure 2.14.2: Performance of IRI for Predicting Dynamic Amplification

Another simple model (quarter-car model) was assessed that included representation of the vehicle but ignored bridge behavior. Position of the profile on the bridge was included by applying a half-sine window to the vehicle response over the time period for which the vehicle is on the bridge. The maximum of the windowed contact force is reported as a factor of the vehicle self-weight. This contact-force amplification metric is compared to FE predictions in the plot below. The metric exhibited some correlation with dynamic amplification, but the correlation coefficient was not consistent between bridges and therefore is not recommended for any amplification predictions.

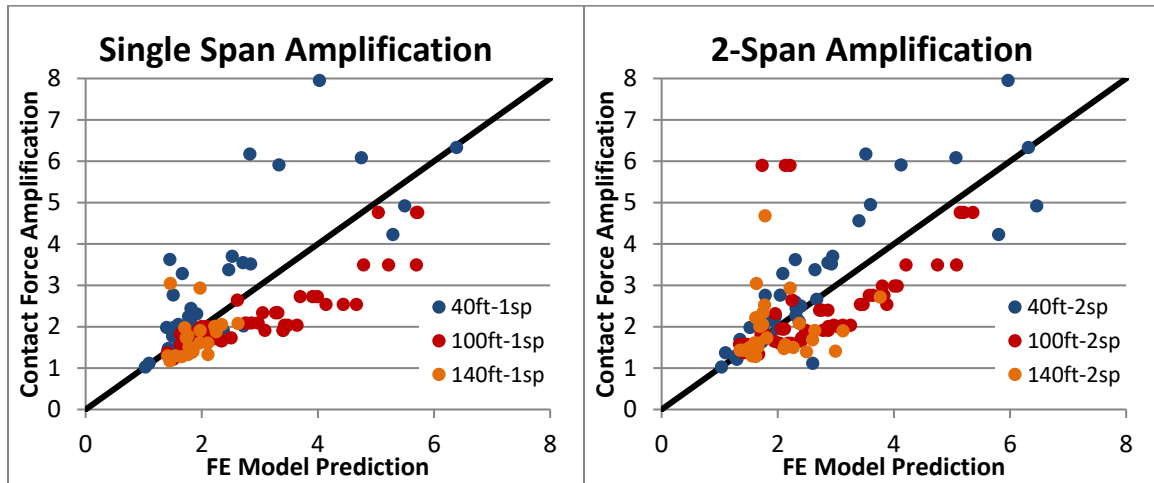


Figure 2.14.3: Performance of Quarter-Car Vehicle Model for Predicting Dynamic Amplification

Conclusions

This chapter examined the performance of roughness parameters and simplified vehicles models for predicting dynamic amplification. Because these methods include no consideration of the bridge, they ultimately fail to reliably predict dynamic amplification. It can also be concluded that bridge roadway profiles with low IRI are likely to experience low levels of dynamic amplification.

Chapter 15: VBI Mechanisms and Parameters

In several of the simulation studies described in this section the simplified 2-DOF state-space model was employed. This model type was used when appropriate due to the minimal computing power required, permitting a large number of simulations to be automated and performed in a relatively short amount of time. This model (state-space) is described in detail in Chapter 13.

The objectives of the efforts described in this chapter were to identify and characterize the influence of bridge and vehicle mechanisms and parameters.

Bridge and vehicle decoupled

In the interest of further understanding the degree to which the vehicle and bridge interact, the vehicle motion is decoupled from the bridge. Therefore, the contact force is only computed as a function of vehicle motion and profile elevation. This method neglects bridge motion and therefore represents the contact force for a completely rigid bridge. As a result, this method's accuracy will suffer with increased bridge flexibility and vehicle mass (i.e. as bridge deformation increases).

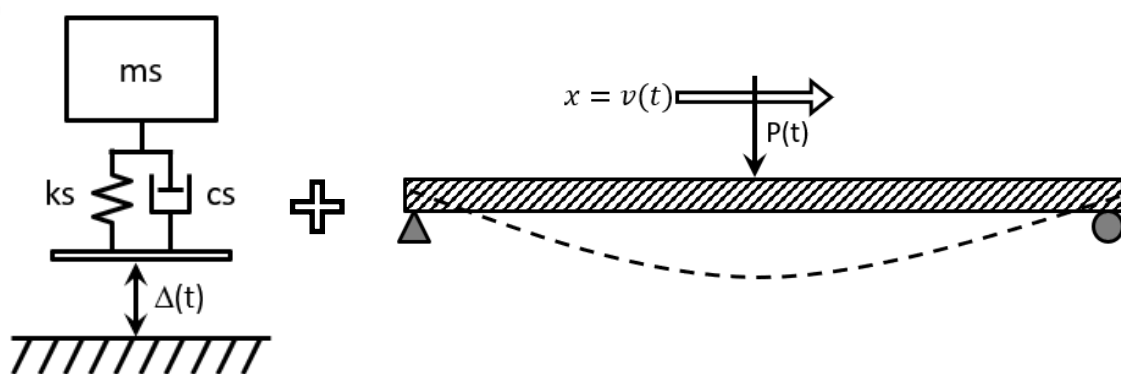


Figure 2.15.1: Diagram of Decoupled Model

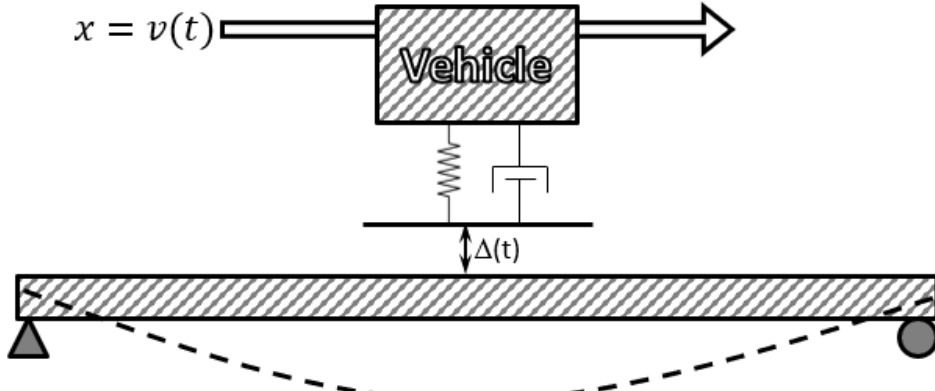


Figure 2.15.2: Diagram of Coupled 2-DOF Model

The simplified 2-DOF state-space model presented in Chapter 13 was altered to decouple the beam degree of freedom from the vehicle degree of freedom. The force (p_0) applied by the vehicle is calculated based on the vertical motion of the vehicle, including profile elevation, as shown below.

$$p_0 = k_t * (u_t - \Delta) + c_t(\dot{u}_t - \dot{\Delta}) \quad (92)$$

Where u_t is the vertical position of the vehicle and Δ is the profile elevation at the vehicle location. Single dot notation indicates the first derivative and therefore \dot{u}_t is the vertical velocity of the vehicle and $\dot{\Delta}$ is the rate of change in profile elevation.

Equations of motion when the vehicle is on the bridge

The equations of motion of the generalized beam and moving vehicle may therefore be composed as follows for $0 \leq t \leq t_d$.

$$\text{Vehicle DOF: } m_t \ddot{u}_t + c_t (\dot{u}_t - \dot{\Delta}) + k_t (u_t - \Delta) + m_t g = 0 \quad (93)$$

$$\text{Beam DOF: } \tilde{m} \ddot{z}_b + \tilde{c} \dot{z}_b + \tilde{k} z_b + [k_t (-u_t + \Delta) + c_t (-\dot{u}_t + \dot{\Delta})] * \sin\left(\frac{\pi v t}{L}\right) = 0 \quad (94)$$

Double-dot notation is used in the preceding equations to indicate the second derivative (with respect to time) and therefore \ddot{u}_t is the vertical acceleration of the vehicle and \ddot{z}_b is the acceleration of the generalized bridge coordinate (z_b).

State Space

The equations of motion are reorganized in terms of the defined states as follows.

$$Z = \begin{bmatrix} Z_1 \\ Z_2 \\ Z_3 \\ Z_4 \end{bmatrix}; \dot{Z} = \begin{bmatrix} \dot{Z}_1 \\ \dot{Z}_2 \\ \dot{Z}_3 \\ \dot{Z}_4 \end{bmatrix} \quad (95)$$

$$\dot{Z} = AZ + BU + F \quad (96)$$

$$A = \begin{bmatrix} -\zeta\omega_n & -\frac{\pi^4 EI}{L^3 m_b} & \frac{2c_t}{m_b} \sin \frac{\pi vt}{L} & \frac{2k_t}{m_b} \sin \frac{\pi vt}{L} \\ 1 & 0 & 0 & 0 \\ 0 & 0 & -\frac{c_t}{m_t} & -\frac{k_t}{m_t} \\ 0 & 0 & 1 & 0 \end{bmatrix} \quad (97)$$

$$B = \begin{bmatrix} -\frac{2c_t}{m_b} \sin \frac{\pi vt}{L} & -\frac{2k_t}{m_b} \sin \frac{\pi vt}{L} \\ 0 & 0 \\ \frac{c_t}{m_t} & \frac{k_t}{m_t} \\ 0 & 0 \end{bmatrix} \quad (98)$$

$$F = \begin{bmatrix} 0 \\ 0 \\ -g \\ 0 \end{bmatrix} \quad (99)$$

The state-space matrices for when the vehicle is not on the bridge are the same as presented for the coupled state-space model (Chapter 13).

Coupled and Decoupled Models Compared

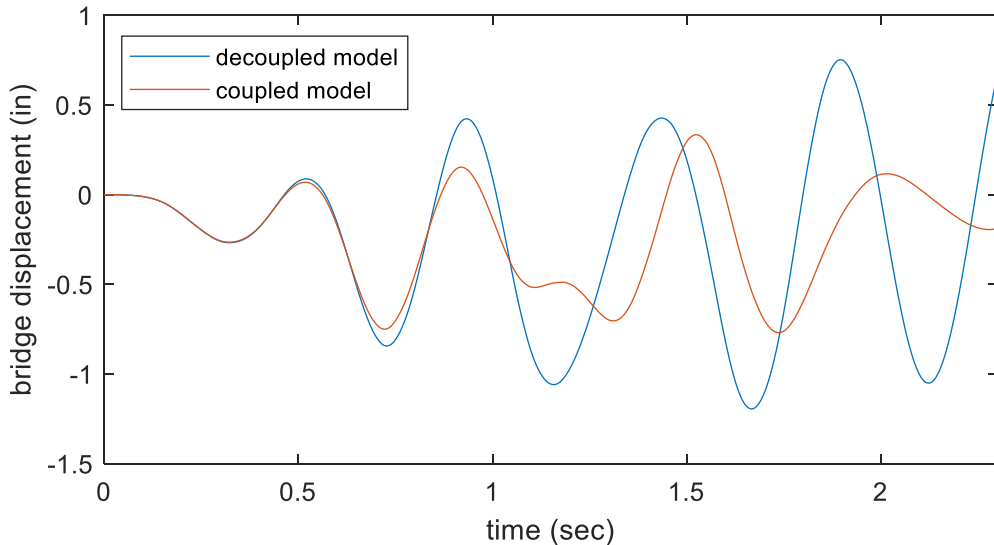
The coupled and decoupled models were compared by performing simulations with each using the same beam and vehicle parameters as summarized in the following table.

Table 2.15.1: Coupled and Decoupled Model Parameters

Span Length (L)	140	ft
Distributed Mass (m_b/L)	7283.3	lb/ft
Distributed Stiffness (EI)	2.196E+13	lb-in ²
Vehicle Mass (m_t)	200	sling
Vehicle Suspension Stiffness (k_t)	4.935E+04	lb/in
Vehicle Damping Ratio (ζ)	10%	

An artificial profile was created according to ISO 8608 standards with parameters that resulted in a very rough bridge ($C_{10} = 600E-6$; $w = -2$). The vehicle speed was set to 720 in/sec (65.8 kmh). These parameter values were chosen as they were known to result in large dynamic amplification and thus would provide good demonstration of the differences between the two models.

The following plot compares the bridge response from this decoupled analysis to that from the coupled vehicle-bridge model.

**Figure 2.15.3: Displacement Predicted by Coupled Model and Decoupled Model**

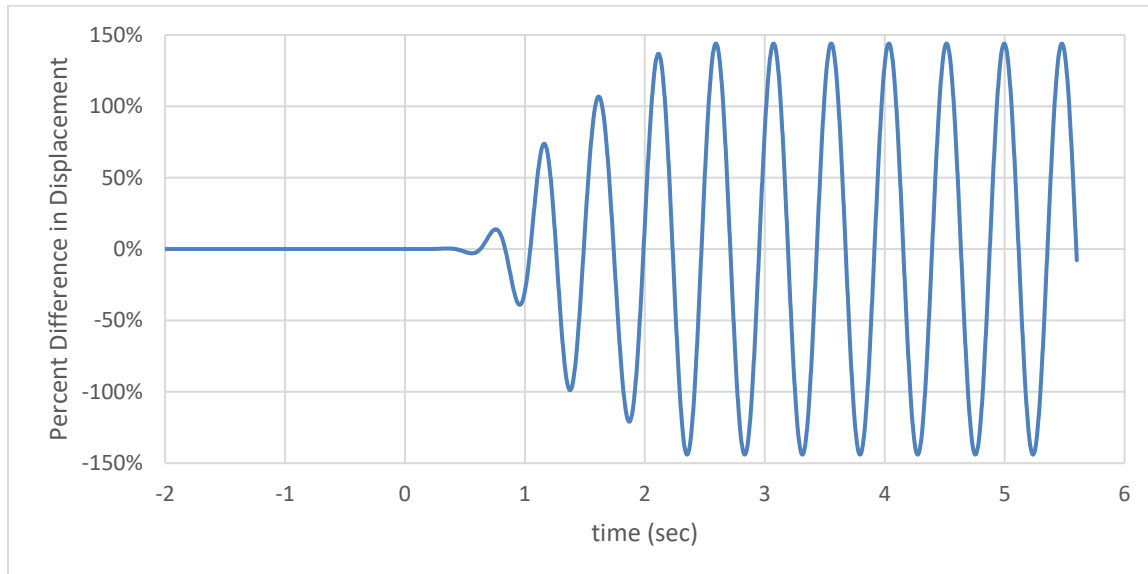


Figure 2.15.4: Difference between Displacement from Coupled Model and Uncoupled Model as a Percent of Maximum

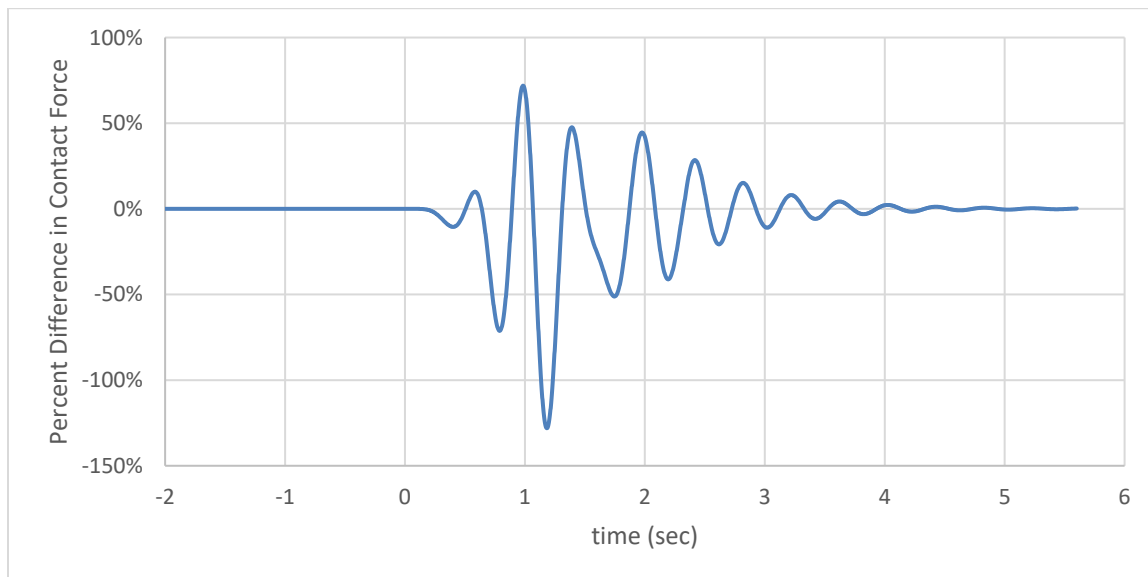


Figure 2.15.5: Difference between Contact Force from Coupled Model and Uncoupled Model as a Percent of Vehicle Weight

The displacement difference plot above was computed by dividing the difference by the maximum displacement predicted by the coupled model. The contact force difference plot above was computed by dividing the difference by the static weight of the vehicle. The difference between the maximum predicted displacements and the mean-absolute-error

between the displacements predicted by the coupled and decoupled models are summarized in the following table.

Table 2.15.2: Difference between Predicted Midspan Displacement for Coupled and Decoupled Models

Max Coupled Model (in)	Max Decoupled Model (in)	% Diff.	MAE	%MAE
-0.7689	-1.1944	55.34%	0.2793	36.33%

Despite the simplicity of the model used to obtain the above results, it is still effective at modelling the exchange of energy between the two systems. As can be seen, decoupling the bridge and vehicle in simulations reduces the accuracy of the analysis and tends to overestimate the bridge response, especially at higher levels of amplification. This is because the uncoupled model fails to consider the influence of bridge motion on the vehicle contact force.

The roadway profile may be thought of as having a thickness equal to the difference between the roadway surface elevation and the mean surface elevation. When that profile is on a rigid roadway, the entire thickness imposed by the profile must be accommodated by the vehicle (i.e. only the vehicle can displace vertically). However, when that the profile is on a bridge, a portion of that imposed thickness is accommodated by the bridge, as it is accelerated by the resulting force. Therefore, the total displacement imposed on the vehicle suspension is reduced, thereby reducing the contact force.

In the case of the decoupled model, the contact force is overestimated because the roadway is assumed to be rigid and the reduction neglected. It is therefore recommended that any simulation of bridges under vehicle crossings include the interaction of the two systems if accurate prediction of bridge responses is desired.

Approach Profile

The vehicle model used in the previous study (10% damping) was again utilized to examine how long of an approach length was necessary when performing simulations of vehicle-bridge interaction. This question can be answered by determining the time required for profile induced motion to damp out.

The maximum displacement experienced by the vehicle in the decoupled model for the simulations performed in the previous section was taken as initial conditions for an additional simulation with the same vehicle model. The vehicle was allowed to free vibrate, essentially simulating a “pull-release”. The resulting contact force is plotted below as a fraction of the static vehicle weight (contact force amplification).

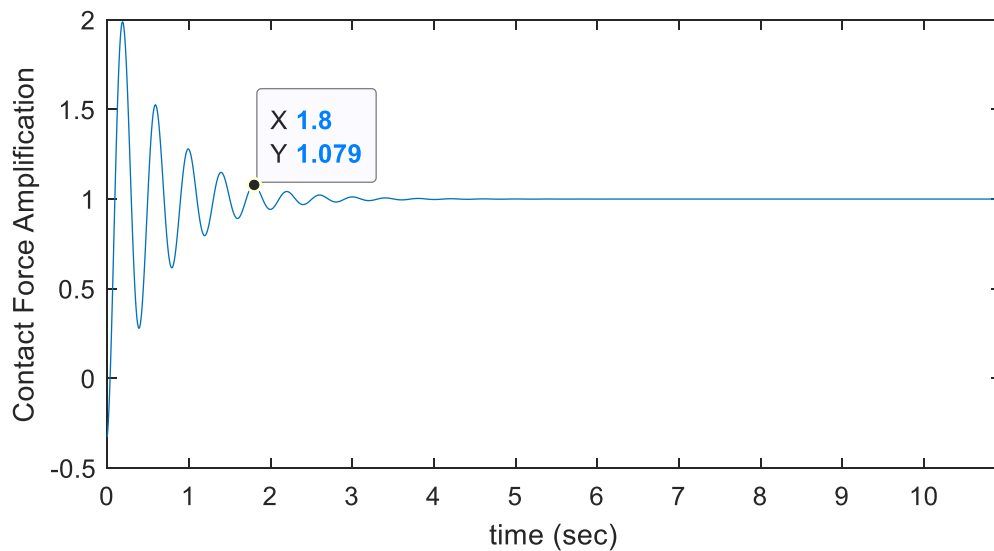


Figure 2.15.6: Free Decay of Vehicle Contact Force

After 1.8 seconds the peak amplification falls below 10% amplification. At highway speeds of 75 mph (120 kmh) this 1.8 seconds requires 200 feet (60 m) of roadway. While it is unlikely that these extreme conditions (due to the roughness of the profile used in simulations) would be

present on real life bridges, this length provides a conservative upper bound for approach roadway length to be used in simulations with measured profiles.

Influential System Parameters

Many studies on vehicle-bridge interaction will examine the role of parameters separately, and it was the original intention to organize this study in a similar manner. However, as it will soon be made clear, the parameters that effect VBI are interdependent. The following section therefore seeks to demonstrate and characterize the interdependency by first examining roadway profile which the case study showed to be critical to VBI and dynamic amplification.

A given profile is composed of elevation changes over the length of the roadway. This surface may be approximated by a summation of harmonic functions, and thus spectral analysis may be performed in much the same way as was done for acceleration data. The profile can therefore be described by its spatial frequency (cycles per unit distance) content. When a vehicle travels over a harmonic profile, the elevation change experienced at the vehicle's location is harmonic with a frequency determined by the velocity of the vehicle. A profile with a given spatial frequency will therefore induce a force that acts on the vehicle with a frequency equal to the product of the spatial frequency and vehicle velocity. Therefore, the effect of profile is dependent on the velocity of the vehicle.

Several simulations with a 3D FE model ([140ft](#); single-span) were performed for a sinusoidal profile with 30-foot wavelength and $\frac{1}{2}$ in. amplitude. The bridge model had the first and second natural frequencies between 2.2 and 2.5 Hz, while the first natural frequency of the vehicle model was 2.8 Hz. The plot below shows the peak vehicle and bridge response at different vehicle speeds and the resulting forcing frequencies. It is no surprise that the peak responses occur at speeds that induce a forcing frequency that matches their respective natural frequency.

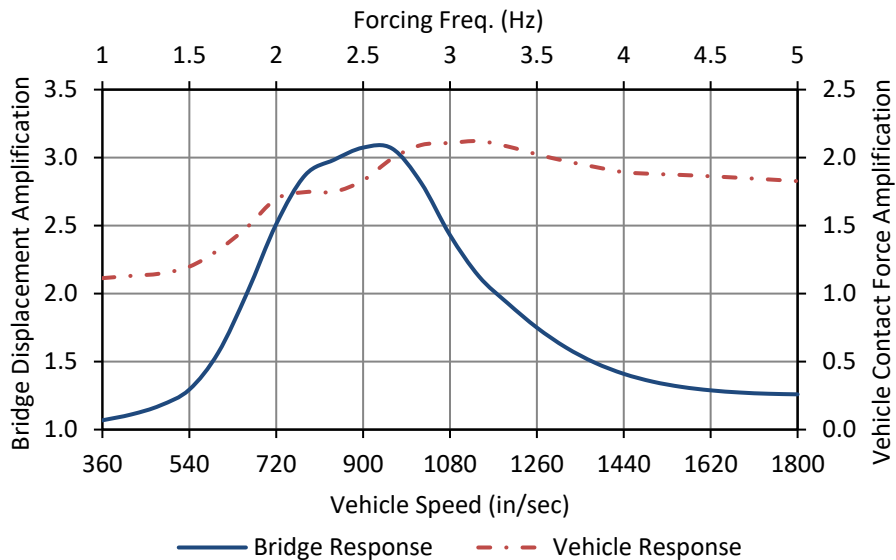


Figure 2.15.7: Effect of Vehicle Forcing Frequency on Bridge Displacement and Vehicle Contact Force

The bridge displacement amplification was calculated by dividing the maximum midspan displacement by the static bridge displacement. The vehicle contact force amplification was calculated by dividing the maximum contact force by the vehicle's static weight.

Multi-dimensional parametric study

Additional simulations were performed with the simplified state-space model. Vehicle stiffness was varied to produce vehicle models with natural frequencies ranging from 2 to 5 Hz. Bridge stiffness was also varied to produce bridge models with natural frequencies of the same range. Simulations were performed with the same harmonic profile with a wavelength of 30 ft. Vehicle speeds ranged from 540 to 2400 in/sec (10-136 mph) to produce forcing frequencies between 1.5 and 6.7 Hz.

Table 2.15.3: Bridge Attributes for Parametric Study

	Bridge 1	Bridge 2	Bridge 3	Bridge 4	
Span Length	100	100	100	100	ft
Mass (total)	2000	2000	2000	2000	s-linch
EI	5.603E+12	1.261E+13	2.241E+13	3.502E+13	lb-in ²
Damping Ratio	1.0%	1.0%	1.0%	1.0%	
1 st Nat. Freq.	2	3	4	5	Hz

Table 2.15.4: Vehicle Attributes for Parametric Study

	Truck 1	Truck 2	Truck 3	Truck 4	
Mass	200	200	200	200	s/inch
spring k	31582.7	71061.2	126330.9	197392.1	lb/in
Damping Ratio	10.0%	10.0%	10.0%	10.0%	
Nat. Freq.	2	3	4	5	Hz

The following plots summarize the results of this parametric study.

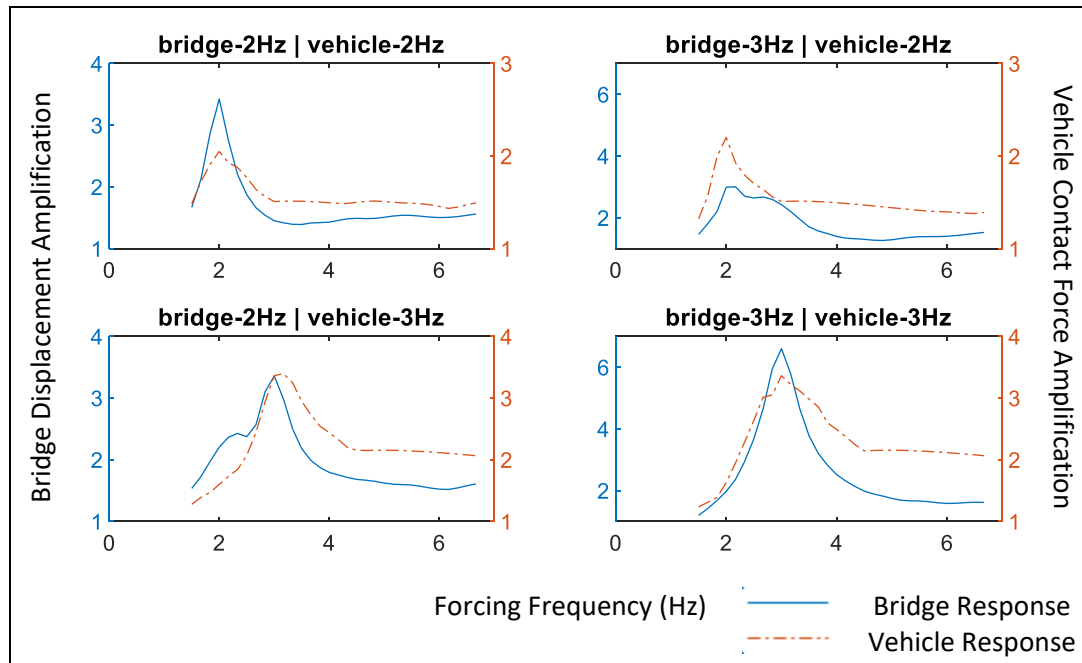


Figure 2.15.8: Effect of Bridge and Vehicle Frequency on Bridge Displacement and Vehicle Contact Force (1/4)

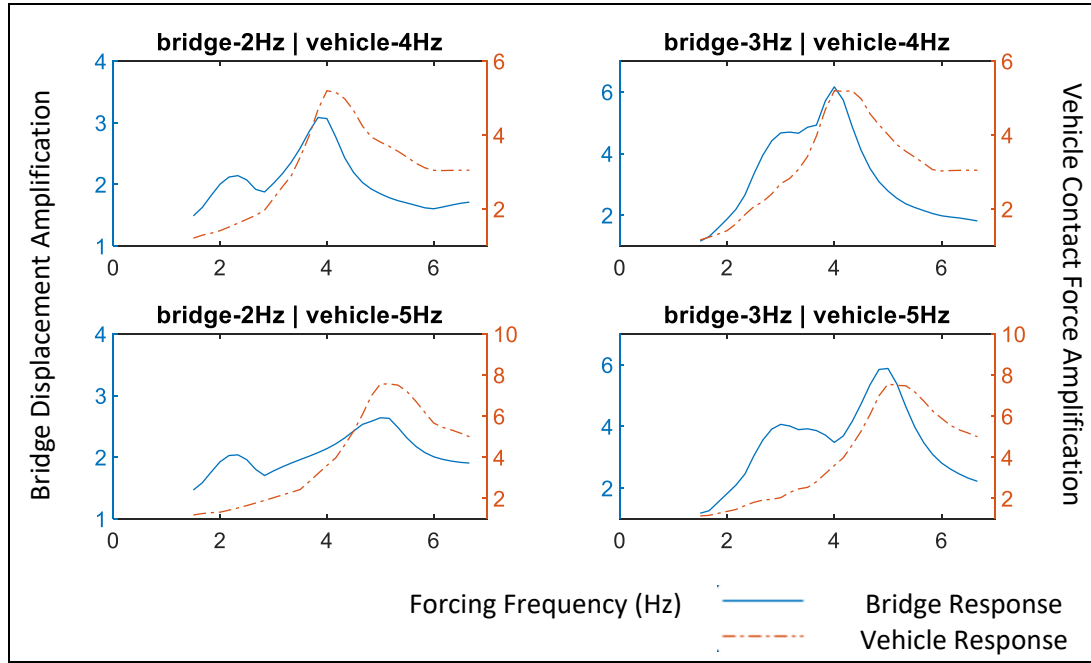


Figure 2.15.9: Effect of Bridge and Vehicle Frequency on Bridge Displacement and Vehicle Contact Force (2/4)

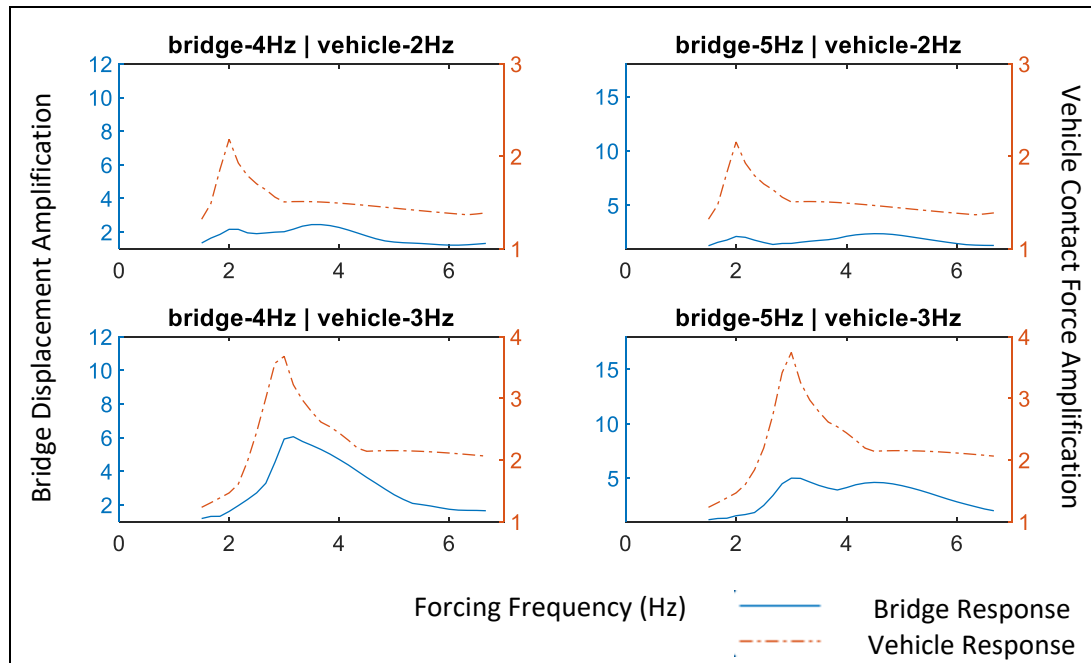


Figure 2.15.10: Effect of Bridge and Vehicle Frequency on Bridge Displacement and Vehicle Contact Force (3/4)

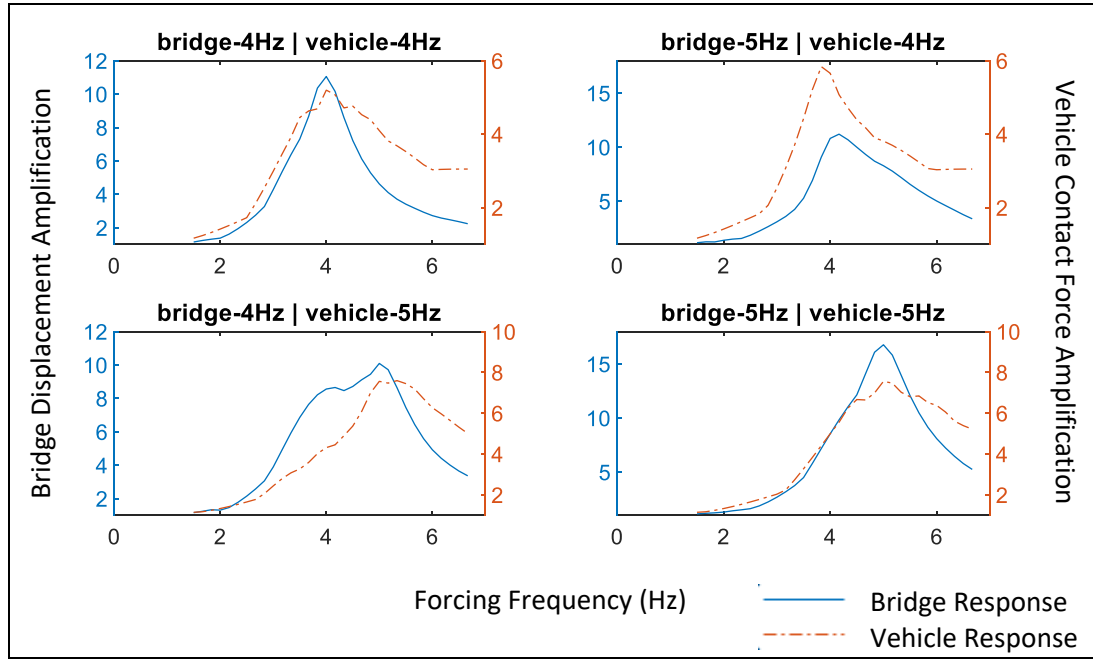


Figure 2.15.11: Effect of Bridge and Vehicle Frequency on Bridge Displacement and Vehicle Contact Force (4/4)

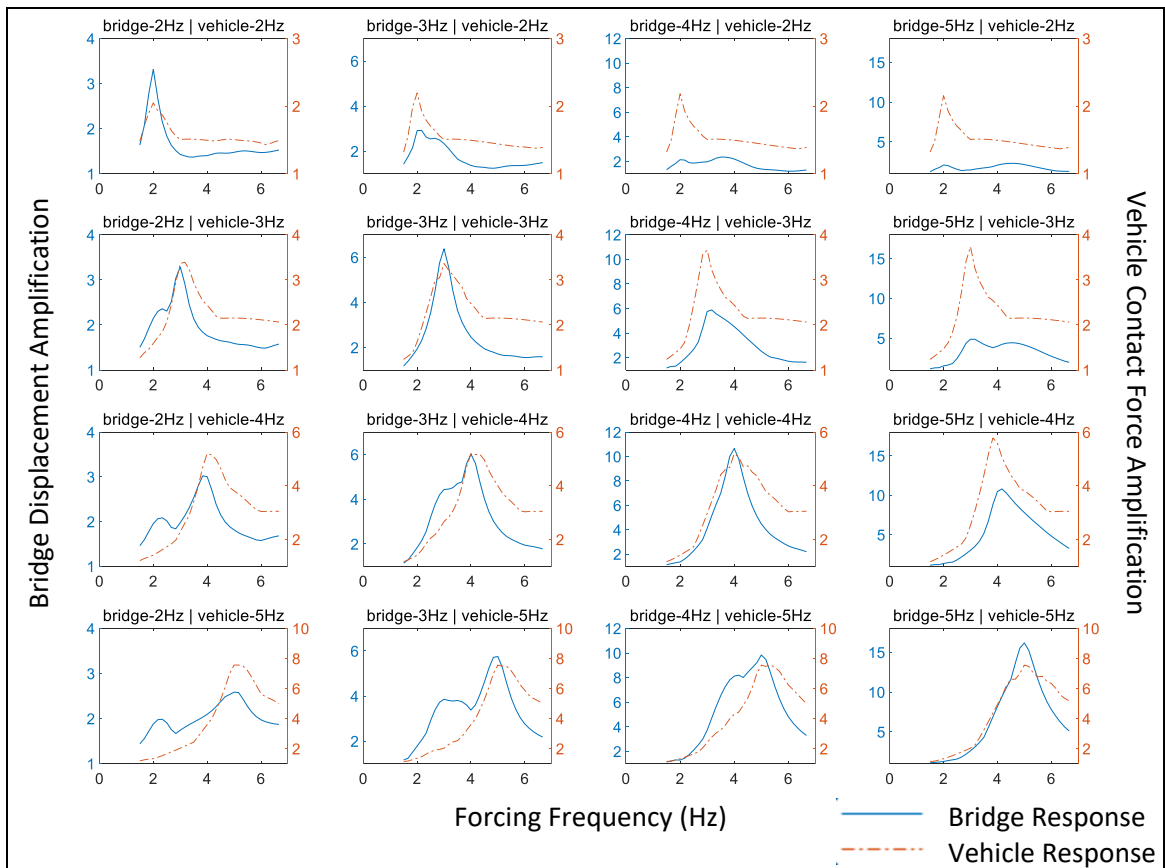


Figure 2.15.12: Effect of Bridge and Vehicle Frequency on Bridge Displacement and Vehicle Contact Force (Total)

In the preceding figures the amplification of bridge and vehicle responses is plotted. The bridge displacement amplification is calculated by dividing the maximum midspan displacement by the static response (δ_{st}) given by the following (dictated by shape function):

$$\delta_{st} = \frac{2PL^3}{\pi^2 * EI} \quad (100)$$

Where P is the static weight of the vehicle, L is the span length, E is the beam modulus of elasticity and I is the beam's moment of inertia.

The vehicle contact force amplification is calculated by dividing the maximum contact force by the static force of the vehicle which is merely the vehicle's weight.

These results conclude that bridge responses are greatest when the profile induces oscillation in the vehicle close to the bridge's natural frequency and when the vehicle natural frequency is near that of the bridge. These results are consistent with past studies that found that amplification is increased when the bridge and vehicle natural frequency match (Ding et al., 2009; Green et al., 1995b; Li et al., 2008; Schwarz and Laman, 2001; Wang and Huang, 1992).

Simulations with the 5 idealized bridge models were again performed with the simplified state-space model and an artificial profile created according to ISO 8608 standards ($C_{10} = 300E-6$; $w = -2$). The vehicle parameters were varied such that their natural frequency was a function of bridge natural frequency. The mass of the vehicles was held constant at 200 slinch (35025 kg), as was the damping ratio at 10%. The vehicle suspension stiffness was assigned such that the vehicles natural frequency varied from 0.8 to 4 times the bridge's natural frequency. The following plot illustrates the optimum ratio of vehicle frequency to bridge frequency for the 5 bridge models that results in the greatest dynamic amplification.

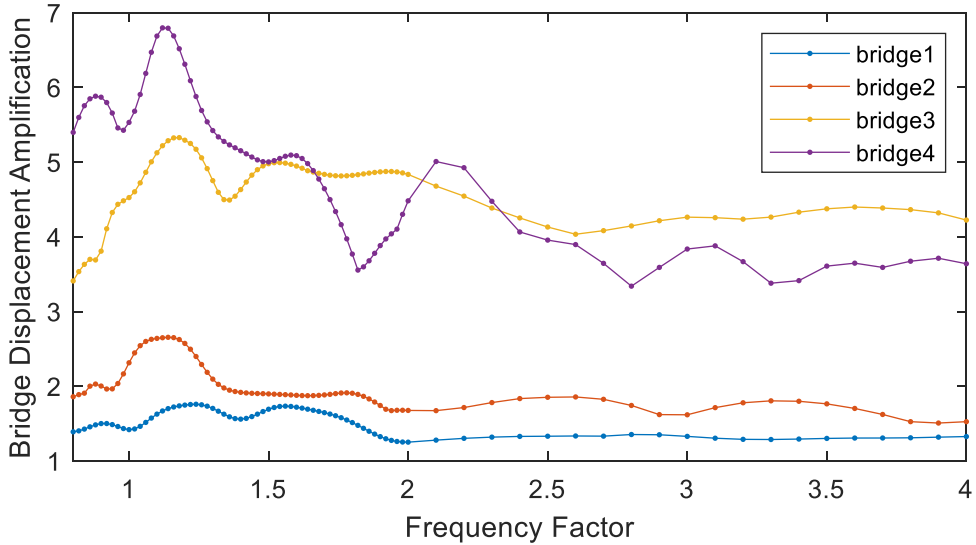


Figure 2.15.13: Effect of Vehicle Frequency as a Fraction of Bridge Natural Frequency on Bridge Displacement Amplification.

The following tables summarizes the frequency factor (vehicle frequency/bridge frequency) at which a maximum response as achieved.

Table 2.15.5: Frequency Factor for Maximum Amplification

	Freq. Factor
Bridge1	1.24
Bridge2	1.14
Bridge3	1.18
Bridge4	1.12

The above simulations demonstrate the role of the profile as well as other parameters in vehicle-bridge interaction. The profile best excites the vehicle when its forcing frequency matches that of the vehicle, and the bridge is most excited when the profile forcing frequency matches its own natural frequency and the vehicle natural frequency is slightly higher than its own.

Profile Effects

The previous section demonstrated that profile frequency content that results in a forcing frequency similar to the bridge's natural frequency produces maximum bridge response.

However even a harmonic profile cannot be entirely described by its frequency content. The distribution of phase angles for the different harmonic components have a large effect on the final form of the profile and how the vehicle-bridge system responds to that profile. The following plot is of two profiles created according to ISO 8608 standards with identical frequency content but different phase angle distribution ($C_{10} = 300$; $w = -2$). These ISO parameter values result in a profile with a great deal of lower frequency (large wavelengths) content (largest included wavelength was 20 meters).

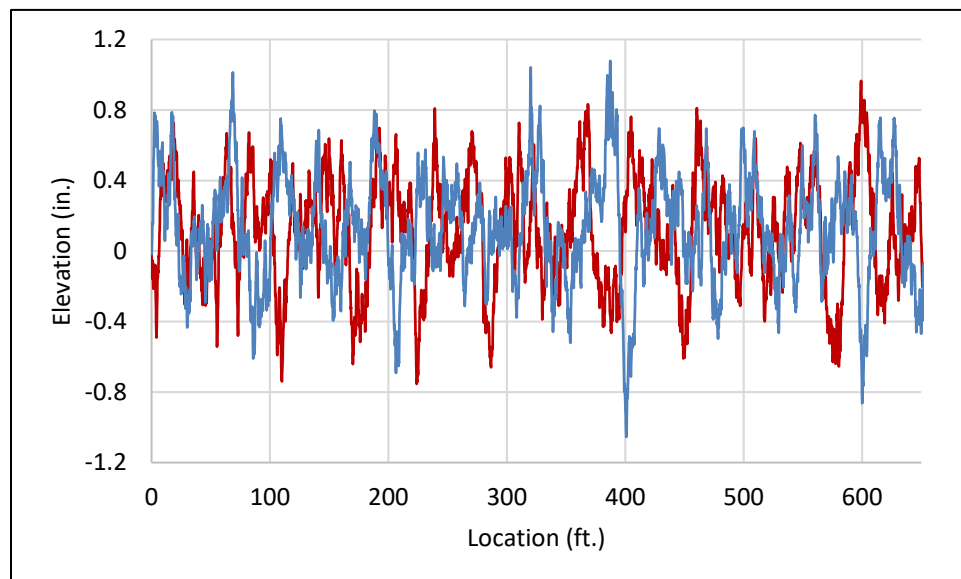


Figure 2.15.14: Profiles with Matching Frequency Content but Different Phase Angle Distribution

Simulations were performed with these two profiles and the 2.5 Hz vehicle described in the previous section on the 140 ft single-span 3D FE model. The resulting bridge displacement is compared in the following plot.

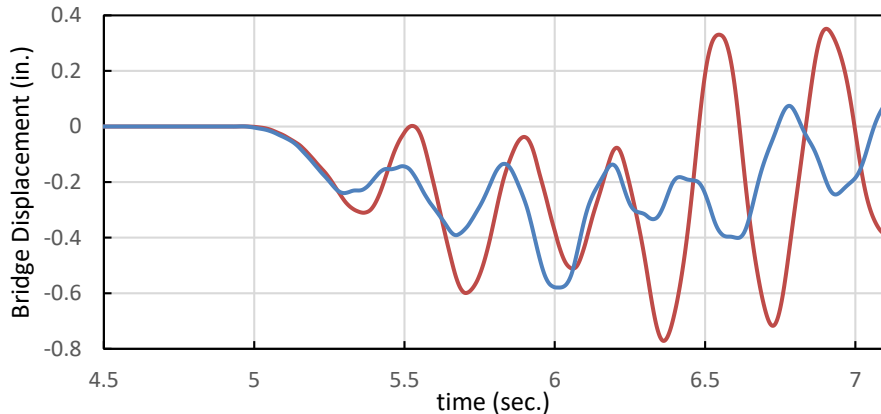


Figure 2.15.15: Bridge Displacement for Profiles with Different Phase Distribution

As can be seen, two profiles with identical frequency content but different phase angle distribution will cause different bridge responses. Similarly, the position of the profile can make a large difference in vehicle and bridge response. Simulations were performed with one of the profiles used in the previous simulation using the 2-DOF simplified model (Bridge 1 & Truck 1). The position of the profile was varied by offsetting it in increments of 5 feet.

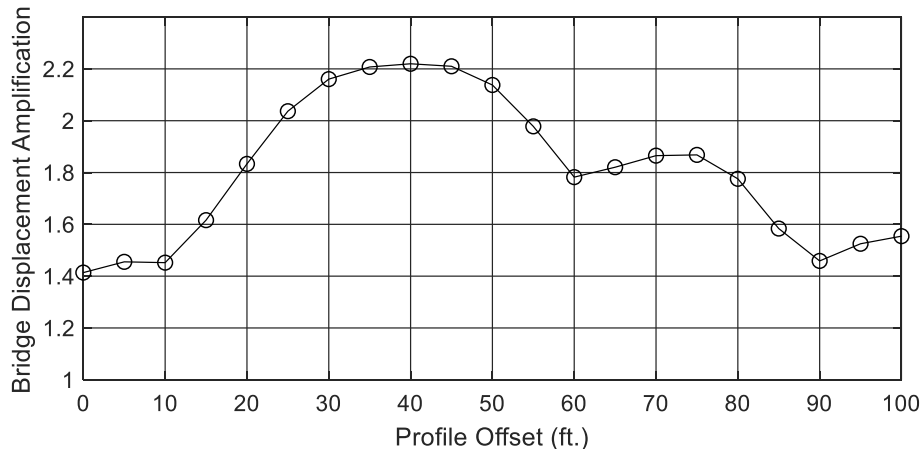


Figure 2.15.16: Effect of Profile Position on Bridge Displacement Amplification

As can be seen in the plot above, the bridge response varies greatly by just adjusting the position of the profile on the bridge. This is because the profile features that result in large contact forces will induce greater bridge response when they are located near the more flexible regions of the bridge (i.e. midspan). Furthermore, most real profiles are not harmonic but rather

have many transient features. Profiles that contain harmonic content with large wavelengths that result in forcing frequencies similar to vehicles or the bridge should be avoided (e.g 5-50ft.). However, the frequency content of the profile alone has no reliable correlation with dynamic amplification and spatial information must be included in any dynamic amplification analysis.

Conclusions

The roadway profile, on and off the bridge, serves to induce vertical oscillation in the vehicle. That oscillation results in an oscillating force at the point of contact between vehicle and roadway. As the vehicle crosses the bridge, the contact force excites the mass of the bridge. The exchange of energy from the vehicle to the bridge serves to reduce the motion of the vehicle and thus the dynamic component of the vehicle contact force.

Vehicle and bridge parameters therefore effect dynamic amplification based on their influence on the dynamics of the system and how those system dynamics relate to the profile characteristics. While parameter effect cannot be quantified independently, this chapter succeeded in establishing the following conclusions:

- Ignoring the interaction of vehicle and bridge (i.e. computing contact force without consideration of the bridge) results in conservative estimates of bridge response.
- Harmonic profile content with spatial wavelengths resulting in forcing frequencies similar to the bridge's natural frequency should be avoided as these components induce the greatest dynamic bridge response.
- Bridge dynamic responses are amplified when the vehicle natural frequency is 10-20% greater than that of the bridge.
- Position of the profile and phase angle distribution of harmonic components have significant effect on bridge response.

- Higher bridge mass, stiffness and damping generally serve to reduce dynamic amplification.
- Higher vehicle mass increases dynamic amplification while vehicle damping helps to reduce amplification.
- Higher vehicle speed leads to increased dynamic amplification.
- Longer bridge length results in a longer period of time for which the vehicle is present on the bridge and may therefore result in greater dynamic amplification.

Anything further than these generalizations requires simulation of vehicle-bridge interaction with the specific profile or direct measurement by field experiment.

Chapter 16: Part 2 Summary and Conclusions

Simulations were performed with 3D FE models and with simplified 2-DOF models to better characterize the effects of bridge, vehicle and profile parameters on bridge dynamic response and amplification. These studies resulted in the following conclusions:

- The vehicle and bridge comprise a coupled dynamic system that is energized by the vehicle traversing a profile.
- Determining dynamic amplification of in-service bridges may be performed with operational monitoring or a load test. In either case, strain gauges are recommended over displacement gauges or accelerometers.
- Dynamic amplification estimated by filtering operational monitoring data may overestimate amplification.
- A 3D FE model is capable of simulating vehicle-bridge interaction and is recommended for predicting dynamic amplification for structures with complex geometry or that are otherwise ill-suited to the simplified state-space models.
- A simple model that reduces both the bridge and vehicle to SDF systems has been shown to reliably predict dynamic amplification and is recommended when FE simulation is impractical.
- Any metric that is to be used for predicting dynamic amplification must include a representation of the bridge. Therefore, dynamic amplification should not be predicted by current roughness metrics (e.g. IRI and ISO 8608) that only consider the profile and vehicle.
- It is conservative to compute bridge response with contact forces determined without consideration of bridge motion.
- The effect of bridge, vehicle and profile parameters are interdependent.

- Bridge responses are greatest when the profile induces oscillation in the vehicle close to the bridge's natural frequency and when the vehicle's natural frequency is 10-20% greater than that of the bridge.

Part 3: Applications in Vehicle-Bridge Interaction

The simulation tools demonstrated in Part 1 and developed in Part 2 are leveraged in this part to address some of the challenges facing bridges associated with VBI.

Parts 1 and 2 both demonstrated the influence of roadway profile roughness on bridge response and dynamic amplification. In Part 2 it was shown that IRI has a strong (but inconsistent) correlation with dynamic amplification. Chapter 17 once again addresses profile roughness with examination of rolling straightedge criteria. Various straightedge limits are used to modify a real (measured) profile and the effect of these modifications on dynamic amplification is quantified.

Chapter 18 extends vehicle-bridge interaction to include multiple vehicles. While a single vehicle (per lane) is often the load case analyzed for design and evaluation, real world structures are routinely subjected to traffic conditions in which the bridge is subjected to multiple vehicles. The additional response due to multiple vehicles is traditionally ignored in design and evaluation methodologies because of the inherent conservatism associated with the live-load model (i.e. it is unlikely that every lane will be simultaneously occupied with a HL-93 truck). However, the effect of multiple vehicles on bridge dynamics and dynamic amplification has not been addressed.

Therefore, chapter 18 seeks to identify the effect of multiple vehicles on dynamic amplification and provide guidance on how the effect of multiple vehicles should be considered when it is impractical to perform VBI simulation (i.e. static analysis). This is accomplished by first examining the effects of a few traffic patterns and then extended to truck platoons.

Chapter 17: Remediation and Smoothness Criteria

If a bridge is suspected to exhibit large dynamic amplification as a result of a rough roadway, the bridge owner may wish to grind the roadway smooth. Furthermore, to reduce dynamic amplification in new construction, deck profile specifications should provide smoothness targets. Currently, smoothness criteria are prescribed differently depending on the region.

The IRI, which is widely used as a smoothness criterion by providing upper limits, has already been shown to influence dynamic amplification. The IRI is a measure of vehicle response and can therefore only be implemented as a performance metric. As such it provides no methods for specifying or monitoring the smoothness during construction or as a result of grinding and will not be presented in this section. However, if a deck profile is shown to have a high IRI, intervention should be considered.

Rolling straightedge requirements are widely used for specifying localized roughness criteria and are expressed in terms of deviation over a certain length. Parameters commonly range from 1/8 to $\frac{1}{4}$ inch deviation over a 10 to 16-foot distance. A computer algorithm was developed that effectively smooths the profile according the straightedge requirements.

This algorithm steps through the profile, incrementally advancing the reference point and assessing if any point, between the reference point and a point at a distance equal to the straightedge length, exceeds a straight-line fit between the two points by more than the specified deviation. If a point falls outside of the bounds specified by the deviation value, the elevation of the point is reduced such that the deviation equals the specified deviation. This is accomplished in the following steps.

- Linearly interpolate every point within the straightedge window based on the elevation of the first and last point (i.e. create a straight line between the first and last point).

- Compute the vertical deviation that results in a perpendicular (to the interpolated road surface) deviation equal to the specified deviation.
- Find indices of points that exceed the interpolated surface (line) plus the vertical deviation and set equal to the interpolated surface plus the vertical deviation.

The effect of this smoothing is illustrated in the following plots whereby a measured profile (measured during Part 1, Phase 3 testing) is compared to the same profile after applying the smoothing algorithm.

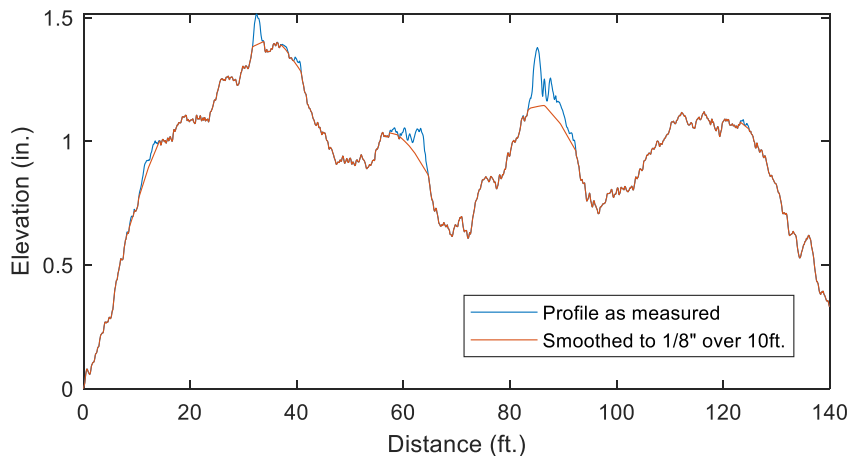


Figure 3.17.1: Effect of Smoothing (1/8" over 10ft.) on Real Profile

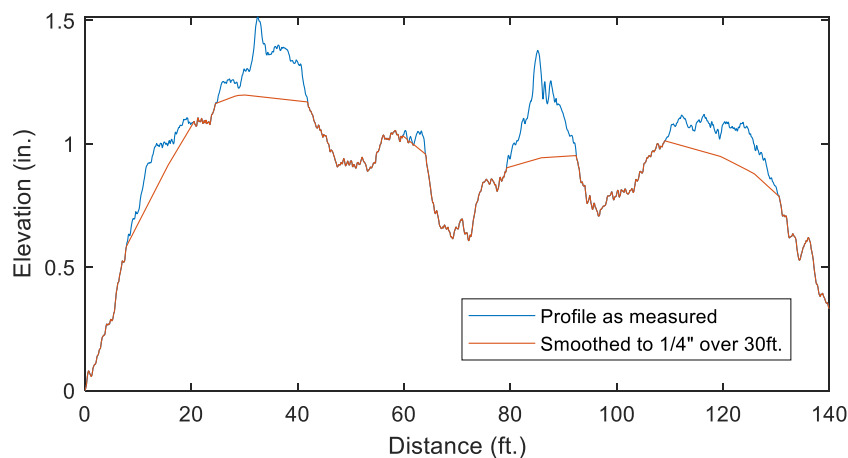


Figure 3.17.2: Effect of Smoothing (1/4" over 30ft.) on Real Profile

The ability of straightedge criteria to limit dynamic amplification is assessed by simulating vehicle-bridge interaction with a problematic profile, and again with the profile smoothed according to specified criteria. The FE model of a single 140 ft. span with the 2.5 Hz vehicle model as described in Part 2 was utilized for this study. Simulation parameters are summarized in the following table.

Table 3.17.1: Simulation Parameters for Smoothing Studies

Number of modes included	15	
Incremental distance along load-path	6	inches
Structural damping	1%	
Vehicle speed	720	in/sec
Solution time-step	0.0015	sec

The following plot compares bridge midspan displacement amplification for the previously plotted profile with smoothing applied according to 1/8th inch over 10 feet. Amplification was computed according to equation (89), for which the static displacement was taken as the maximum quasi-static (i.e. 5 in/sec) displacement.

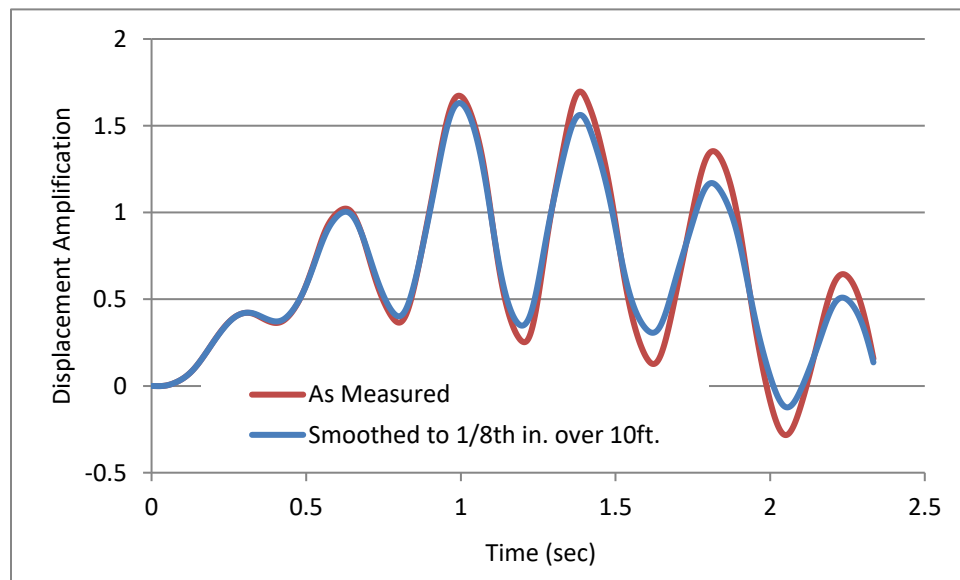


Figure 3.17.3: Comparison of Bridge Dynamic Amplification with Rough Profile and with Smoothed Profile

The above plot clearly shows the $1/8^{\text{th}}$ inch over 10 feet criterion is ineffective at limiting dynamic amplification.

The straightedge requirements target features with lengths less than the straightedge length. At normal traffic speeds profile features with lengths of 5-50 feet result in forcing frequencies within the range of natural frequencies commonly exhibited by bridges. Therefore, the straightedge length should be specified long enough to avoid/remove features in this range. For a speed of 720 in/sec, a feature wavelength of 30 feet results in a forcing frequency equal to 2 Hz.

A variety of straightedge criterion were assessed with the 2-DOF state-space model of the 140ft single-span bridge (as described in Part 2, Chapter 13). Straightedge smoothing of the same profile was performed with maximum specified deviation ranging from $1/8^{\text{th}}$ inch to $\frac{1}{2}$ inch and straightedge length ranging from 10 to 50 feet. The results are plotted below.

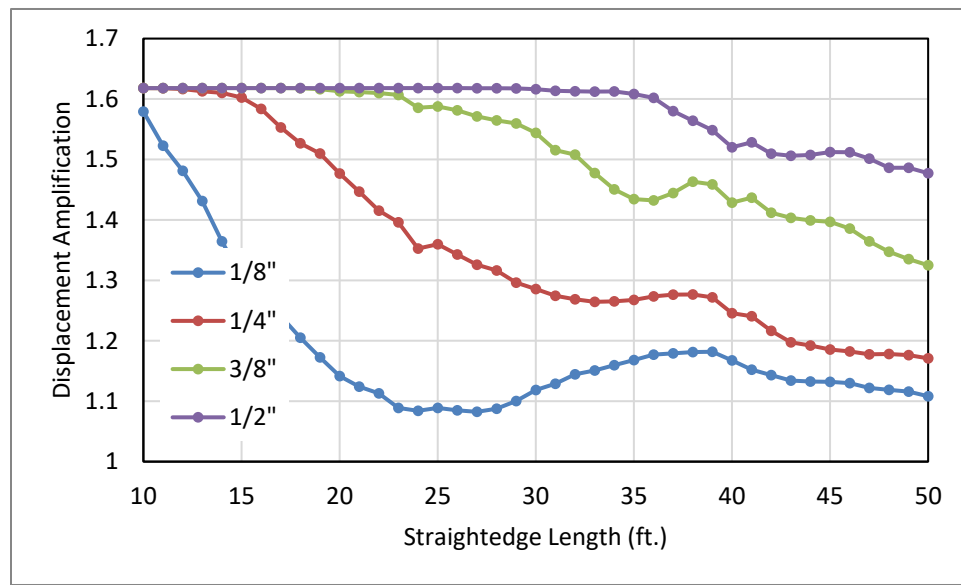


Figure 3.17.4: Effect of Smoothing Parameters on Dynamic Amplification

The preceding plot demonstrates the ability of straightedge requirements to limit dynamic amplification. Criteria that specify deviation limits greater than $\frac{1}{4}$ " are ineffective at limiting

amplification. Even criteria with $\frac{1}{4}$ " deviation limits were only successful at reducing the amplification to 1.33 when the straightedge length was greater than 27 feet. Based on these findings it is recommended that straightedge criteria specify a straightedge length of at least 16 feet for a deviation of $1/8^{\text{th}}$ inch, and a straightedge length of at least 30 feet for a deviation of $\frac{1}{4}$ inch.

Conclusions

Rolling straightedge criteria with common limits (i.e. $1/8$ to $\frac{1}{4}$ inch deviation over 10 to 16 feet) are not effective at reducing dynamic amplification. This is because (1) deviations even as small as $\frac{1}{4}$ of an inch (0.635 cm) can significantly influence bridge response, and (2) short straightedge lengths fail to remove features with large wavelengths that still have appreciable effect on bridge response. The shorter the straightedge length, the more stringent the deviation limit must be. Based on these simulations, if this criterion is to continue being used, the straightedge length should be at least 16 feet (4.88 m) for a deviation limit of $1/8^{\text{th}}$ inch (0.318 cm), and at least 30 feet (9.14 m) for a deviation limit of $\frac{1}{4}$ inch (0.635 cm).

Chapter 18: Multiple Vehicles

The many simulations that have thus far been reported, have considered only a single vehicle traversing a bridge. In reality, bridges experience a large variety of different live-load configurations and many times are subjected to multiple vehicles at the same time. This is investigated in the following sections.

Traffic

The scenario of multiple-vehicle loading is accounted for in most design methodologies through the use of multi-presence factors. These factors serve to reduce the load presented by vehicles in adjacent lanes based on the assumption that vehicles with legal-limit weights are unlikely to occupy adjacent lanes at the same time. While this assumption may be valid for static bridge responses, other vehicles may contribute to the dynamic response. The effect of other vehicles (traffic) on a bridge's dynamic response and the dynamic amplification of a major load event are investigated.

Methods

Several traffic patterns were created with randomly distributed vehicles and varying density (i.e. vehicle spacing). Each pattern sampled 8 different vehicles that included HS20 trucks, a dump truck, a tractor-trailer, and small passenger vehicles. The vehicles, their axle configurations and suspension parameters are provided below.

Table 3.18.1: Vehicle Parameters for Traffic Simulations

Vehicle #	Axle #	Name	Distance from rear axle (ft)	Weight (kip)	Spring Stiffness (kip/in)	Damping Coefficient (lb-s/in)	Damping Ratio	Natural Frequency
1	1	HS20-32_1	0	32	20	257.529	0.1	2.472
	1	HS20-32_1	14	32	20	257.529	0.1	2.472
	2	HS20-8_1	28	8	15	111.513	0.1	4.282
2	3	HS20-32_2	0	32	16	460.682	0.2	2.211
	3	HS20-32_2	30	32	16	460.682	0.2	2.211
	4	HS20-8_2	44	8	8	407.189	0.5	3.127
3	5	HS20-32_3	0	32	13	415.253	0.2	1.993
	5	HS20-32_3	22	32	13	415.253	0.2	1.993
	6	HS20-8_3	36	8	10	455.251	0.5	3.496
4	7	tst-tand	0	17	15	162.557	0.1	2.937
	7	tst-tand	6	17	15	162.557	0.1	2.937
	8	tst-drive	29	17	15	162.557	0.1	2.937
	8	tst-drive	35	17	15	162.557	0.1	2.937
	9	tst-front	51	12	2.2	261.522	0.5	1.339
5	10	dump-rear	0	25	12	176.318	0.1	2.166
	10	dump-rear	5	25	12	176.318	0.1	2.166
	11	dump-front	20	20	12	315.407	0.2	2.422
6	12	car1	0	1.5	0.2	27.878	0.5	1.142
	12	car1	8	1.5	0.2	27.878	0.5	1.142
7	13	car2	0	2	0.4	45.525	0.5	1.398
	13	car2	10	2	0.4	45.525	0.5	1.398
8	14	car3	0	3	2	124.676	0.5	2.553
	14	car3	14	3	2	124.676	0.5	2.553

Six traffic patterns were created with the following parameters. Each traffic pattern concluded with the dump truck (vehicle 5). Every other vehicle in a traffic pattern was randomly selected from the vehicle list and the spacing was randomly (uniform) sampled between the bounds specified in the following table.

Table 3.18.2: Traffic Pattern Parameters

	Num. of Vehicles	Min. Spacing	Max. Spacing
1	36	20 ft.	100 ft.
2	36	40 ft.	200 ft.
3	36	60 ft.	300 ft.
4	36	80 ft.	400 ft.
5	36	100 ft.	500 ft.
6	36	280 ft.	1400 ft.

The 3D FE model of the 2-span bridge with span lengths of 140 ft (Part 2, Chapter 13: [140ft. Bridge](#)) was used for the simulations. Each traffic pattern was simulated at a speed of 960 in/sec (≈ 55 mph) as well as at 5 in/sec to provide the quasi-static response. A real profile (as measured in Part 1) was included in the simulations. The first 15 modes of vibration were included in the simulation. Simulation time-steps of 0.002 seconds and 0.5 seconds were used for the 960 in/sec and quasi-static simulations, respectively.

Results

The bridge responses acquired from the simulations of the traffic patterns are summarized in the following table.

Table 3.18.3: Maximum Responses from Traffic Simulations

	Max. Static Disp. (in.)		Max. Dynamic Disp. (in.)		Max. Amplification	
	Span 1	Span 2	Span 1	Span 2	Span 1	Span 2
Traffic1	-0.41113	-0.41906	-0.588347	-0.48383	1.431056	1.154555
Traffic2	-0.32891	-0.32505	-0.369981	-0.54378	1.12486	1.672918
Traffic3	-0.26793	-0.26538	-0.407771	-0.38494	1.521942	1.450507
Traffic4	-0.26009	-0.25963	-0.438268	-0.40802	1.685082	1.571517
Traffic5	-0.26012	-0.25962	-0.380595	-0.40768	1.463129	1.570283
Traffic6	-0.25986	-0.25962	-0.356183	-0.37011	1.370688	1.425589

Except in a few cases, large dynamic amplifications were observed for the traffic patterns. The time history corresponding to the events that produced the largest dynamic response are plotted below along with the quasi-static response.

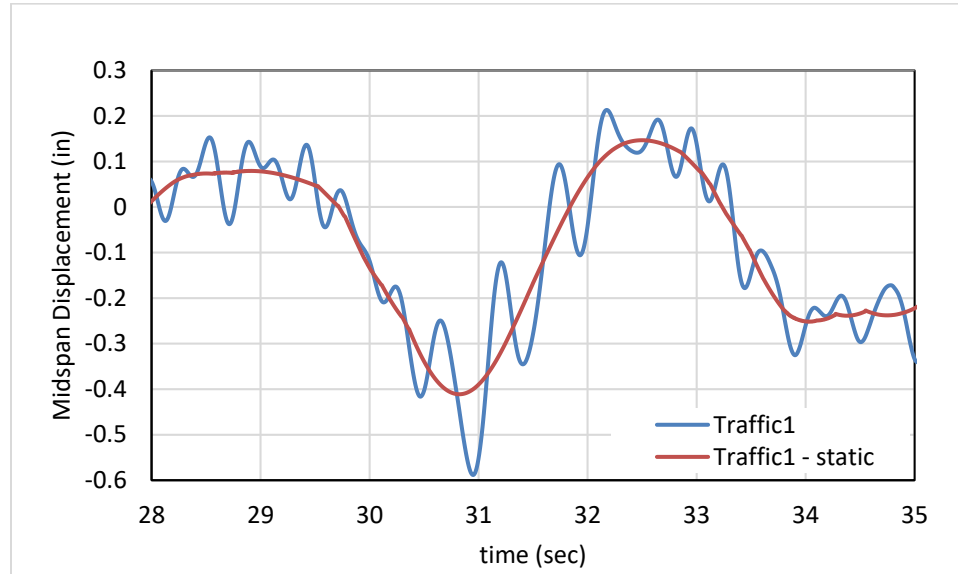


Figure 3.18.1: Span-1 response to traffic pattern no. 1

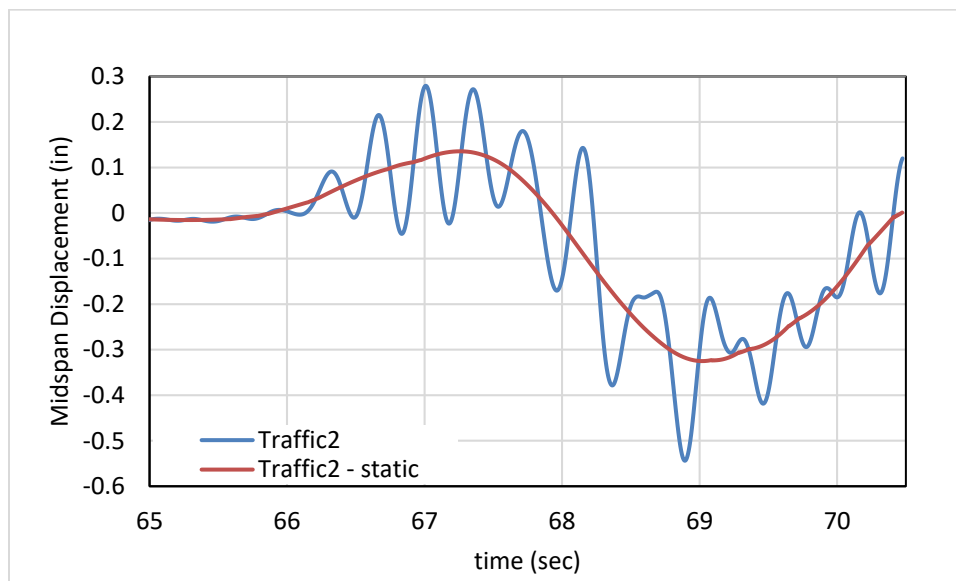


Figure3.18.2: Span-2 response to traffic pattern no. 2

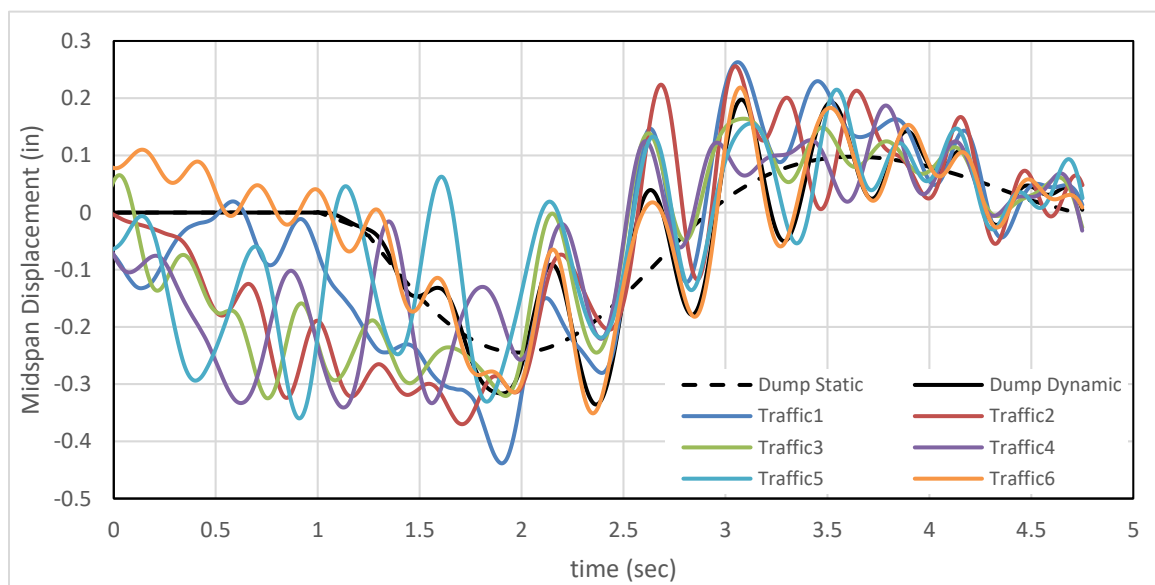
The vehicles that are inducing the response shown in the above plots are vehicle numbers 3 and 5 (HS-20 and dump truck), respectively. The responses that these vehicles alone produce are provided below for comparison.

Table 3.18.4: Single Vehicle Responses for Vehicles 3 and 5

	Max. Static Disp. (in.)		Max. Dynamic Disp. (in.)		Max. Amplification	
	Span 1	Span 2	Span 1	Span 2	Span 1	Span 2
Vehicle3	-0.251	-0.252	-0.304	-0.320	1.21	1.27
Vehicle5	-0.245	-0.245	-0.336	-0.337	1.37	1.38

All but two of the amplifications induced by the traffic patterns presented in Table 3.18.3 meet or exceed the amplification produced by a single vehicle. It can therefore be concluded that multiple vehicle loading serves to not only increase the static bridge response but may also result in dynamic amplification even greater than that which would be observed for a single vehicle.

The response of span 1 to the final vehicle (dump truck) is compared in the following plot and serves to illustrate the effect that bridge initial conditions (preexisting motion) has on bridge response to a vehicle crossing.

**Figure 3.18.3: Time History of Bridge Displacement for Last Vehicle in Traffic Patterns**

The (dynamic) bridge response over the duration for which the last vehicle was on the bridge was a maximum for the first span under traffic pattern number 1 for which the final vehicle was

preceded by an HS-20 (vehicle 3) with a headway of 20 ft. That for span 2 was a maximum under traffic pattern number 2, for which the final vehicle was preceded by a tractor-trailer (vehicle 4) with a headway of 40 ft. Those responses are plotted below.

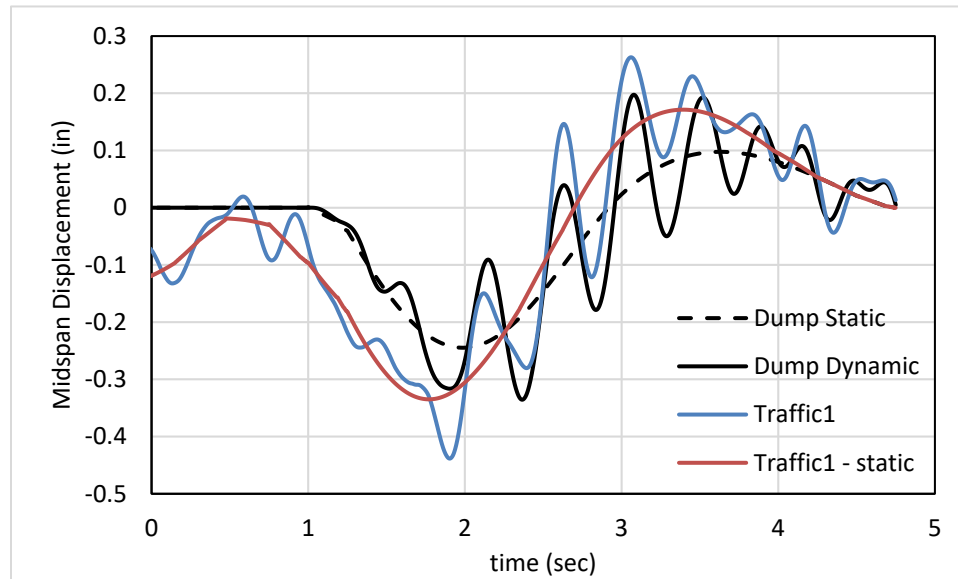


Figure 3.18.4: Span-1 Response to final vehicle (#5) in traffic pattern 1

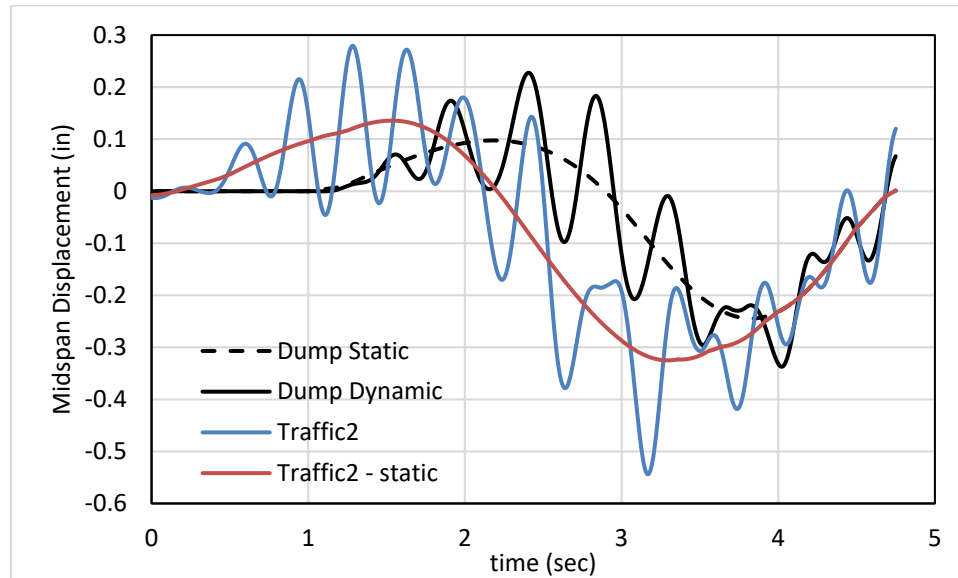


Figure 3.18.5: Span-2 Response to final vehicle (#5) in traffic pattern 2

The remaining traffic patterns failed to produce greater responses than if the final vehicle had no preceding vehicles. Incidentally, for all these remaining traffic patterns, the final vehicle was

preceded by either a dump truck (vehicle 5) or HS-20 (vehicle 3) and at a distance not less than 60ft. The maximum responses for this final loading event for all traffic patterns are summarized in the following table.

Table 3.18.5: Maximum Responses for Final Vehicle Loading Event

	Max. Dynamic Disp. (in.)		Dynamic Amplification		Preceding Vehicle	Distance (ft.)
	Span 1	Span 2	Span 1	Span 2		
Traffic1	-0.438	-0.484	1.31	1.15	3	20
Traffic2	-0.370	-0.544	1.12	1.67	4	40
Traffic3	-0.348	-0.350	1.30	1.32	3	60
Traffic4	-0.341	-0.301	1.39	1.23	5	80
Traffic5	-0.360	-0.326	1.77	1.33	5	100
Traffic6	-0.351	-0.344	1.43	1.41	3	280
Vehicle5	-0.336	-0.337	1.37	1.38	-	-

The results provided in the previous table further demonstrate that traffic serves to increase structural response due to both increased static effects as well as increased dynamic amplification. However, small passenger vehicles have insufficient mass to appreciably excite the structure and thus will not have significant impact on bridge response to truck loads. Therefore, it is repeated truck loading that results in the greatest bridge response. The following section explores this further.

Platooning

Platooning is when several trucks follow closely with reduced headway supported by control and communications technologies, resulting in a “train” of trucks. Therefore, a truck-train may be described by the following parameters:

1. Number of vehicles
2. Individual vehicle dynamics (mass and suspension properties)
3. Vehicle spacing
4. Speed

To reduce simulation computing requirements, the number of vehicles will first be investigated. We may first bound this parameter by considering that the upper limit for number of vehicles is controlled by the time it takes for bridge motion induced by past trucks to damp out. Therefore, this parameter is dependent on vehicle spacing and speed and bridge length. Vehicle spacing is conservatively bounded at 15 feet for the closest spacing, and vehicle speed is not likely to exceed 1200 in/sec (68 mph).

Therefore, the number of vehicles in a platoon was investigated while holding vehicle spacing to the conservative minimum of 15 feet and platoon speed to the conservative maximum of 1200 in/sec (68 mph), thereby maximizing the energy input to the bridge. Platoons were therefore composed of dump trucks (vehicle 5) spaced at 15 feet. The number of vehicles in each platoon was varied: {1, 2, 4, 6, 8, 10}. Simulations were repeated for a vehicle headway spacing of 150 feet.

Simulations were performed using the 3D FE model of the 2-span bridge with span lengths of 140 ft (Part 2, Chapter 13) and a real profile (measured in Part 1). The first 15 modes of vibration were included in the simulation. A time-step of 0.002 seconds was used.

The following plot displays the effect the number of vehicles has on dynamic bridge response.

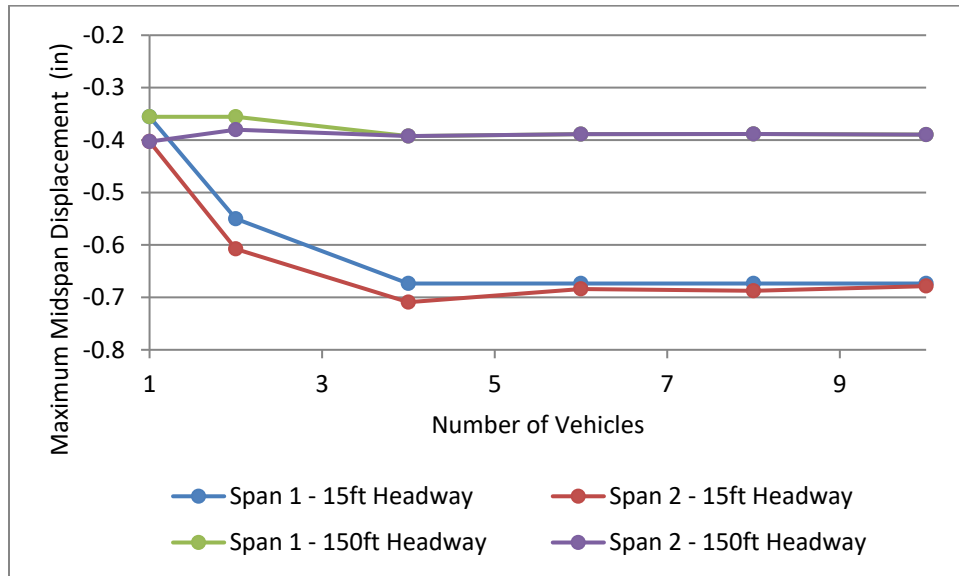


Figure 3.18.6: Effect of Number of Sequential Vehicles on Bridge Response

As can be seen in the above plot, for both large and small vehicle spacing, the maximum response is captured with just 4 vehicles and any additional vehicles fail to increase the bridge response or appreciably change the nature of its motion.

The vehicle spacing was further investigated with the single-span 100-ft. FE model and with the single-span 140-ft. FE model; the same profile was used. Four dump trucks (vehicle 5) were arranged with a constant headway spacing. That spacing was varied from 15 feet to 100 feet for the 140 ft. model and from 15 feet to 75 feet for the 100 ft model. Platoons were assigned a speed of 1200 in/sec (110 kmh). The results are summarized in the following plots which illustrate the effect of vehicle spacing on bridge response: amplification and displacement.

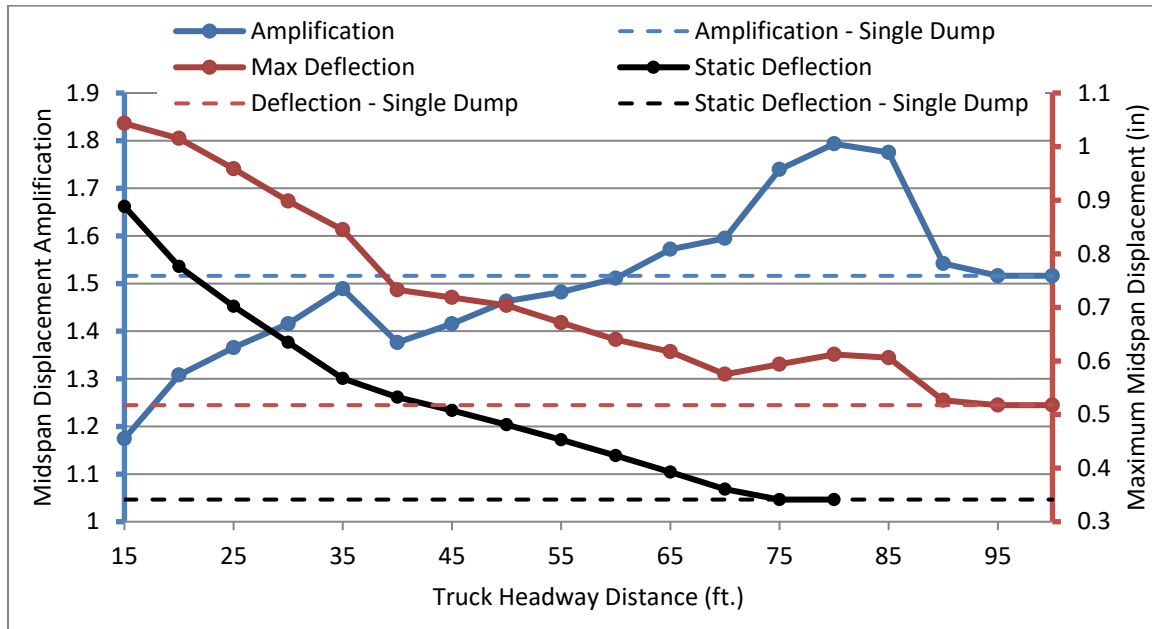


Figure 3.18.7: Response summary for 140ft single-span model

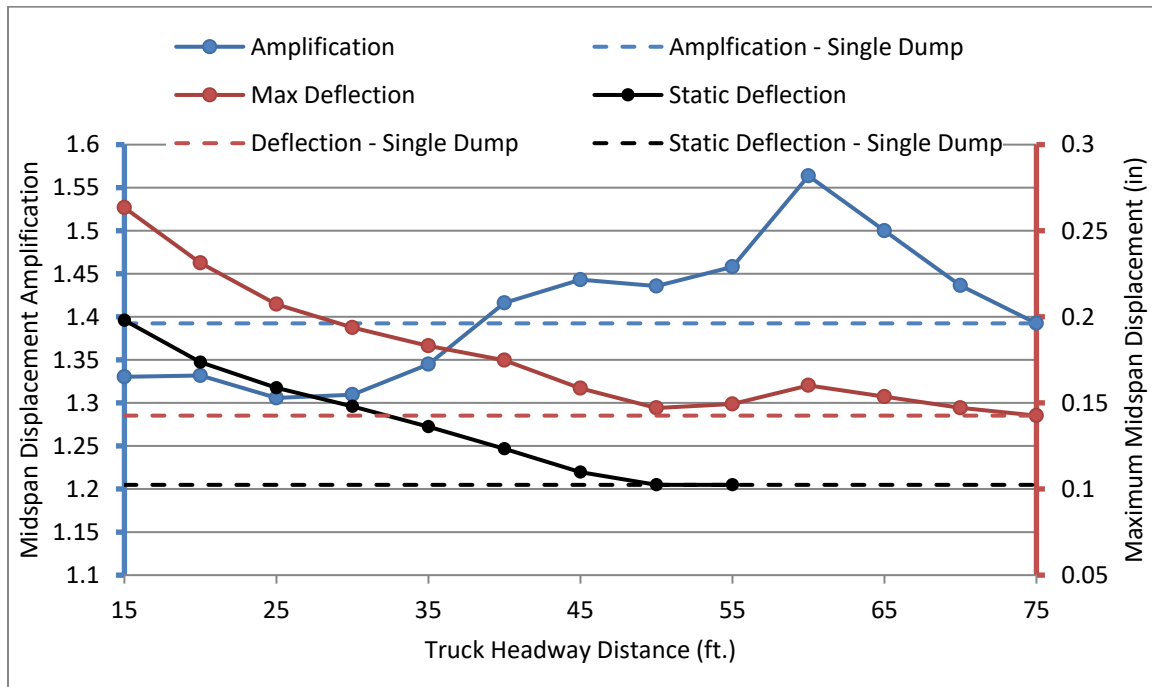


Figure 3.18.8: Response summary for 100ft single-span model.

Amplification in the above plots was computed by dividing the maximum dynamic displacement by the maximum quasi-static displacement (5 in/sec), thereby accounting for the static effect of multiple vehicles.

As vehicle spacing decreases, more vehicles are able to fit on the bridge, thus increasing the total load experienced by the bridge and increasing the bridge response (both static and dynamic). However, the dynamic amplification associated with this increased load tends to decrease as the vehicle spacing decreases (number of vehicles present on the bridge increases).

The dynamic amplification reaches the level corresponding to just a single vehicle when the spacing is greater than 75% of the bridge length. The dynamic amplification is a maximum when the vehicle spacing is roughly 60% of the bridge length and is greater than the dynamic amplification experienced for a single vehicle. For the single-span simulations, the maximum dynamic amplification was 12% greater (than the dynamic amplification for a single vehicle) for a headway spacing of 60 feet for the 100-foot span length and 18% greater for a headway spacing of 80 feet for the 140-foot span length.

If a bridge is to be designed for closer vehicle spacing (less than 35% of bridge length) and the additional load is considered in static analyses, the dynamic amplification factor computed for a single vehicle will suffice.

The simulations were repeated with the two-span continuous model with 140-foot span lengths (Part 2, Chapter 13). The headway spacing was varied from 20 feet to 500 feet. Platoons were assigned a speed of 1200 in/sec. The results are summarized in the following plots which illustrate the effect of vehicle spacing on bridge response: amplification and displacement.

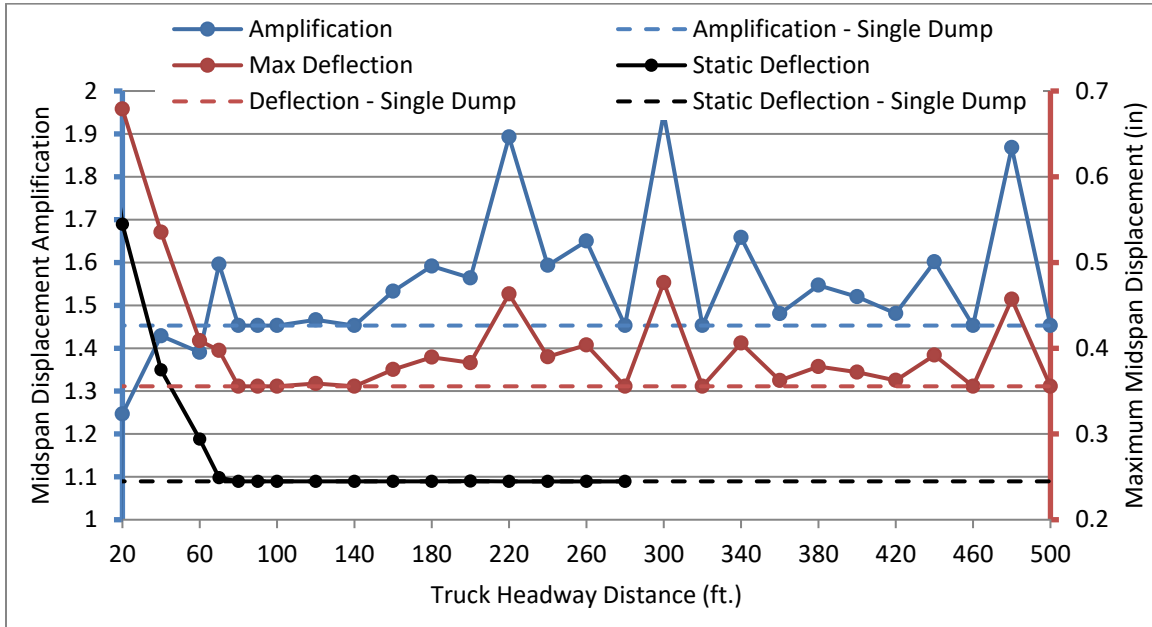


Figure 3.18.9: Response Summary for 140ft 2-Span Model (Span 1)

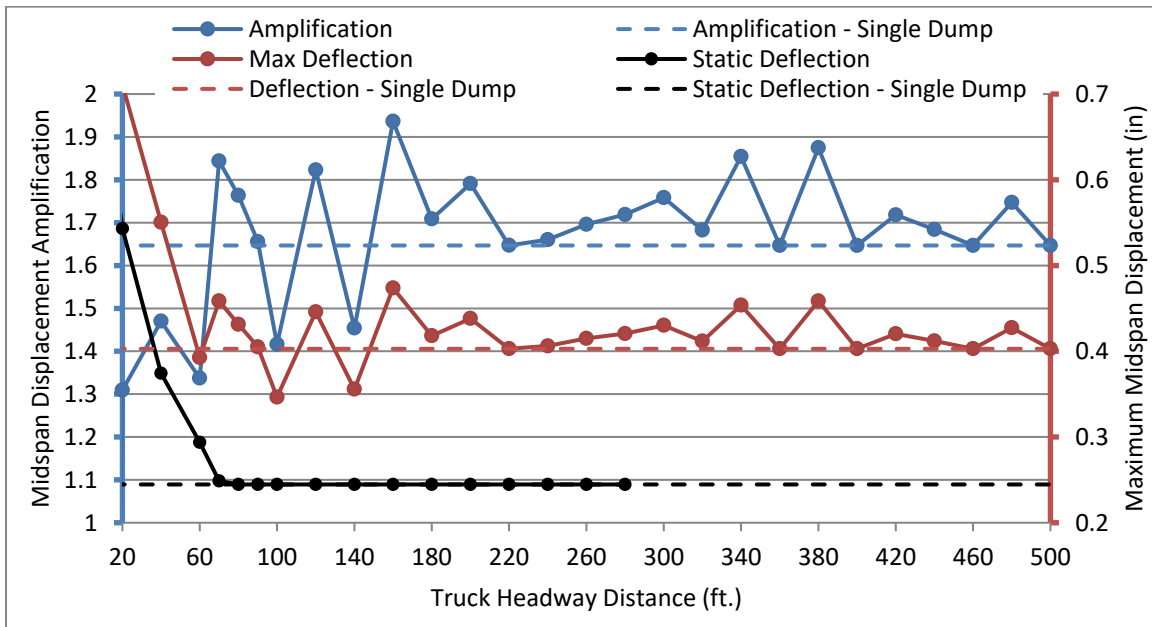


Figure 3.18.10: Response Summary for 140ft 2-Span Model (Span 2)

The results presented in the previous two plots illustrate the wide variation in dynamic response and dynamic amplification. Depending on the headway spacing, the contact force from the multiple vehicles may result in constructive interference, increasing the dynamic response, or destructive interference, reducing dynamic response. Furthermore, when headway spacing

increases to the point that only a single vehicle is ever present on the bridge at one time, the same constructive or destructive interference may occur depending on the phase of bridge oscillation when the vehicle enters the bridge, which is dependent on vehicle spacing and the profile. The interference is demonstrated in the following plot which compares the responses of the second span for 140 ft. and 160 ft. headway spacing.

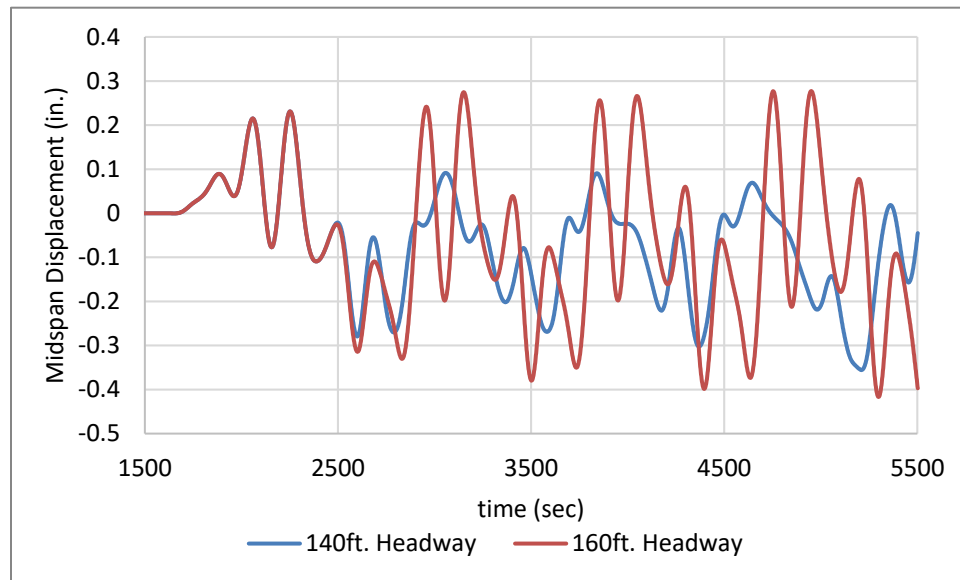


Figure 3.18.11: Span 2 Displacement Time History for Varied Platoon Headway Spacing

The inconsistent sensitivity of the 2-span model to platoon headway spacing prevents a clear relationship between headway spacing and dynamic amplification from being established. However, the simulation results still demonstrate that as headway spacing decreases to the point that the static load effects exceed those from a single vehicle (i.e. multiple vehicles are simultaneously present), the dynamic amplification associated with this increased load tends to decrease. The results also indicate that the bridge motion induced by a previous vehicle may significantly increase the dynamic amplification. For the two-span simulations, the maximum dynamic amplification was 34% greater (than the dynamic amplification for a single vehicle) for

a headway spacing of 300 feet for span 1 and 18% greater for a headway spacing of 160 feet for span 2.

Conclusions

Additional vehicles present additional loads to the bridge and ultimately increase bridge response. The response will exhibit dynamic amplification which may exceed that experienced for a single vehicle when a vehicle enters the bridge while it is still in motion from the previous vehicle crossing. But vehicles also present damping sources and will generally serve to reduce bridge vibration and thus dynamic amplification as they become more numerous on the bridge (simultaneously).

This is echoed by simulations of truck platoons, which suggest that platooned vehicles present no greater risk to increased bridge dynamics than posed by other traffic conditions because it only takes a single previous truck to induce the bridge conditions that result in maximum dynamic amplification.

Similarly, the amplification experienced when multiple lanes are occupied would be less than if only a single vehicle is present. Therefore, the conservatism introduced by considering loading in multiple lanes is further increased if dynamic amplification for a single vehicle is implemented. It should be stressed that even though multiple vehicles, when present on the bridge simultaneously, serve to reduce the level of dynamic amplification, it is still present and should be considered in analysis.

If the total response of the bridge is to be minimized, spacing between sequential trucks should be such that the bridge has time to settle down. When performing analysis for platoons with very small headway spacing, the effect of the additional simultaneous vehicles should be included in a static analysis with an amplification factor as predicted for a single vehicle.

Estimations of dynamic amplification for a single vehicle event should consider the possibility that the bridge may already have been excited by a previous vehicle. However, the additional amplification experienced by the bridge in this scenario is not likely to be more than 35% greater than that predicted for a single vehicle.

Chapter 19: Conclusions and Future Work

Conclusions

A case structure was extensively investigated through field testing and simulation. The results from field testing were used to validate FE models that were subsequently used to simulate VBI.

These investigations yielded the following conclusions:

- A validated 3D FE model is capable of simulating bridge-vehicle interaction if roadway profile is included and accurately positioned on the model.
- The observed vibrations may be principally attributed to the bridge deck roadway profile. The vehicle is excited by the profile, which in-turn excites the bridge.
- The high dynamic amplification does not seem to pose a risk to the structure's performance (at strength or service limit states).
- The bridge exhibits dynamic amplification in excess of 1.75 even under heavy vehicles (compared to AASHTO recommended 1.33).

The VBI simulation methods validated in Part 1 were used to develop and validate a simplified VBI model that reduced the bridge to a single degree of freedom. This model was leveraged to investigate the role of influential parameters on VBI from which the following conclusions may be gleaned:

- Amplification factors determined from displacement measurements will be greater (more conservative) than those determined from strain measurements.
- Ignoring the interaction of vehicle and bridge (i.e. computing contact force without consideration of the bridge) results in conservative estimates of bridge response.

- Bridge responses are greatest when the profile induces oscillation in the vehicle close to the bridge's natural frequency and when the vehicle's natural frequency is 10-20% greater than that of the bridge.
- Position of the profile and phase angle distribution for harmonic components have significant effect on bridge response.
- Current roughness metrics (e.g. IRI and ISO 8608) cannot reliably predict dynamic amplification.

The simulation tools developed in Part 2 were further leveraged through a series of parametric studies to generate recommendations related to roadway smoothness criteria and repeated vehicle loading (truck platooning). Key findings include:

- Rolling straightedge criteria with common limits (i.e. $1/8$ to $\frac{1}{4}$ inch deviation over 10 to 16 feet) are not effective at reducing dynamic amplification. Rolling-straightedge length should be no less than 16 feet for a specified deviation of $1/8^{\text{th}}$ inch, and no less than 30 feet for a specified deviation of $\frac{1}{4}$ inch.
- Traffic and truck platoons can result in increased dynamic amplification because even a single previous truck can induce the bridge conditions (motion) that result in increased dynamic response ($\approx 20\%$).
- As spacing between vehicles decreases and more vehicles are present on the bridge, the static load effect increases, but the dynamic amplification will likely be less than what would occur for a single vehicle.
- When designing for truck platoons, if static analysis accounts for multiple simultaneous vehicles, the dynamic amplification factor for a single vehicle can be used to conservatively account for the total dynamic response.

- Dynamic amplification for simultaneous loading of multiple lanes can be conservatively estimated as that for a single vehicle.

Future Work

The studies presented in this part are, by no means, exhaustive. Bridge type and geometry, vehicle characteristics and speed, and profile were selected to provide a reasonable upper bound for responses and dynamic amplification. Therefore, these results should be corroborated by larger scale studies that include a greater range of bridge types and parameter values. Furthermore, this thesis considered only harmonic profiles and a real profile from a single bridge and the bridge responses at midspan. Therefore, the following are suggestions for the continuation of this work.

- Perform simulations with a greater sample of real profiles as well as profiles with a bump at the beginning of the bridge and profiles with ramped approaches.
- Identify construction practices that produce harmonic profile content (e.g. paving machines).
- Evaluate the influence of VBI parameters on the dynamic amplification of responses at other locations and the dynamic amplification of shear.
- Perform simulations with a greater variety of vehicle parameters, preferably based on vehicle suspension population statistics.

The investigation of smoothness considered only rolling-straightedge criteria. Additional criteria should be developed and assessed that are appropriate for actual mitigation strategies (i.e. grinding).

Finally, the simplified models presented in Part 2 included only a single mode of vibration/deformation. The accuracy of these models, especially the 2-span model, could be improved by including more modes.

Appendix

Testing Equipment

Accelerometer

Table A 1: PCB 393A03 Model Specifications

Sensitivity:	($\pm 5\%$) 1000 mV/g ($102 \text{ mV}/(\text{m/s}^2)$)
Measurement Range:	$\pm 5 \text{ g pk}$ ($\pm 49 \text{ m/s}^2 \text{ pk}$)
Broadband Resolution:	0.00001 g rms (0.0001 m/s ² rms)
Frequency Range:	($\pm 5\%$) 0.5 to 2000 Hz
Electrical Connector:	2-Pin MIL-C-5015
Weight:	7.4 oz (210 gm)

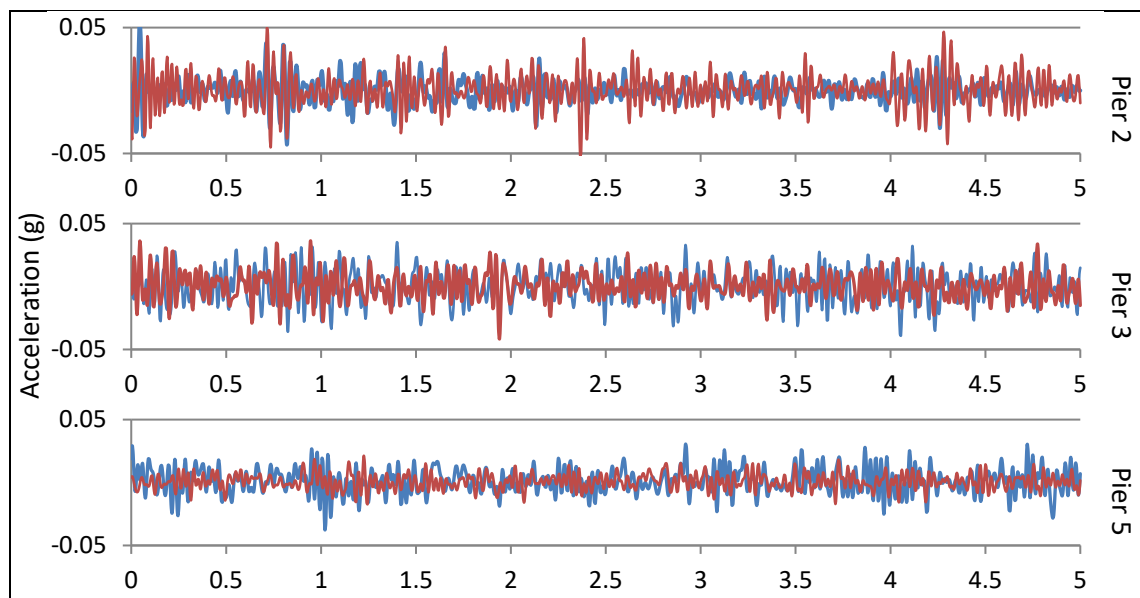
Strain Gauge

Table A 2: Geokon Model 4000 Specifications

Measurement Range:	3000 $\mu\epsilon$
Resolution:	1.0 $\mu\epsilon$
Accuracy:	$\pm 0.5\%$ F.S.
Nonlinearity:	<0.5% F.S.
Temperature Range:	-20°C to +80°C
Active Gauge Length	150 mm

Phase 1 Testing

Acceleration Data



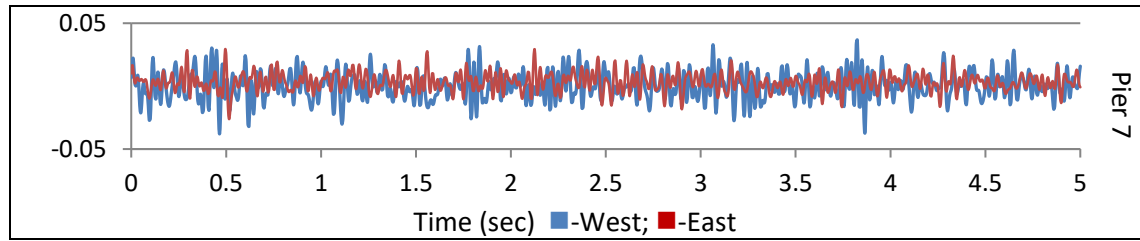


Figure A 1: Longitudinal acceleration of piers

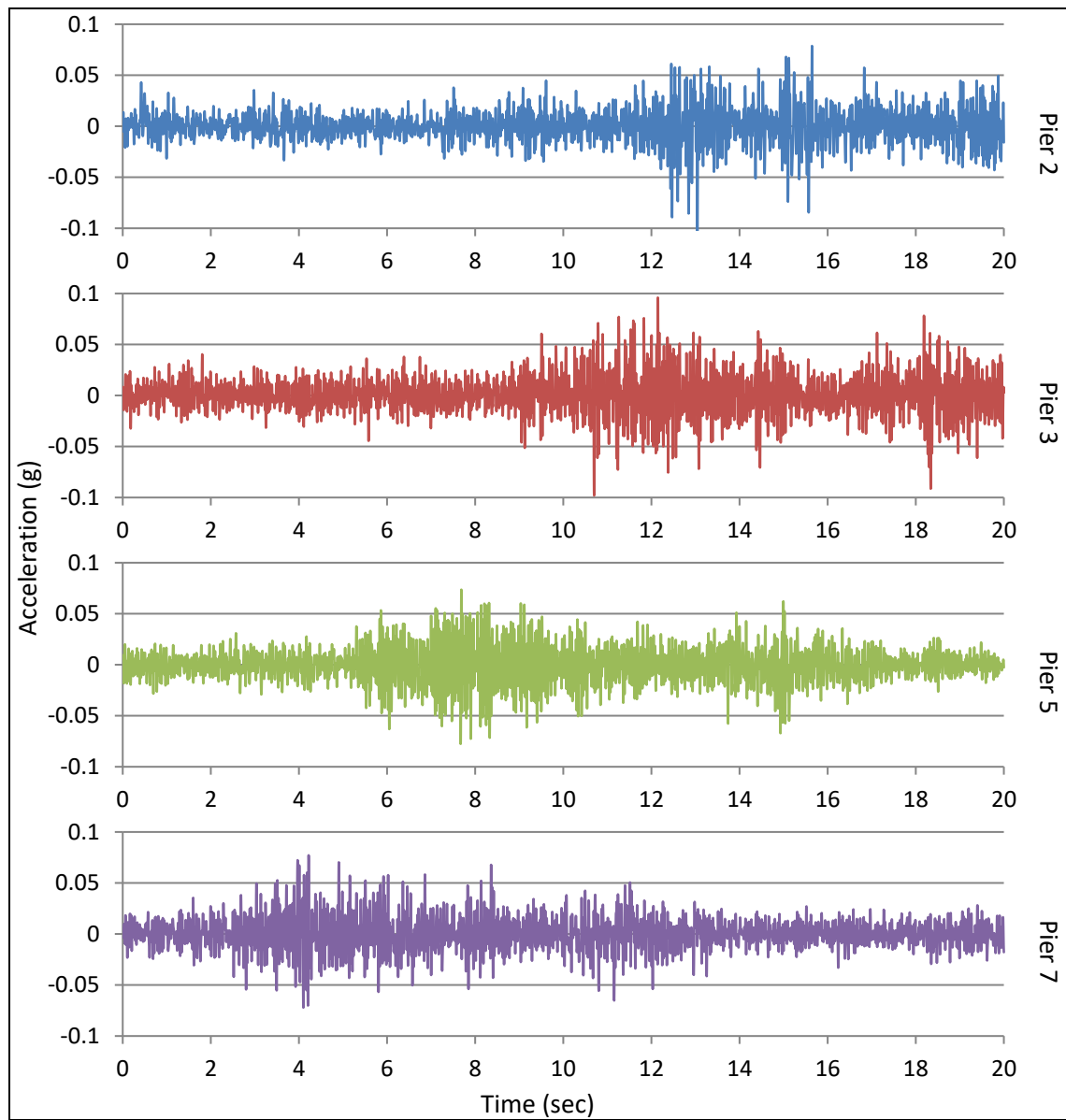


Figure A 2: Vertical acceleration of piers

Phase 2 Testing

Mode shapes

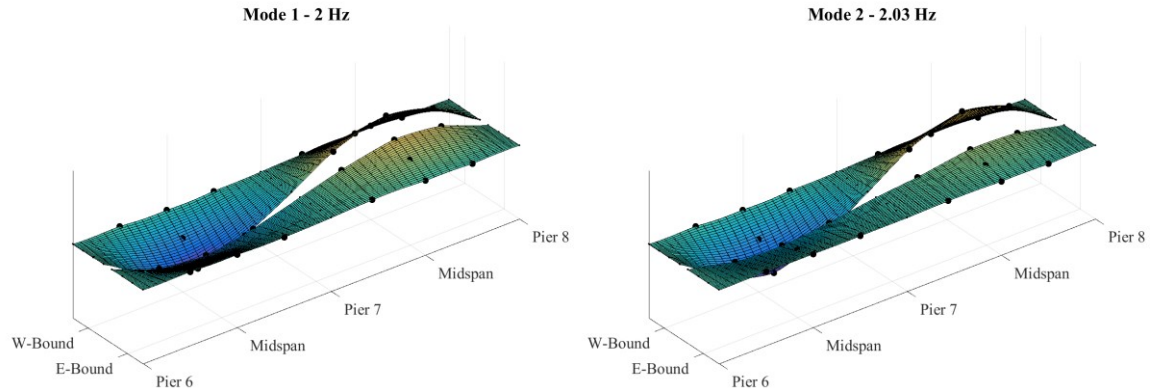


Figure A 3: Experimental Mode 1

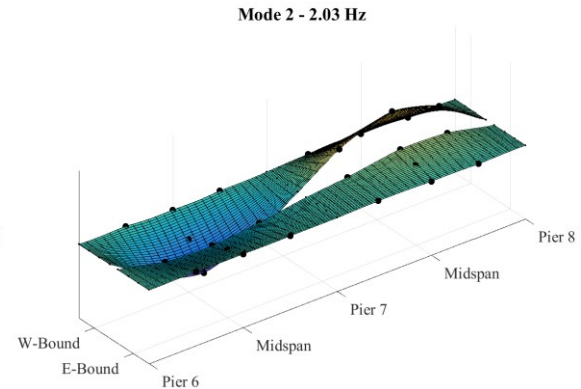


Figure A 4: Experimental Mode 2

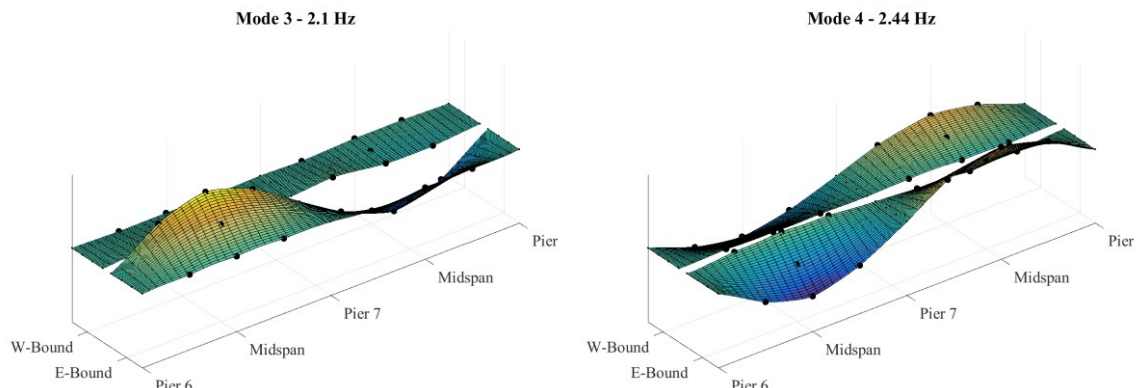
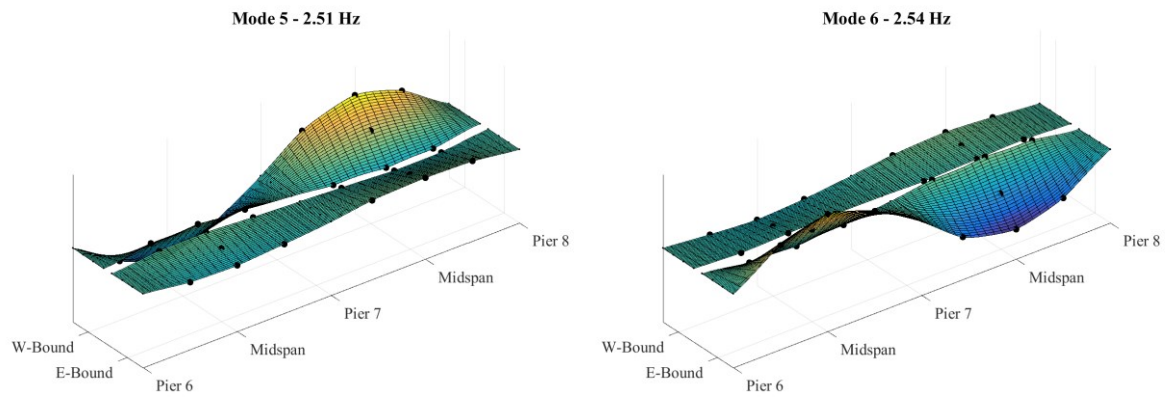
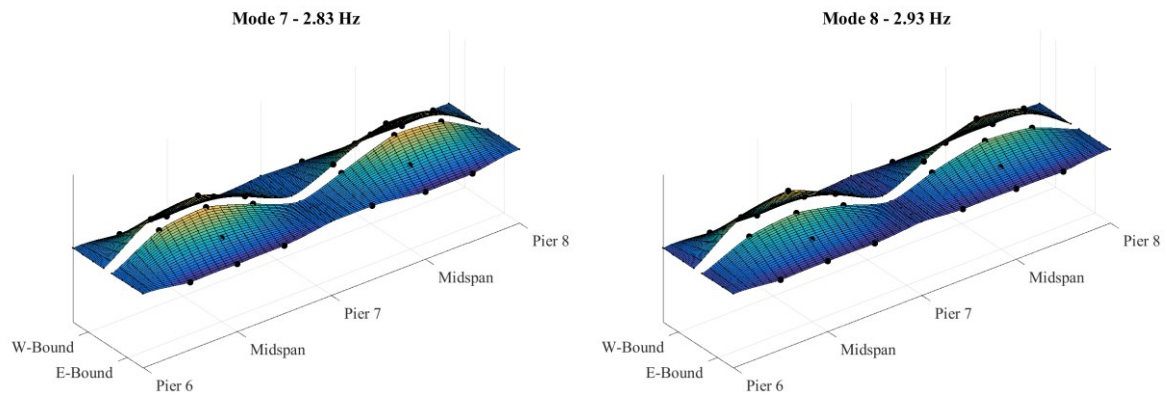
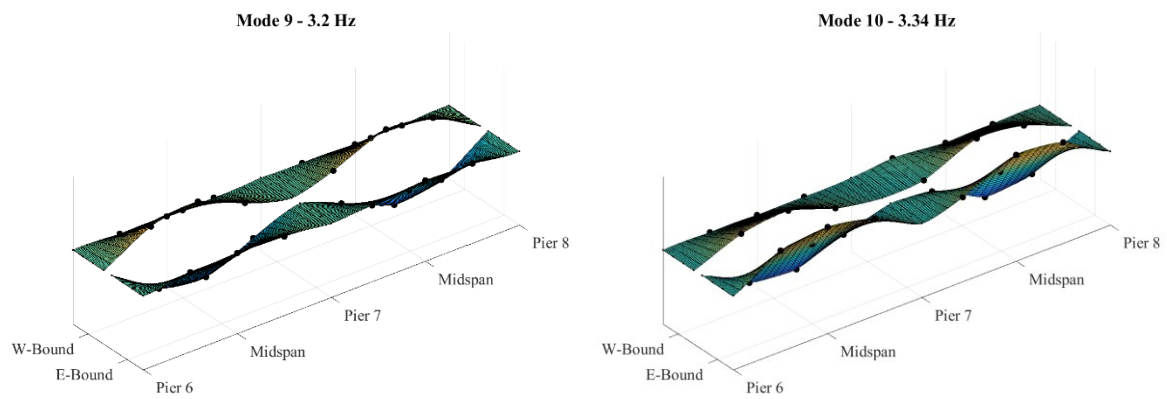
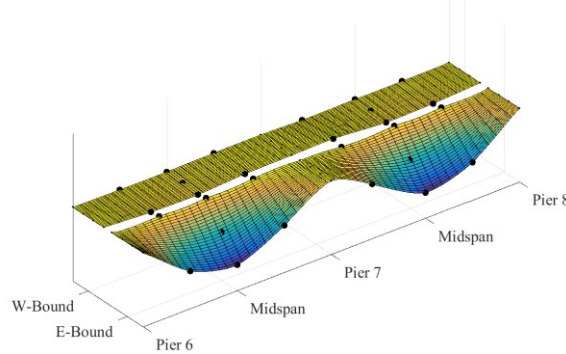
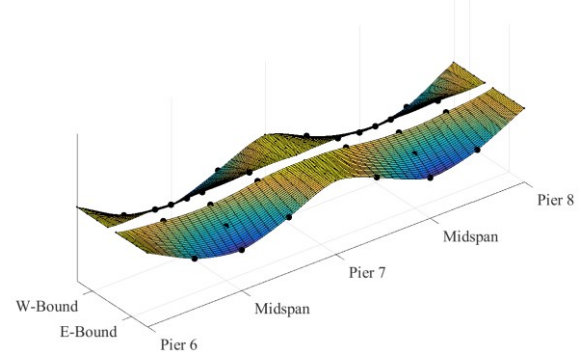
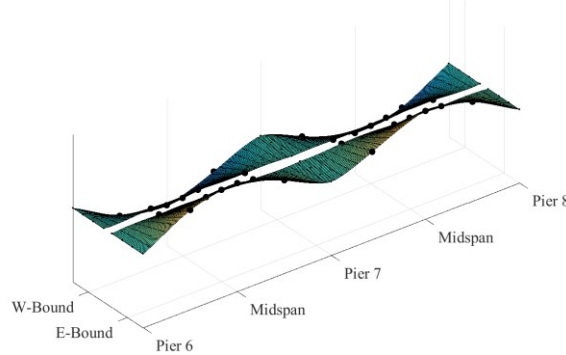
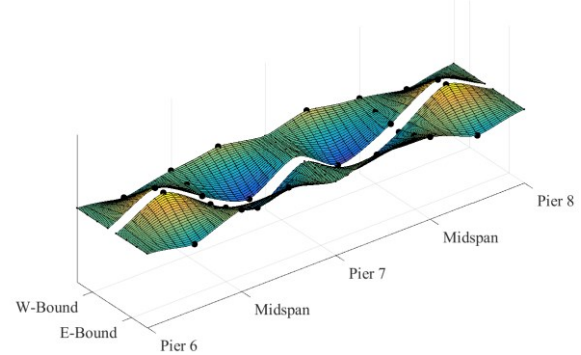
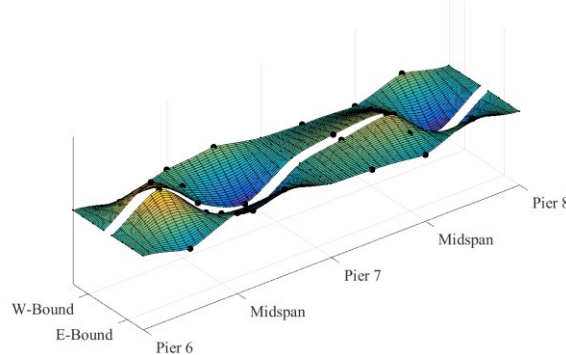
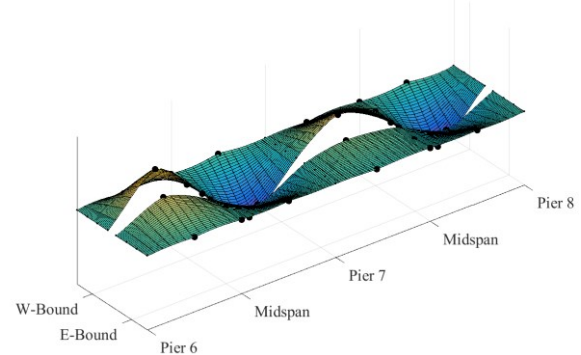


Figure A 5: Experimental Mode 3

Figure A 6: Experimental Mode 4

**Figure A 7: Experimental Mode 5****Figure A 8: Experimental Mode 6****Figure A 9: Experimental Mode 7****Figure A 10: Experimental Mode 8****Figure A 11: Experimental Mode 9****Figure A 12: Experimental Mode 10**

Mode 11 - 3.52 Hz**Figure A 13: Experimental Mode 11****Mode 12 - 3.56 Hz****Figure A 14: Experimental Mode 12****Mode 13 - 3.56 Hz****Figure A 15: Experimental Mode 13****Mode 14 - 5.44 Hz****Figure A 16: Experimental Mode 14****Mode 15 - 5.69 Hz****Figure A 17: Experimental Mode 15****Mode 16 - 7.45 Hz****Figure A 18: Experimental Mode 16**

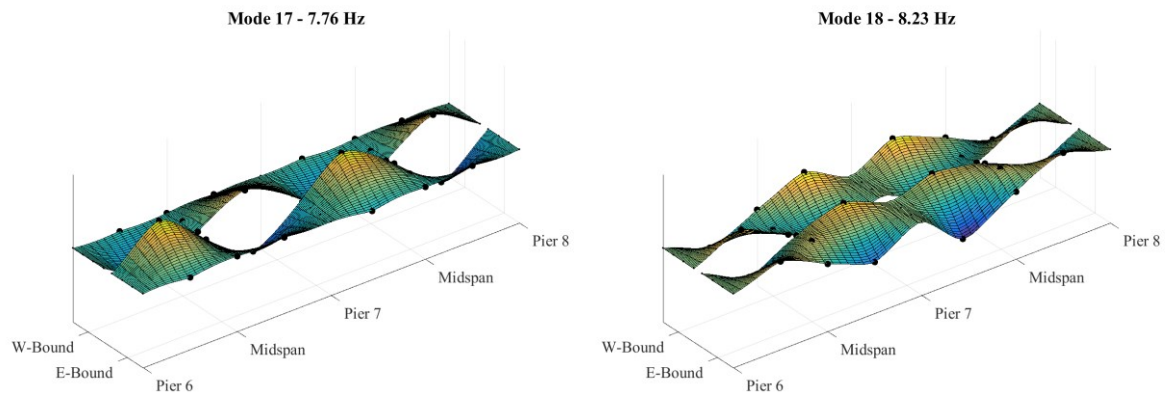
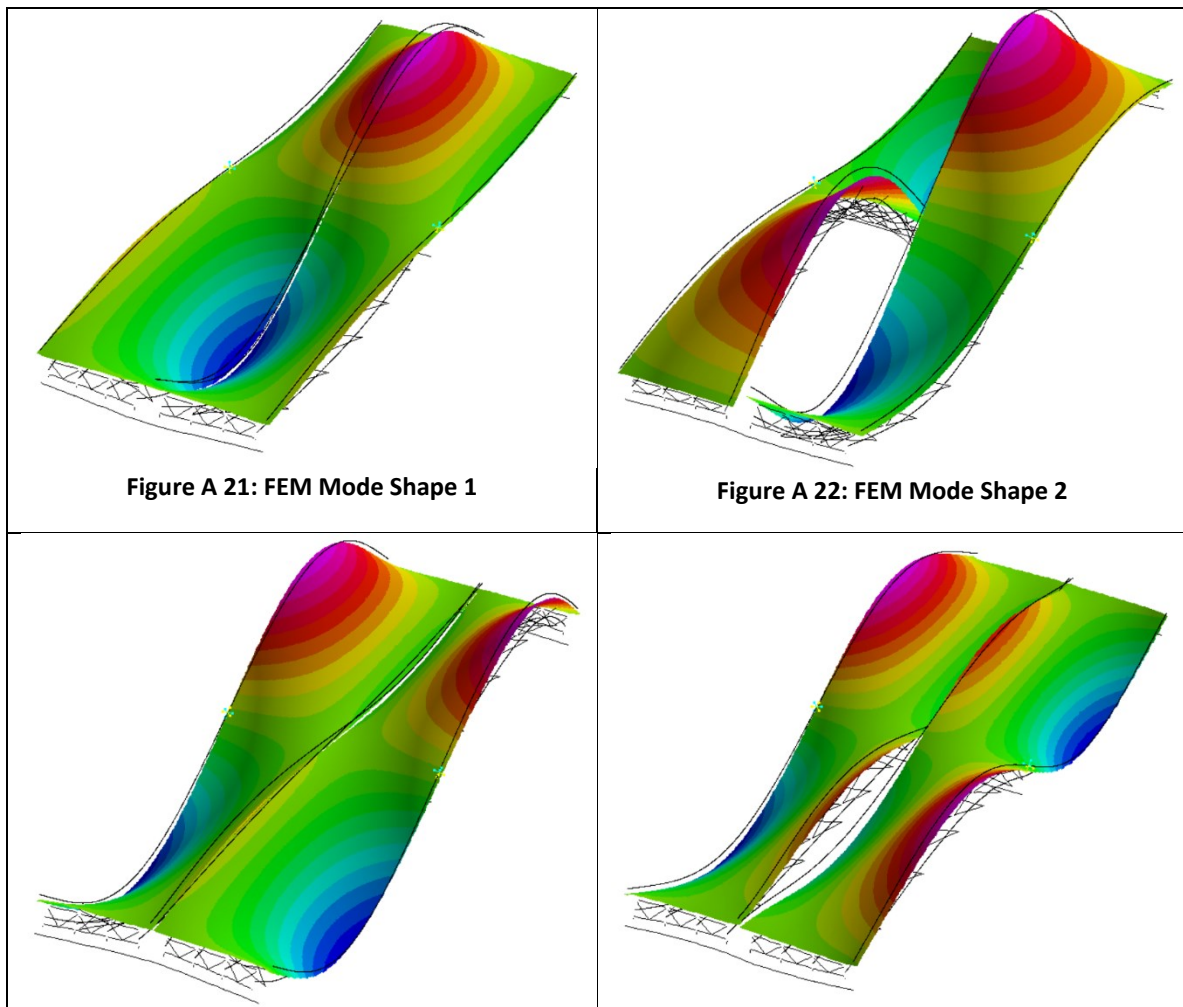


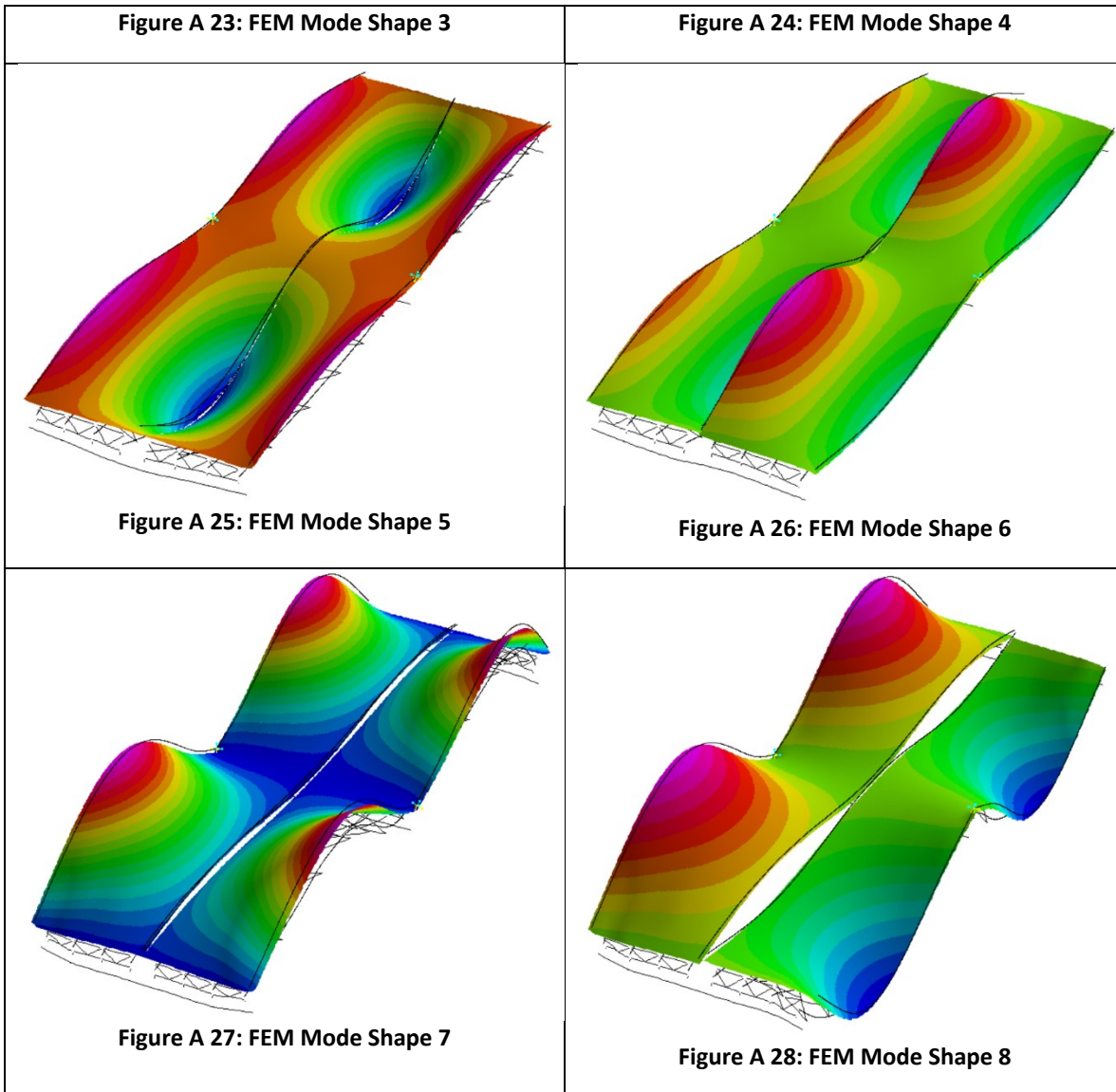
Figure A 19: Experimental Mode 17

Figure A 20: Experimental Mode 18

Phase 2 FE Model Validation

Calibrated FE Model Mode Shapes





Methods of Performing Load Rating through Refined Analysis

Model Building

- Models are geometrically consistent with the real structure (e.g. elements located at centerline)
- Girders are modeled with 2-node beam elements
- Diaphragms are modeled with 2-node beam elements (or arrangement of beam elements)
- Deck and sidewalk are modeled with 3 and 4 node shell elements
- Barriers may be modeled with 2-node beam elements
- Continuity is enforced with rigid links so as to maintain realistic geometry

- Conservative Boundary Conditions for rating (minimal realistic restraint while maintaining stability). For example:
 - No rotational restraint
 - Long. Restraint at exterior bearings (1 end)
 - Translational restraint at center bearing (1 end)
 - Vertical restraint at all bearings
- Composite Action is modeled as elements connecting deck and girders.
 - Rigid Links, or...
 - Connection Elements (If updating of composite action is desired)
- Beam Discretization and Deck Meshing
 - Beam Discretization should be on the order of 1/4 the girder spacing, and as consistent as reasonably possible
 - Deck meshing should have an aspect ratio less than 2:1, and no elements shall have an aspect ratio greater than 3:1
 - Quad shell elements should have no internal angle greater than 45 degrees
 - The deck meshing should match the beam discretization longitudinally
- Non-structural mass (e.g. wearing surface) may be modeled as point non-structural mass at appropriate nodes and equivalent to the mass of the component being represented.

Model Error Screening

- A natural frequency analysis shall be performed on the completed model. The first several modes shall be examined for local deformations which suggest discontinuities or improper stiffness assignments. Sufficient number of modes shall be analyzed such that at least 4 global modes are identified.
- The deflected shape under multiple load cases (dead load and live load) shall be examined for atypical behavior (e.g. nonsymmetrical deformation, unintended breaks or discontinuities).
- When further error screening is deemed necessary (recommended for any manually constructed model) the following procedures may be performed:
 - Manual calculation of structure weight shall be compared to the sum of dead load vertical reactions.
 - FE responses (e.g. deflection, moment, etc.) under simple load cases shall be compared to the corresponding theoretical responses for single line girder models (i.e. approximate analysis)

Model Loading and Result Extraction

- Dead Load consists of the weight of the deck, girders, and diaphragms and is carried by the structure with an uncured deck. Thus, the stiffness of the deck, sidewalk and

barriers is turned off for this load case (i.e. Modulus of elasticity set to 0 or arbitrarily low value that does not produce numerical errors).

- Superimposed Dead Load consists of the weight of the barriers and sidewalk after the deck has cured. Therefore, the stiffness of the deck is set to its nominal value, while sidewalk and barriers should have stiffness turned off.
- Live Load (and Wearing Surface when applicable) is carried by the completed structure. Stiffness of all acting mechanisms is included, unless certain mechanisms are to be considered inactive (e.g. stiffness of barriers and sidewalks turned off).
- Wheel loads shall consist of point loads placed on the deck element at the appropriate locations (center of tire).
- Lane loads may consist of point loads on all deck nodes within the lane load region such that the total load applied is equal to the distributed load specified.
- Composite moment may be calculated by the following equation:

$$M_c = M_1 + F_A * \frac{D + t_D}{2} \quad (\text{A } 1)$$

Where:

M_1 = Principle Bending Moment

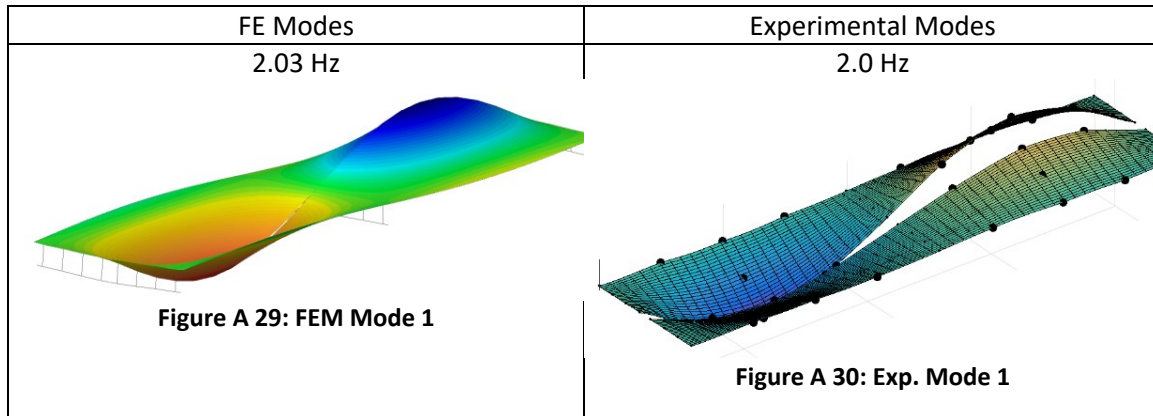
F_A = Axial Force

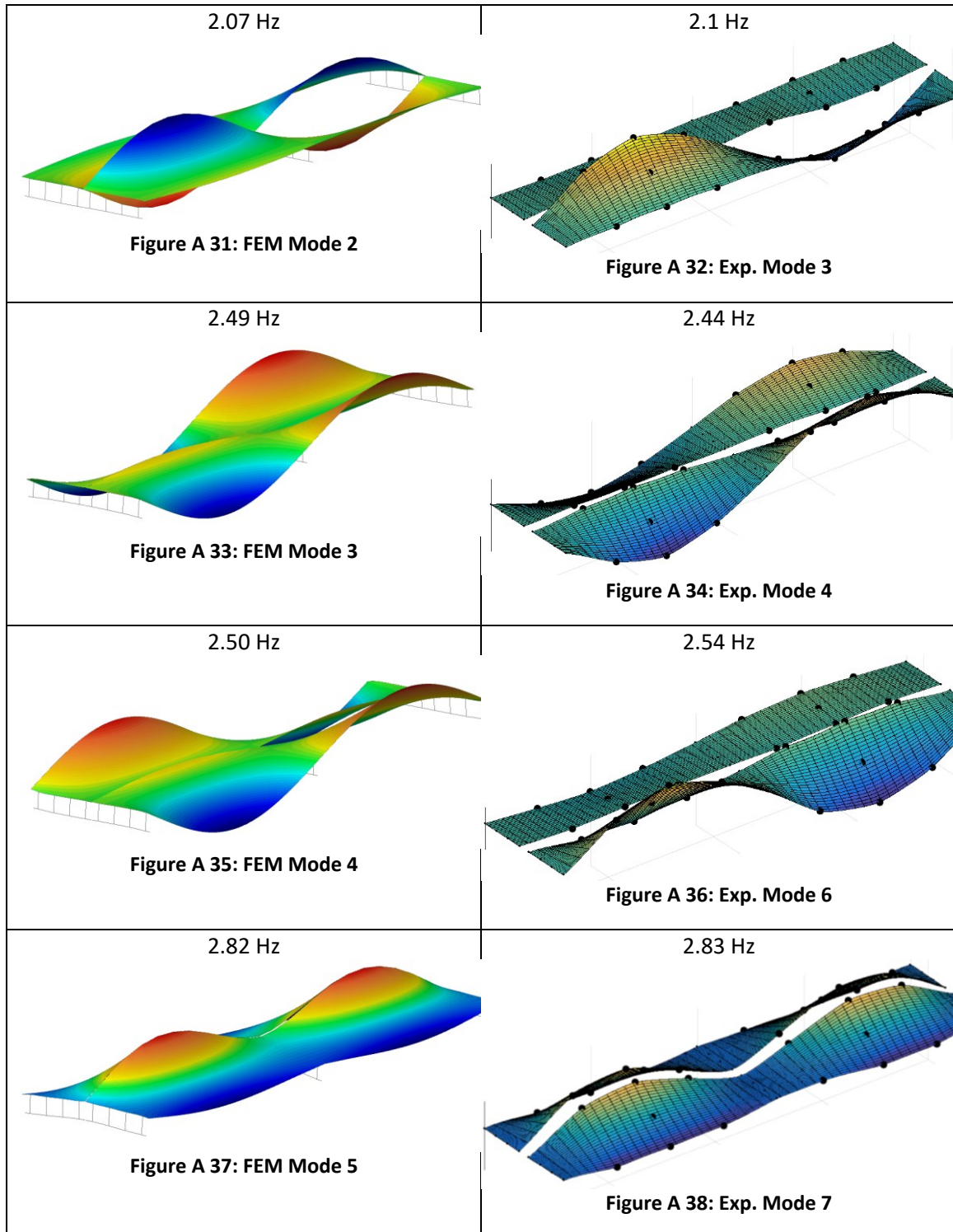
D = Girder Depth

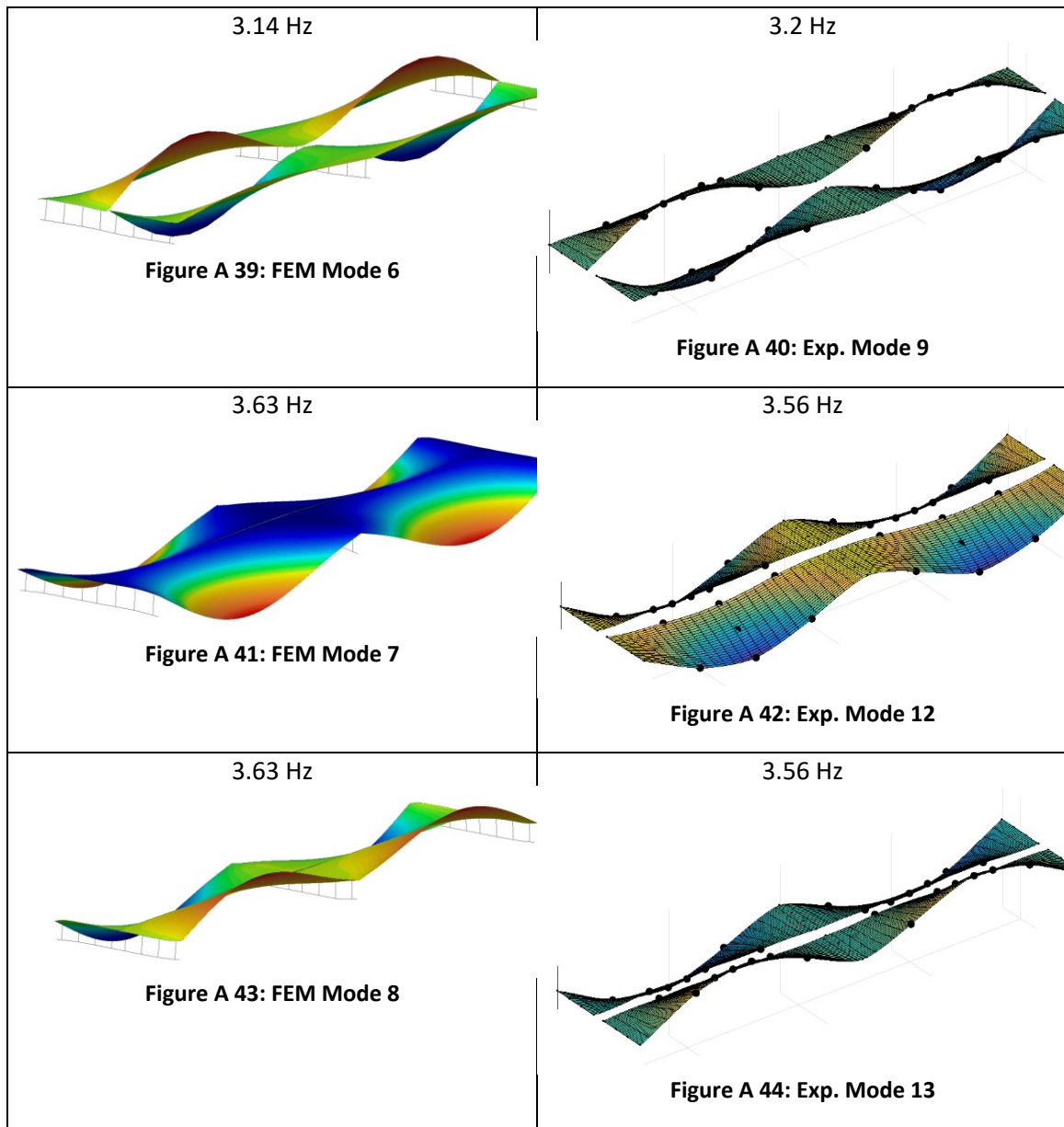
t_D = Deck Thickness

Phase 3

Comparison of Experimental and FEM Mode Shapes







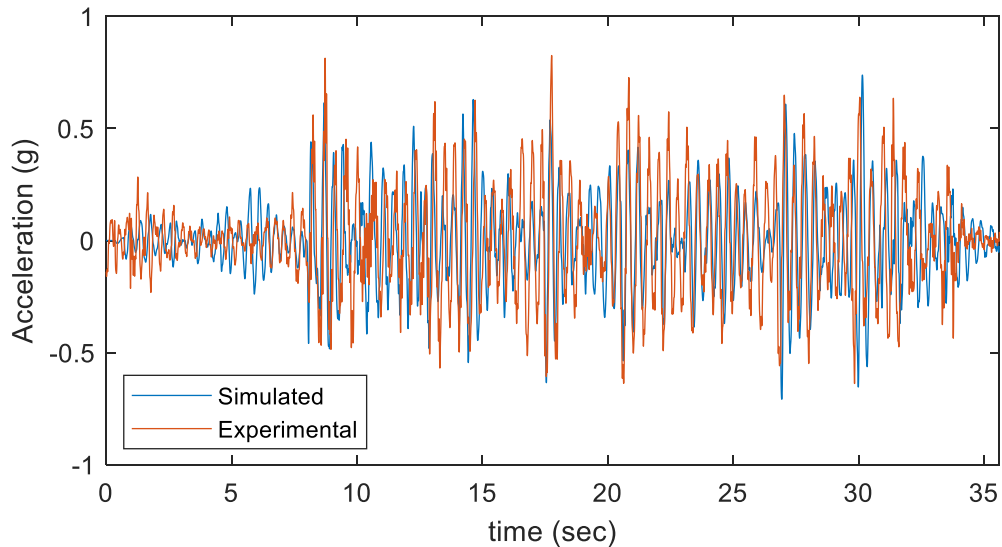
VBI Modeling Validation

Table A 3: Error of Maximum Responses for Experiment vs Simulation

	Run 3			Run 14		
	Max Exp.	Max Sim.	%Diff.	Max Exp.	Max Sim.	%Diff.
Truck (Avg. Rear)	0.9352	0.6345	-32.15%	0.825	0.738	-10.58%
Span 2	0.0750	0.0890	18.58%	0.137	0.210	53.61%
Span 3	0.1177	0.1190	1.09%	0.162	0.225	38.31%
Span 4	0.1055	0.1230	16.68%	-	-	-
Span 7	0.0705	0.0926	31.48%	0.100	0.168	68.84%

Table A 4: Error of Minimum Responses for Experiment vs Simulation

	Run 3			Run 14		
	Min Exp.	Min Sim.	%Diff.	Min Exp.	Max Sim.	%Diff.
Truck (Avg. Rear)	-0.8044	-0.7861	-2.28%	-0.638	-0.708	11.02%
Span 2	-0.0713	-0.0875	22.71%	-0.129	-0.164	26.62%
Span 3	-0.1115	-0.1361	22.01%	-0.143	-0.220	53.68%
Span 4	-0.1115	-0.1187	6.47%	-	-	-
Span 7	-0.0798	-0.0827	3.60%	-0.094	-0.160	69.56%

Run 14 Acceleration Time Histories**Figure A 45: Experiment vs Simulation for Vehicle Acceleration over Bridge (Filtered and Decimated)**

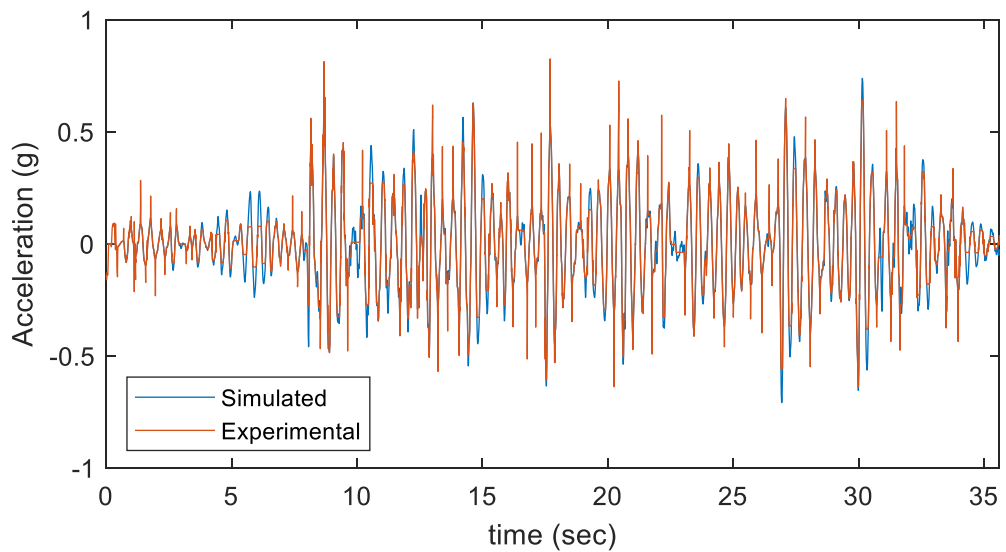


Figure A 46: "Warped" Experimental and Simulated Vehicle Acceleration

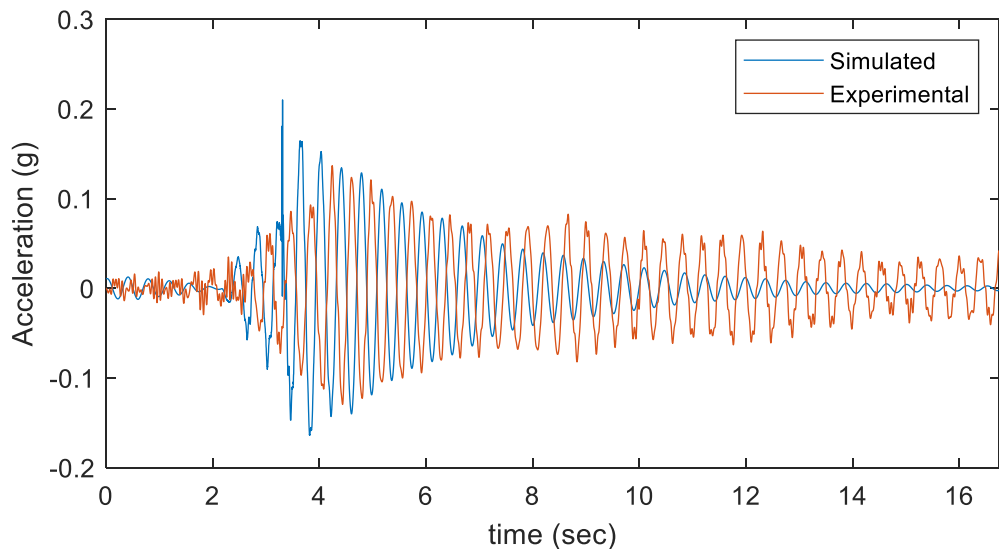


Figure A 47: Experiment vs Simulation for Span 2 Midspan Acceleration of Girder 8 (Filtered and Decimated)

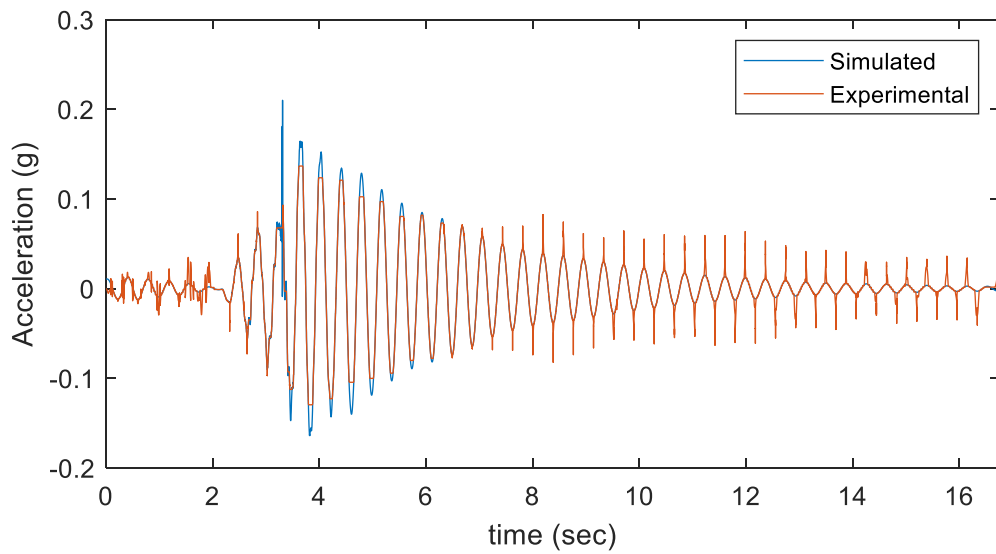


Figure A 48: Experiment vs Simulation for Span 2 Midspan Acceleration of Girder 8 (Dynamic Time Warped)

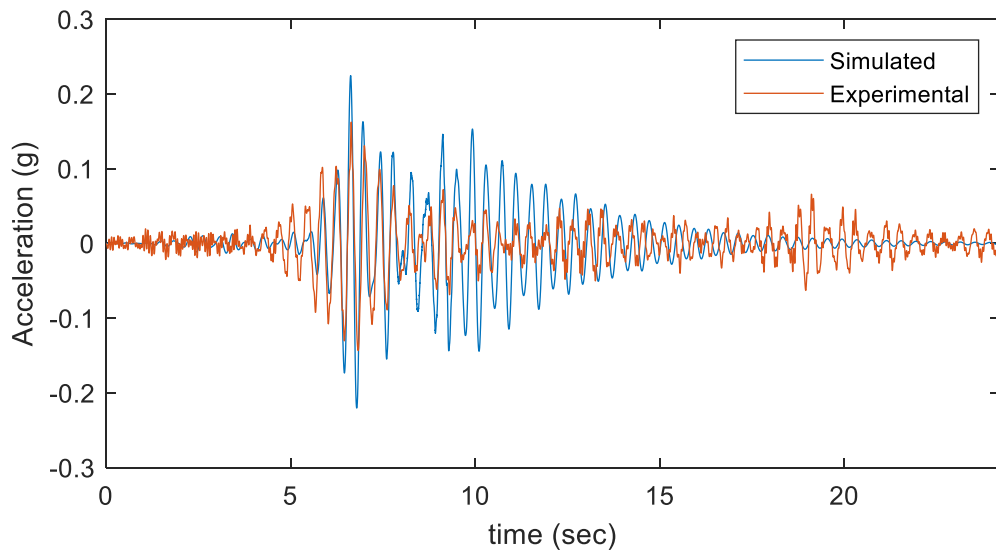


Figure A 49: Experiment vs Simulation for Span 3 Midspan Acceleration of Girder 8 (Filtered and Decimated)

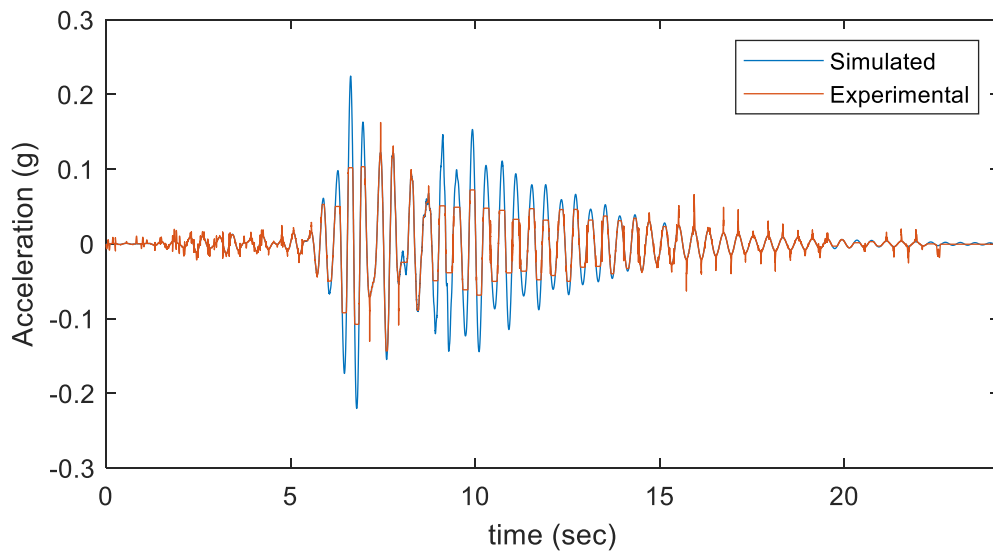


Figure A 50: Experiment vs Simulation for Span 3 Midspan Acceleration of Girder 8 (Dynamic Time Warped)

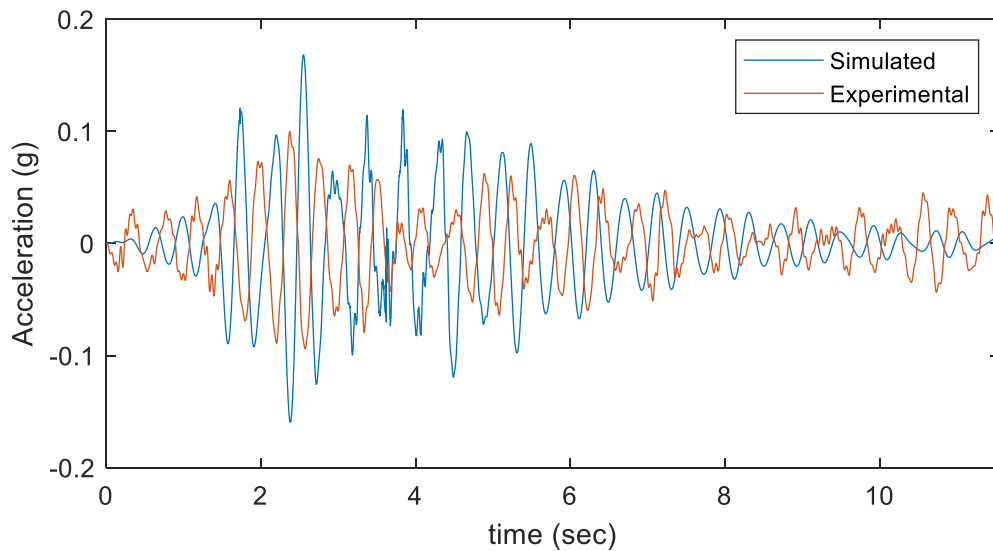


Figure A 51: Experiment vs Simulation for Span 7 Midspan Acceleration of Girder 8 (Filtered and Decimated)

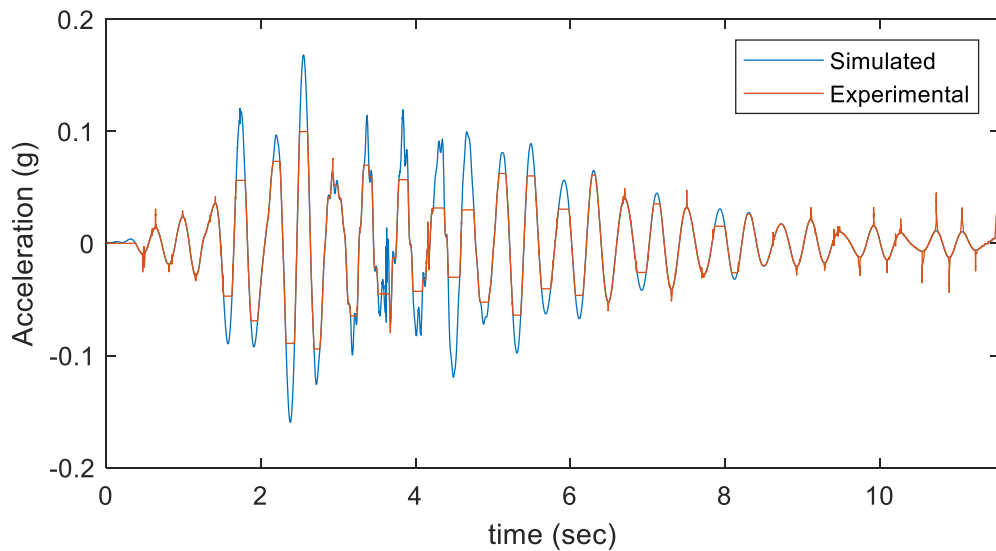


Figure A 52: Experiment vs Simulation for Span 7 Midspan Acceleration of Girder 8 (Dynamic Time Warped)

Run 3 Acceleration Time Histories

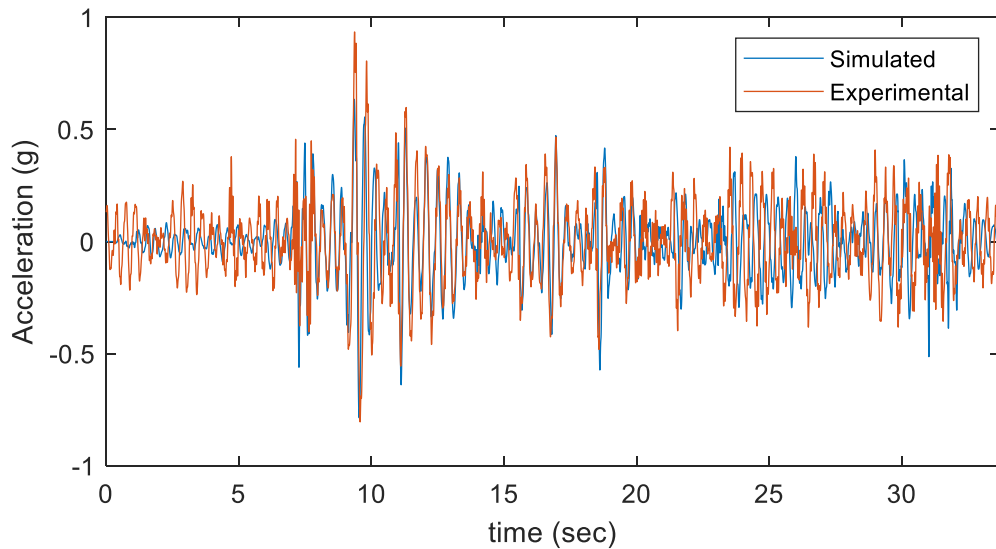


Figure A 53: Experiment vs Simulation for Vehicle Acceleration over Bridge (Filtered and Decimated)

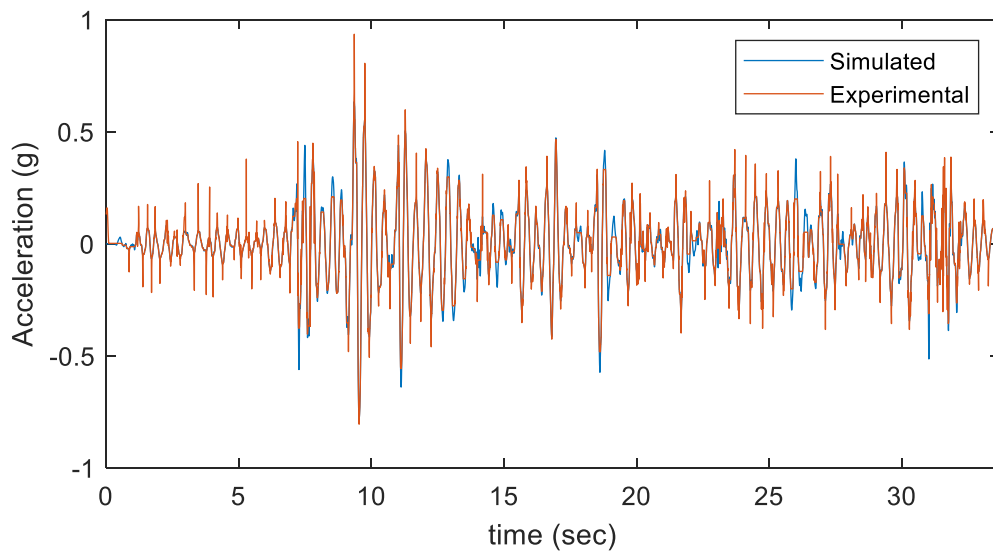


Figure A 54: "Warped" Experimental and Simulated Vehicle Acceleration

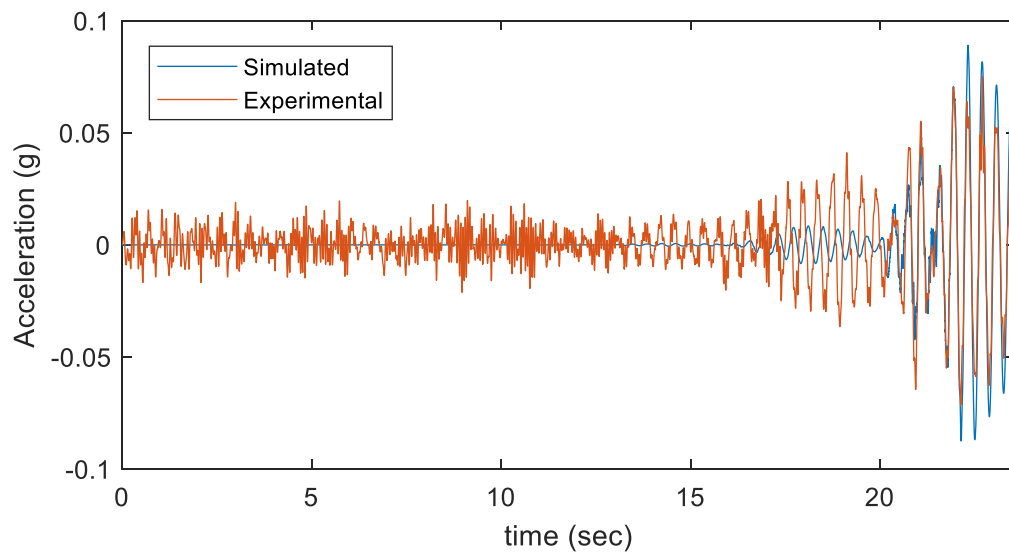


Figure A 55: Experiment vs Simulation for Span 2 Midspan Acceleration of Girder 8 (Filtered and Decimated)

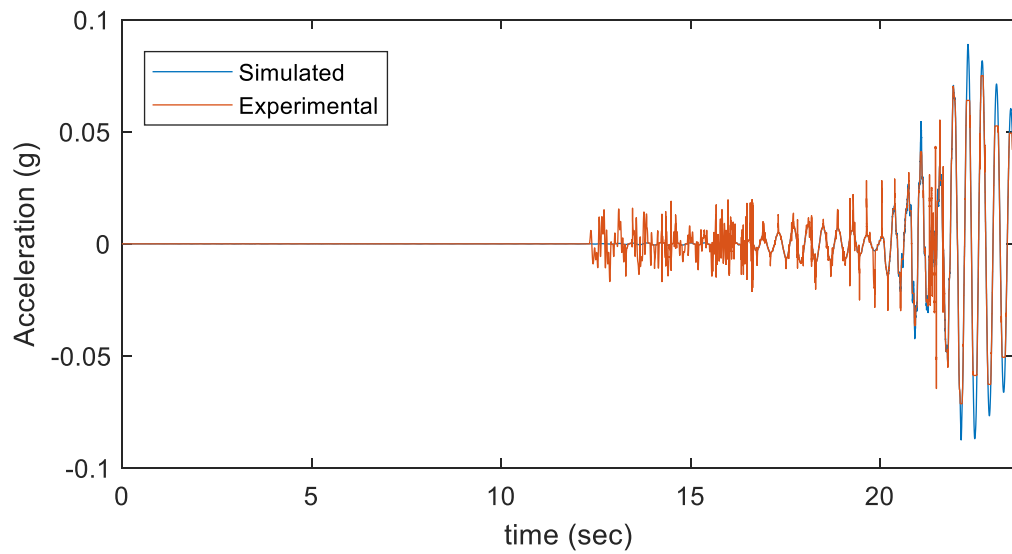


Figure A 56: Experiment vs Simulation for Span 2 Midspan Acceleration of Girder 8 (Dynamic Time Warped)

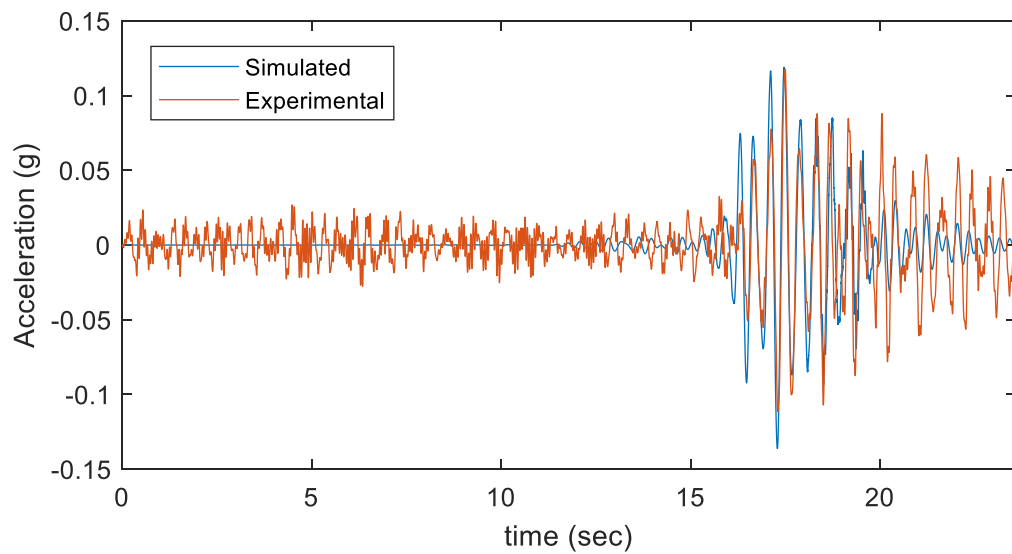


Figure A 57: Experiment vs Simulation for Span 3 Midspan Acceleration of Girder 8 (Filtered and Decimated)

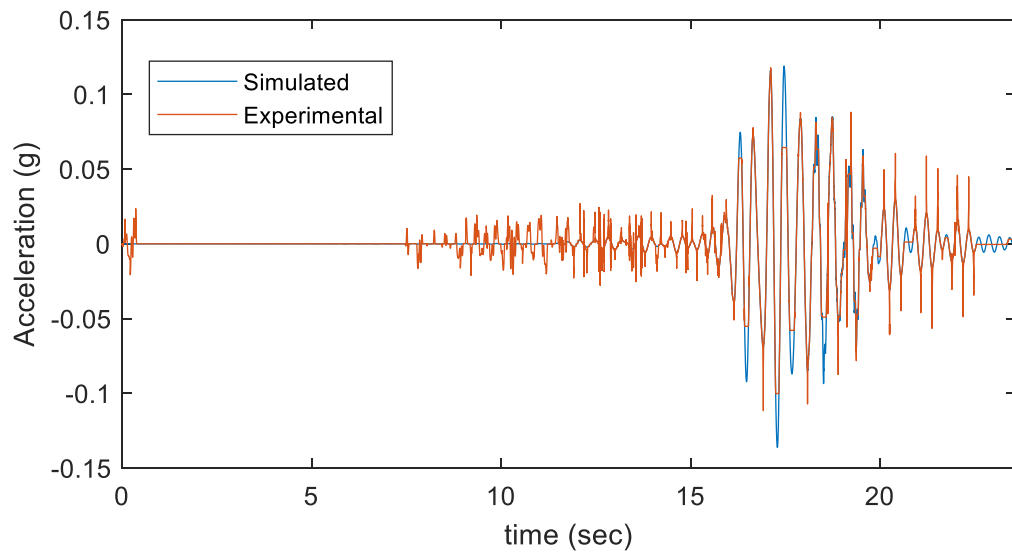


Figure A 58: Experiment vs Simulation for Span 3 Midspan Acceleration of Girder 8 (Dynamic Time Warped)

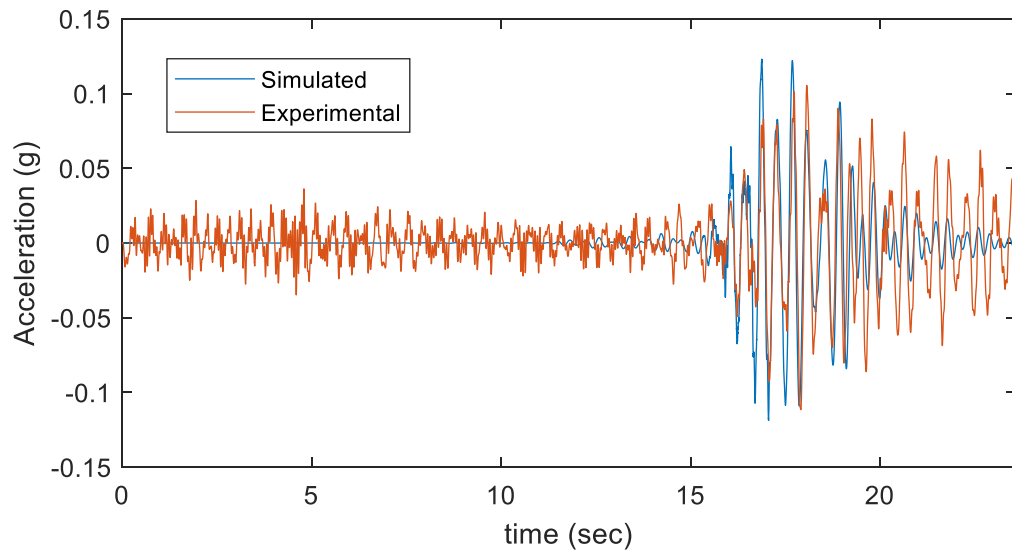


Figure A 59: Experiment vs Simulation for Span 7 Midspan Acceleration of Girder 8 (Filtered and Decimated)

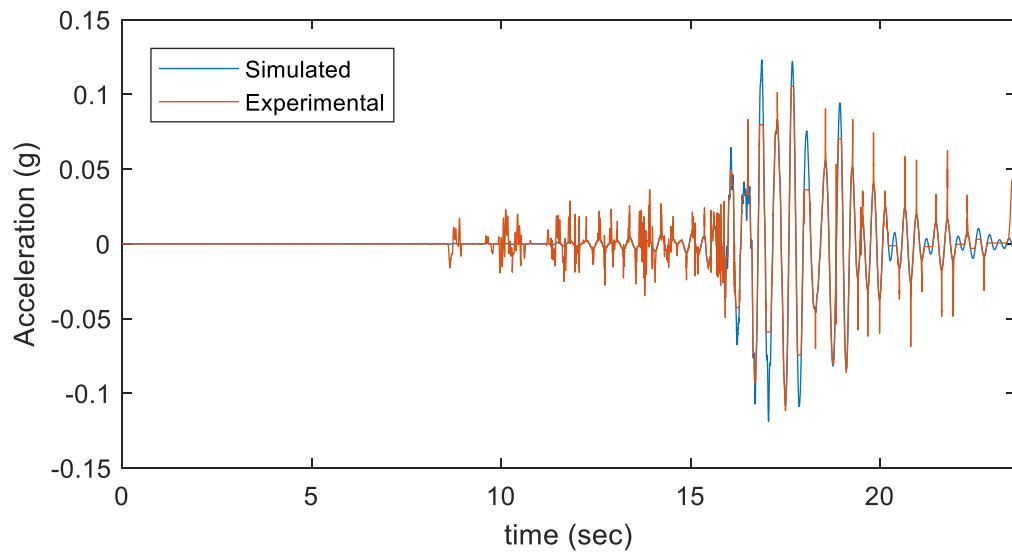


Figure A 60: Experiment vs Simulation for Span 7 Midspan Acceleration of Girder 8 (Dynamic Time Warped)

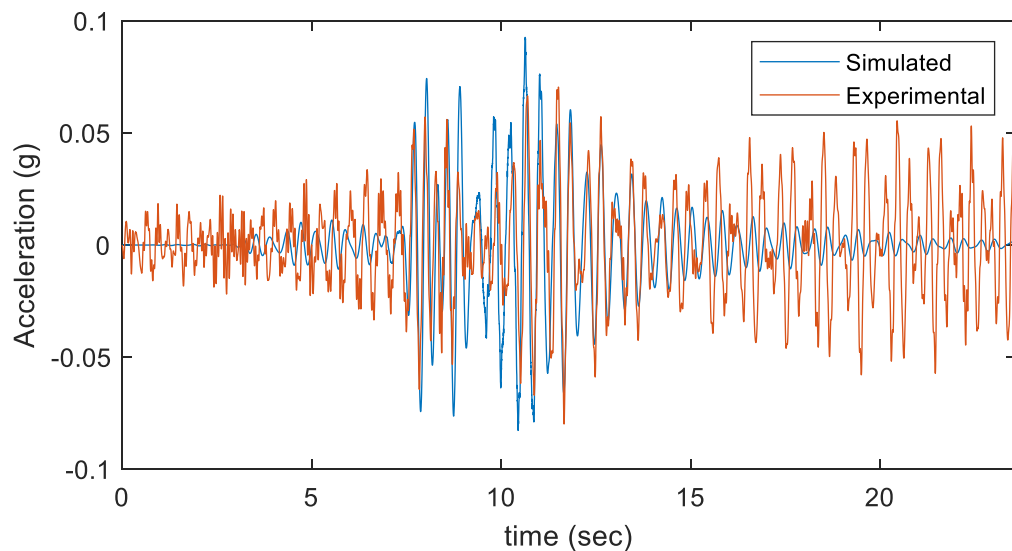


Figure A 61: Experiment vs Simulation for Span 8 Midspan Acceleration of Girder 8 (Filtered and Decimated)

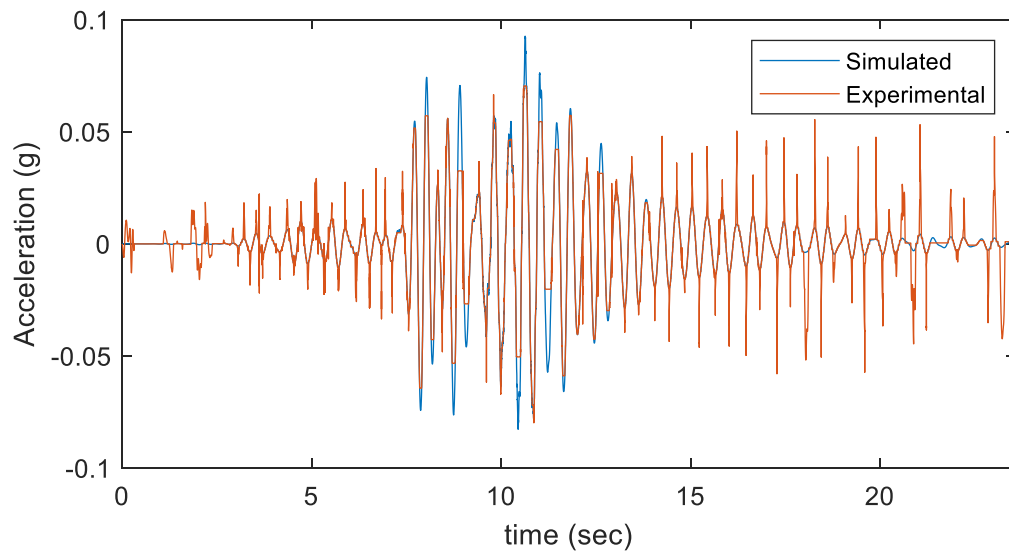


Figure A 62: Experiment vs Simulation for Span 8 Midspan Acceleration of Girder 8 (Dynamic Time Warped)

State-Space Model Validation

Validation of the 2-DOF state-space models was performed by comparing responses to those predicted by 2D FE models of the beams. The following lists the beam parameters as assigned in the state-space model.

Table A 5: Model parameters for model validation

Bridge/Beam Parameters		Vehicle/Sprung Mass Parameters	
Length	1200 in	Mass	100 slinch
EI	7.50E+12 lb-in ²	Spring K	6.32E+04 lb/in
Total Mass	460000 lb	Damping Coefficient	502.65 lb-s/in
Length	1200 in		

The FE models were constructed with 2D Kirchhoff beam elements which are parabolically curved thin beam elements in which shear deformations are excluded. The beams were discretized with a mesh length of 6 inches. The elements were assigned the following attributes.

Table A 6: FEM Beam Attributes

Moment of Inertia (I)	1500	in ⁴
Cross sectional area (A)	10	in ²
Modulus of Elasticity (E)	5.00E+09	psi
Material Density	0.099286	slinch/in ³

The sprung-mass in the FE model was assigned the same attributes as listed for the state-space model.

The profile was constructed using ISO 8608 standards whereby two parameters describe the frequency content of the profile. For these simulations a profile was constructed with a roughness coefficient (C_{10}) of 300 and a waviness (w) of -2. A profile with these parameters would be categorized as average according to ISO 8608. The profile was located such that the beam began at the profile's distance of 100 feet.

The sprung mass was assigned a velocity of 720 in/sec. Its path began 100 feet before the beam at the beginning of the profile. The state-space model evaluated each state in increments of 1 inch thus resulting in a time-step of 0.0014 sec. The FE simulations were performed with a time-step of 0.0015 sec.

Comparison of state-space to FEM for single-span

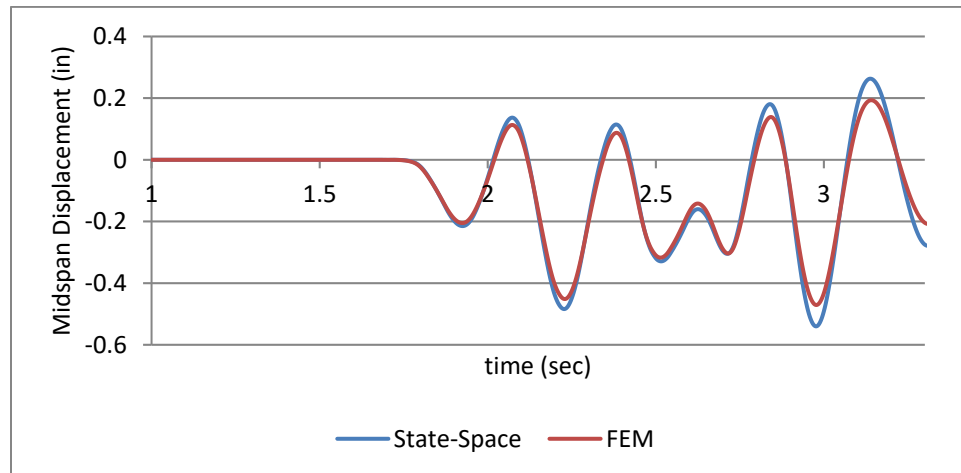


Figure A 63: Comparison of midspan displacement

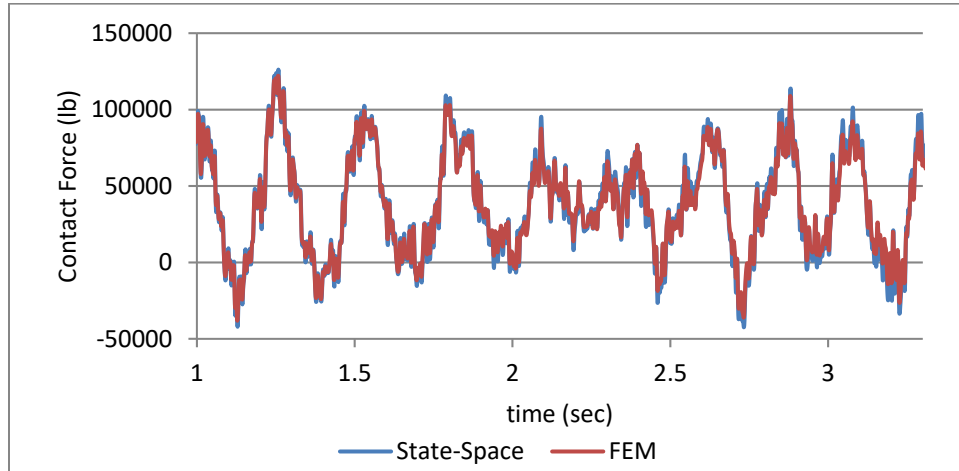


Figure A 64: Comparison of force at vehicle contact point

Comparison of state-space to FEM for two-span continuous

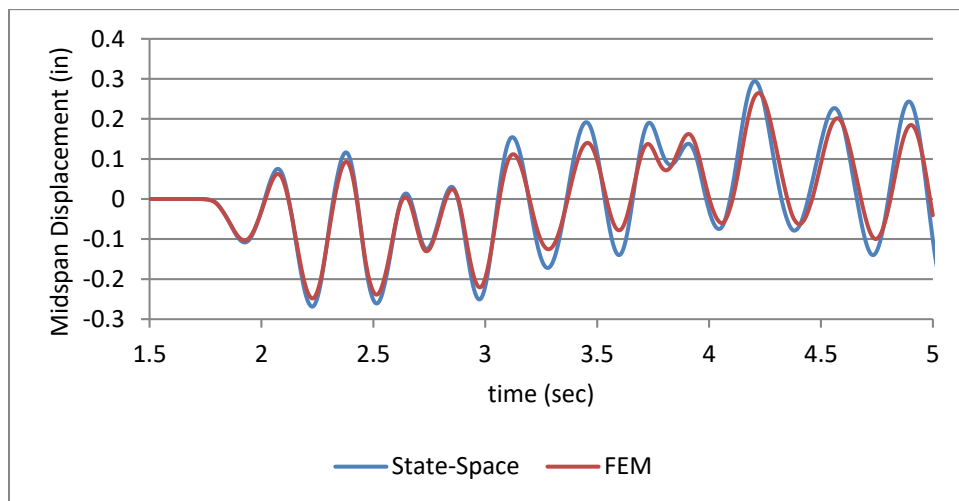


Figure A 65: Comparison of midspan (span 1) displacement

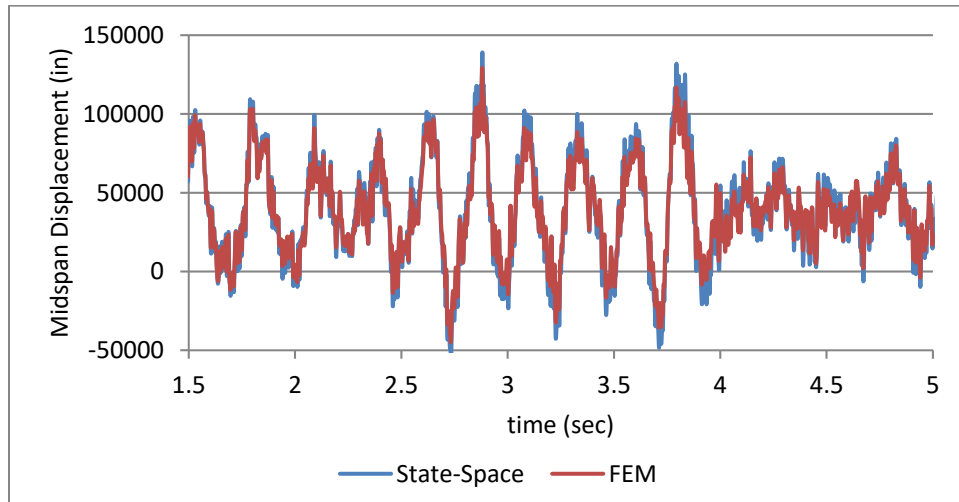


Figure A 66: Comparison of force at vehicle contact point

Simulation of VBI with Traffic

Table A 7: Spring-mass configurations for traffic patterns

1		2		3		4		5		6	
Location (in)	Axle #										
0	6	0	2	0	9	0	9	0	4	0	4
-168	5	-168	1	-192	8	-192	8	-168	3	-168	3
-432	5	-336	1	-264	8	-264	8	-528	3	-528	3
-1260	2	-2028	6	-540	7	-540	7	-2676	2	-17220	12
-1428	1	-2196	5	-612	7	-612	7	-2844	1	-17316	12
-1596	1	-2460	5	-3096	2	-2496	14	-3012	1	-21672	12
-1860	6	-4260	14	-3264	1	-2664	14	-6816	9	-21768	12
-2028	5	-4428	14	-3432	1	-4584	11	-7008	8	-35880	9
-2292	5	-5568	12	-5208	6	-4764	10	-7080	8	-36072	8
-2880	9	-5664	12	-5376	5	-4824	10	-7356	7	-36144	8
-3072	8	-6828	2	-5640	5	-9192	12	-7428	7	-36420	7
-3144	8	-6996	1	-7752	13	-9288	12	-10320	13	-36492	7
-3420	7	-7164	1	-7872	13	-11100	6	-10440	13	-43068	14
-3492	7	-8772	13	-9396	6	-11268	5	-12408	14	-43236	14
-4632	12	-8892	13	-9564	5	-11532	5	-12576	14	-47508	2
-4728	12	-10860	12	-9828	5	-13092	13	-16788	4	-47676	1
-5640	14	-10956	12	-11520	11	-13212	13	-16956	3	-47844	1
-5808	14	-11760	6	-11700	10	-15780	12	-17316	3	-56724	14
-6960	12	-11928	5	-11760	10	-15876	12	-22140	9	-56892	14
-7056	12	-12192	5	-12672	11	-18036	14	-22332	8	-61128	6
-8064	11	-14148	4	-12852	10	-18204	14	-22404	8	-61296	5

-8244	10	-14316	3	-12912	10	-21132	4	-22680	7	-61560	5
-8304	10	-14676	3	-15180	4	-21300	3	-22752	7	-75024	11
-8904	12	-16632	2	-15348	3	-21660	3	-26928	9	-75204	10
-9000	12	-16800	1	-15708	3	-25524	13	-27120	8	-75264	10
-10092	11	-16968	1	-17316	12	-25644	13	-27192	8	-84300	11
-10272	10	-18336	4	-17412	12	-28644	14	-27468	7	-84480	10
-10332	10	-18504	3	-19740	11	-28812	14	-27540	7	-84540	10
-10680	9	-18864	3	-19920	10	-30504	9	-29844	2	-98004	12
-10872	8	-19824	14	-19980	10	-30696	8	-30012	1	-98100	12
-10944	8	-19992	14	-23040	13	-30768	8	-30180	1	-102528	2
-11220	7	-21540	2	-23160	13	-31044	7	-33036	6	-102696	1
-11292	7	-21708	1	-24312	12	-31116	7	-33204	5	-102864	1
-12204	6	-21876	1	-24408	12	-35664	11	-33468	5	-109392	14
-12372	5	-23760	6	-25596	11	-35844	10	-39420	6	-109560	14
-12636	5	-23928	5	-25776	10	-35904	10	-39588	5	-122256	2
-13584	12	-24192	5	-25836	10	-37584	12	-39852	5	-122424	1
-13680	12	-25716	9	-28620	6	-37680	12	-44664	13	-122592	1
-14460	14	-25908	8	-28788	5	-39312	14	-44784	13	-139116	13
-14628	14	-25980	8	-29052	5	-39480	14	-46188	6	-139236	13
-15456	13	-26256	7	-30588	6	-43752	12	-46356	5	-146268	12
-15576	13	-26328	7	-30756	5	-43848	12	-46620	5	-146364	12
-16368	13	-27276	11	-31020	5	-45696	13	-51708	6	-156360	2
-16488	13	-27456	10	-33636	11	-45816	13	-51876	5	-156528	1
-17280	9	-27516	10	-33816	10	-49164	9	-52140	5	-156696	1
-17472	8	-28356	12	-33876	10	-49356	8	-54936	9	-162732	2
-17544	8	-28452	12	-35028	13	-49428	8	-55128	8	-162900	1
-17820	7	-30072	11	-35148	13	-49704	7	-55200	8	-163068	1
-17892	7	-30252	10	-36588	13	-49776	7	-55476	7	-171156	6
-18348	13	-30312	10	-36708	13	-50904	4	-55548	7	-171324	5
-18468	13	-32340	12	-39492	12	-51072	3	-57480	11	-171588	5
-19236	11	-32436	12	-39588	12	-51432	3	-57660	10	-175704	4
-19416	10	-34416	4	-41280	11	-55764	11	-57720	10	-175872	3
-19476	10	-34584	3	-41460	10	-55944	10	-61608	12	-176232	3
-20052	2	-34944	3	-41520	10	-56004	10	-61704	12	-183612	14
-20220	1	-37224	13	-42312	4	-57408	12	-63660	2	-183780	14
-20388	1	-37344	13	-42480	3	-57504	12	-63828	1	-198480	4
-21372	11	-38256	12	-42840	3	-61176	2	-63996	1	-198648	3
-21552	10	-38352	12	-45336	6	-61344	1	-66264	9	-199008	3
-21612	10	-39456	14	-45504	5	-61512	1	-66456	8	-213192	4
-22716	12	-39624	14	-45768	5	-63360	2	-66528	8	-213360	3
-22812	12	-41688	11	-47256	4	-63528	1	-66804	7	-213720	3
-23244	12	-41868	10	-47424	3	-63696	1	-66876	7	-225048	14
-23340	12	-41928	10	-47784	3	-66756	9	-72240	2	-225216	14

-24504	11	-44004	6	-50268	13	-66948	8	-72408	1	-239328	12
-24684	10	-44172	5	-50388	13	-67020	8	-72576	1	-239424	12
-24744	10	-44436	5	-53832	6	-67296	7	-77412	12	-243732	9
-25068	11	-46416	12	-54000	5	-67368	7	-77508	12	-243924	8
-25248	10	-46512	12	-54264	5	-71616	2	-81696	6	-243996	8
-25308	10	-47664	12	-56676	4	-71784	1	-81864	5	-244272	7
-26232	14	-47760	12	-56844	3	-71952	1	-82128	5	-244344	7
-26400	14	-48684	12	-57204	3	-73116	4	-85752	11	-252432	9
-27096	12	-48780	12	-60420	2	-73284	3	-85932	10	-252624	8
-27192	12	-50520	12	-60588	1	-73644	3	-85992	10	-252696	8
-27696	9	-50616	12	-60756	1	-75912	9	-91596	13	-252972	7
-27888	8	-51444	12	-61584	11	-76104	8	-91716	13	-253044	7
-27960	8	-51540	12	-61764	10	-76176	8	-95220	6	-261276	2
-28236	7	-52248	14	-61824	10	-76452	7	-95388	5	-261444	1
-28308	7	-52416	14	-63888	6	-76524	7	-95652	5	-261612	1
-28896	6	-53988	12	-64056	5	-79344	6	-98028	4	-266820	14
-29064	5	-54084	12	-64320	5	-79512	5	-98196	3	-266988	14
-29328	5	-55884	13	-66372	2	-79776	5	-98556	3	-278844	2
-30132	6	-56004	13	-66540	1	-81156	9	-102936	4	-279012	1
-30300	5	-56856	12	-66708	1	-81348	8	-103104	3	-279180	1
-30564	5	-56952	12	-68292	9	-81420	8	-103464	3	-291204	12
-30804	2	-59124	9	-68484	8	-81696	7	-109104	11	-291300	12
-30972	1	-59316	8	-68556	8	-81768	7	-109284	10	-305184	6
-31140	1	-59388	8	-68832	7	-85044	9	-109344	10	-305352	5
-31776	2	-59664	7	-68904	7	-85236	8	-112152	14	-305616	5
-31944	1	-59736	7	-70512	9	-85308	8	-112320	14	-319728	2
-32112	1	-60216	11	-70704	8	-85584	7	-116232	6	-319896	1
-32712	6	-60396	10	-70776	8	-85656	7	-116400	5	-320064	1
-32880	5	-60456	10	-71052	7	-88620	11	-116664	5	-336072	6
-33144	5			-71124	7	-88800	10	-121332	11	-336240	5
-34056	6			-72708	14	-88860	10	-121512	10	-336504	5
-34224	5			-72876	14	-90132	9	-121572	10	-348972	6
-34488	5			-74076	6	-90324	8	-125028	12	-349140	5
-35616	6			-74244	5	-90396	8	-125124	12	-349404	5
-35784	5			-74508	5	-90672	7	-130368	13	-352764	11
-36048	5			-77904	6	-90744	7	-130488	13	-352944	10
-36288	11			-78072	5	-94620	12	-135372	2	-353004	10
-36468	10			-78336	5	-94716	12	-135540	1		
-36528	10			-79056	11	-98316	11	-135708	1		
				-79236	10	-98496	10	-137640	11		
				-79296	10	-98556	10	-137820	10		
						-103164	11	-137880	10		
						-103344	10	-139080	11		

					-103404	10	-139260	10		
					-104364	11	-139320	10		
					-104544	10				
					-104604	10				

Table A 8: Simulation Decisions

Decision	Selection	Units
Number of modes to solve for/include	15	
Incremental distance along load-path	6	inches
Time integration scheme	Hilber Hughes Taylor (HHT)	
Profile interpolation method	Linear	
Structural damping	1%	
Traffic speed	960, 5	in/sec
Solution time-step	0.0015, 0.5	sec

List of References

- AASHTO, 2018. Manual for Bridge Evaluation, 3rd ed. American Association of State Highway and Transportation Officials, Washington, D.C.
- AASHTO, 2014. AASHTO LRFD Bridge Design Specifications, 7th ed. American Association of State Highway and Transportation Officials, Washington, DC.
- AASHTO, L., 1998. Bridge design specifications. American Association of State Highway and Transportation Officials, Washington, DC.
- Allemang, R.J., 1999. Vibrations: analytical and experimental modal analysis. Struct. Dyn. Res. Lab. Dep. Mech. Ind. Nucl. Eng. Univ. Cincinnati.
- Allen, D.E., Rainer, J.H., 1976. Vibration criteria for long-span floors. Can. J. Civ. Eng. 3, 165–173.
- Aramraks, T., 1975. Highway Bridge Vibration Studies: Interim Report.
- Ashebo, D.B., Chan, T.H., Yu, L., 2007. Evaluation of dynamic loads on a skew box girder continuous bridge Part I: Field test and modal analysis. Eng. Struct. 29, 1052–1063.
- Au, F.T.K., Cheng, Y.S., Cheung, Y.K., 2001a. Vibration analysis of bridges under moving vehicles and trains: an overview. Prog. Struct. Eng. Mater. 3, 299–304.
- Au, F.T.K., Cheng, Y.S., Cheung, Y.K., 2001b. Effects of random road surface roughness and long-term deflection of prestressed concrete girder and cable-stayed bridges on impact due to moving vehicles. Comput. Struct. 79, 853–872.
- Beyond Traffic 2045, 2017. . US DOT.
- Billing, J.R., 1984. Dynamic loading and testing of bridges in Ontario. Can. J. Civ. Eng. 11, 833–843.
- Billing, J.R., Green, R., 1984. Design provisions for dynamic loading of highway bridges. Transp. Res. Rec.
- Bolotin, V.V., Armstrong, H.L., 1965. The dynamic stability of elastic systems. Am. J. Phys. 33, 752–753.
- BS, 2006. EN-1993-2: Eurocode 3: Design of steel structures-Part 2: Steel Bridges. Br. Stand. Inst. U. K.
- Canadian Standards Association, 2006. Canadian Highway Bridge Design Code. Mississauga, ON, Canada.
- Cantieni, R., 1983. Dynamic load tests on highway bridges in Switzerland-60 years experience of EMPA.
- Caprani, C.C., 2012. Lifetime highway bridge traffic load effect from a combination of traffic states allowing for dynamic amplification. J. Bridge Eng. 18, 901–909.
- Çatbaş, F.N., Kijewski-Correa, T., Aktan, A.E., 2013. Structural identification of constructed systems: approaches, methods, and technologies for effective practice of St-Id. American Society of Civil Engineers.
- Chang, D., Lee, H., 1994. Impact factors for simple-span highway girder bridges. J. Struct. Eng. 120, 704–715.

- Chatterjee, P.K., Datta, T.K., Surana, C.S., 1994. Vibration of continuous bridges under moving vehicles. *J. Sound Vib.* 169, 619–632.
- Cooper, D.I., 1997. Development of short span bridge-specific assessment live loading. *Saf. Bridg.* 64–89.
- Csagoly, P., Dorton, R.A., 1978. The development of the Ontario highway bridge design code. *Transp. Res. Rec.*
- Deng, L., Cai, C.S., 2010. Development of dynamic impact factor for performance evaluation of existing multi-girder concrete bridges. *Eng. Struct.* 32, 21–31.
- Deng, L., Yu, Y., Zou, Q., Cai, C.S., 2015. State-of-the-Art Review of Dynamic Impact Factors of Highway Bridges. *J. Bridge Eng.* 20, 04014080. [https://doi.org/10.1061/\(ASCE\)BE.1943-5592.0000672](https://doi.org/10.1061/(ASCE)BE.1943-5592.0000672)
- Ding, L., Hao, H., Zhu, X., 2009. Evaluation of dynamic vehicle axle loads on bridges with different surface conditions. *J. Sound Vib.* 323, 826–848.
- European Committee for Standardization (CEN), 2003. Eurocode 1: Actions on structures—Part 2: Traffic loads on bridges. Brussels, Belgium.
- Fenves, S.J., Veletsos, A.S., Siess, C.P., 1962. Dynamic Studies of the AASHO Road Test Bridges. *Highw. Res. Board Spec. Rep.* 73.
- FHWA, 2012. Highway Statistics Summary To 1995.
- Gaunt, J.T., Sutton, C.D., 1981. Highway bridge vibration studies.
- González, A., Cantero, D., OBrien, E.J., 2011. Dynamic increment for shear force due to heavy vehicles crossing a highway bridge. *Comput. Struct.* 89, 2261–2272.
- González, A., OBrien, E.J., Cantero, D., Li, Y., Dowling, J., Žnidarič, A., 2010. Critical speed for the dynamics of truck events on bridges with a smooth road surface. *J. Sound Vib.* 329, 2127–2146.
- Green, M.F., Cebon, D., Cole, D.J., 1995a. Effects of vehicle suspension design on dynamics of highway bridges. *J. Struct. Eng.* 121, 272–282.
- Green, M.F., Cebon, D., Cole, D.J., 1995b. Effects of vehicle suspension design on dynamics of highway bridges. *J. Struct. Eng.* 121, 272–282.
- Han, W., Wu, J., Cai, C.S., Chen, S., 2015. Characteristics and Dynamic Impact of Overloaded Extra Heavy Trucks on Typical Highway Bridges. *J. Bridge Eng.* 20, 05014011. [https://doi.org/10.1061/\(ASCE\)BE.1943-5592.0000666](https://doi.org/10.1061/(ASCE)BE.1943-5592.0000666)
- Honda, H., Kajikawa, Y., Kobori, T., n.d. Spectra of Road Surface Roughness on Bridges. *J. Struct. Div.* 108, 1956–1966.
- Huang, D., Wang, T.-L., Shahawy, M., 1995. Dynamic behavior of horizontally curved I-girder bridges. *Comput. Struct.* 57, 703–714.
- Huang, D., Wang, T.-L., Shahawy, M., 1993. Impact studies of multigirder concrete bridges. *J. Struct. Eng.* 119, 2387–2402.
- Huang, D., Wang, T.-L., Shahawy, M., 1992. Impact analysis of continuous multigirder bridges due to moving vehicles. *J. Struct. Eng.* 118, 3427–3443.

- Inbanathan, M.J., Wieland, M., 1987. Bridge vibrations due to vehicle moving over rough surface. *J. Struct. Eng.* 113, 1994–2008.
- Japan Road Association (JRA), 1996. Specifications for highway bridges. Part 1: Common specifications. Tokyo.
- Kim, C.W., Kawatani, M., Kim, K.B., 2005. Three-dimensional dynamic analysis for bridge–vehicle interaction with roadway roughness. *Comput. Struct.* 83, 1627–1645.
- Kim, C.-W., Kawatani, M., Kwon, Y.-R., 2007. Impact coefficient of reinforced concrete slab on a steel girder bridge. *Eng. Struct.* 29, 576–590.
- Kou, J.-W., DeWolf, J.T., 1997. Vibrational behavior of continuous span highway bridge— influencing variables. *J. Struct. Eng.* 123, 333–344.
- Kurihara, M., Shimogo, T., 1978. Vibration of an elastic beam subjected to discrete moving loads. *J. Mech. Des.* 100, 514–519.
- Kwark, J.W., Choi, E.S., Kim, Y.J., Kim, B.S., Kim, S.I., 2004. Dynamic behavior of two-span continuous concrete bridges under moving high-speed train. *Comput. Struct.* 82, 463–474.
- Kwasniewski, L., Li, H., Wekezer, J., Malachowski, J., 2006a. Finite element analysis of vehicle–bridge interaction. *Finite Elem. Anal. Des.* 42, 950–959.
- Kwasniewski, L., Wekezer, J., Roufa, G., Li, H., Ducher, J., Malachowski, J., 2006b. Experimental evaluation of dynamic effects for a selected highway bridge. *J. Perform. Constr. Facil.* 20, 253–260.
- Law, S.S., Zhu, X.Q., 2005. Bridge dynamic responses due to road surface roughness and braking of vehicle. *J. Sound Vib.* 282, 805–830.
- Leonhardt, F., 1988. Cracks and Crack Control in Concrete Structures. *PCI J.* 33, 124–145.
<https://doi.org/10.15554/pcij.07011988.124.145>
- Li, H., Wekezer, J., Kwasniewski, L., 2008. Dynamic response of a highway bridge subjected to moving vehicles. *J. Bridge Eng.* 13, 439–448.
- Li, J., Su, M., 1999. The resonant vibration for a simply supported girder bridge under high-speed trains. *J. Sound Vib.* 224, 897–915.
- Li, Y., OBrien, E., González, A., 2006. The development of a dynamic amplification estimator for bridges with good road profiles. *J. Sound Vib.* 293, 125–137.
- Lipari, A., Caprani, C.C., OBrien, E.J., 2017. Heavy-Vehicle Gap Control for Bridge Loading Mitigation. *IEEE Intell. Transp. Syst. Mag.* 9, 118–131.
- Liu, C., Huang, D., Wang, T.-L., 2002. Analytical dynamic impact study based on correlated road roughness. *Comput. Struct.* 80, 1639–1650.
- Loprencipe, G., Zoccali, P., 2017. Use of generated artificial road profiles in road roughness evaluation. *J. Mod. Transp.* 25, 24–33. <https://doi.org/10.1007/s40534-017-0122-1>
- Majka, M., Hartnett, M., 2008. Effects of speed, load and damping on the dynamic response of railway bridges and vehicles. *Comput. Struct.* 86, 556–572.

- McGetrick, P., Kim, C.-W., González, A., 2013. Dynamic axle force and road profile identification using a moving vehicle. *Int. J. Archit. Eng. Constr.* 2, 1–16.
- Ministry of Transport of the People's Republic of China (MTPRC), 2004. General code for design of highway bridges and culverts. Beijing.
- Nassif, H.H., Nowak, A.S., 1995. Dynamic Effect Of Truck Loads On Girder Bridges, in: Proceedings of the International Symposium on Heavy Vehicle Weights and Dimensions. Road Transport Technology. pp. 383–387.
- New Zealand Transport Agency (NZTA), 2013. Bridge Manual. Wellington, New Zealand.
- OBrien, E., Li, Y., González, A., 2006. Bridge roughness index as an indicator of bridge dynamic amplification. *Comput. Struct.* 84, 759–769.
- OBrien, E.J., Cantero, D., Enright, B., González, A., 2010. Characteristic dynamic increment for extreme traffic loading events on short and medium span highway bridges. *Eng. Struct.* 32, 3827–3835.
- OBrien, E.J., Keenahan, J., 2015. Drive-by damage detection in bridges using the apparent profile. *Struct. Control Health Monit.* 22, 813–825.
- O'Brien, E.J., McGetrick, P., González, A., 2014. A drive-by inspection system via vehicle moving force identification. *Smart Struct. Syst.* 13, 821–848.
- Park, Y.S., Shin, D.K., Chung, T.J., 2005. Influence of road surface roughness on dynamic impact factor of bridge by full-scale dynamic testing. *Can. J. Civ. Eng.* 32, 825–829.
- Paultre, P., Chaallal, O., Proulx, J., 1992. Bridge dynamics and dynamic amplification factors-a review of analytical and experimental findings. *Can. J. Civ. Eng.* 19, 260–278.
- Reiher, H., Meister, F.J., 1931. The effect of vibration on people. *Forsch. Auf Dem Geb. Ingenieurwesens* 2, 381–386.
- Romano, N., Masceri, D., Moon, F., Samtani, N., Murphy, T., de Murphy, M.L., 2017. Bridge Superstructure Tolerance to Total and Differential Foundation Movements.
- Schwarz, M., Laman, J.A., 2001. Response of prestressed concrete I-girder bridges to live load. *J. Bridge Eng.* 6, 1–8.
- Tyan, F., Hong, Y.-F., Tu, S.-H., Jeng, W.S., 2009. Generation of random road profiles. *J. Adv. Eng.* 4, 1373–1378.
- Wang, T.-L., Huang, D., 1992. Cable-stayed bridge vibration due to road surface roughness. *J. Struct. Eng.* 118, 1354–1374.
- White, D.W., 2012. Guidelines for analysis methods and construction engineering of curved and skewed steel girder bridges. Transportation Research Board.
- Willis, R., 1849. The effect produced by causing weights to travel over elastic bars. Rep. Comm. Appoint. Inq. Appl. Iron Railw. Struct. Append. HM Station. Off. Lond. UK.
- Wright, D.T., Green, R., 1964. Highway Bridge Vibrations: Part II, Ontario Test Programme. Department of Civil Engineering, Queen's University.
- Wu, Y.-S., Yang, Y.-B., Yau, J.-D., 2001. Three-dimensional analysis of train-rail-bridge interaction problems. *Veh. Syst. Dyn.* 36, 1–35.

- Yang, Y.B., Lin, C.W., 2005. Vehicle–bridge interaction dynamics and potential applications. *J. Sound Vib.* 284, 205–226.
- Yang, Y.-B., Lin, C.W., Yau, J.D., 2004. Extracting bridge frequencies from the dynamic response of a passing vehicle. *J. Sound Vib.* 272, 471–493.
- Yang, Y.-B., Yau, J.-D., Hsu, L.-C., 1997. Vibration of simple beams due to trains moving at high speeds. *Eng. Struct.* 19, 936–944.
- Zhang, Q.-L., Vrouwenvelder, A., Wardenier, J., 2001. Dynamic amplification factors and EUDL of bridges under random traffic flows. *Eng. Struct.* 23, 663–672.